DESIGN AND PERFORMANCE OF HIGH-EFFICIENCY FLEXIBLE THERMOELECTRIC MATERIALS AND DEVICES

A Thesis submitted by

Shuai Sun

For the award of

Doctor of Philosophy

2023

ABSTRACT

Thermoelectric (TE) materials, realizing the conversions between heat and electrics, have grasped intensive interest in temperature control, power generation, wearable electronics, and low-grade (< 400 K) waste heat recycling. Particularly, flexible TEs (FTEs) exhibit exceptional mechanical properties, light weight features, and outstanding processing performance. However, some unavoidable shortcomings such as insufficient TE performances, high toxicity, high price, and tedious pre-/post-processing steps still exist. Thus, this thesis focuses on preparing high-efficiency flexible TE materials, optimizing their performances, and digging into internal theories. Furthermore, as-prepared materials are utilized to install TE devices, ensuring their practical applications. We initially developed a super-large 25×20 cm^2 commercial-graphite produced p-type composite films, by one-step standard industrial hot-pressing process. The prepared composite films with an optimized power factor (S^{2}σ) of 94 μW m^{-1} K^{-2} are highly flexible and industrially promising. Furthermore, we utilized the ultrafast and cost-effective hot-pressing method to fabricate an ionic liquid/phenolic resin/carbon fiber/expanded graphite hybrid n-type film. The expanded graphite as the major component enables high flexibility, the introduction of phenolic resin and carbon fiber enhances the shear resistance and toughness of the film, while the ion-induced carrier migration contributes to a high power factor of 38.7 μW m^{-1} K^{-2}. At last, a graphene oxide hybrid ionic FTE film was prepared, showing high comprehensive TE performance of S of −76.7 mV K^{-1}, $S^2\sigma$ of 85.9 μW m^{-1} K^{-2}, and ZT of 0.086 at 383 K, which is competitive among existing ionic thermoelectric materials. Simultaneously, tensile strength of 219.7 kPa, elongation at break of 389 %, Young's module of 84.1 kPa, toughness of 0.4 MJ m^{-3}, and flexibility of 180° bending are performed in this film. The in-situ integrated 9-leg 25×25 mm^2 flexible device generates a superior output voltage of 205 mV under a small temperature difference of 5.7 K. This work involves the comprehensive study in the FTE area, where the results will provide general and valuable guidance to the material preparation, performance enhancement, devices designation, and industrial amplification.

CERTIFICATION OF THESIS

I Shuai Sun declare that the PhD Thesis entitled *Design and performance of high-efficiency flexible thermoelectric materials and devices* is not more than 100,000 words in length including quotes and exclusive of tables, figures, appendices, bibliography, references, and footnotes.

This Thesis is the work of Shuai Sun except where otherwise acknowledged, with the majority of the contribution to the papers presented as a Thesis by Publication undertaken by the student. The work is original and has not previously been submitted for any other award, except where acknowledged.

Date: 05/07/2023

Endorsed by:

Zhigang Chen
Principal Supervisor

Xiaolei Shi
Associate Supervisor

Student and supervisors' signatures of endorsement are held at the University.

STATEMENT OF CONTRIBUTION

Paper 1:

Sun, S., Li, M., Shi, X.-L., & Chen, Z.-G. (2023). **ADVANCES IN IONIC THERMOELECTRICS: FROM MATERIALS TO DEVICES**, *Advanced Energy Materials*, *13*, 2203692. https://doi.org/10.1002/aenm.202203692.

The student **Shuai Sun** contributed 70% to this paper. Collectively Meng Li, Xiao-Lei Shi, Zhi-Gang Chen contributed the remainder.

Paper 2:

Sun, S., Shi, X.-L., Liu, W.-D., Wu, T., Wang, D., Wu, H., Zhang, X., Wang, Y., Liu, Q., & Chen, Z.-G. (2022). **CHEAP, LARGE-SCALE, AND HIGH-PERFORMANCE GRAPHITE-BASED FLEXIBLE THERMOELECTRIC MATERIALS AND DEVICES WITH SUPERNORMAL INDUSTRY FEASIBILITY**, *ACS Applied Materials & Interfaces*, *14*, 8066-8075. https://doi.org/10.1021/acsami.1c24649.

The student **Shuai Sun** contributed 70% to this paper. Collectively Xiao-lei Shi, Wei-Di Liu, Ting Wu, Dezhuang Wang, Hao Wu, Xiaoyong Zhang, Yu Wang, Qingfeng Liu, Zhi-Gang Chen contributed the remainder.

Paper 3:

Sun, S., Shi, X.-L., Li, M., Wu, T., Yin, L., Wang, D., Liu, Q., & Chen, Z.-G. (2023). **ULTRAFAST AND COST-EFFECTIVE FABRICATION OF HIGH-PERFORMANCE CARBON-BASED FLEXIBLE THERMOELECTRIC HYBRID FILMS AND THEIR DEVICES**, *ACS Applied Materials & Interfaces*, *15*, 25650-25660. https://doi.org/10.1021/acsami.3c05226.

The student **Shuai Sun** contributed 60% to this paper. Collectively Xiao-lei Shi, Meng Li, Ting Wu, Liangcao Yin, Dezhaung Wang, Qingfeng Liu, Zhi-Gang Chen contributed the remainder.

Paper 4:

Sun, S., Shi, X.-L., Lyu, W., Hong, M., Chen, W., Li, M., Cao, T., Yin, L., Hu, B., Mao, Y., Yang, Q., Liu, W., Liu, Q., & Chen, Z.-G. (2023). **STABLE, SELF-HEALABLE, AND HIGH-PERFORMANCE GRAPHENE-OXIDE-MODIFIED FLEXIBLE IONOGEL THERMOELECTRIC FILMS AND THEIR DEVICES**, under submission.

The student **Shuai Sun** contributed 60% to this paper. Collectively Xiao-lei Shi, Wanyu Lyu, Min Hong, Wenyi Chen, Meng Li, Tianyi Cao, Liangcao Yin, Boxuan Hu, Yuanqing Mao, Qingfeng Liu, and Zhi-Gang Chen contributed the remainder.

ACKNOWLEDGEMENTS

TABLE OF CONTENTS

LIST OF FIGURES

ABBREVIATIONS

TE: thermoelectric

FTE: flexible thermoelectric

i-TEs: ionic TEs

TEGs: TE generators

σ: conductivity

S: Seebeck coefficient

κ: thermal conductivity

ZT: figure of merit

PF: power factor

η: thermoelectric power generation efficiency

Φ: thermoelectric cooling efficiency

PEDOT:PSS: poly(3,4-ethylenedioxythiophene):poly(styrene sulfonate)

PA: polyacetylene

PANI: polyaniline

PVDF: polyvinylidene fluoride

PbTe: lead telluride

TiS_2: titanium disulfide

WS_2: tungsten disulfide

$NbSe_2$: niobium diselenide

CNTs: carbon nanotubes

SWCNTs: single-walled carbon nanotubes

MWCNTs: multi-walled carbon nanotubes

GO: graphene oxide

rGO: reduced graphene oxide

AM: acrylamide

APS: ammonium persulfate

XRD: X-ray diffraction

XPS: X-ray photoemission spectroscopy

SEM: scanning electron microscopy

EDS: energy dispersive X-ray spectrometer

DSC: differential scanning calorimetry

CHAPTER 1: INTRODUCTION

1.1. Background

Energy and environment are the key resources for human beings to survive and develop. However, conventional fossil energy brings strong drawbacks of releasing large amounts of greenhouse gas and producing polluting smokes, threatening the global ecology. Besides, with the continuous exploitation, the exhaustion of fossil energy is inevitable. Thus, new strategies of green and environmental-friendly energy are significant as a long-term human inheritance project, for instance the wind power, hydropower, geothermal power, nuclear power, solar power (Wan Mahari et al., 2021). The diversification and multi-leveling of energy supply will become an effective way for future energy assignment and environment protection (**Figure 1.1**) (Veers et al., 2019). As a result, our dependence on fossil consumption will be weakened, in which way energy utilization will become more reasonable and effective.

End-use energy consumption by sector, world
quadrillion British thermal units

End-use energy consumption by fuel, world
quadrillion British thermal units
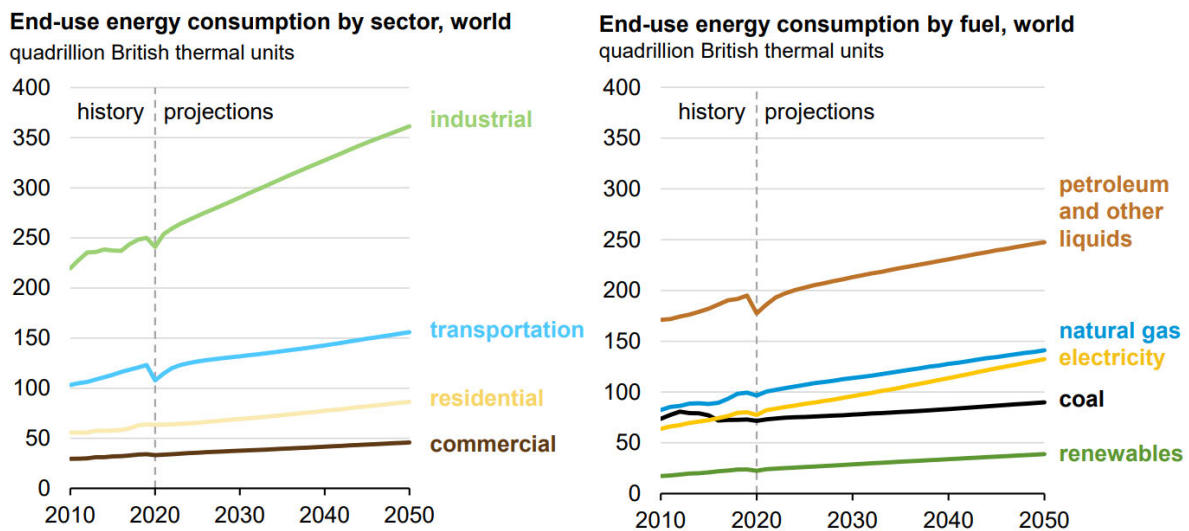
Figure 1.1. Global energy use nowadays and forecasts.

Thermoelectric (TE) technology, as a promising energy strategy, has grasp intensive interest to harvest and exploit low-grade waste heat (< 400 K). Last decade has witnessed great progresses in TE materials and devices (X. L. Shi, Zou, & Chen, 2020). It is well recognized that waste thermal power and temperature difference are commonly ubiquitous on the earth. TE conversion achieves collection and conversion from waste heat energy to electricity energy (Xun Shi & Chen, 2016; Tan, Zhao, &

Kanatzidis, 2016). For example, the mining or burning of fossil fuels inevitably brings heat lost. The secondary utilization of waste heat can improve energy efficiency, which is a meaningful way to solve the energy crisis and environmental pollution problems. Moreover, there are temperature differences and thermal potentials between the human body and the ambient, which is a tremendous heat source due to the huge population density. The efficient application and storage of human body heat is thereby a super sustainable and powerful energy strategy.

Generally, TE technology can be used for remote tasks, implantable/wearable devices, automotive industry as electricity generator, temperature sensors, and solid-state refrigeration (**Figure 1.2**) (Gusev et al., 2011; Han et al., 2017; Li, Liu, Liu, & Chen, 2022; Scheunemann et al., 2022). Historically, thermoelectric materials were initially used in some uncommon fields such as space exploration (Yang, Ma, Lei, Liu, & Li, 2013). Afterwards, in the early 1980s, the output power of military TE generators were developed to 500~1000 W in the USA. Meanwhile, a photovoltaic-thermoelectric composite system was developed in Japan, where a 500 W grade electricity can be generated utilizing waste incineration heat. In recent years, scientists and engineers have successfully developed micro TE generators and relevant TE theories (Fang et al., 2020; Hong et al., 2018; Wu, Xie, Chao, Yang, & He, 2019). With the advantages of small size, light weight, noiseless, mechanical irrotational, environmental friendly and timeproof, such efforts are of great significance.

Figure 1.2. Representative applications of thermoelectric technology.

TE materials, as the key point of TE technology, convert heat into electricity and vice versa (Bubnova et al., 2011; B. Kim, Shin, Park, Lim, & Kim, 2013; Vining, 2009). Specifically, flexible thermoelectric (FTE) materials have a few superior characteristics, such as low cost, stretchability, solution processability, and low toxicity, showing great potential in flexible and wearable electronics (L. Huang et al., 2020; Kee et al., 2019; Sevilla, Inayat, Rojas, Hussain, & Hussain, 2013). The sorts of FTE have also been expanded from conductive polymers/organic small molecules to metal-organic coordination polymers, carbon composite materials, *etc.* (Fan, Zhang, Guo, & Chen, 2019; Nonoguchi et al., 2013). In terms of morphology, FTEs can be divided into flexible fibers, flexible thin films, and few flexible bulks (Carey et al., 2015; Hicks & Dresselhaus, 1993; MacLeod et al., 2017). In terms of material species, FTEs can be divided into organic conjugated polymers, organic small molecules, inorganic carbon composites, and inorganic metal alloys (Nonoguchi et al., 2013; Paul, Lu, & Eklund, 2017; H. Wang et al., 2020). Recently, FTE researches have boomed, where high-performance FTEs are constantly being discovered. However, performances of FTEs are still inferior to solid TE materials (L. Zhang, Shi, Yang, & Chen, 2021). Besides, with the continuous development of processing technology, it is required to promote the production and practical application of FTEs. For these reasons, novel high performance FTE materials and their application technologies are still under discovery.

1.2. Objective and Scope

The aim of this project is to prepare high performance flexible TE materials and devices. Moreover, the cost-effectiveness, industrial feasibility and biocompatibility of materials have also been taken into consideration. In order to obtain the desired materials, comprehensive objectives and scopes of the research are listed as follows:

i. Design a novel conventional-graphite based composite film with high flexibility and TE performance. Although kinds of TE materials are continuously being discovered, no large-scale application method has been established till now. As the first reason, TE conversion efficiency is still insufficient to gather practical-supporting energy. On the other hand, industrial feasible fabrication method and low-cost material consumption are of equal research importance. Herein, we aim to develop an industrial

grade FTE material with facile preparation method, which will provide reference for the follow-up research in this aspect.

ii. Discover strategies for further improving the TE performance of the above designed materials. After establishing method for preparing industrial realizable FTE materials, the improvement TE performance is of great importance. Therefore, the second object of this project is to modify the TE performance and fabricate both p-type and n-type materials. For example, ionic liquid and carbon fiber are designed as doping agents. Ionic liquids have been investigated to boost the Seebeck coefficient by previous research. Carbon fiber can provide enhanced strength and electric conductivity (σ).

iii. Design carbon material hybrid ionogel FTEs with further improved TE performance and flexibility. As a new member of TE family, ionic TEs (i-TEs) exhibit exceptional Seebeck coefficient and applicable power factor, as well as outstanding stretchability and biocompatibility. However, the major drawback of i-TEs is the generally unstable performance. By hybrid with carbon materials and employing the annealing process, we aim to obtain stable and high performance ionogel FTEs, which can be molded into films at the same time.

iv. Design FTE devices and adapt them to different application scenarios. In this project, devices suitable for different application environments and conditions will be studied. Specifically, human wrist will be designed as the heat source where PET thin film will be designed as the substrate due to its efficient heat transfer ability. River water will be designed as the cold source where silica gel will be designed as the substrate due to its encapsulation effect. After simulating practical application environments, the corresponding output power densities will be evaluated.

1.3. Thesis Outline
This thesis is outlined into 7 chapters in sequence as follows:

Chapter 1 is the background and objective of this thesis.

Chapter 2 overviews the latest advances of FTEs in literature, including fundamentals, materials, properties, optimizations, moldings, and devices.

Chapter 3 is the statements, introductions, and basic principles of the experimental methods involved in this project.

Chapter 4 describes the development of super-large 25×20 cm^2 graphite based composite films, produced *via* one-step standard industrial hot-pressing process. The composite flexible films are featured by great promising points of high TE performance and super promising industrialization operability. Additionally, two types of flexible thermoelectric devices adapt to different application scenarios are installed based on such novel composite.

Chapter 5 describes the development an ultrafast and cost-effective hot-pressing method to fabricate a novel carbon-based hybrid film, which consists of ionic liquid/phenolic resin/carbon fiber/expanded graphite. After the comparison based on the ratios between power factor with fabrication time and cost among the current conventional carbon-based thermoelectric composites, our hybrid films show the best cost-effective. Besides, a flexible thermoelectric device, assembled by the as-designed hybrid films, shows great potential for temperature sensing.

Chapter 6 describes the development a stable, self-healable and high-performance graphene oxide modified flexible ionic TE material, where graphene oxide particles are well-dispersed. The $S^2\sigma$ and *ZT* value reach 85.9 µW m^{-1} K^{-2} and 0.086 respectively. Moreover, promising flexibility, stretchability, and self-adhesivity are simultaneously achieved by the as-prepared film. Comprehensive properties of the as-prepared films are stable after depositing in air for 7 days. Besides, an in-situ integrated 25×25 mm^2 device generates outstanding thermopower of 205 mV under a temperature difference of 5.7 K.

Chapter 7 draws the conclusions of this thesis and point out the potential outlooks in this research area.

CHAPTER 2: LITERATURE REVIEW

In this part, an overview of TE effect will be initially summarized to introduce fundamental theories for TE design and performance tuning. Then typical organic and inorganic FTE materials will be presented, and their properties will be studied. Some modification strategy including doping, pre-/post-processing, annealing, compounding, and morphology adjustment will be discussed simultaneously in this part. In the end, the current challenge and outlook will be point out towards prospects.

2.1. Thermoelectric mechanisms

2.1.1. Thermoelectric effects

Thermoelectric effect is a summation of electricity generated by temperature difference and temperature difference generated by electricity, including Seebeck effect, Peltier effect and Thomson effect, as shown in **Figure 2.1** (Rowe, 2018; Slack & Rowe, 1995).
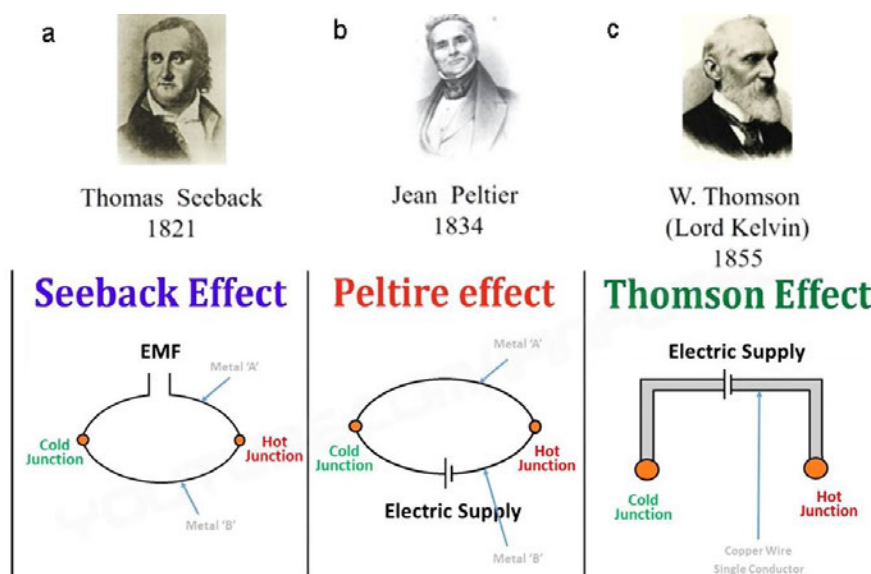
Figure 2.1. Schematic diagram of thermoelectric effects (a) Thomas Johann Seebeck (German) and Seebeck effect, (b) Jean Charles Athanase Peltier (French) and Peltier effect, (c) William Thomson (Ireland) and Thomson effect.

In 1823, Thomas Johann Seebeck (German) first reported the discovery of Seebeck effect in the "Prussian Academy of Sciences". He claimed that in a circuit bonded by two different metals, an electric potential will be raised if there is a temperature difference between the two contact points. This theory was confirmed by numerous following experiments and practices, which provides the working principles of

thermocouples (to measure temperature) and thermoelectric generators (to achieve TE power generation). Generally, Seebeck effect can be expressed as (X. L. Shi et al., 2020):

$$S_{ab} = S_a - S_b = \frac{\Delta V}{\Delta T} \ (\Delta T \to 0) \tag{1}$$

where S_{ab} is the relative Seebeck coefficient of two conductive materials, S_a and S_b are the absolute Seebeck coefficient of conductive materials a and b, and V is the thermoelectromotive voltage. The Seebeck coefficients are intrinsic properties of the materials, which is directly determined by the electronic structure. Seebeck effect is the primarily fundamental mechanism for TE generator design.

Twelve years after Seebeck effect was discovered, Jean Charles Athanase Peltier (French) published in the French "Annual Book of Physics and Chemistry" about the Peltier effect. Specifically, if a current is imposed to a circuit composed of two different metals, one of the contact points will releases heat and the other will absorbs heat. Peltier effect is the inverse effect of the Seebeck effect. As a result, heat can be used directly to generate electricity, and electricity can also be used in reverse for refrigeration (**Figure 2.2**). Peltier effect can be expressed as the following general formula (X. L. Shi et al., 2020):

$$\pi = \frac{Q}{I} \tag{2}$$

where π is the Peltier coefficient, Q presents the heat energy, and I is the electric current across the circuit. Peltier effect is the fundamental working principle of TE coolers.
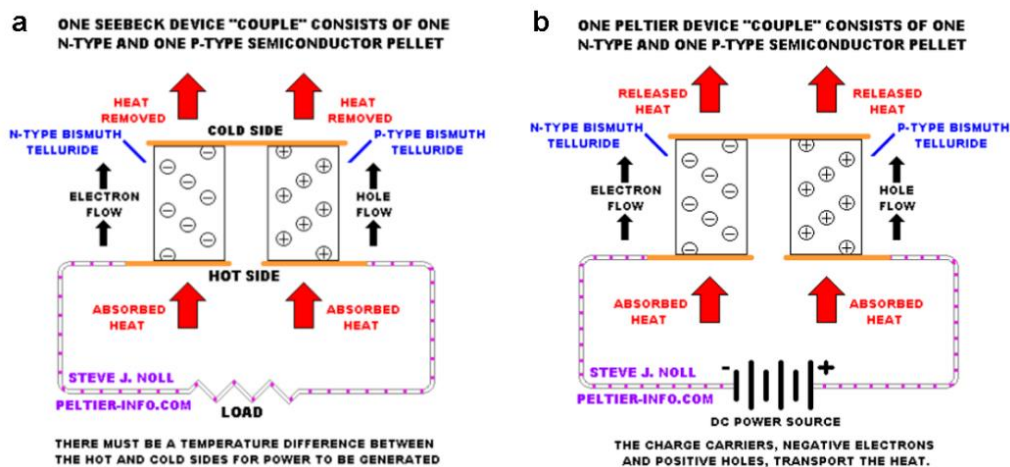
Figure 2.2. Principle of (a) Seebeck effect and (b) Peltier effect (Shafiei et al., 2016).

Subsequently in 1855, William Thomson, one of the founders of thermodynamics, used the thermodynamic theory to analysis the Seebeck phenomenon and the Peltier phenomenon (Thomson, 1857). The physical relationship between the above processes was thus established, which is exactly the Thomson effect written as (X. L. Shi et al., 2020):

$$\beta = \frac{Q}{I\Delta T} \tag{3}$$

where β is the Thomson coefficient, and ΔT is the temperature difference. Thomson effect is suitable for homogeneous materials without conjunctions. However, the value of Thomson coefficient is tiny, leading to a less widespread application than the Seebeck and Peltier effect.

The relationship between the Seebeck coefficient, Peltier coefficient, and Thomson effect can be expressed as follows (X. L. Shi et al., 2020):

$$\pi_{ab} = S_{ab}T \tag{4}$$

$$\beta_a - \beta_b = \frac{\mathrm{d}S_{ab}}{\mathrm{d}T}T \tag{5}$$

2.1.2. Thermoelectric parameters

The comprehensive performance of TE materials is usually measured by the dimensionless parameter figure of merit (*ZT*) (Aghelinejad, Zhang, & Leung, 2019; Allouhi, 2019). Advanced TE materials will show high *ZT* values. Relevant calculation formula is shown as follows (L. Zhang et al., 2021):

$$ZT = \frac{S^2\sigma}{\kappa_e + \kappa_l}T \tag{6}$$

where S is the Seebeck coefficient, σ is the conductivity, T refers to the absolute temperature, κ_e is the electronic thermal conductivity, and κ_l is the lattice thermal conductivity. The value of $S^2\sigma$ is defined as power factor (*PF*), which is another important parameter to evaluate the TE performance, especially FTE films.

From formula (6), it can be found that the enhancement of *ZT* value can be achieved by increasing the numerator term (S and σ), or reducing the denominator term (κ_e and κ_l). However, the biggest challenge to boost *ZT* is that these key coefficients are all determined by the electronic structure, carrier concentration and transport characteristics of the material. It can be seen from **Figure 2.3** that S, σ and κ which

comprehensively determine the thermoelectric properties of the material are interrelated and mutually restrictive (Mateeva, Niculescu, Schlenoff, & Testardi, 1998). Specifically, the Seebeck coefficient is negatively related to the carrier concentration, while the conductivity ($\sigma = \mu n e$, where μ is the carrier mobility, n is the carrier concentration, and e is the elementary charge) is positively related to the carrier concentration (Wood, 1988). Consequently, an appropriate carrier concentration must be optimized to maximize the *ZT* value of thermoelectric materials.
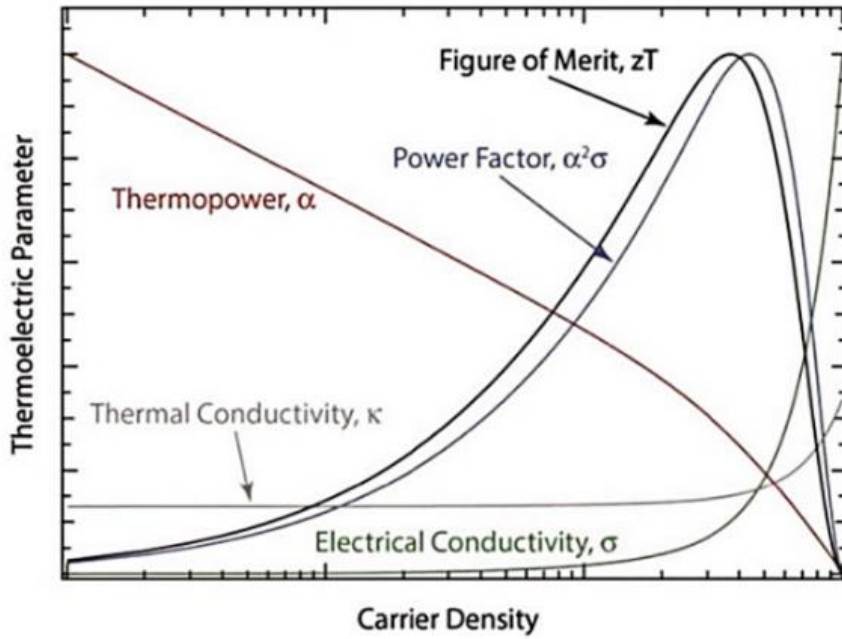
Figure 2.3. The dependence of TE properties on carrier density (Blackburn, Ferguson, Cho, & Grunlan, 2018).

2.1.3. Thermoelectric conversion efficiency

TE technology can be classified to both power generation and thermal refrigeration working modes (Cao, Shi, & Chen, 2023). Therefore, TE conversion efficiency is discussed in terms of TE power generation efficiency (η) and TE cooling efficiency (Φ) specifically. The maximum corresponding efficiencies are functions of *ZT* and temperature, and the expressions are as follows (X. L. Shi et al., 2020):

$$\eta_{max} = \left(\frac{T_h - T_c}{T_h}\right) \left[\frac{\sqrt{1+zT}-1}{\sqrt{1+zT}+\left(\frac{T_h}{T_c}\right)}\right] \tag{7}$$

$$\Phi_{max} = \left(\frac{T_c}{T_h - T_c}\right) \left[\frac{\sqrt{1+zT}-\left(\frac{T_h}{T_c}\right)}{\sqrt{1+zT}+1}\right] \tag{8}$$

where T_h and T_c are the maximum temperature and the minimum temperature, at the hot and cold ends respectively. *ZT* is the figure of merit (for both n-type and p-type units) at the average temperature, $T=(T_h+T_c)/2$.

In terms of the η, which is majorly investigated in this project, the value of T_h-T_c/T_h is limited by the Carnot cycle efficiency to be lower than 1 (**Figure 2.4**). Thus, the key factor to maximize η is the *ZT* value, as revealed from formula (7). Thermoelectric conversion efficiency will be improved as the *ZT* value raises. As the *ZT* value improved, η approaches to the Carnot cycle efficiency. Among current TE systems, the *ZT* values of inorganic TE materials have reached 3, while the highest *ZT* value of organic TE materials are still less than 1. Generally, when the *ZT* value exceeds 1, TE materials will be practically application valuable. Moreover, TE materials can be applied to large-scale power generation or refrigeration when the *ZT* value is improved to 3, such as the recycle of solar thermal energy, and factory waste heat, *etc.* (Xiaolei Shi et al., 2018).
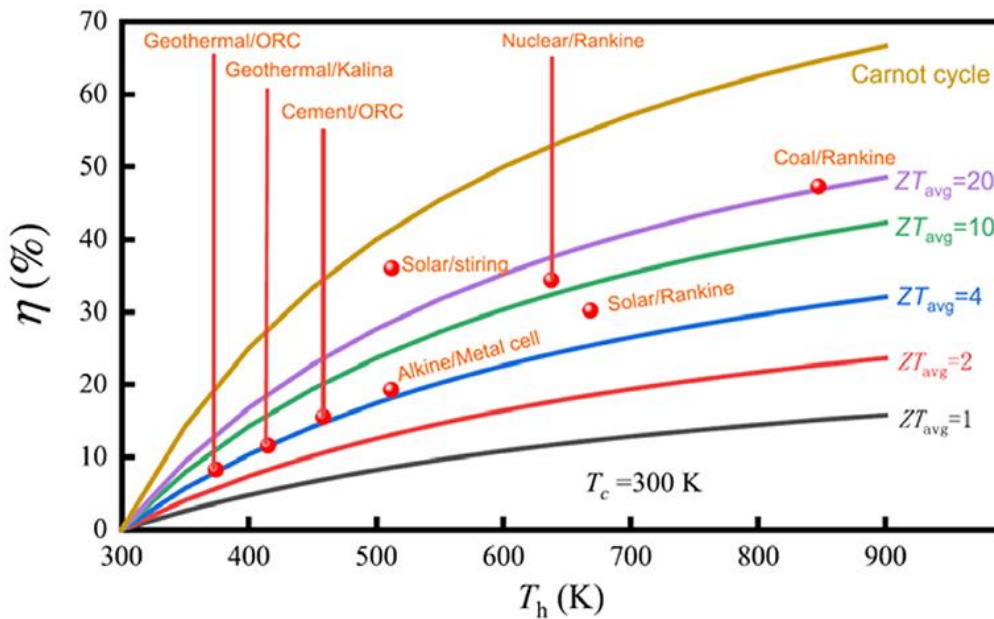
Figure 2.4. Relationships between the thermoelectric conversion efficiency and the *ZT* value (Yu et al., 2019).

In conclusion, the large-scale and low-cost application of TE materials are still under development. New material systems are in urgent to be explored aiming in practical servings.

2.2. Flexible thermoelectric materials

2.2.1. Organic small molecule-based thermoelectric materials

Small molecule organic TE materials are advanced due to simple structure, high purity, rapid processing, *etc.*, which have been developed in a long term. To date, typical small molecule organic TE materials involve charge transfer complexes (Kwak, Beni, & Chaikin, 1976; Ogawa et al., 1987), pentacene (Hayashi, Shinano, Miyazaki, & Kajitani, 2011; Xing et al., 2020), copper phthalocyanine (Inabe et al., 1985), fullerenes derivatives (J. Liu et al., 2019; J. Liu et al., 2018), and DPP molecular systems (**Figure 2.5**) (D. Huang et al., 2016; D. Huang et al., 2017).
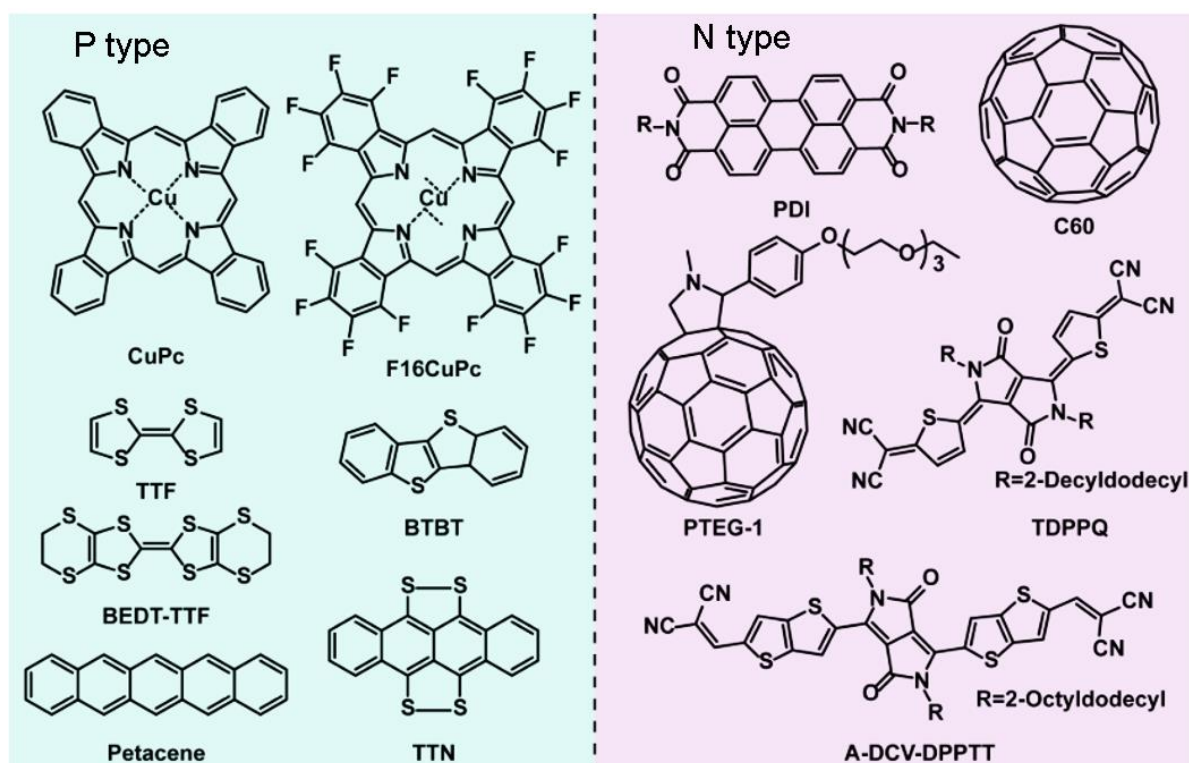
Figure 2.5. Molecular structures of representative small molecule organic thermoelectric materials.

In the 1980s, Ibers *et al.* prepared a novel single-crystal iodine-doped copper phthalocyanine showing TE performance (Ogawa et al., 1987). The σ and S reached 1000 S cm^{-1} and 45 μV K^{-1} respectively, where the PF value can achieve 202.5 μW m^{-1} K^{-2}. This performance maintained as the record high value of the copper phthalocyanine system since then. Müller *et al.* reported the TE properties of [(C$_6$H$_5$)$_3$AsCH$_3$]$^+$TCNQ$_2^-$ composite crystals with σ of 106 S cm^{-1} and S of -30 μV K^{-1} at room temperature (Müller, Ritschel, & Hänsel, 1969). Moreover, the S altered from

negative to positive with decreasing the temperature, indicating a transfer of the carrier type. Relevant research from D. Schweitzer's group were focused on the perylene-based charge transfer complexes (Jacobsen, Mortensen, Andersen, & Bechgaard, 1978). Plenty perylene compositions have been obtained including: $(pe)_2X_{1.1} \cdot 0.8CH_2Cl_2$, $(pe)_2X_{1.4}$, $(pe)_2X_{1.5} \cdot 0.5THF$, $(pe)_6X_1$, $(pe)_3X_1$, and $(pe)_2X_1 \cdot 2/3THF$, where X represents an $-As_6$ group or a PF_6^- group. Huewe *et al.* investigated the TE properties of p-type TTT_2I_3 and n-type $DCNQI_2Cu$ single crystal materials (Huewe et al., 2017). The *PF* of TTT_2I_3 and $DCNQI_2Cu$ reached 387 and 110 μW m^{-1} K^{-2} respectively at room temperature. Recently, researchers have significantly improved the performance and stability of small molecule TE materials. For instance, the A-DCV-DPPTT system was optimized through the molecular framework modification and doping strategy, a *PF* value up to 236 μW m^{-1} K^{-2} and a *ZT* value exceeded 0.2 were obtained (D. Huang et al., 2017).

2.2.2. Organic polymer-based thermoelectric materials

Compared with small molecules, polymer based organic TE materials provide the characteristics of superior molecular designability and wide energy level adjustment range (Goel, Heinrich, Krauss, & Thelakkat, 2019; Rojo et al., 2014; Yao, Zhang, & Zhang, 2019). Generally, the reported TE performance of polymer-based materials are higher than small molecule based materials, including conjugated polymers, coordination polymers and polymer hybrid composites, *etc.* Specifically, typical polymer based TE materials involve poly(3,4-ethylenedioxythiophene):poly(styrene sulfonate) (PEDOT:PSS), polyacetylene (PA) (Y. W. Park, Denenstein, Chiang, Heeger, & MacDiarmid, 1979; Zuzok, Kaiser, Pukacki, & Roth, 1991), polyaniline (PANI) (Chen, Kou, Cai, Yin, & Shen, 2017; Epstein et al., 1994; Hsieh et al., 2019; H. Liu, Hu, Wang, & Boughton, 2002), thiophene polymers (Burke & Bird, 2019; Glaudell, Cochran, Patel, & Chabinyc, 2015; Kiefer et al., 2019; Patel, Glaudell, Kiefer, & Chabinyc, 2016), and the recently developed PDPP polymer system (Ding et al., 2019; Jung et al., 2017) (see **Figure 2.6** for more details).
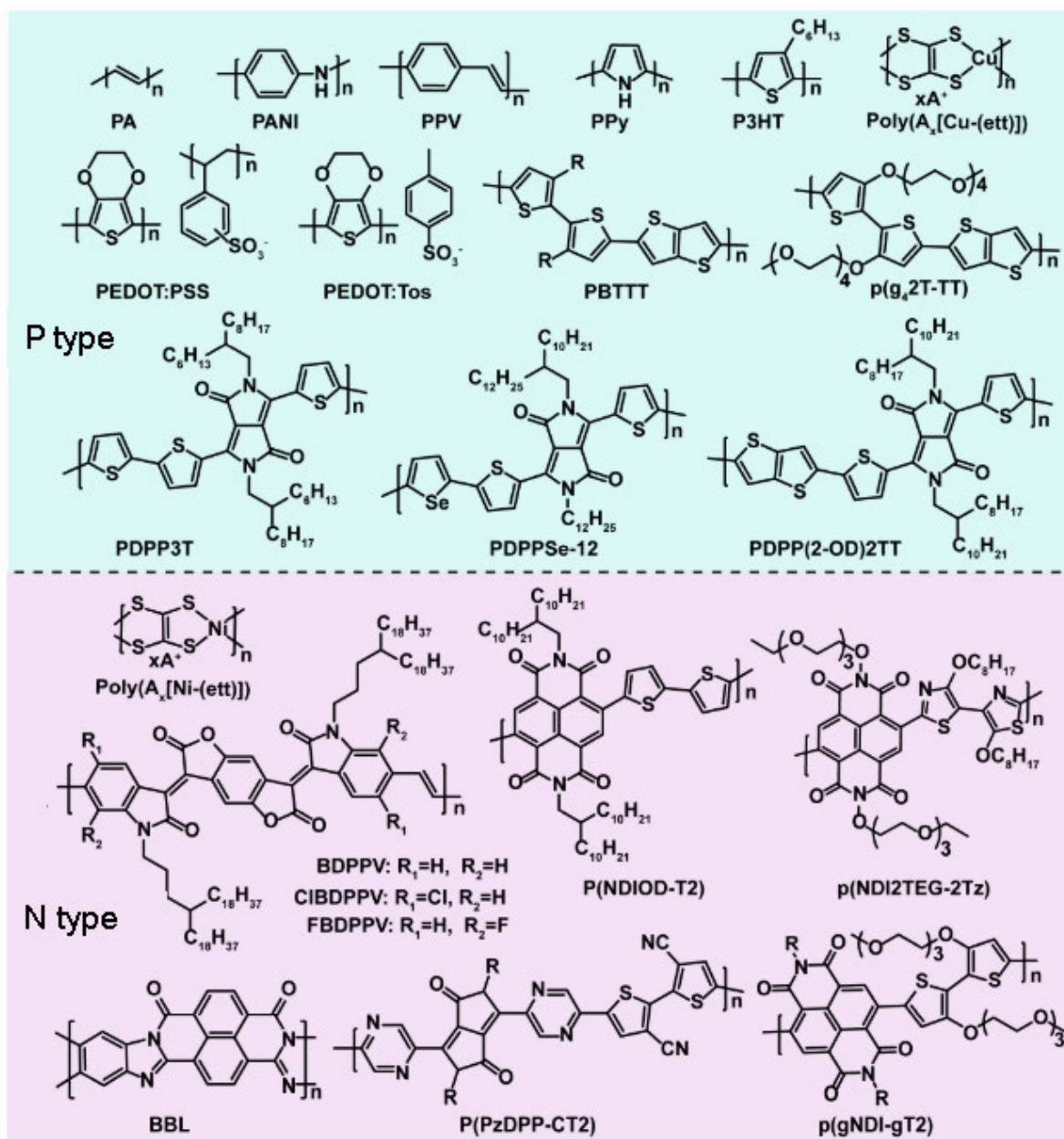
Figure 2.6. Molecular structures of representative polymer based thermoelectric materials.

PA was studied initially among conductive polymers. Zuzok *et al.* reported that after doping with iodine vapor, PA exhibited enhanced TE properties (Zuzok et al., 1991). Shinohara *et al.* fabricated polythiophene TE films firstly, using the electrochemical polymerization method. They found that, for polythiophene derivatives, the TE performance can be improved when small side chains are introduced (Shinohara, Hiraishi, Isoda, Imai, & Oikawa, 2008). Tsai *et al.* found that the combination of different conductive polymers can effectively increase the charge carrier concentration

(Tsai, Chang, Chen, Huang, & Whang, 2014). Additionally, new polymer-based TE materials are constantly being explored, such as open-shell polymers, stable radical polymers, *etc.*, basing on reasonable electronic structure designations (Noriega, Rivnay, Vandewal, & Koch, 2013). For example, pendant radicals can be attached to insulating main chains, to achieve hopping conduction after partial oxidation/reduction. Bubnova *etc.* prepared water-dispersible p-methylbenzenesulfonic acid doped PEDOT, instead of PEDOT:PSS (Bubnova et al., 2011). By adjusting the PEDOT oxidation degree, the *ZT* value was obtained to reach 0.25. Park *et al.* reported a water-dispersible PEDOT mixed polypyrrole with a power factor of 1270 $\mu W\ m^{-1}\ K^{-2}$ (T. Park, Park, Kim, Shin, & Kim, 2013). Under a temperature difference of 5 K, the average voltage generated by the film reached (592±18) μV. Recent efforts from Pipe *et al.* focused on the drop-coated commercialized PEDOT:PSS films (G. H. Kim, Shao, Zhang, & Pipe, 2013). By controlling the doping degree of DMSO and EG in the PEDOT:PSS thin film, excess PSS was dissolved to realize the major breakthrough *ZT* of 0.42. Liu *et al.* also proposed that the adding of ionic liquids to PEDOT can provide a pathway for boosting the S and the σ (C. Liu, Xu, Lu, Yue, & Kong, 2012).

2.2.3. *Inorganic metal-based thermoelectric materials*

As has been widely known, nano-structured materials behave higher *ZT* regarding inorganic metal-based materials. Besides, nanostructures can also bring flexibility to metal bulks to a certain extent, making it achievable to prepare inorganic FTE materials (Venkatasubramanian, Siivola, Colpitts, & O'Quinn, 2001).

Wu *et al.* reported a novel lead telluride (PbTe) nanocrystal coated flexible fiber in 2012 (Liang, Yang, Finefrock, & Wu, 2012). As shown in **Figure 2.7a**, the thickness of the PbTe layer was ~300 nm, which was coated on the surface of a single glass fiber. The κ was decreased to 0.22 $W\ m^{-1}\ K^{-1}$ due to the nanocrystalline structures. After further annealing, the *ZT* was improved to 0.7 at 400 K. More recently, their group also investigated the TE properties of the self-assembled Ag_2Te nanocrystalline thin films (Yanming Sun et al., 2015). It was found that the existence of small molecules promoted the thermoelectric properties optimizing of the Ag_2Te self-assembled films. The maximum *ZT* reached 0.712 by introducing 1,2-ethanedithiol dopants. Another research of Carroll's team focused on the preparation of one-dimensional/two-dimensional composite TE materials. Specifically, tellurium nanorods served as the

main TE component, and the polyvinylidene fluoride (PVDF) film served as a flexible substrate. The room temperature PF of the composite film reached 45.8 µW m^{-1} K^{-2} (Dun et al., 2015). Wan *et al.* pioneered an organic cation inserted titanium disulfide (TiS$_2$), by means of electrochemical intercalation (**Figure 2.7b**) (Wan et al., 2015). The obtained σ was 790 S cm^{-1}, PF was 450 µW m^{-1} K^{-2}, and κ was 0.12 W m^{-1} K^{-1}. At 373 K, its ZT reached 0.28. Lee *et al.* reported the TE applications of transition metal-based chalcogenides (Oh et al., 2016). The PF values of the n-type tungsten disulfide (WS$_2$) and p-type niobium diselenide (NbSe$_2$) films reached 7 and 34 µW m^{-1} K^{-2} respectively at room temperature. They also prepared FTE devices afterwards, which generated an output power of 38 nW under the temperature difference of 60 K.
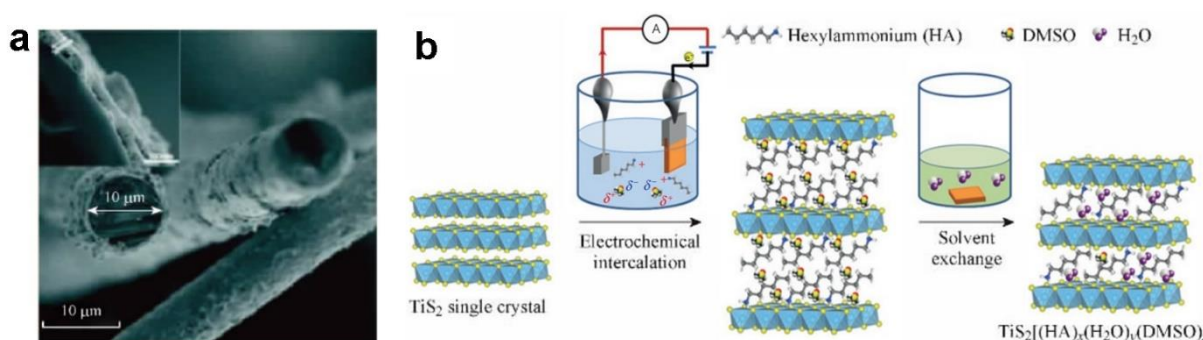
Figure 2.7. (a) SEM image of PbTe nanocrystal-coated glass fibers, (b) Synthesis of TiS$_2$ based inorganic-organic superlattices (Wan et al., 2015).

Although nano-sized inorganic compounds are endowed certain flexibility, the flexible substrates and complex treatments are required as well, to obtain ideally FTE devices. Thus, the development of novel inorganic FTEs is still of great significance.

2.2.4. Inorganic carbon-based thermoelectric materials

The fullerene-based film is the first-reported inorganic flexible TE films. In 1993, Wang *et al.* prepared an n-type potassium doped fullerene (K$_X$C$_{70}$) film with σ, S, and PF of 550 S cm^{-1}, -22.5 µV K^{-1} and 2.8 µW m^{-1} K^{-2} respectively (Z. H. Wang et al., 1993). Subsequently, most of the studies on carbon based flexible materials were focused on carbon nanotubes (CNTs) and graphene.

CNTs (including single-walled carbon nanotubes SWCNTs and multi-walled carbon nanotubes MWCNTs) are featured with small diameter, large surface area, high aspect ratio, and narrow band gap. However, SWNTs show better electrical properties compared with MWNTs, which are more suitable for TE preparation. Theoretical

calculations show that the maximum *ZT* value of SWCNTs can reach as high as 2 (Zhao et al., 2012). Generally, SWCNTs will inevitably absorb oxygen-containing impurities in the air, exhibiting p-type TE properties. However, p-type SWCNTs can convert to n-type after doping with an electron donor as dopant (Vavro et al., 2003). Nonoguchi *et al.* selected 33 kinds of organic dopants respectively to prepare both p-type and n-type optimized SWCNTs (**Figure 2.8a**) (Nonoguchi et al., 2013). The obtained materials were installed into a flexible device as shown in **Figure 2.8b**, generating 9.5 mV output voltage under a temperature difference of 33 K. Toshima *et al.* also prepared a novel TE composite film by combining CNTs with nickel coordination poly(vinyl tetramercaptan) (Toshima et al., 2015). As a result, high σ of 630 S cm^{-1}, low κ of 0.07 W m^{-1} K^{-1} and promising *ZT* value of 0.3 were obtained, which is one of the optimal CNT-based TE films.
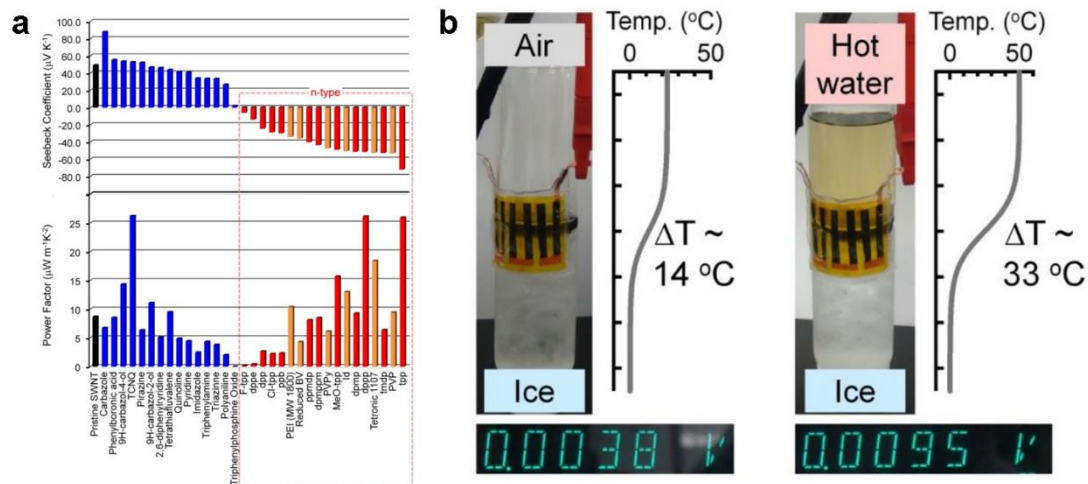
Figure 2.8. (a) Electrical conductivities and Seebeck coefficients of SWCNT films doped with shown molecules and (b) image of the flexible SWCNTs thermoelectric device and the thermovoltage-generation measurement (Nonoguchi et al., 2013).

2D graphene is a single-layered crystalline material, with hexagonal planar structures consisted by sp2 hybridized carbon atoms. The theoretical calculation results show that the *ZT* value of graphene can reach up to 4 (Ni, Liang, Wang, & Li, 2009; Sevinçli & Cuniberti, 2010). However, the experimental results are far inferior (Checkelsky & Ong, 2009). Sim *et al.* first prepared few-layer graphene using chemical vapor deposition method, obtaining a *S* of 40 µV K^{-1} (Sim et al., 2011). After deposing in the 1, 3, 6, 8-pyrene tetrasulfonic acid and 1, 1'-azobis(cyclohexanecarbonitrile) solution and heating for 15 min, the solution molecules were adsorbed into the graphene

sheets. At 523 K, the S was improved to 140 µV K^{-1}, whereas at 573K, the S was further improved to 180 µV K^{-1}. More recently, Guo *et al.* pioneered a reduced graphene oxide (rGO) flexible material as shown in **Figure 2.9** (Guo et al., 2016). Under a temperature difference of 75 K, the output power reached 0.43 µW. Besides, this device can work stably at a temperature up to 550 K.
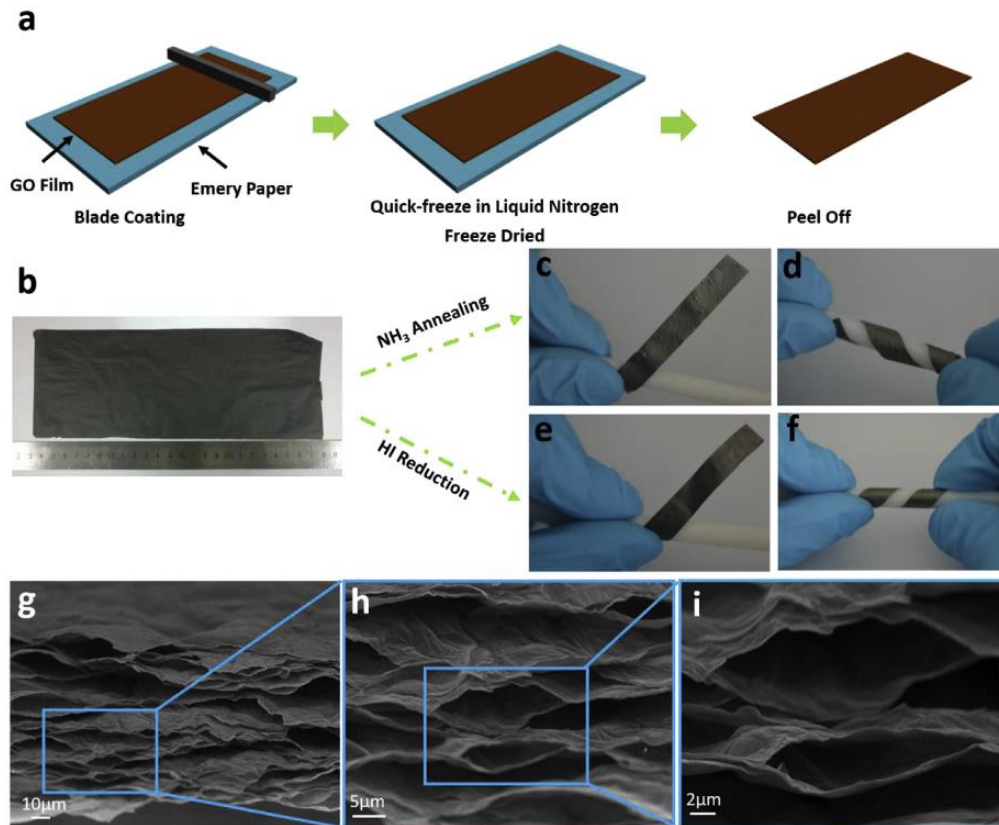
Figure 2.9. (a) Schematic illustration of the fabrication process of the porous graphene oxide films, (b) a piece of 25×11 cm^2 large film, (c-f) flexibility of the annealed films, (g-i) scanning electron microscopy (SEM) image of a cross-section of the porous graphene films (Guo et al., 2016).

2.2.5. Ionic thermoelectric materials (Paper 1)

I-TE materials are important boosting FTE materials, which is one of the main topics of this project. Therefore, we investigated this promising field in detail and prepared a literature publication here (presented afterward). As a framework of this review publication, we present several aspects of i-TE fundamentals, materials, properties, optimizations, moldings, and devices in turn. In the end, the current challenge and future prospect are introduced on this booming field.

Advances in Ionic Thermoelectrics: From Materials to Devices

Shuai Sun, Meng Li, Xiao-Lei Shi,* and Zhi-Gang Chen*

As an extended member of the thermoelectric family, ionic thermoelectrics (i-TEs) exhibit exceptional Seebeck coefficients and applicable power factors, and as a result have triggered intensive interest as a promising energy conversion technique to harvest and exploit low-grade waste heat (<130 °C). The last decade has witnessed great progress in i-TE materials and devices; however, there are ongoing disputes about the inherent fundamentals and working mechanisms of i-TEs, and a comprehensive overview of this field is required urgently. In this review, the prominent i-TE effects, which set the ground for i-TE materials, or more precisely, thermo-electrochemical systems, are first elaborated. Then, TE performance, capacitance capability, and mechanical properties of such system-based i-TE materials, followed by a critical discussion on how to manipulate these factors toward a higher figure-of-merit, are examined. After that, the prevalent molding methods for assembling i-TE materials into applicable devices are summarized. To conclude, several evaluation criteria for i-TE devices are proposed to quantitatively illustrate the promise of practical applications. It is therefore clarified that, if the recent trend of developing i-TEs can continue, the waste heat recycling landscape will be significantly altered.

1. Introduction

Due to relentless exhaustion of fossil fuels and more frequent climate disasters than ever before, human society has been facing with unprecedent energy crisis since stepping into the 21st century. This has drawn tremendous attention from both academia and industries on energy conversion techniques, which can produce electric energy from exploiting renewable power sources, as shown in **Figure 1**a.[1] Recently, increasing interest has been focused on thermoelectric (TE) technology, which can literally convert ambient heat into high value-added electricity.[2] Compared to its analogous heat-to-electricity technologies, TE takes the advantage of light weight, quietness, zero pollution emission, and an infinite lifetime (Figure 1b), making it ideal for self-powering applications that are equipped on human body or installed in rural areas.[3] The performance of TE devices is mainly governed by the dimensionless figure-of-merit of their constituent TE materials, defined as $ZT = S^2\sigma T/\kappa$, where T refers to absolute temperature, S, σ, and κ are the Seebeck coefficient, electrical conductivity, and thermal conductivity, respectively.[4] Practically, "Z" reflects the premise of TE materials being used for power generation, namely as a thermoelectric generator, while "T" regulates the working temperature under which heat transfer is valid.[5] As can be seen in Figure 1c, TE materials with high heat transfer property and a Z of $>10^{-3}$ K^{-1} (corresponds to $ZT > 0.3$ at room temperature) are suitable for making temperature sensors; in comparison, TE materials with a much higher Z of 10^{-2} K^{-1} (corresponds to $ZT > 3$ at room temperature) and low heat transfer property are preferable for making wearable devices.

On the attainment of satisfactory Z value, a large S, which is proportional to the magnitude of thermovoltage per temperature difference (ΔT), is highly desirable. However, the S of conventional electronic thermoelectric (e-TE) materials is limited to an order of 10^1–10^2 µV K^{-1} due to relatively low electronic enthalpy of inorganic materials, i.e., the S of electron gas is merely ≈87.5 µV K^{-1} at room temperature.[6] Considering a small ΔT of 20 °C as that between human skin and ambient environment, more than 100 inorganic TE legs are required to work comparably with a 1.5 V solid battery via calculation, which indicates that e-TE materials are unsuitable for low-grade (<130 °C) applications. As most of waste heat is emitted from low-grade sources such as industrial plants and vehicle exhaust, traditional e-TE devices are in niche market. As another form of charge carrier, ions can induce a much larger S in an order of a few mV K^{-1} due to higher ionic enthalpy than electronic enthalpy.[7] As a result, an ionic thermoelectric (i-TE) device needs only ≈8 legs to generate a 1.5 V voltage at a ΔT of 20 °C, indicating that i-TE device is feasible for microminiaturization and can be incorporated with wearable devices and electronic skins. Other advantages of i-TEs over e-TEs include i) good flexibility stemming from the normally organic matrix,

S. Sun, Z.-G. Chen
Centre for Future Materials
University of Southern Queensland
Springfield Central, Queensland 4300, Australia
E-mail: zhigang.chen@usq.edu.au

M. Li, X.-L. Shi, Z.-G. Chen
School of Chemistry and Physics
Queensland University of Technology
Brisbane, QLD 4000, Australia
E-mail: xiaolei.shi@qut.edu.au

**ADVANCED
SCIENCE NEWS**

www.advancedsciencenews.com

**ADVANCED
ENERGY
MATERIALS**

www.advenergymat.de
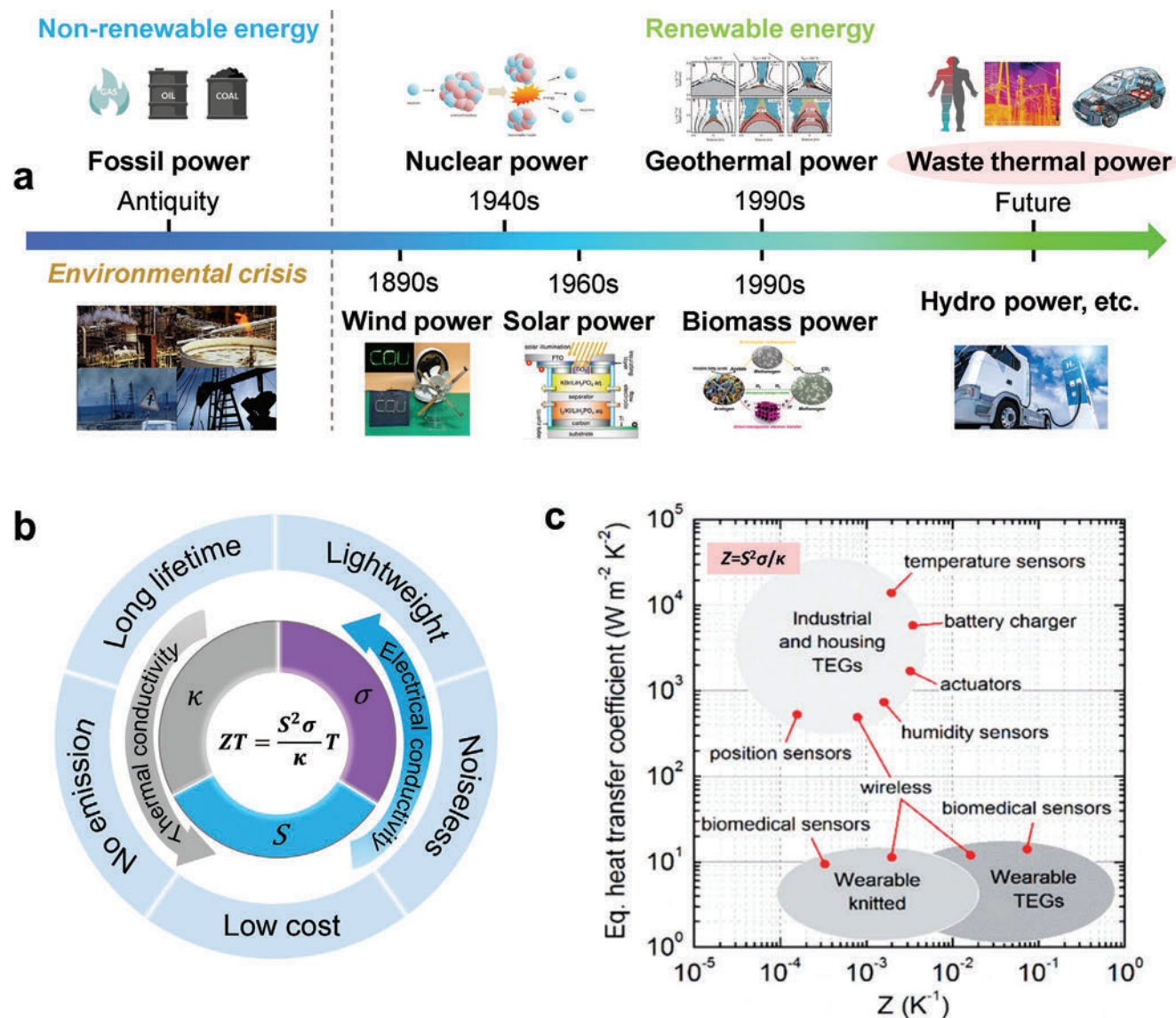
Figure 1. a) Evolution of energy utilization in industrialization process. Reproduced with permission.[8] Copyright 2015, Springer Nature. Reproduced with permission.[9] Copyright 2019, Elsevier. Reproduced with permission.[1a] Copyright 2020, Springer Nature. Reproduced with permission.[10] Copyright 2018, American Chemical Society. b) Superiorities and terminologies of thermoelectrics. c) Roadmap toward applications of TE devices. Reproduced with permission.[5] Copyright 2017, Royal Society of Chemistry.

ii) scalability due to facile fabrication process, and iii) low-cost and earth-abundance of raw materials.

Benefited from the colossal S which is reckoned as the most prominent parameter of TE materials, i-TE systems have been continuously developed. In the pioneering stage of i-TEs, material systems are focused on ionic solutions, including aqueous of acid (e.g., HNO_3),[11] base (e.g., NaOH),[12] salt (e.g., LiCl),[13] and ionic liquids (ILs) (e.g., 1-ethyl-3-methylimidazolium dicyanamide ([EMIM:DCA])).[14] As the i-TE technology steps forward for decades, diverse ongoing i-TE systems have been designed for acquiring exceptional S, e.g., 2.2 mV K^{-1} in redox liquid electrolytes,[15] 19 mV K^{-1} in solid polyelectrolytes,[16] −7.7 mV K^{-1} in n-type polymers,[17] 16.2 mV K^{-1} in p-type polymers,[18] 25.4 mV K^{-1} in polymer ionogels,[19] 14.8 mV K^{-1} in

nanoparticle ionogels,[20] 17 mV K^{-1} in IL embedded gelatins,[21] 24 mV K^{-1} in IL embedded celluloses,[12] and −18 mV K^{-1} in electronic/ionic combined systems.[22] There is also a trend of structure optimization for increasing S, which will be discussed in detail later.

Such progressive and short-term developments, however, have also led to controversies surrounding the understanding of the underlying mechanisms of i-TE materials and specified applications of i-TE devices, making future i-TE research far beyond simply envisaging for a higher S or ZT. This is the motivation behind this review, which is divided into six sections. In Section 2, the fundamentals and related theories are elucidated. In Section 3, the composition, physical state, and charge carrier feature of i-TE materials are summarized. In Section 4, the

**ADVANCED
SCIENCE NEWS**

www.advancedsciencenews.com

**ADVANCED
ENERGY
MATERIALS**

www.advenergymat.de

key properties of i-TE materials are overviewed, including TE performance, capacitance capability, and mechanical flexibility. In Section 5, the factors influencing TE performance and optimization approaches are discussed. In Section 6, the existing molding methods to make i-TE materials into feasible devices are iterated. In Section 7, the design strategies and practical performance of i-TE devices are examined. Perspective remarks on the outlook and challenges of this field are provided in the end. Interested readers are also referred to other reviews of thermoelectrochemistry.[23]

2. Ionic Thermoelectric Mechanisms

In this section, we explain the fundamental thermodiffusion and thermogalvanic effects, which result in i-TE phenomenon. To understand how i-TE effects can generate electric potential difference, several phenomenological models are examined. Heat transfer principles of i-TE materials are discussed from the perspective of the latest progress. Some existing disputes about i-TE conversion are presented as an open point of view in the end.

2.1. Fundamental Effects

Despite that both e-TE and i-TE materials can be functionalized to convert heat into electricity, their mechanisms are different. As shown in **Figure 2**a, in e-TE materials, electrons (holes) as charge carriers are driven by an electromotive force under an applied ΔT, which is known as the Seebeck effect.[24] Electrons in higher energy state populates from hot side to cold side, generating an electric potential difference along the opposite direction to temperature gradient, given the negative
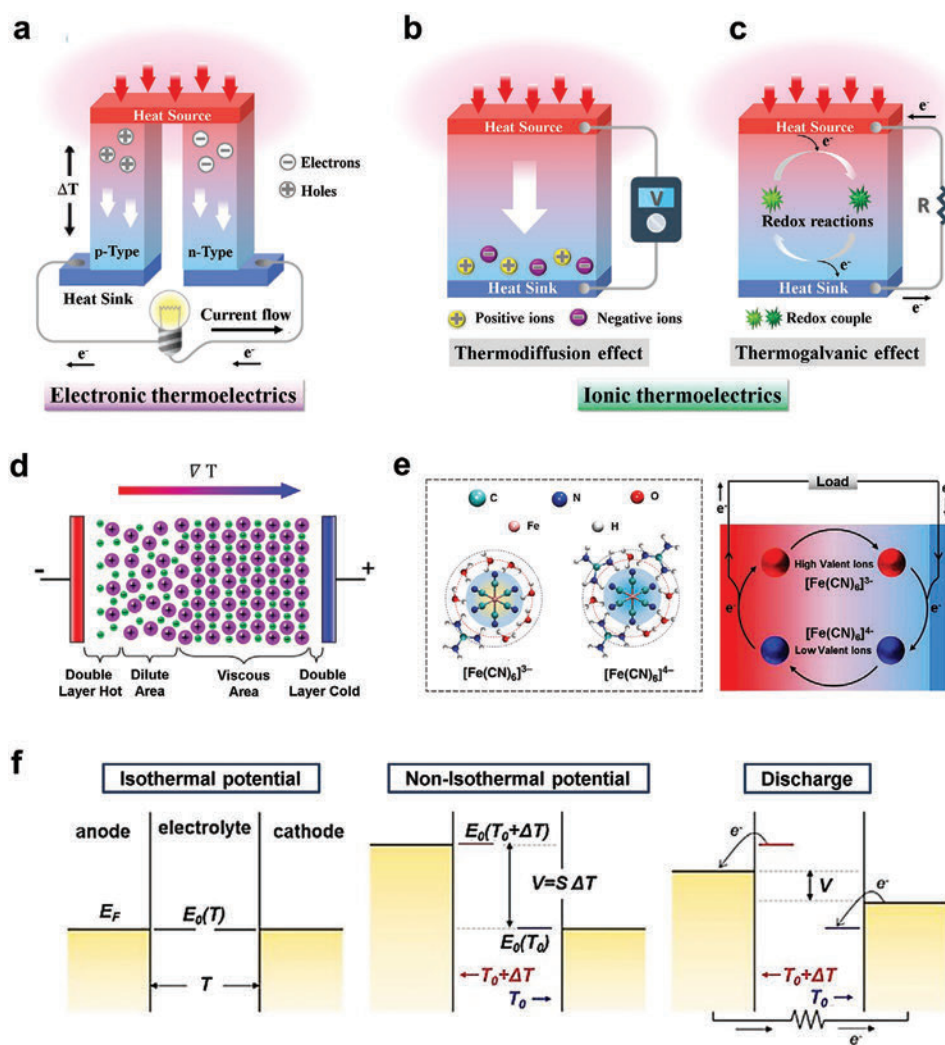
Figure 2. Schematic diagram of a) a group of p-type and n-type electronic thermoelectric (e-TE) materials, b) a thermodiffusive ionic thermoelectric (i-TE) material, and c) a thermogalvanic i-TE material. d) Internal structure of a thermodiffusive i-TE material in working mode. Reproduced with permission.[29] Copyright 2021, Wiley-VCH. e) Coordination structure and working mechanism of $Fe(CN)_6^{3-}/Fe(CN)_6^{4-}$ redox couple working in i-TEs. Reproduced with permission.[34] Copyright 2018, Springer Nature. f) The electric potential evolution in a thermogalvanic i-TE material. Reproduced with permission.[35] Copyright 2017, Elsevier.

sign of electrons. Whereas for i-TE materials, the generation of electric potential is rooted in two distinguished origins: thermodiffusion effect[25] and thermogalvanic effect,[26] as shown in Figure 2b,c.

2.1.1. Thermodiffusion Effect

Thermodiffusion effect derives from the Soret effect, which was first observed by Soret and Ludwig in the 19th century.[27] As illustrated in Figure 2b, in a thermodiffusive i-TE material subjected to a ΔT, the ion concentration is different at two electrode surfaces because of migration of ions from hot side to cold side. Considering the electronic neutrality, cationic and anionic ions coexist in i-TE materials. However, ions are normally featured with different migration speed (diffusion rate) due to distinctive size, activation energy and Coulomb force.[27] The dissimilar diffusion rate between cations and anions result in an imbalance of their respective ion concentration. According to the Gouy–Chapman–Stern theory, a double-layer area near the electrolyte/electrode interface will be formed, which consists of a Helmholtz layer and a diffusion layer, as illustrated in Figure 2d.[28] The ion concentration difference induces a viscous area near one electrode and a dilute area near the other, which can generate different chemical potential in their respective Helmholtz layers.[29] The chemical potential difference between two Helmholtz layers conversely triggers an electric potential difference between two electrodes.

I-TE materials based on the Soret effect are in analogy to e-TE materials based on the Seebeck effect, because both can generate a thermovoltage related to charger transfer enthalpy.[30] However, there are several apparent differences. i) An electron carries only unit charge, while an ion can carry much more charge depending on its overall valence state. ii) The transport of electrons should obey Fermi–Dirac statistical functional which is restricted within a small energy window,[31] while the transport of ions does not. iii) Electrons as major carriers contribute to electrical conductance solely in e-TE materials, while cations and anions exist simultaneously in i-TE materials; and most importantly. iv) Electrons can be cycled through external circuit, but ions agglomerate at electrodes, therefore, in i-TE materials, convection of electrolytes or connecting to capacitor are needed.[32]

2.1.2. Thermogalvanic Effect

The thermogalvanic effect is the second fundamental i-TE effect, which is defined based on thermally driven redox reactions,[33] as shown in Figure 2c. It can be seen that a thermogalvanic i-TE material contains at least one redox couples, which are oxidized at anode and reduced at cathode. The inclusive redox reaction can be expressed as $Ox + ne^- \rightleftarrows Red$, with a reaction rate related to local temperature. Figure 2e illustrates the internal structure of an i-TE material working based on the thermogalvanic effect, with assuming that hot electrode is cathode and cold electrode is anode. When a ΔT is applied, continuous redox reactions endow hot and cold electrodes with dissimilar chemical potential, leading to an electric potential difference.

Notably, unlike e-TE materials or thermodiffusive i-TE materials, enthalpy changes discontinuously in thermogalvanic i-TE materials, so the magnitude of generated thermovoltage is solely determined by redox couple species. For instance, as shown in Figure 2e, $Fe(CN_6)^{3-}/Fe(CN_6)^{4-}$ based i-TE materials normally exhibit an S larger than 2 mV K^{-1} arising from the huge Eastman entropy due to resonant valence state of $Fe(CN_6)$ ions.[34] Figure 2f schematically illustrates the chemical potential evolution in a thermogalvanic process. In which, thermogalvanic i-TE material is under an isothermal state, and the anode and cathode possess a balanced electric potential (E_0). Upon heating one of the electrodes, the equilibrium is destroyed, and the correspondent electric potential increases if an oxidation reaction occurs, or vice versa. After this system is connected to an external load, namely in a discharge process, electrons flow from anode to cathode through external circuit to balance electric potential difference.[35]

2.2. Ionic Transport Characteristics

In most cases, i-TE materials can be seen as a colloidal suspension, which means the thermodiffusion behavior of ions cannot be merely described by the Brownian motion theory.[36] Instead, colloid-based theories are adopted afterward, which is more appropriate for analyzing the kinetics and dynamics of i-TEs.[23a]

2.2.1. Ion Transport with No External Force[37]

Thermoelectric effects are basically carrier transport phenomena, the underlying transport fundamental is critically associated with S. In principle, the ion diffusion process occurs in every nonequilibrium moment with the appearance of dissipation. Onsager's theory was first used to describe the irreversible ion transport with a formal skeleton in 1931.[38] With approximations, the ion flux density of a specific ion source is

$$J = -\mu k_B T \cdot \nabla c - c\mu Q^* \cdot \frac{\nabla T}{T} \tag{1}$$

where the first term refers to mass diffusion (Fick's law) and the second term refers to thermophoresis (Onsager cross-coupling),[32a] Q^* is the "heat of transport", μ is ion mobility, and c is ion concentration.

However, the quantitative analysis of a nonequilibrium system is difficult. Assumption of equilibrium condition is usually needed to deal with ion transfer, as shown in **Figure 3**a. In this way, Equation (1) can be rewritten as[39]

$$\begin{aligned} J &= J_D + J_T \\ &= -D \cdot \nabla c - D_T c \cdot \nabla T \\ &= -D \cdot \nabla c - Q^* \frac{D}{2k_B T^2} \left[1 + \left(\frac{\partial \ln \gamma_{a\pm}}{\partial \ln m} \right)_T \right]^{-1} c \cdot \nabla T \end{aligned} \tag{2}$$

where D is the Brownian motion coefficient, and D_T is the thermodiffusion coefficient. The first and second terms

**ADVANCED
SCIENCE NEWS**

www.advancedsciencenews.com

**ADVANCED
ENERGY
MATERIALS**

www.advenergymat.de
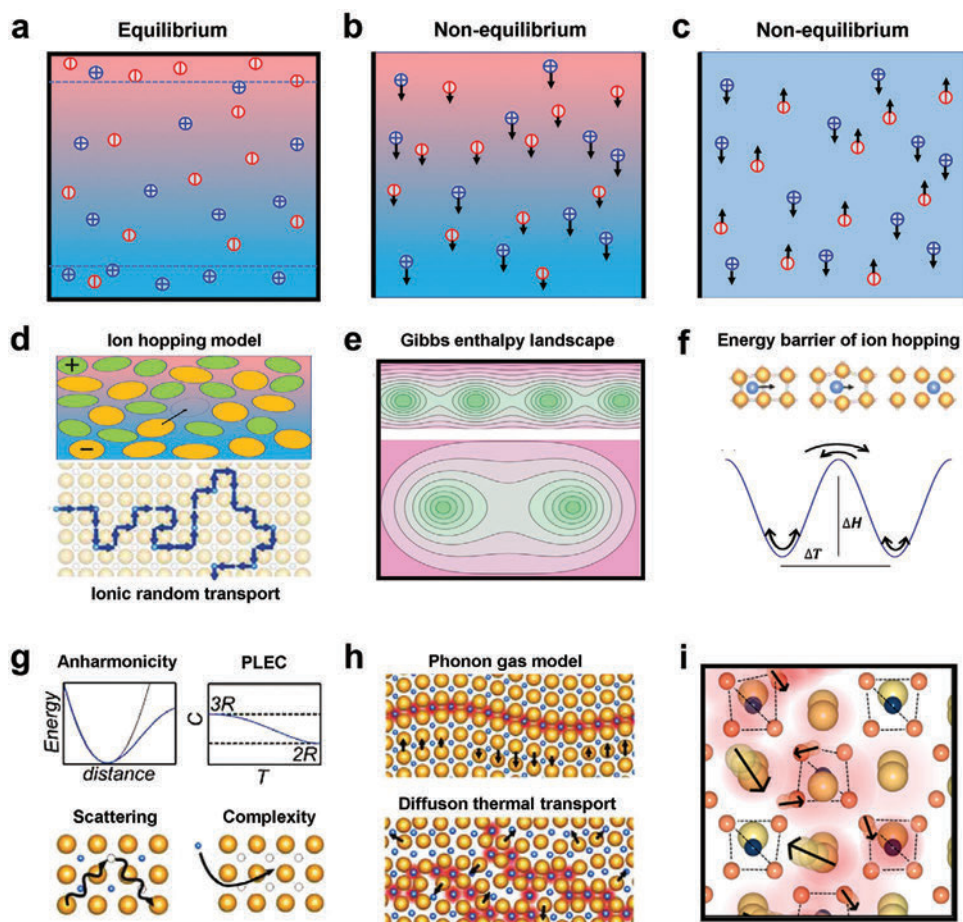
Figure 3. Schematic diagram of a) equilibrium state of isothermal i-TE systems, with no ion flows. Nonequilibrium state of isothermal i-TE systems, where cations and anions flow toward the b) same direction, and c) opposite directions. Reproduced with permission.[40] Copyright 2020, American Physical Society. d) Ion hopping model indicating the formation of vacancy (top) and ionic random transport path (bottom). e) Gibbs enthalpy landscape where ion hops over the barrier to neighboring sites. f) Gibbs enthalpy during hopping dynamics, where the temperature on the left is higher than the right side, showing stronger thermal fluctuations and more frequent jumps to the right side. Reproduced with permission.[63] Copyright 2021, American Physical Society. g) Underlying effects for low ion thermal conductivities. h) Long-range phonon-gas model (top) and local-scale diffuson model with correlated atomic displacements (black arrows), and heat transfer (red lines). Reproduced with permission.[60b] Copyright 2022, Wiley-VCH. i) Heat transport between uncorrelated atomic vibrations in the diffuson model, where arrows show schematic eigenvectors. Reproduced with permission.[60a] Copyright 2022, American Chemical Society.

are reflections of kinetic diffusion under the concentration gradient and thermal diffusion under the temperature gradient, respectively. Note that the latter term can be regarded as a product of c and thermodiffusive drift velocity $v = -D_T \nabla T$.[23a]

2.2.2. Cross-Coupling Effects

Despite mass diffusion and thermophoresis effect have been considered in the above discussions, i-TE systems are practically more complicated where cross-coupling effects are of importance. In the nonequilibrium simulation, cations and anions allowing charge flow in both cooperation and confrontation approaches (Figure 3b,c).[40] Turbulent flow is caused by specific neighboring vicinity, in which the collision and friction between free carriers and adjacent layers can occur. Ion currents drag themselves within layer surfaces, which bring either

positive or negative isotropy deviations.[28] The quantification of such ion pair-interaction potential is difficult and determined by the inherent characteristic (volume, viscosity, permittivity, etc.) of individual i-TE species.[41]

On the other hand, in the static equilibrium simulation, ions gradually accomplish accumulation driven by temperature difference. A counter electrical field will be generated to prohibit ion species transfer. Considering such cross-coupling situation, the drift of ion flux density is redefined as[42]

$$J = J_D + J_T + J_E \approx -D\left(\nabla c + c \frac{Q^*}{k_B T^2} \cdot \nabla T - c \frac{qE}{k_B T} \right) \tag{3}$$

where $J_E = \frac{qD}{k_B T} cE$ is the ion flux density driven by the counter electric field, q is the unit ion charge, and E is the electric field intensity which is further described as[43]

22

**ADVANCED
SCIENCE NEWS**

www.advancedsciencenews.com

**ADVANCED
ENERGY
MATERIALS**

www.advenergymat.de

$$E = -\psi_0 \cdot \frac{\nabla T}{T} \tag{4}$$

where ψ_0 is the thermoelectric potential factor, determined by the i-TE system nature. Specifically, in a binary monovalent i-TE system, there is[36b]

$$\psi_0 = \frac{Q_C^* - Q_A^*}{2e} \tag{5}$$

where Q_C^* and Q_A^* are the "heat of transport" of cation and anion species, respectively.

2.2.3. Derivation of Soret and Seebeck Coefficient

First, according to the Soret effect, the thermovoltage is mainly due to different thermodiffusion rates from cations to anions, which is rooted in their respective mobility. Under an equilibrium state with no external force, given $J = 0$, we have the definition of stationary ionic concentration gradient regarding Equation (2)

$$\nabla c = -\frac{D_T}{D} c \cdot \nabla T = -S_T c \cdot \nabla T \tag{6}$$

where $S_T = \frac{D_T}{D}$ is the Soret coefficient.[23a] The essence of S_T is to indicate relative ion concentration gradient against temperature gradient $\left(\frac{\nabla c}{c} = -S_T \cdot \nabla T \right)$, leading to the derivation of S envisaging for thermodiffusive i-TEs as thermovoltage against temperature difference, namely $\Delta V = -S \cdot \Delta T$. Based on the classical thermodynamic model, S_T is related to Q^*, which is the driving force[44]

$$S_T = \frac{Q^*}{k_B T^2} \tag{7}$$

Second, the key parameter differentiating i-TEs from e-TEs is the S, which determines the magnitude of thermovoltage under a certain ΔT. The Born model was also proposed in 1920 to define the ionic Seebeck coefficient[45]

$$S = \frac{Q^*}{N_A |q| T} \tag{8}$$

where N_A is Avogadro's constant.

In addition, the Seebeck coefficient for dual-ion electrolytes can be expressed by combining the Q^* difference between the cation and anion species[40]

$$S = \frac{w_+ Q_+^* - w_- Q_-^*}{eT} \tag{9}$$

where $Q_\pm^*$ is the weight mean, and $w_\pm = \frac{n_\pm}{n_+ + n_-}$ is the weight factor of positive and negative ions. The value of $\hat{S}^* = \frac{Q^*}{T}$ is

defined as the Eastman entropy, which is a combination of the transported entropy and the partial molar entropy.[46] Therefore in the microscopic scheme, the normally much larger S of i-TE materials than that of e-TE materials can be attributed to the difference in electronic Eastman entropy conceived in their respective thermoelectric process.[47]

2.2.4. Heat of Transport

As the value of Q^* plays an important role in the i-TE Soret coefficient and Seebeck coefficient, its evaluation should be summarized case by case. In liquid solutions, the evaluation of Q^* consists of thermodynamic and hydrodynamic two aspects, which is in accordance with Equation (1).[48] By assuming a most simple model, where charge interactions are restricted to electrostatics forces without dispersion, solvation, hydrogen bonds, etc., Q^* can be described based on the Stokes–Einstein friction law[49]

$$Q^* = \tau \frac{q^2}{8\pi\varepsilon a} \tag{10}$$

where $\tau = -\frac{d\ln\varepsilon}{d\ln T}$ is the numerical factor for temperature-dependent correction, ε is the permittivity, a is the radius of spherical-regarded particles.

More recently, the Debye screening length λ was considered to the expression of Q^*. It was found the ratio of a to λ crucially determined the calculation of Q^*, where small size and large size ions are deduced respectively as[36a,50]

$$Q^* = \left(\tau + (\tau+1)\frac{a}{2\lambda} \right) \frac{q^2}{8\pi\varepsilon a}, \quad (a < \lambda) \tag{11}$$

$$Q^* = (\tau+1)\frac{\lambda^2}{a^2}\frac{q^2}{8\pi\varepsilon a}, \quad (a > \lambda) \tag{12}$$

Regarding the solid-state matrix and gel-like systems, where strong interactions contribution need to be considered, hopping theory is introduced to describe the ionic transport behavior.[40] As shown in Figure 3d, ion carriers as the effective components of the entire i-TE system, are trapped at given sites and hop between neighbors after activation. Thus, their transport routine is random, which is disagree with e-TE materials. The hopping enthalpy landscape of a transport channel is displayed in Figure 3e, and the diagrammatic sketch of hopping energy is shown in Figure 3f. During the hopping process, the Gibbs enthalpy is reflected by the height of the energy peak, and the Gibbs entropy is reflected by the width of the valley at the adjacent degenerate minima. Under certain ΔT, forward hops are faster than backward hops, which leads to unidirectional net thermodiffusion with a Q^* expression of[51]

$$Q^* = \Delta H + k_B T - \frac{d\Delta G}{dc} T \frac{dc}{dT} \tag{13}$$

23

ADVANCED
SCIENCE NEWS

www.advancedsciencenews.com

ADVANCED
ENERGY
MATERIALS

www.advenergymat.de

2.3. Fundamentals of Ion Thermo-Redox

Completely different from physical thermodiffusion based i-TE materials, the thermo-redox process is essentially a thermal-driven chemical reaction. Thus, the TE conversion fundamental is more complex, which cannot be analogized from the analysis of chemical potential. In this section, we describe the relevant contents of current density according to the redox kinetics. However, the expression of S is deduced based on redox thermodynamics.

2.3.1. Redox Kinetics

As a basic kinetic relationship in the field of electrochemistry, the Butler–Volmer equation gives the dynamic current density as[52]

$$J = J_0 \cdot \left[\exp\left(\alpha_a \frac{nF}{RT} \eta \right) - \exp\left(-\alpha_c \frac{nF}{RT} \eta \right) \right] \tag{14}$$

where J_0 is the exchange current density, α_a and α_c are charge transfer coefficients along the anode and cathode direction respectively, and $\eta = E - E_{eq}$ is the activation overpotential.

While J is defined as the current per unit area on the electrode surface, an additional expression can be deduced by the volumetric reaction rate across the electrode/electrolyte interface, in charge balance condition[53]

$$J \cdot A = nF R_V \tag{15}$$

where R_V is redox reaction rate (positive sign for the cathodic reaction), and A is electrode surface area.

2.3.2. Redox Thermodynamics

Unlike what happens in e-TE or thermodiffusive i-TE materials, a thermogalvanic i-TE material is free from electronic transport, and therefore is independent on the flux density of charge carriers. Instead, it is the enthalpy change during the redox process that determines the magnitude of generated thermovoltage. Irrespective of an oxidation or a reduction reaction, its redox reaction enthalpy (H) can be expressed using the Gibbs free energy (G) as[54]

$$\Delta G = \Delta H - T \Delta \hat{S} \tag{16}$$

where $\hat{S}$ is the redox reaction entropy. Based on the definition, the relationship between electric potential (E) at electrodes and G is[55]

$$\Delta G = -nFE \tag{17}$$

where F is the Faraday constant, and n represents the number of electrons that are exchanged in the redox procedure. Combining Equations (16) and (17), E can be expressed as

$$E = \frac{T \Delta \hat{S} - \Delta H}{nF} \tag{18}$$

At this stage, we can define the ionic Seebeck coefficient of thermogalvanic i-TE materials as

$$S = \frac{dE}{dT} = \frac{\Delta \hat{S}}{nF} \tag{19}$$

where the dynamic value of nF can be evaluated from the kinetics analysis of Equations (14) and (15).

2.4. Heat Conductivity

I-TE materials are featured with low thermal conductivity values, which are commonly explained by the influences due to anharmonicity (phonon–phonon scattering),[56] "phonon liquid electron crystal,"[57] structural disorder (point-defects),[58] and component complexity (phonon boundaries),[59] as shown in Figure 3g. Rather than the conventional phonon-gas transport model, a dynamic diffuson model has been proposed very recently to contrapuntally explain the heat transport of i-TE materials based on the effective medium theory.[60] As demonstrated in Figure 3h, phonons carry heat in a long-scale range via propagation (phonon-gas model), which is generally accepted in ordered crystallized TE materials.[61] However, diffusons are recognized as the heat transport medium of i-TE materials. Instead of propagation, random diffuson happens on a local length scale. Atomic-level mass migration promotes diffuson squeeze to the adjacent vacancy, where thermal energy is carried (Figure 3i). Plenty experimental results in assistance with the diffuson model are verified. Moreover, unlike ion transfer which alters with the external environment (e.g., temperature), the ion vibrations contribute equally to heat transfer at a temperature >100 K.

More reasonably, the thermal conductivity of i-TE materials is attributed to a two-channel model, by parallel integration of the phonon-gas-type term and the diffuson-type term[56b,60]

$$\kappa = \kappa_{ph} + \kappa_{diff} \tag{20}$$

$$\kappa_{diff} = \frac{n^{\frac{1}{3}} k_B}{\pi} \int_0^\omega \frac{C(\omega)}{k_B} \frac{g(\omega)}{3n} \omega d\omega \tag{21}$$

where n is the atom number density, $g(\omega)$ is the diffuson vibrational density of states, and $C(\omega)$ is the heat capacity.

Regarding the attribution of κ_{ph}, the Mattheissen's rule is normally used to determine the temperature-dependent phonon scattering rate[62]

$$\tau^{-1} = \tau_p^{-1} + \tau_b^{-1} = C_1 \omega^2 T e^{-\frac{C_2}{T}} + A\omega \tag{22}$$

where C_1, C_2, and A are experimental constants capturing the phonon–phonon scattering (C_1, C_2) and the boundary scattering (A), respectively.

24

**ADVANCED
SCIENCE NEWS**

www.advancedsciencenews.com

**ADVANCED
ENERGY
MATERIALS**

www.advenergymat.de
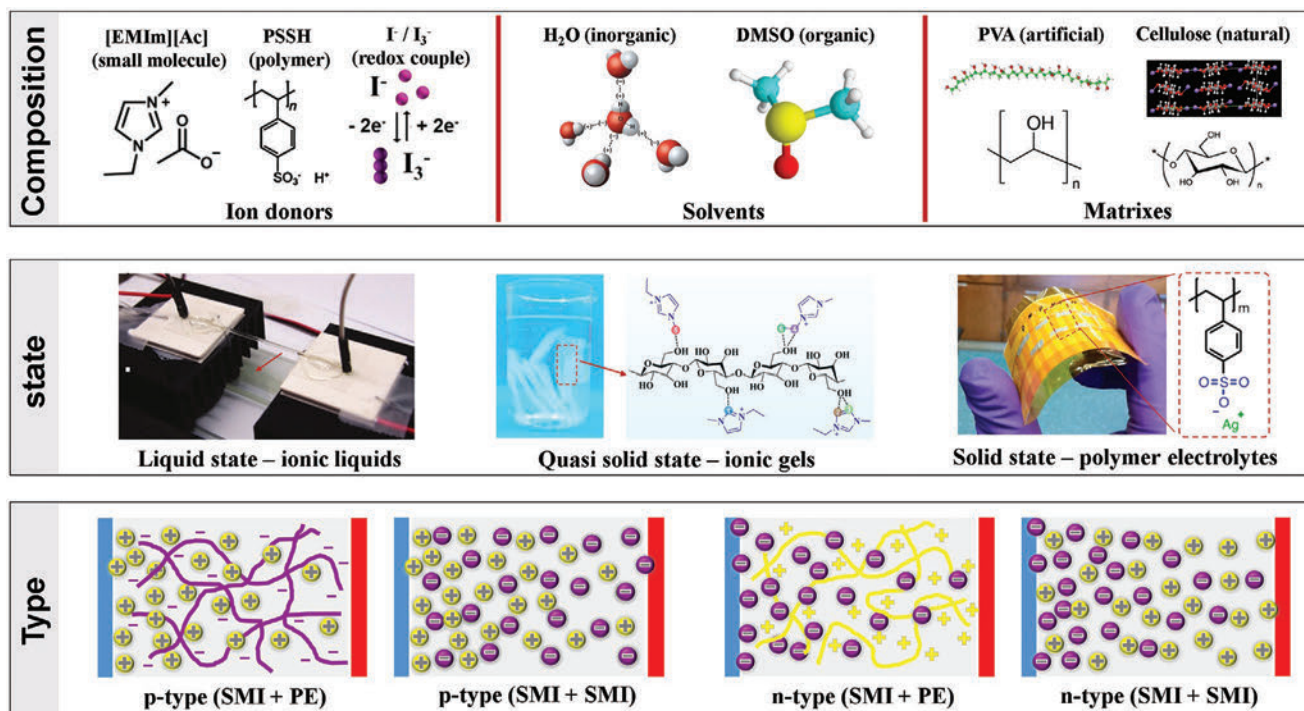
Figure 4. The classification of i-TE materials based on material composition, physical state, and dominant charge carrier type. Reproduced with permission.[66] Copyright 2019, Cell Press. Reproduced with permission.[12] Copyright 2019, Springer Nature. Reproduced with permission.[67] Copyright 2019, Elsevier. Reproduced with permission.[68] Copyright 2016, Wiley-VCH. Reproduced with permission.[69] Copyright 2021, Wiley-VCH. Reproduced with permission.[70] Copyright 2013, American Chemical Society.

2.5. Existing Disputes

There is a disputing opinion about the S of i-TE materials taking the electrode properties into account. Instead of an inherent nature of the materials, such a viewpoint proposes that the S value is determined by the assembly engineer of the whole device.[64] Specifically, the theory of ionic adsorption infers that the thermovoltage arises from the ion adsorption on the electrode surfaces. The adsorption degree at unit temperature is suggested to judge the TE conversion capability instead of the Soret effect. Herein, we assign the electrode ionic adsorption effects to the capacitance property of i-TE device. Although the interchange of the electrode will influence the measured S value, it can be regarded as an apparent exhibition extent rather than the intrinsic TE conversion capacity of the material. Detailed discussions about how electrode materials influence device capacitance will be involved in this article hereafter.

Recently, researchers also questioned the rationality of using ZT value to comprehensively evaluate i-TE performance. Perspectives are presented that the S value is only determined by the Eastman entropy, whereas the ionic diffusion coefficient relies on the speed of steady-state establishment. Different from the present cognition of $ZT = S^2\sigma T/\kappa$, a larger response time of i-TE equilibrium leads to instability in voltage formation, which is closely dependent on the temperature field evolution. As a result, a novel expression is accordingly given for i-TE materials, taking the magnitude of accumulated net charge (C) and the rate of electricity generation $\left(\frac{G_{T}}{\rho c}\right)$ into account[65]

$$ZT = \frac{CS^2 G_{\mathrm{T}}}{\kappa \rho c} T \tag{23}$$

where G_{T} is the interfacial thermal conductance, ρ is the material density, and c is the specific heat capacity.

3. I-TE Materials

In this section, we overview the common composition and physical state of i-TE materials, as shown in **Figure 4**. Diverse types of ionic charge carriers based on which the taxonomy of i-TE materials can be classified are also discussed. As compared in **Figure 5**, the unique physical and chemical properties of i-TE materials endow them with a wide range of application including thermal sensors, energy conversion, and energy storage, while e-TE materials are generally applied for thermal management, thermal sensor, and energy conversion.

3.1. Composition

Unlike e-TE materials which are normally in a single homogeneous phase, i-TE materials usually refer to a complicated system consisting of ions as function component, solvents to promote ion migration, and matrixes to support the material strength. If using liquid ion species, external packaging materials should also be applied to prevent evaporation, which are out of the scope of this review and will not be discussed exhaustively.

**ADVANCED
SCIENCE NEWS**
www.advancedsciencenews.com

**ADVANCED
ENERGY
MATERIALS**
www.advenergymat.de
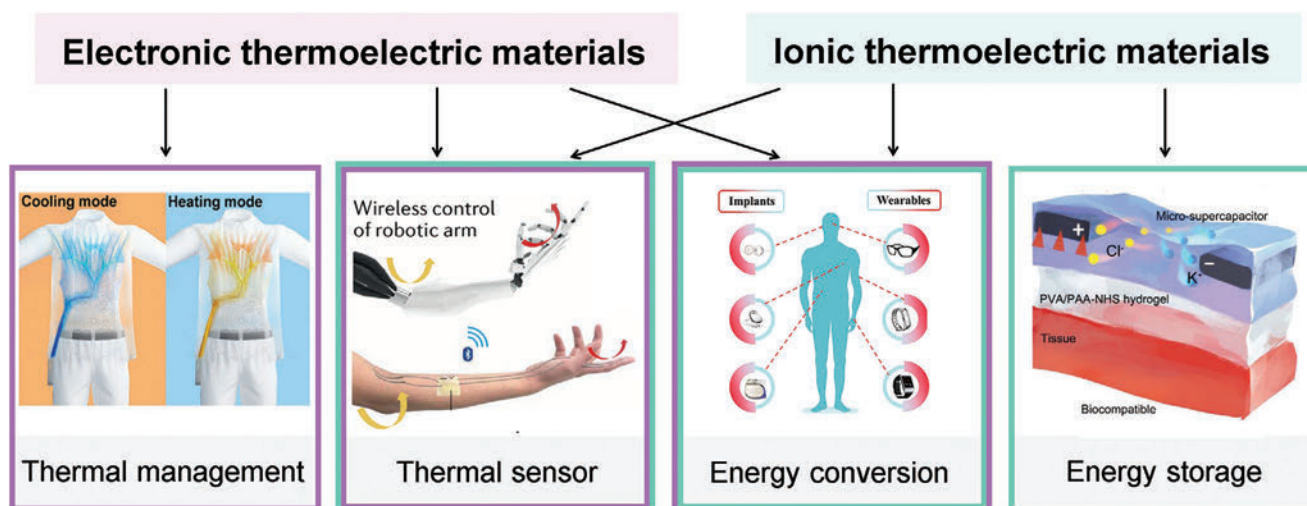
Figure 5. Distinctive application areas of e-TE and i-TE materials. Reproduced with permission.[71] Copyright 2022, Wiley-VCH. Reproduced with permission.[72] Copyright 2020, American Association for the Advancement of Science. Reproduced with permission.[73] Copyright 2019, Wiley-VCH. Reproduced with permission.[74] Copyright 2021, Wiley-VCH.

3.1.1. Ion Donor

Ion donors play a dominant role in generating thermovoltage. Potential sources of ions are provided by polar electrolytes, such as ILs, salt solution, and polyelectrolytes.[12] ILs are a widely used type of electrolytes providing ion species for i-TE materials, which are in liquid state at room temperature.[75] Due to the superiorities of low vapor pressure, low κ, wide operating temperature range, and desirable thermal and chemical stability, ILs have been increasingly used in i-TEs.[76] **Table 1** summarizes the chemical structure, TE performance, and melting point (T_m) of ILs reported recently. As can be seen, ILs are feasible for both n-type and p-type (as per the sign of S) i-TE materials, with the magnitude of S ranging from hundreds of µV K^{-1} to several mV K^{-1}.[28,77] Analogous to ILs, acid/base/salt solutions are inorganic small-molecule i-TE ion donors. However, unlike room temperature ionizable ILs, most of the acids/bases/salts are solid crystals, where pre-preparation of solutions is demanded.

Organic polyelectrolyte is another type of i-TE ion donors. Organic polyelectrolyte has the advantages of cheap, widely available, formable, and self-standing over inorganic ILs.[79] The general ion diffusion mobility in polyelectrolytes is normally lower than that in ILs, while conversely, the diffusion mobility difference between cations and anions is larger, making polyelectrolyte-based i-TE materials have a comparable S with that of IL-based i-TE materials. For instance, poly(sodium 4-styrenesulfonate) (PSSNa) exploits the concentration difference of PSS$^-$ and Na$^+$ for generating thermovoltage.[80] Under a low-grade ΔT, PSS$^-$, a type of covalently bonded macromolecule chain, can hardly migrate, while Na$^+$ tends to populates on one of the electrodes than the other, resulting in a S of 4 mV K^{-1}. There are two working modes implemented by i-TE ion donors, as schematically illustrated in **Figure 6**. Figure 6a shows the case where cations and anions are all mobile (inclusive ILs and acid/base/salt solutions), which has a relatively small S.[81] Figure 6b

shows the case of negatively charged backbone and itinerant protons, or vice versa (inclusive polyelectrolytes), which has a relatively large S.

Redox couple is a specific type of ion-donor mainly contributing to thermogalvanic effect.[82] Unlike thermodiffusion based ion donors, outstanding ability of continuous generating energy can be realized by redox ion species, without by-product emissions and irreversible ion consumptions.[83] $Fe(CN)_6^{3-}/Fe(CN)_6^{4-}$, Fe^{3+}/Fe^{2+}, I^{3-}/I^-, Sn^{2+}/Sn^{4+}, and Co^{2+}/Co^{3+} are all reported redox couples adopted by in i-TE systems.[23a,84] The S of the most common redox ion species has been measured or calculated.[83c,85] $Fe(CN)_6^{3-}/Fe(CN)_6^{4-}$ is one of the efficient couples with a S of ≈2 mV K^{-1}.[84d,86] More recently, combinations of dual redox couples (dibutanoylferrocene and iodine) with a synergistic effect were reported with a maximum S of 1.67 mV K^{-1}, raising from the formation of charge-transfer complexes.[87] Another newly explored organic redox couple of thiolate/disulphide was reported with a S of −0.6 mV K^{-1},[88] with great potential in avoiding electrochemical corrosions.

3.1.2. Solvent

Solvents are commonly applied as i-TE component to facilitate the dissociation and migration. Both inorganic solvents and organic solvents have been reported as i-TE additives. H_2O is the most widely accepted solvent which is biocompatible, environmentally friendly, and noncorrosive. However, H_2O has its weakness lying in high volatility, which results in material instability and requires packaging treatment.[89] In addition, there are a variety of organic solvent reported with promise in forming i-TE materials. For instance, dimethyl sulfoxide (DMSO) was adopted to fabricate poly(3,4-ethylenedioxythiophene) PEDOT/IL i-TE thin films via 3D-printing process, which have outstanding mechanical properties and reasonable

26

**ADVANCED
SCIENCE NEWS**

www.advancedsciencenews.com

**ADVANCED
ENERGY
MATERIALS**

www.advenergymat.de

Table 1. Chemical structures, TE parameters, and melting points of common ionic liquids (ILs).[29,68,77,78]

ILs	Chemical structure	σ [mS cm^{-1}]	S [mV K^{-1}]	T_m [°C]
[EMIM:Ac]		3.7	2.22	−20
[EMIM:BF$_4$]		15.7	−0.19	15
[EMIM:TFSI]		8.6	−1.45	−15
[EMIM:CF$_3$SO$_3$]		9.7	−0.36	−10
[BMIM:TFSI]		0.4	−0.94	−16
[BMIM:PF$_6$]		1.4	−0.62	−8
[BMIM:BF$_4$]		4.5	−0.61	−75
[HMIM:TFSI]		2.1	−0.78	−4
[HMIM:I]		0.2	0.13	<RT

27

Table 1. Continued.

ILs	Chemical structure	σ [mS cm^{-1}]	S [mV K^{-1}]	T_m [°C]
[HMIM:PF$_6$]		0.6	−1.01	−8
[OMIM:PF$_6$]		0.3	−1.07	−82
[OMIM:Ac]		3.5	2.34	N.A.
[OMIM:Cl]		0.09	0.64	N.A.
[OMIM:TFSI]		1.2	−0.38	<RT
[EAN]		25.2	0.68	12
[EAF]		16.3	−1.40	N.A.
[EATA]		46.1	0.58	N.A.
[P666,14:Cl]		5.9	0.23	N.A.

TE performance.[77a,90] The assembled TE generator enjoys a favorable working stability (power density retained above 85% compared with the original value of 6.8 µW cm^{-2}) under repeatedly stretching and cutting–repair cycles. Deep eutectic solvent of choline chloride (ChCl):ethylene glycol (EG), supported by 50% waterborne polyurethane (WPU), was also reported with a colossal S of 19.5 mV K^{-1} at a 90% relative humidity environment and favorable mechanical stretchability of 216%.[91]

3.1.3. Matrix

Matrixes serve as i-TE supports to work for ensuring form-ability, flexibility, and mechanical strength, covering artificial polyvinyl alcohol (PVA),[92] polyvinylidene fluoride (PVDF),[14] and natural cellulose,[12] gelatin.[21] For instance, inorganic additives blended PVA i-TE biomedical hydrogels are flexible, transparent, and cost-effective.[92] Nanofibrillated cellulose (NFC) was also adopted as the matrix to prepare an i-TE paper,
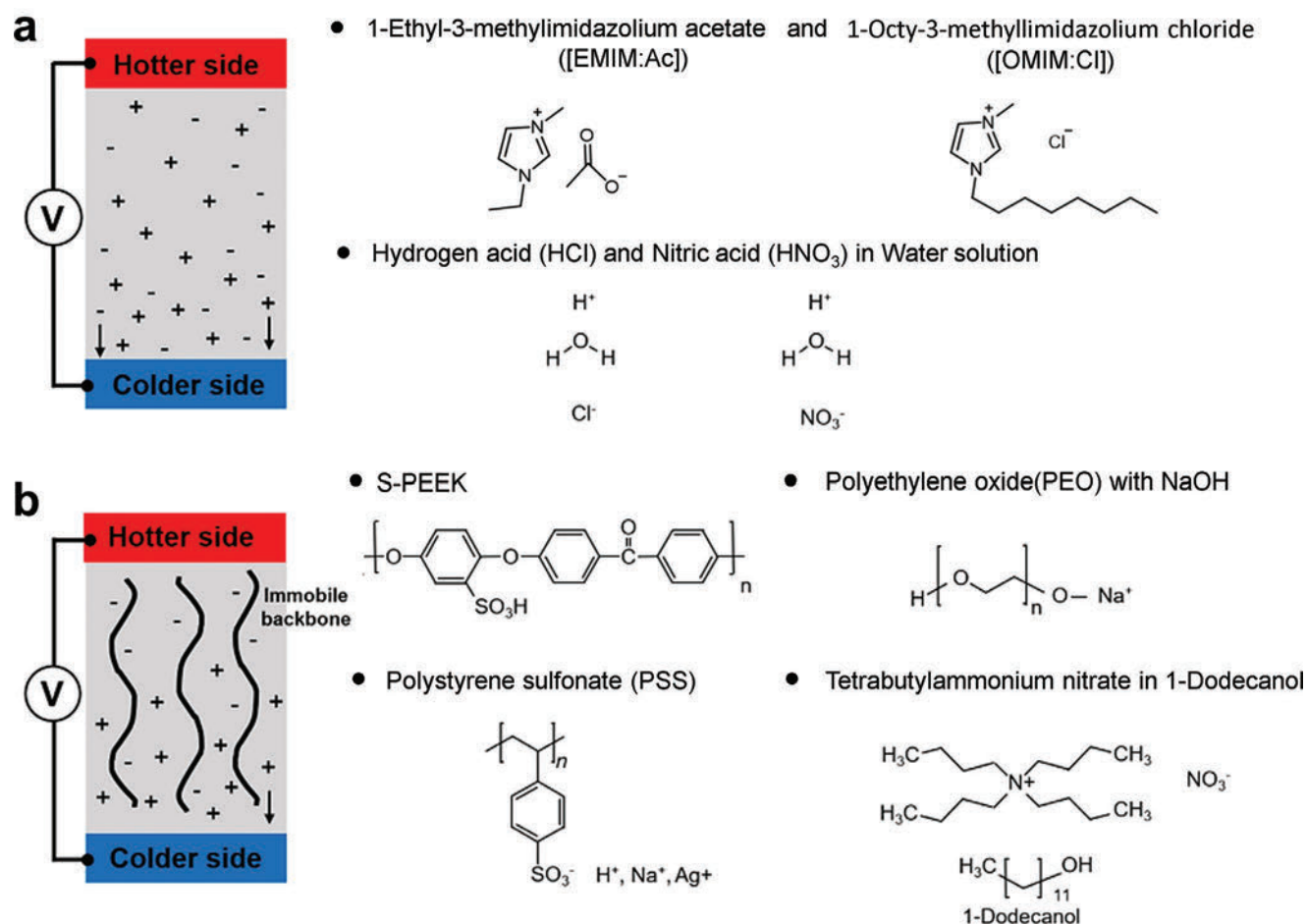
Figure 6. Working mechanism of ion donors of a) both cations and anions are mobile, and b) immobile polyelectrolyte backbone and mobile counter ions. Reproduced with permission.[81] Copyright 2021, Elsevier.

which can stand a weight of 100 g with only 80 μm thickness, therefore is suitable for roll-to-roll processing.[93] By introducing bacterial cellulose (BC) as skeleton support, advantages of high mechanical strength of 42 MPa, high crystallinity of 80%, and admirable ionic capacity of 99 wt% were endowed.[69] Polyurethane (PU) reinforced i-TE gels favor a high ZT of 0.99 ± 0.3, excellent elongation at a break of 300%, and self-healable competence.[94] More recently, inorganic SiO_2 nanoparticles were reported as a matrix to support i-TE materials.[20] An exceptional $S^2\sigma$ of 1040.4 μW m^{-1} K^{-2} at room temperature was achieved, which is one of the largest value reported in this field. Except for external matrix species, polyelectrolytes can stand for both the ion donor and the matrix single-handed. One should notice that partial insulative matrixes may hinder the ions transfer, where the specific gravity of matrixes should be optimized.

3.2. Physical State

I-TE materials can be classified with three physical states: liquid state, quasi-solid state, and solid state. Unlike e-TE materials, i-TE materials have been investigated in a com-

pletely liquid state, such as pure ILs, salt aqueous solutions, and salt organic solutions.[95] For instance, 1-ethyl-3-meth-ylimidazolium bis(trifluoromethylsulfonyl)imide ([EMIm][TFSI]) and 1-octyl-3-methylimidazolium hexafluorophos-phate ([OMIm][PF$_6$]) sealed in a flexible silicone tube have been reported as a liquid i-TE material with the highest S of 1.446 mV K^{-1}.[68] However, its κ is supposedly to be high because both heat transfer and heat convection contribute to thermal conduction.

Quasi-solid state i-TE materials are solid–liquid coexistence state i-TE materials (mainly refers to ionic hydrogels or ionogels), which exhibit larger S and lower σ than ILs, as compared in **Table 2**.[77a,96] For instance, a poly(vinylidene fluoride-*co*-hexafluo-ropropylene) (PVDF-HFP)/[EMIM:DCA] ionogel was reported to exhibit a giant S of 26.1 mV K^{-1}, a high σ of 6.7 mS cm^{-1}, and a ZT of 0.75.[14] Very recently, it was reported that inorganic SiO_2 nanoparticle incorporated [EMIM:DCA] ionogels exhibit a state-of-the-art ZT of 1.47 at room temperature. The corresponding S, σ, and κ are 14.8 mV K^{-1}, 47.5 mS cm^{-1}, and 0.21 W m^{-1} K^{-1}, respectively.[20] Polymethylmethacrylate (PMMA)/single-wall carbon nanotube (SWCNT) is another typical quasi-solid composite gel, which can be incorporated with Sn^{2+}/Sn^{4+} redox couples to render a high σ to 105 mS cm^{-1} and a maximum $S^2\sigma$ of

Table 2. Selective state-of-art i-TE materials.

Matrixes	Ion donors	Type	σ [mS cm^{-1}]	S [mV K^{-1}]	$S^2\sigma$ [µW m^{-1} K^{-2}]	K [Wm^{-1}K^{-1}]	ZT	Relative humidity [%]	Refs.
Salt solutions									
	TBAN-dodecanol	p	0.01	7.2	0.06	0.17	1.08×10^{-4}	N.A.	[46a]
Polyelectrolytes									
	PSSH	p	90.0	7.9	562.0	0.38	0.44	70	[98]
	Nafion-Ag	p	≈10.0	1.1	1.2	0.22	0.016	≈95	[70]
	PSS-Ag	n	≈16.0	−2.1	7.1	0.40	0.053	≈95	[70]
	PSSNa	p	11.8	4.0	18.9	0.49	0.012	100	[80]
	S-PEEK	p	20.0	5.5	60.5	N.A.	N.A.	70	[16]
	PDDAc	p	19.0	18.0	615.6	N.A.	N.A.	70	[16]
	Nafion	p	19.0	3.6	24.6	N.A.	N.A.	70	[16]
	Graphene oxide	p	4.0	9.0	32.4	3.0	3.22×10^{-3}	N.A.	[100]
Gels									
PEO	NaOH	p	0.08	11.1	1.0	0.22	1.35×10^{-3}	N.A.	[101]
Cellulose/PEO	NaOH	p	20.0	24.0	1152.0	0.48	0.71	N.A.	[12]
PVA	NaOH	n	0.07	−37.6	10.5	0.48 ± 0.03	0.065	N.A.	[92]
PVDF-HFP	[EMIM:DCA]	p	6.7	26.1	456.4	0.18	0.75	68–72	[14]
WPU	[EMIM:DCA]	p	8.4	34.5	999.8	0.23	1.30	90	[102]
SiO$_2$	[EMIM:DCA]	p	47.5	14.8	1040.4	0.21	1.47	72	[20]
PVDF-HFP (ethanol treated)	[EMIM:DCA]	p	17.6	25.4	1135.5	0.19	1.78	70–75	[19]
BC	[EMIM:DCA]	p	28.8	18.0	937.3	0.21	1.33	N.A.	[69]
PU	[EMIM:DCA]	p	12.8	25.6	838.9	0.24	0.99	70	[94]
PEO	[EMIM:Ac]	p	1.1	18.0	35.6	N.A.	N.A.	60	[103]
PVDF-HFP/PEG	[EMIM:TFSI]	p	0.8	14.0	15.7	N.A.	N.A.	N.A.	[12]
WPU	[ChCl:EG]	p	8.4	19.5	319.4	0.20	0.48	90	[91]
PANI/PAAMPSA	H$_3$PO$_4$	p	237.0	8.1	1555.0	0.45	1.04	90	[104]
Graphene oxide	PSSH	p	114.0	12.6	1809.9	0.64	0.85	N.A.	[105]
PVA	NaI	p	51.5	42.8	9434.0	0.54	5.18	50–70	[97]
Polyacrylamide/ poly(sodium alginate)	LiCl	p	10.0	10.5	109.7	N.A.	N.A.	N.A.	[13b]
Redox-induced materials									
	[Fe(CN)$_6$]$^{3-}$/[Fe(CN)$_6$]$^{4-}$ (guanidinium and urea modified)	p	≈50.0	4.2	88.2	≈0.30	0.087	N.A.	[34]
PMMA/SWCNT	Sn^{2+}/Sn^{4+}	p	105.0	1.1	13.5	N.A.	N.A.	N.A.	[84a]
PVA	Fe^{2+}/Fe^{3+}	p	≈9.5	1.0	1.0	1.88	1.59×10^{-4}	N.A.	[84c]
PVA	[Fe(CN)$_6$]$^{3-}$/[Fe(CN)$_6$]$^{4-}$	n	~6.0	−1.2	0.9	1.85	1.45×10^{-4}	N.A.	[84c]
Anisotropic PVA	[Fe(CN)$_6$]$^{3-}$/[Fe(CN)$_6$]$^{4-}$	p	46.0	1.5	10.4	0.40	7.60×10^{-3}	N.A.	[106]
Gelatin/KCl	[Fe(CN)$_6$]$^{3-}$/[Fe(CN)$_6$]$^{4-}$	p	≈5.0	17.0	144.5	0.15	0.29	N.A.	[21]
Poly(N-isopropylacryl-amide)	I$^-$/I^{3-}	n	1.0	−1.9	0.4	~0.45	2.38×10^{-4}	N.A.	[67]
PVDF-HFP/3-methoxy-propionitrile	[Co(bpy)$_3$]$^{2+}$/[Co(bpy)$_3$]$^{3+}$	p	N.A.	2.2	N.A.	0.67	N.A.	N.A.	[15]
i-TE/e-TE hybrid materials									
PEDOT:PSS	CuCl$_2$	n	52.6	−18.2	1700.0	0.34	1.54	80	[22]
PEDOT:PSS	PSSH	p	120.0	16.2	3149.3	N.A.	N.A.	90	[18]

**ADVANCED
SCIENCE NEWS**

www.advancedsciencenews.com

**ADVANCED
ENERGY
MATERIALS**

www.advenergymat.de

$13.5 \pm 3.0 \ \mu W \ m^{-1} \ K^{-2}$ at room temperature.[84a] A very inspiring result was reported in a PVA-NaI ionogel, where the ZT value can be calculated to be 5.18.[97]

Both liquid and quasi-solid i-TE materials are facing the disadvantages of leakage and instability, leading to large scope of the development of solid i-TE materials, which are mainly based on unblended bulk polyelectrolytes, such as PVA, PSSNa, silver Nafion (Nafion-Ag), silver polystyrene-sulfonate (PSS-Ag), poly(4-styrenesulfonic acid) (PSSH), sulfonated polymer polyether-ether-ketone (S-PEEK), poly(vinylphosphonic acid-*co*-acrylic acid) (P(VPA-AA)), and poly(diallyldimethylammonium chloride) (PDDAC). Specifically, unipolar polymers of Nafion-Ag and PSS-Ag were first studied their ion conduction properties in 2016,[70] which shows an exceptional positive S of 5 mV K^{-1} and a negative S of 1.5 mV K^{-1}, respectively. The PSSH film-assembled i-TE supercapacitors can generate a thermovoltage of 38 mV under a small ΔT of 5 K.[98] Recently, a maximum S of 19 mV K^{-1} at 70% relative humidity was achieved in PDDAC-based i-TE solid thin films, which is attributed to the synergistic effect of Cl^- dissociation and thermodiffusion.[16] However, solid i-TE materials also suffer from relatively low σ in a range of 10^{-5}–10^{-2} S cm^{-1} due to degraded ionic mobility, and therefore their ZT are commonly lower than those of quasi-solid i-TE materials.[77a]

3.3. Conduction Nature

In e-TE materials, if no bipolar conduction occurring, the conduction nature is decided by the type of charge carriers. By contrast, in i-TE materials, the conduction nature is decided by active ion species. Overall, if anions cumulate near cold electrode and cations cumulate near hot electrode, the correspondent i-TE materials are of n-type conduction, while the opposite conduction represents p-type i-TE materials. There are four practical cases envisaged by an i-TE process, which results in n-type or p-type i-TE materials. First, mobile cations and immobile backbone, the i-TE materials are p-type. Second, mobile cations and anions, while cations have higher mobility than that of anions, the i-TE materials are p-type. Third, mobile anions and immobile backbone, the i-TE materials are n-type. Fourth, mobile cations and anions, while cations have lower mobility than that of anions, the i-TE materials are n-type (opposite to the second case).

It should be mentioned that the p–n conversion of i-TE materials can be achieved by tuning the cation/anion mobility and cation/anion confinement. For instance, a reverse of S from +14 to −4 mV K^{-1} can be realized by incorporating liquid neutral polyethylene glycol (PEG) into the polymer matrix.[99] Piling up 18 pairs of these p-type and n-type i-TE materials electrically in series and thermally in parallel, a total effective S of 0.333 V K^{-1} can be obtained. The positive ferric/ferrous chloride/PVA complex thermogalvanic i-TE materials and negative potassium ferricyanide/ferrocyanide/PVA complex thermogalvanic i-TE materials shows the respective S being 1.02 and −1.21 mV K^{-1}.[84c] An assembled i-TE device using 59 pairs of such n-type and p-type i-TE materials can generate a large open-circuit thermovoltage of 0.7 V within 15 s and a favorable output power

of 0.3 mW at the ΔT between human skin and ambient environment. Table 2 listed TE properties of partial in-progressed thermodiffusion-derived i-TE materials. As can be seen, i-TE gels exhibit relatively high TE performance where the maximum ZT value has reached 5.18.

4. Properties of I-TE Materials

In this section, we overview the TE properties and capacitance of i-TE materials, followed by discussing the mechanical properties and other favorable characteristics on the practical application viewpoint.

4.1. Measurement Method

Measurement methods for i-TE properties are totally different from those for e-TE properties, mainly due to the charge transfer hysteresis in i-TE materials.[107] Specifically, the mass of a single ion is about three orders of magnitude higher than that of a single electron, making ion migration consume a relatively long time to reach equilibrium state.[108] While e-TE properties are usually measured by transient methods, including the "four probe" method for measuring σ and S,[109] the measurement of i-TE σ and S are separately mainly via AC impedance method and homemade instruments as mainstream. The 3ω method is employed for measuring κ of both e-TE and i-TE materials at present.

The alternating current (AC) impedance simulation is the most widely used method for estimating σ of i-TE materials, by electrochemical workstation equipment. In principle, ions and electrons behavior different reaction time with the application of AC voltage.[110] Electrons respond more quickly to the alternating current, while ions are much slower. As a result, the detachment between ionic impedance and electronic impedance can be realized via AC frequency scanning. During practical testing, AC impedance is a numerically varying value with a real part and an imaginary part, which is related to the applied frequency.[111] The key difference between the AC impedance method and the "four probe" method are:[70,90,98,105] i) AC impedance measures bulk resistance, whereas "four probes" method measures in-plane resistance, ii) AC impedance method measures an open-circuit system, while the "four probes" method is only applicable for closed-circuit system. **Figure 7**a–c exhibits the AC impedance results, plotted in the polar coordinates, namely, the Nyquist spectroscopy.[112] Typically, the Nyquist plots of i-TE materials consist of two segments. The signal in the low-frequency region (close to the end of the abscissa) corresponds with the electronic impedance R_e, and the signal in the high-frequency region (close to the origin of the abscissa) is mainly related to the ionic impedance R_i (R_e and R_i can simultaneously exist in i-TE systems).[113] The interpretations of Nyquist curves are based on the proper establishment of equivalent circuits. For instance, i-TE materials can be sorted as three classes via the inserted Maxwell's equivalent fitting spectroscopy:[92,102,112] i) as shown in Figure 7a, the i-TE polyelectrolyte PSSNa exhibits merely R_i characteristics, where a specific spike appears at the low-frequency region, ii) as shown in Figure 7b, complete electronic conductor PEDOT-Tos

ADVANCED
SCIENCE NEWS

www.advancedsciencenews.com

ADVANCED
ENERGY
MATERIALS

www.advenergymat.de
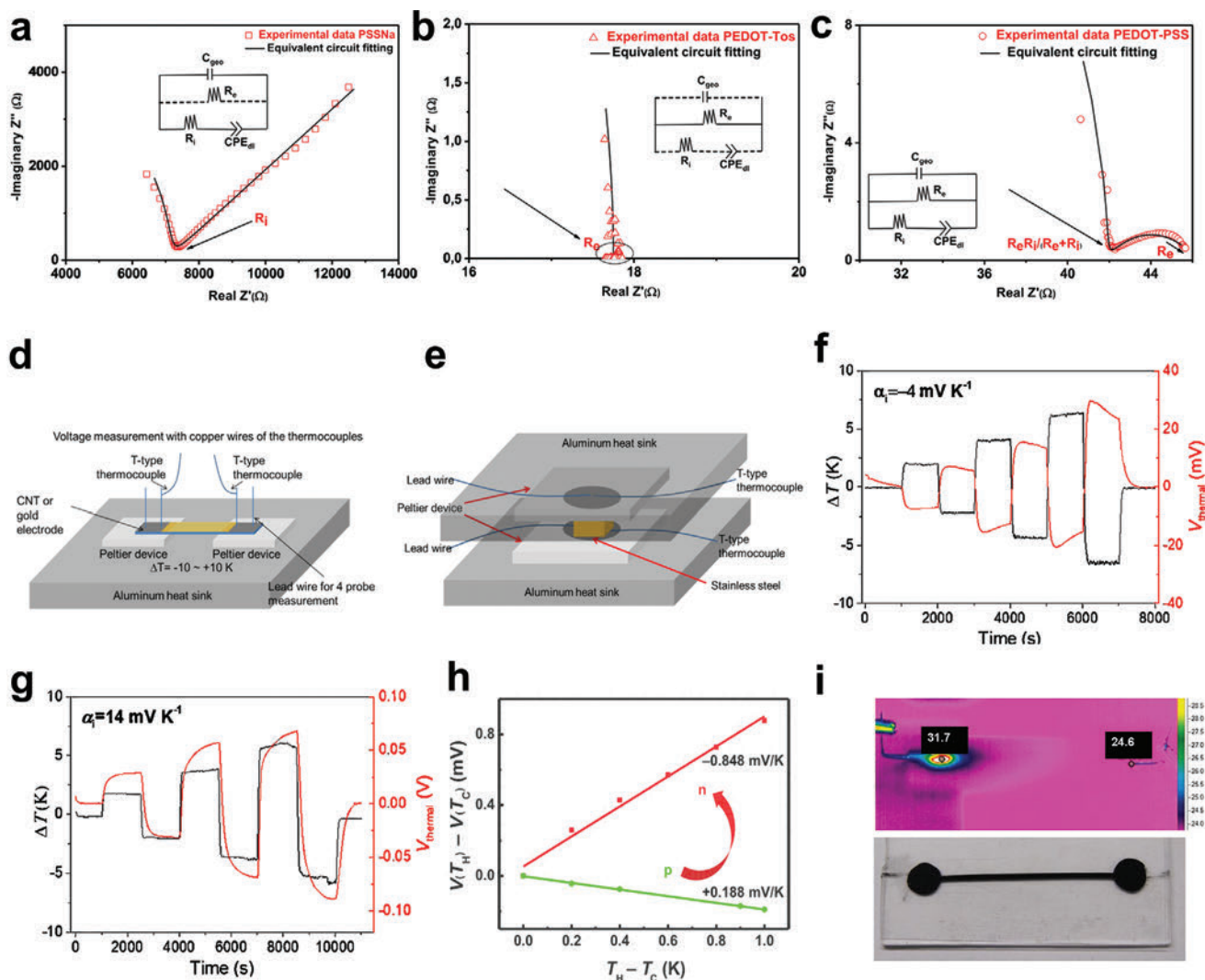
Figure 7. Measurement of i-TE properties. The Nyquist plot of a) sodium polystyrene sulfonate (PSSNa), b) PEDOT-Tos, and c) PEDOT-PSS. Reproduced with permission.[112] Copyright 2015, Wiley-VCH. Illustration of the ionic Seebeck measurement setups along the d) in-plane direction, and e) out-of-plane direction. Reproduced with permission.[98] Copyright 2016, Wiley-VCH. Plot of thermovoltage versus ΔT for f) n-type i-TE gels of 1-ethyl-3-methylimidazolium bis(trifluoromethylsulfonyl)imide/poly(vinylidene fluoride-co-hexafluoropropylene) ([EMIM:TFSI]/PVDF-HFP), and g) p-type i-TE gels of 1-ethyl-3-methylimidazolium bis(trifluoromethylsulfonyl)imide/poly(vinylidene fluoride-co-hexafluoropropylene)/polyethylene glycol ([EMIM:TFSI]/PVDF-HFP/PEG). Reproduced with permission.[99] Copyright 2019, Springer Nature. h) Thermopower of 0.1 mM NaOH aqueous solution (green) and fully swollen NaOH/polyvinyl alcohol (PVA) hydrogels after air-drying at room temperature (red). Reproduced with permission.[92] Copyright 2021, American Association for the Advancement of Science. i) IR photo and digital image of the 1-ethyl-3-methyl imidazolium bis[(trifluoromethyl) sulfonyl]imide ([EMIm][Tf$_2$N]) IL converter after heating at one end. Reproduced with permission.[68] Copyright 2016, Wiley-VCH.

exhibits merely R_e characteristics, where all of the fitted points distributed at the high-frequency region, iii) as shown in Figure 7c, PEDOT-PSS exhibits both R_i and R_e characteristics, where a depressed semicircle at lower frequency and a segment of a macro semicircle within the higher frequency region can be observed from the fitting curve. The first intercept on the real axis represents R_e as tagged, whereas the second intercept in the high-frequency area represents the parallel combination of R_e and R_i, i.e., $[R_e \cdot R_i/(R_e+R_i)]$.

The experimental set-ups for measuring S along in-plane direction and out-of-plane direction are schematically displayed in Figure 7d,e.[98,99,114] As can be seen, the temperature controls

employ Peltier devices attached to aluminum heat sinks, while the detections of temperature are recorded by thermocouples or thermal images, and the thermovoltages are collected by an electrochemical workstation or a source measure unit.[68,78,91] Figure 7f,g plots the typical measurement results that are recorded by such instruments for both p-type and n-type i-TE materials.[99] Two points are worth mentioning. First, a certain time is required for the establishment of steady-state.[115] Second, the thermovoltage response to ΔT is proportional reproducible, implying the reliability of homemade instruments. Figure 7h shows the direct plots of thermovoltage versus ΔT, which behave excellent linear correlations. The positive and negative

slopes indicate n-type and p-type conductance, and the absolute value of slope is numerically equal to the magnitude of S.[92,99]

For measuring κ, both the differential 3ω method[101] and the laser flash apparatus method[12] have been employed. Besides, κ values of i-TE materials have also be estimated based on the effective medium theory suitable for composites when the κ of every individual component is known.[99] The calculation formula is described as follows regardless convections: $\kappa_T = \kappa_1 \cdot \Phi_1 + \kappa_2 \cdot \Phi_2$ (Φ refers to the weight ratio, and the subscripts T, 1, and 2 are on behalf of the total composite, component 1, and component 2 respectively). Owing to the presence of large amounts of organics and solvents within i-TE materials, the heat transmit abilities are generally of a relatively low grade. Besides, the κ of i-TE materials is at a low-grade level due to the absence of a long-range crystalline region as well. For instance, the infrared imaging of 1-ethyl-3-methyl imidazolium bis[(trifluoromethyl) sulfonyl]imide ([EMIm][Tf$_2$N]) in Figure 7i intuitively demonstrates the thermal resistance effect.[68] As a result, the establishment of effective ΔT is feasible between two ends of the i-TE materials.

4.2. TE Performance

Although the performance of both e-TE and i-TE materials can be evaluated via ZT, their underlying microscopic characteristics are different. As can be seen in **Figure 8**a, the TE parameters of both e-TE and i-TE materials vary as the function of the density of charge carriers.[102,116] In e-TE materials, the S value is negatively related to the carrier concentration, while the σ value is positively related to the carrier concentration. By contrast, κ is relatively independent on carrier concentration due to con-

taining a considerable fraction of lattice thermal conductivity κ_l. Consequently, carrier concentration must be optimized to maximize ZT.[117] However, detailed summarization of analogous performance trend forecasts corresponding to i-TE materials has not been reported till now. Whereas in i-TE materials, there is no explicit trade-off between the S and the σ. It is acceptable to speculate that the ionic σ keeps consistently increasing/decreasing with the carrier densities, which is similar to the σ of e-TE materials. By contrast, the variation of S on carrier concentration in i-TE materials is rather complicated, because the S of i-TE materials can be rationalized via both thermodiffusion and thermogalvanic effects. In most circumstances, the S of i-TE materials is intrinsically triggered by ion migrations and redox couple thermoreactions. Therefore, higher carrier concentration promotes the boost of gathered charges, leading to higher thermovoltage.[81,102] The permitted simultaneous optimization of S and σ offers potential breakthroughs for the $S^2\sigma$ enhancement in i-TE materials.

The inherently decoupled S and σ in i-TE materials provide exceptional potentials for increasing ZT, which, however, also result in the drawback that thermovoltage gradually decays after ion diffusion reaches saturation. As illustrated in Figure 8b, in the condition of deposing to an external circuit, electric current flows through immediately closed circuit via electrodes. As electron transport is continuously motivated from one electrode to the other, a countered electric potential forms and gradually congests, leading to the decaying trend of thermovoltage.[91] If incorporating i-TE materials with e-TE materials, the S can approach to the exclusive S due to e-TE effect, which otherwise approaches to zero.[101,112]

Figure 8c compares the S of thermodiffusive i-TE materials, thermogalvanic i-TE materials, inorganic e-TE materials,
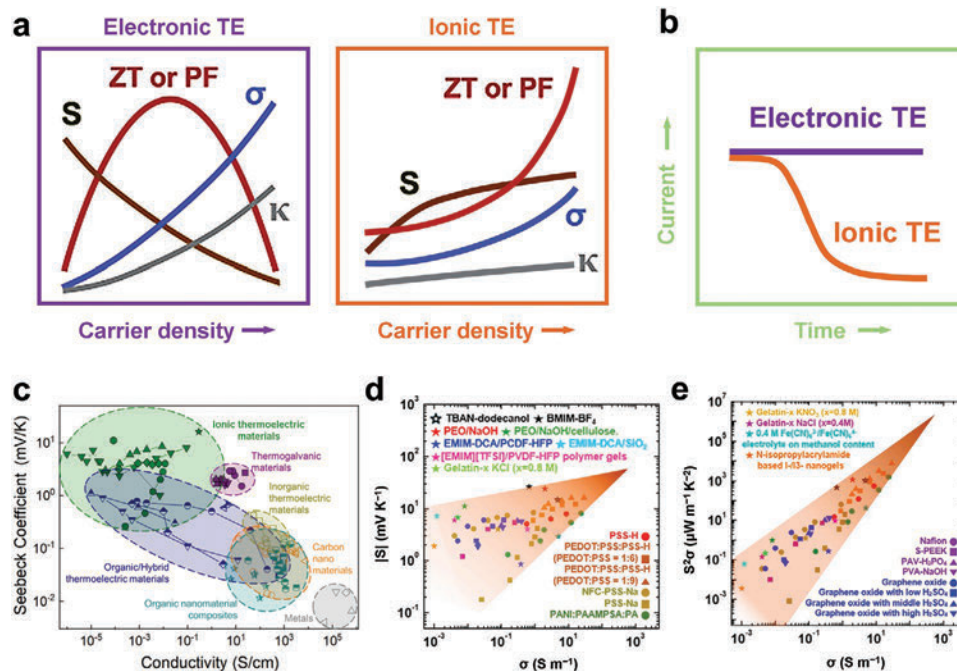
Figure 8. a) Dependence of TE properties on carrier density. b) Relationship between external circuit current and time under a constant ΔT. c) Summary of the S values as a function of σ values for different types of TE materials, Reproduced with permission.[23a] Copyright 2021, American Chemical Society. Plots of d) $|S|$ and e) $S^2\sigma$ as a function of σ for i-TE materials. Reproduced with permission.[81] Copyright 2021, Elsevier.

organic/hybrid TE materials, carbon nanomaterials, organic nanomaterial composites, and metals.[23a] As can be seen, thermodiffusive i-TE materials exhibit the maximum S but a relatively lower σ. Additionally, thermogalvanic i-TE materials exhibit a second largest S with a comparable σ to that of organic/hybrid TE materials. Figure 8d,e further compares the S, σ, and $S^2\sigma$ of the reported i-TE materials.[81] It is interesting to note that these data statistically converge at the $|S|$ of 10^2 mV K^{-1} and the $S^2\sigma$ of μW m^{-1} K^{-2}, which implies the superior performance of i-TE materials.

4.3. Capacitance Performance

Another outstanding benefit of i-TE materials is to serve for energy storage applications, which plays an important role in renewable power generation, smart grids, internet of things.[118] The capacitance performance of i-TE materials determines its potential as supercapacitors, which is incapable for e-TE materials.[32a,119] As shown in **Figure 9**a, ion carriers migrate to the electrode surface under ΔT, which failed in continuously passing through external circuit. As a result, ions accumulate to generate an electric potential difference to work as a capacitor, as depicted in Figure 9b. Specifically, a single charging/discharging cycle contains four-stage process, where the corresponding voltage and ΔT are shown in Figure 9c. In the 1st stage, a certain ΔT is applied between the two electrodes so that

ions accumulate gradually to generate an increasing thermovoltage. In the 2nd stage, a closed loop is built with an external resistor as the constant ΔT is maintained. The generated voltage in the preceding stage decays to ≈0 V gradually by discharging. As the accumulated ion amounts have attained maximum concentration, the balanced voltage keeps at ≈0 V afterward. In the 3rd stage, the ΔT is removed, and the external circuit is disconnected. As a result, the accumulated ions diffuse back to evenly distribute within the i-TE material. In the 4th stage, the external circuit is reconnected, and the electrons flow back to an electrically neutral state. An opposite-direction current compared with the 2nd stage is thus released, which leads to zero voltage.

Figure 9d shows the transformative evolution of voltage during a full charging/discharging cycle. The close loop indicate the repeatability of such a cycle, enabling i-TE materials with potential to be applied as long-term supercapacitors.[92] The voltage decay in the 2nd stage is closely related to the resistance of the external load (Figure 9e). As the external resistance (R) increases, the voltage decay becomes slower. To explain such a phenomenon, the discharge time constant τ is defined, expressed as $\tau = RC$ (C is the capacitance of the i-TE capacitor).[102] A higher τ arises from an increased R, which is equal to a slower voltage decay. The instantaneous decayed voltage is combined by a fast relaxation and a slow relaxation ($V_t = V_1 \cdot e^{-t/\tau 1} + V_2 \cdot e^{-t/\tau 2}$, where τ_1 is the fast relaxation time constant, V_1 is the fast relaxation initial voltage, τ_2 is the slow relaxation time constant, and V_2 is the slow relaxation initial
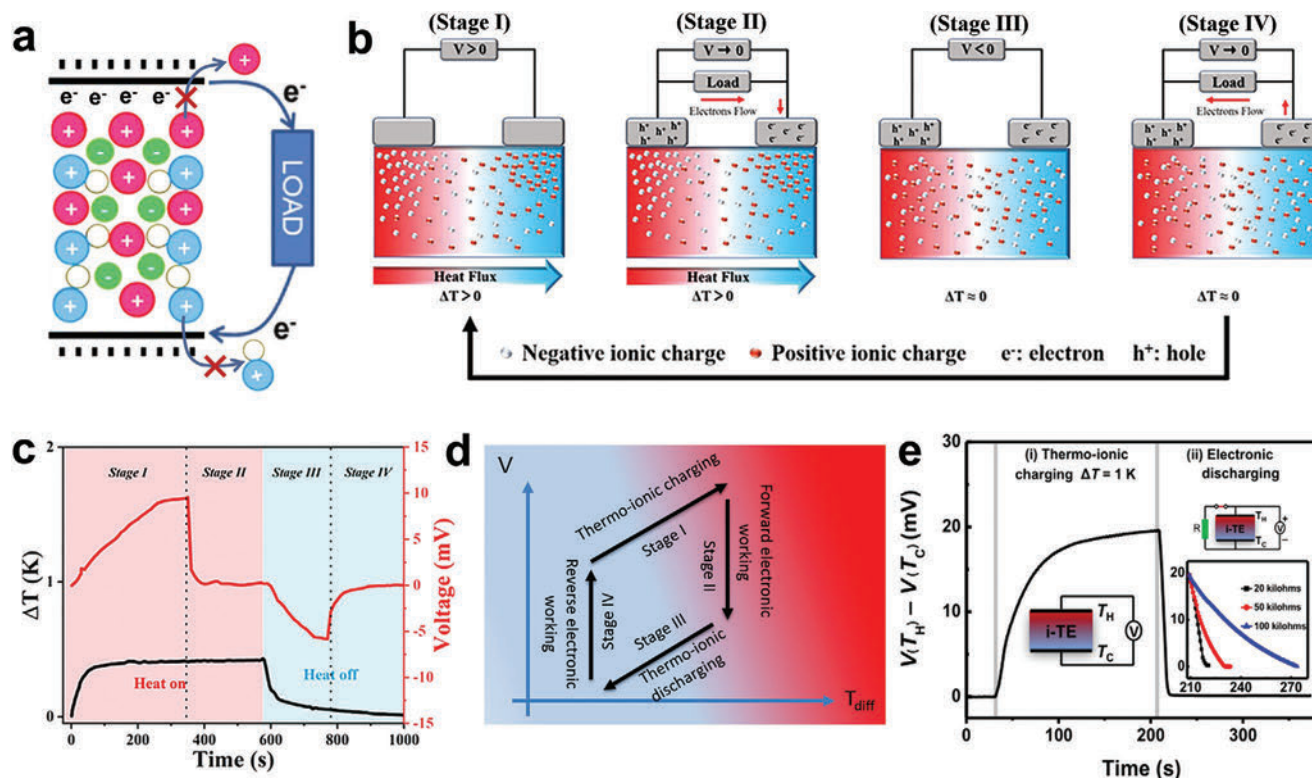
Figure 9. Schematic illustration of a) working mechanism of i-TE capacitance, and b) four stages of an i-TE capacitance cycle. c) Change of voltage and ΔT during the four-stage cycle. Reproduced with permission.[94] Copyright 2021, American Chemical Society. d) Schematic voltage-ΔT cycle during the four-stage charge–discharge process. Reproduced with permission.[14] Copyright 2019, Wiley-VCH. e) Charge–discharge process during stage I and II of a PVA hydrogel with external resistances of 20, 50, and 100 kΩ. Reproduced with permission.[92] Copyright 2021, American Association for the Advancement of Science.

ADVANCED
SCIENCE NEWS
www.advancedsciencenews.com

ADVANCED
ENERGY
MATERIALS
www.advenergymat.de

voltage). The decisive fast relaxation is related to the dielectric capacitive mode decay behavior. The slow relaxation originated from the decay between the electrodes and the i-TE materials.[91]

The capacitance competence of an i-TE material is an intrinsic parameter of the whole system, which is primarily influenced by the design strategy. For instance, a solid supercapacitor with PSSH as electrolyte and polyaniline (PANI) deposited carbon nanotubes (CNTs) as electrodes was fabricated, achieving a considerable voltage of 38 mV and an advanced areal capacitance of 1200 F m^{-2} when the driving force is barely a low-grade ΔT of 5 K.[98] The supercapacitor was promised to work within a potential window range from 0 to 0.8 V. Moreover, a superior Columbic efficiency and stable capacitance are confirmed as well. Another instance is polyethylene oxide (PEO)/NaOH-based i-TE capacitor, which exhibits an extrapolated energy-storing density of 9.4 Wh kg^{-1} at a ΔT of 10 K.[101] For comparison, the homologous energy density of Li-polymer capacitors is ≈200 Wh kg^{-1}. By equaling the e-TE capacity to that of an identical extracapacitor connected with an e-TE material, an i-TE paper supercapacitor composed of PSSNa and NFC

performs three orders higher energy storage than Bi_2Te_3 at the same condition (the ΔT of 10 K).[93]

4.4. Mechanical Performance

Mechanical properties, such as flexibility and stretchability, are important for i-TEs.[120] Currently, i-TE materials with satisfactory mechanical properties have been intensively reported. For instance, a stretchability higher than 30% and Young's modulus higher than 0.60 MPa are demanded to meet the performance requirements of human skin.[106,121] The PU/30 wt% IL ionogel with a mechanical stretchability of 300%, a tensile strength of 1.61 MPa, and a Young's modulus of 0.79 MPa were reported to be qualified as human skin devices.[94] **Figure 10**a–c is optical photos of the i-TE ionogels, which visually display the stretchability and flexibility. As can be seen, well-designed ionogels and hydrogels can be twisted repeatedly (Figure 10a).[102] High tensile strength can simultaneously enable the lift of a bucket of oil (Figure 10b).[106] Besides, superior flexibility was reported to maintain (Figure 10c) even on the iced surface (−20 °C
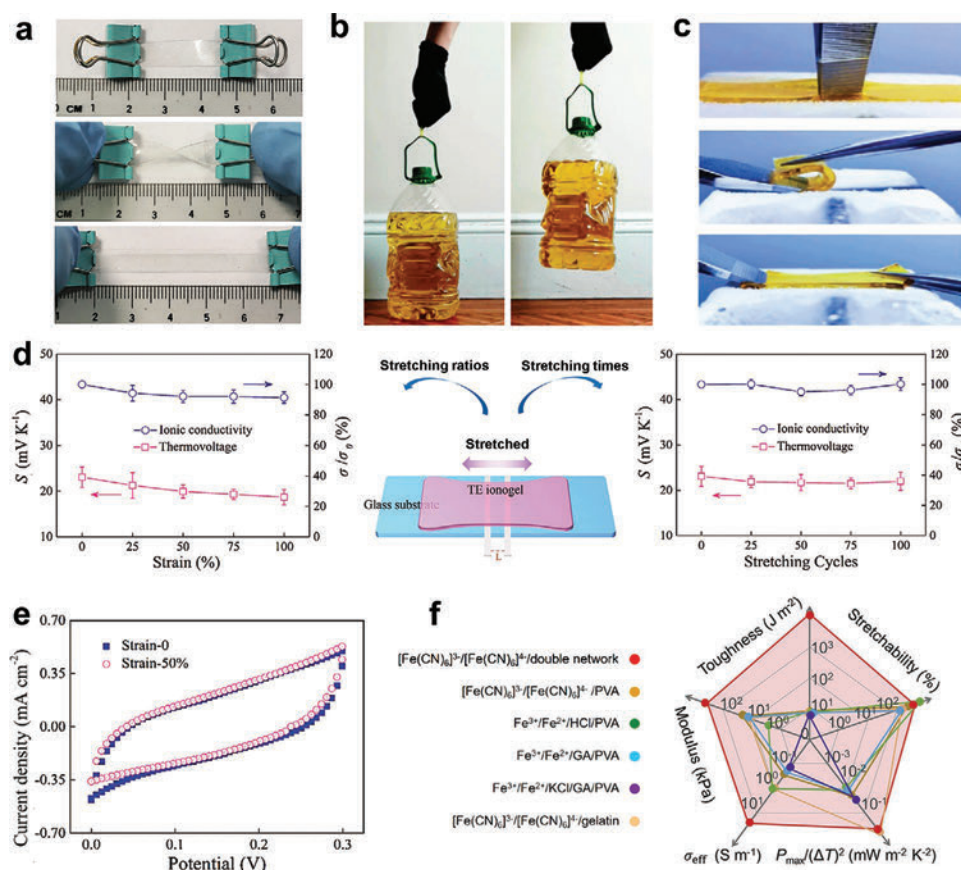
Figure 10. a) Photographs showing the stretched, relaxed, and twisted states of a waterborne polyurethane (WPU)/1-ethyl-3-methylimidazolium dicyanamide ([EMIM:DCA]-40% i-TE ionogel. Reproduced with permission.[102] Copyright 2020, Wiley-VCH. b) A 4 mm width × 2 mm thickness Fe(CN)$_6$$^{3-}$/Fe(CN)$_6$$^{4-}$/PVA i-TE hydrogel film can lift a 3200 g-weight bottle of oil. Reproduced with permission.[106] Copyright 2022, American Chemical Society. c) Pressed, bent, and stretched states on an −20 °C iced surface of a synthesized i-TE organohydrogel. Reproduced with permission.[121a] Copyright 2021, Wiley-VCH. d) Thermovoltage and relative ionic conductivity as functions of stretching ratios and stretching times of a WPU/[EMIM:DCA]-40% i-TE ionogels. e) CV curves at the original and 50% stretched states of a WPU/[EMIM:DCA]-40% i-TE ionogel. Reproduced with permission.[102] Copyright 2020, Wiley-VCH. f) Comparison of Fe(CN)$_6$$^{3-}$/Fe(CN)$_6$$^{4-}$/PVA-based, Fe^{3+}/Fe^{2+}/PVA-based, high power density Fe(CN)$_6$$^{3-}$/Fe(CN)$_6$$^{4-}$/gelatin-based, and high mechanical toughness Fe(CN)$_6$$^{3-}$/Fe(CN)$_6$$^{4-}$/double network-based i-TE materials. Reproduced with permission.[124] Copyright 2018, Cell Press.

35

**ADVANCED
SCIENCE NEWS**

www.advancedsciencenews.com

**ADVANCED
ENERGY
MATERIALS**

www.advenergymat.de

atmosphere) for ionogels.[121a] For polymer-based i-TE materials, their withstand temperature is mainly determined by the specific glass transition temperature (t_g).[122] Recently, i-TE gels compromising polymer matrix (WPU) and ILs ([EMIM:DCA]) was reported with a high ZT value of 1.3 ± 0.2 with desirable stable during tensile deformation.[102] Figure 10d presents the S and the relative conductivity (σ/σ_0, where σ_0 represents the original σ without any stretching) of the i-TE ionogels. Specifically, the S value decreased from 23.1 to 18.7 mV K^{-1} (81% maintained) while the relative conductivity was retained above 91% when the stretching ratio reached 100%. Moreover, both the S and the σ/σ_0 showed no obvious fluctuation during the repeatedly stretching and releasing of 100 times. The CV curves measured in the relax state and 50% stretched state are roughly overlapping as well, as illustrated in Figure 10e, indicating the potential of i-TE device serving in deformed environments.[123]

However, current strategies to optimize mechanical properties mainly focus on modifying the matrix content, which usually in turn ruins TE properties. To overcome such a trade-off, double chemically cross-linked networks are introduced to i-TE materials. The improved cross-linking extent can boost the i-TE mechanical properties without increasing matrix contents. As shown in Figure 10f, a combination of 217% stretchability, 1.19 MPa tensile strength, 2770 J m^{-2} toughness, and 0.61 mW m^{-2} K^{-2} output power density were reported in a $Fe(CN)_6^{3-}/Fe(CN)_6^{4-}$/double-network cross-linked copolymer ionogels.[106] The consequently assembled device

works reliably even after slicing, which is meaningful to prevent the liquid-component leakage issues. Another breakthrough has been accomplished by a ternary-blend material of i) conjugated polymer of PANI, ii) nonconjugated anionic polyelectrolyte of poly(2-acrylamido-2-methyl-1-propanesulfonic acid) (PAAMPSA), and iii) phytic acid (PA).[104] The obtained hybrid i-TE ionogel was intrinsically flexible in all directions with a stretching factor of up to ≈750%. Besides, the S was nearly unchanged after 30 cycles at 50% strain (from 7.2 to 6.8 mV K^{-1}).

4.5. Other Preferable Properties

I-TE materials favor other properties depending on working environment. First, self-healing behaviors have been reported in i-TE ionogels, which is of great benefit to promoting the service life and reducing maintenance intervals. Reversible bond plays an important role in self-healing materials. The self-healing abilities can be achieved by the dynamic breaking and reform of conjugate bond stackings, electrostatic attractions, hydrogen bonds.[94,125] As illustrated in **Figure 11**a, freestanding ternary hybrids of PANI, PAAMPSA, and PA conceive the reversibility of electrostatic interactions and hydrogen bonds. The shaped composite film exhibits autonomous self-recovery ability without any external motivation such as pressure, wave, or heat. After a cutting and self-healing loop, the
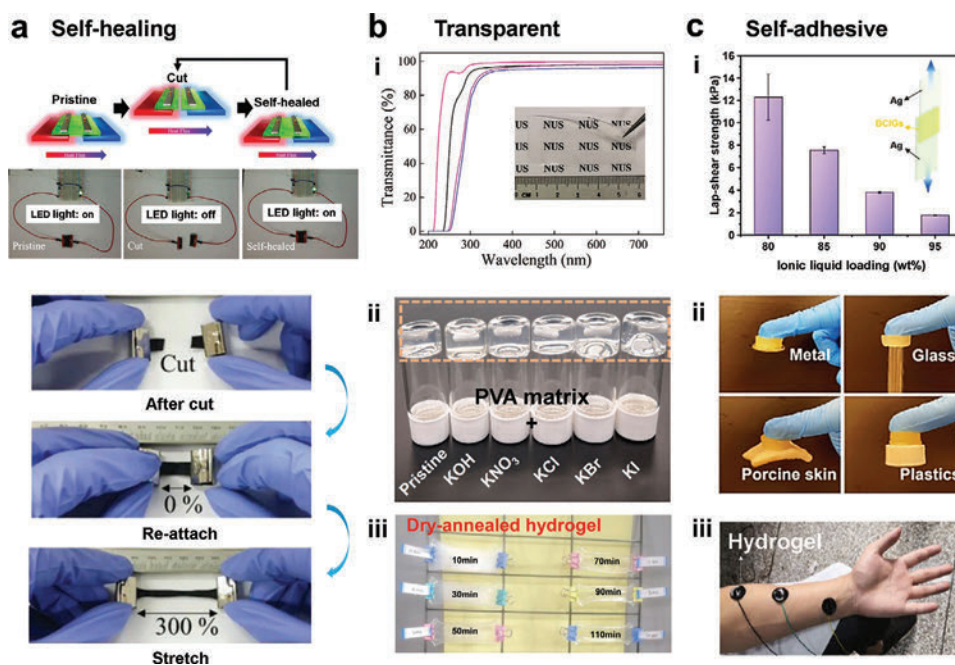
Figure 11. a) Photographs showing the self-healing behavior of polyaniline (PANI), poly(2-acrylamido-2-methyl-1-propanesulfonic acid) (PAAMPSA), and phytic acid (PA) ternary TE hybrid films. Reproduced with permission.[104] Copyright 2020, Royal Society of Chemistry. b) i) The UV–vis transmittance spectrum of a WPU/[EMIM:DCA] i-TE ionogel film, ii) Photographs of PVA hydrogels containing KI, KBr, KCl, KNO_3, KOH, and pristine, iii) the pictures NaOH/PVA ionogels after freeze-thawing 24 h and dry-annealing 10, 30, 50, 70, 90, 110 min. Reproduced with permission.[102] Copyright 2020, Wiley-VCH. Reproduced with permission.[97] Copyright 2022, American Chemical Society. Reproduced with permission.[92] Copyright 2021, American Association for the Advancement of Science. c) i) Lap-shear strengths of Ag plates by bacterial cellulose (BC)/[EMIM:DCA] i-TE ionogels, ii) photographs of the adhesion of poly(acrylic acid-*co*-3-acrylamidophenylboronic acid) hydrogels, iii) photographs of poly(3,4-ethylenedioxythiophene) (PEDOT)/sulfonated lignin (LS)/polyacrylamide (PAM) hydrogels adhered to human arm. Reproduced with permission.[69] Copyright 2021, Wiley-VCH. Reproduced with permission.[127b] Copyright 2021, Royal Society of Chemistry. Reproduced with permission.[128] Copyright 2020, Springer Nature.

**ADVANCED
SCIENCE NEWS**
www.advancedsciencenews.com

**ADVANCED
ENERGY
MATERIALS**
www.advenergymat.de

σ of such i-TE hybrids can be recovered.[104] Recently, self-healing, solution-processable, and 3D-printable i-TE generator has become a hotspot in this field. The constituent material is mixed composite of poly(3,4-ethylenedioxythiophene):poly(styrene sulfonate) PEDOT:PSS, healing agent nonionic surfactant (Triton X-100), and TE performance booster (DMSO). In the process of self-healing, the nonionic surfactant is interacted with PEDOT:PSS chains, which helps to fill the cutting cracks and reduce free volumes. Meanwhile, hydrogen bonds originating from ethylene-oxide groups of Triton X-100 endow the self-healing properties. More than 85% of the pristine power output can be reserved after ten times cutting and reattaching loops.[90]

Second, different from traditional alloys with metallic glossy appearance (inorganic e-TE materials) and dark colored appearance conjugated polymer (organic e-TE materials), i-TE materials can be designed with a transparent appearance through blending transparent ion-donors (such as ILs or salts) and transparent matrixes (such as gelatin or amorphous polymer).[126] As illustrated in Figure 11b, transparency of over 95% in the visible light range of a WPU/[EMIM:DCA] ionogel film can be achieved.[102] PVA hydrogels containing KI, KBr, KCl, KNO$_3$, KOH also exhibit visually admiring transparency.[97] Further regulation of transparency can be realized by controlling the crystallinity degree. For instance, i-TE hydrogels postprocessed

by freeze-thawing 24 h and dry-annealing 10, 30, 50, 70, 90, 110 min were reported with greatly increased transparency (see Figure 11b).[92] This phenomenon is related to the crystallinity differences after post-treatments. Moreover, good compatibility between the components also contributes to increased transparency due to suppressed photon scattering.[69]

Third, self-adhesive properties have also been reported. As shown in Figure 11c, ionogels composed of BC and [EMIM:DCA] are used as the adhesion to bond two layers of Ag plates.[69] As the [EMIM:DCA] loading improves, the interfacial shear strength drops due to the lubricating effect of ILs. In another report, conducting hydrogels are modified to bond a wide variety of substrates, including metal, glass, porcine skin, and plastics.[127] For practical application, a PEDOT-incorporated hydrogel has been pasted on the skin to detect the heartbeat signals.[128]

5. I-TE Performance Optimization

In this section, we examine state-of-the-art strategies to optimize i-TE performance, which can be sorted as two classes: incorporation and structural optimization, as shown in **Figure 12**. Due to the integrated system nature of i-TE materials, the various factors should also be examined, including
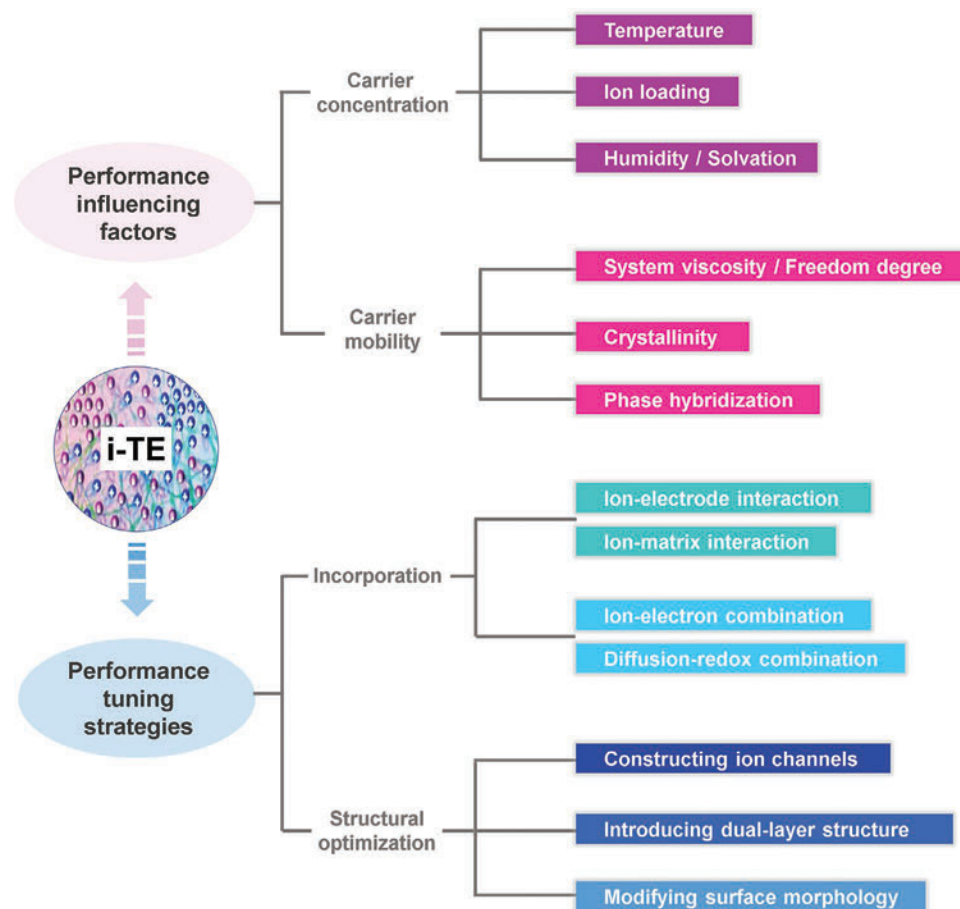

Figure 12. Flow chart of i-TE performance influencing factors and tuning strategies.

ADVANCED
SCIENCE NEWS

www.advancedsciencenews.com

ADVANCED
ENERGY
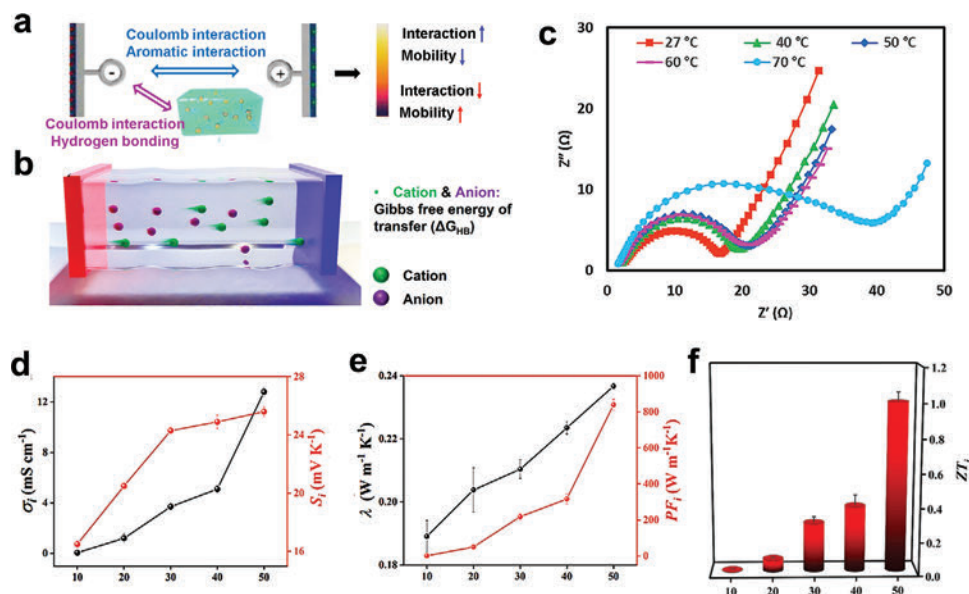**MATERIALS**

www.advenergymat.de

Figure 13. Schematic illustration of a) ion-electrode interactions, and b) ion–matrix interactions. Reproduced with permission.[97] Copyright 2022, American Chemical Society. c) Nyquist impedance spectra of PEGDMA-[N_{2228}]Br ionogel at 27, 40, 50, 60, and 70 °C. Reproduced with permission.[132] Copyright 2019, Elsevier. Variations of d) σ and S, e) κ and PF, and f) ZT values of PU-[EMIM:DCA] i-TE ionogels as a function of ionic loadings. Reproduced with permission.[94] Copyright 2021, American Chemical Society.

temperature, ion loading, and humidity, which are supposedly to have equal impact on anions and cations.[2a,129]

5.1. Performance Influence Factors

Temperature mainly influences TE properties in two aspects: first, the statistical distribution of charge carriers and phonons, and therefore electrical and thermal properties are temperature dependent; second, the overall TE performance is based on the product of Z and T.[130] As shown in **Figure 13**a, there are two dominant fettering forces of ions in i-TE materials: i) forces between ions and the electrodes via Coulomb interactions and aromatic interactions, and ii) forces between ions and the matrix that are basically composed of Coulomb interactions and hydrogen bonding. The migration of ion species therefore lies in overcoming these forces, i.e., a large enough ΔG to overgo the ion migration energy barrier, which usually decreases with increasing temperature (see Figure 13b). This has been profoundly confirmed by experiments,[12,84c,131] for instance, in polyethylene glycol dimethacrylate (PEGDMA)/N,N,N-triethyl octyl ammonium bromide ([N_{2228}]Br) i-TE ionogels (Figure 13c), a rise in temperature leads to decrease in resistance. Specifically, the σ at room temperature was calculated to be 45.3 mS cm^{-1}, which linearly increases to a maximum of 74 mS cm^{-1} at 70 °C.[132]

Ion loading comprehensively influences i-TE properties, in analogy to e-TE materials. As plotted in Figure 13d–f, the σ, S, and κ of a PU/[EMIM:DCA] i-TE ionogel vary simultaneously with increasing ion concentration, leading to a $S^2\sigma$ of 850 W m^{-1} K^{-1} and a ZT of 0.99.[94] Generally, an increasing ion concentration results in higher σ. However, an increased silver ion concentration was reported to cause obvious σ declines for Ag-Nafion polyelectrolytes.[70] This is because the significantly decreased ion mobility arising from ion–ion scattering

contradicts the positive effects of increasing carrier concentration. While in the aspect of ionic S, a Debye–Hückel prediction based on the electrostatic interactions between ions provides theoretical reference, which derives a linear relationship between the Eastman entropy of transport and the square root of the ion loading.[133] An experimental verification that agrees with such speculation has been reported, where the S decreases linearly with $\sqrt{c}$ for tetradodecylammonium nitrate/octanol solutions.[46a]

Humidity has primary impacts on kinetic transfer rate, which mainly influences i-TE materials working in generating mode, while is less important for i-TE materials working as capacitors.[134] Under humid ambient environment, the linear-log plots of humidity versus σ and S are plotted in **Figure 14**a,b.[81] As can be seen, the humidity-σ plots have unanimous trend although differing in orders of magnitude. By contrast, |S| show both positive and negative correlations, which coincides with the water percolation channel theory. In 2018, via comparing |S| of three different types of solid-state polyelectrolytes, the percolated pathway model of nonliquid i-TE materials was raised.[16] As illustrated in Figure 14c(i), interconnected water ion channels cannot be entirely established at low concentrations. While under sufficient humidity, two different situations are determined by the direction of water diffusion. If the water molecules and ions diffuse along the opposite direction, |S| will be weakened with increasing relative humidity (Figure 14c(ii)). In this circumstance, the molar entropy of water transfer in the external environment is larger than that in internals, e.g., Nafion polymer membranes. On the flip side, if the water molecules and ions diffuse along a consistent direction, the S is escalated, such as in the S-PEEK film (Figure 14c(iii)).[16,135]

It is hence promising to maintain high humidity for a better i-TE performance. Inspiration may come from a recent work, in which a self-humidifying bilayer cover sheet was devised by

**ADVANCED
SCIENCE NEWS**

www.advancedsciencenews.com

**ADVANCED
ENERGY
MATERIALS**

www.advenergymat.de
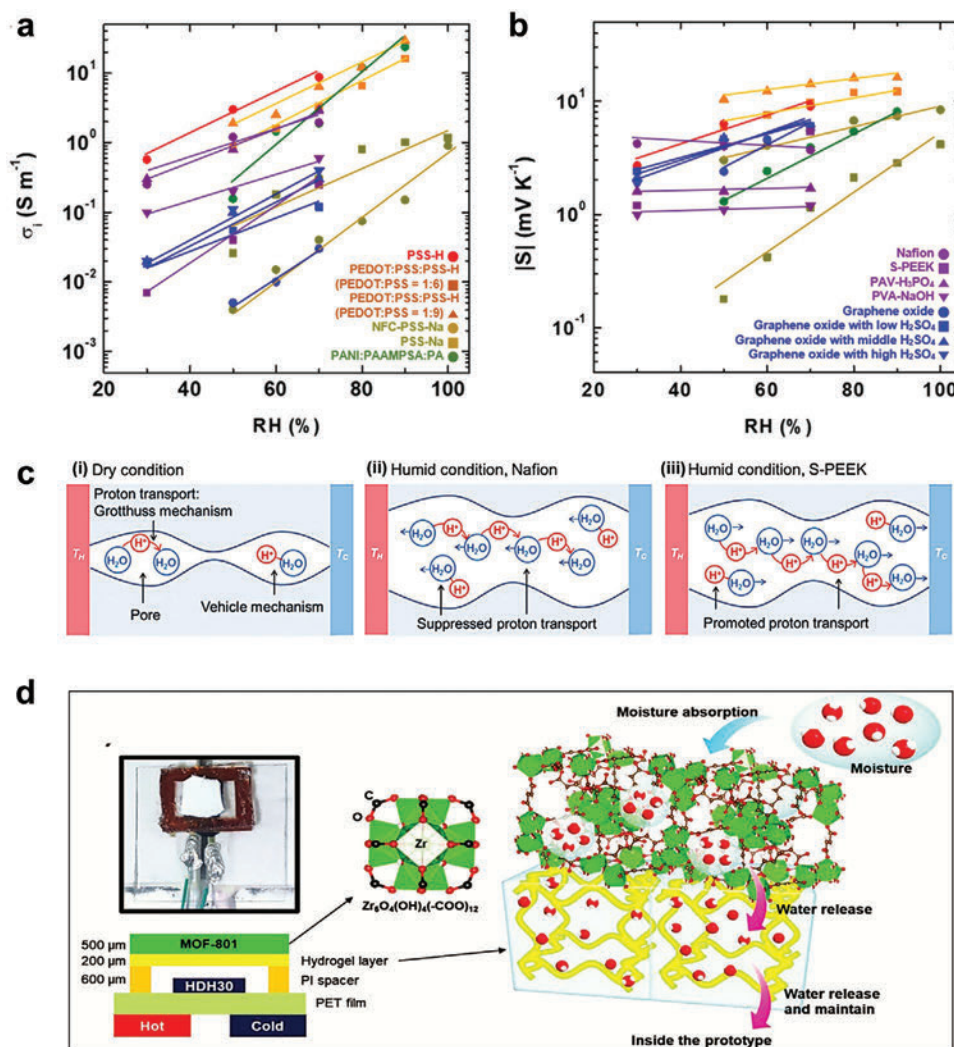
Figure 14. Humidity-dependent a) σ and b) S of the selected i-TE materials. Reproduced with permission.[81] Copyright 2021, Elsevier. c) Schematic illustration of ion transport in dry and humid environments. Reproduced with permission.[16] Copyright 2018, Elsevier. d) Photo and structural diagram of a self-humidifying bilayer sheet. Reproduced with permission.[18] Copyright 2019, Wiley-VCH.

applying metal organic framework (MOF-801®) as the outer layer and hydrogel as the inner layer (Figure 14d).[18] The MOF layer absorbs the moisture from the ambient and then delivers it to the hydrogen layer. Thus the humidity of the attached cavity was maintained where the i-TE materials are deposed.[136] As a result, a humidity of 90% over 72 h can be provided, which is essential to fabricate stable and high-performance i-TE systems.

Viscosity is also related to i-TE performance, where low viscosity usually results in high ion mobility, or vice versa. Referring to Table 1, due to long side-chain alkyl groups increasing viscosity, ILs with [TFSI]$^-$ show descending absolute S values of [EMIM:TFSI] > [BMIM:TFSI] > [HMIM:TFSI] > [OMIM:TFSI].[69] By contrast, EG has the lowest viscosity and show ultrahigh σ due to the promoted ion mobility.[91] Another factor needs to be taken into account is that viscosity is related with ion freedom. For instance, materials with high dielectric constant possess stronger charge bounding capability, which greatly decreases σ.[92] **Figure 15**a shows the mesoporous structure with porous networks made of BC nanofibers. When ILs

flow through BC matrix, the swelling effect occurs, and the interval pores are expanded (Figure 15b). The schematic diagram in Figure 15c demonstrates the evolution of the gradient structures with a surface layer and an inner layer. As the IL loadings increase, corresponding pore diameters expand to greater spacing. Whereas in [EMIM:DCA] ILs, the surface layer is composed of the [DCA]$^-$ by connecting to the hydroxyl of the BC matrix (Figure 15d). The small pore diameter prohibits the movement of cations, in analogy to what happens in Helmholtz electric double layer. With increasing pore diameter, the inner layer zone is disengaged to generate higher σ where ions or ion clusters can pass through near freely. The shrinking and the swelling states of BC/[EMIM:DCA] ionogels are referred to Figure 15e(i),(ii).[69]

Crystallinity is another influence factor for especially polymer-based i-TE materials, which can be rationally modified through material engineering.[137] On the one hand, strategies of annealing, cross-linking, and reducing the soft segment chain proportion can effectively regulate crystallinity.[92,94] On the

**ADVANCED
SCIENCE NEWS**

www.advancedsciencenews.com

**ADVANCED
ENERGY
MATERIALS**

www.advenergymat.de

Figure 15. a) Scanning electron microscopy images of BC. b) Schematic illustration of the BC swelling with the increasing ILs loading. c) Structure evolution of the pores in BC with the increasing ILs loading. d) The ion diffusion of BC before and after swelling. e) Chemical structures of BC-[EMIM:DCA] ionogels under shrinking (left) and swelling (right) states. Reproduced with permission.[69] Copyright 2021, Wiley-VCH.

other hand, the addition of antisolvent further refines the crystalline grain size. As shown in **Figure 16**a, grain refinement can be achieved by mixing an antisolvent into the acetone solution of the PVDF-HFP/[EMIM:DCA] i-TE system before the gelation step.[19] The addition of ethanol, methanol, and isopropanol dramatically increases σ, which is yet observed in cosolvents 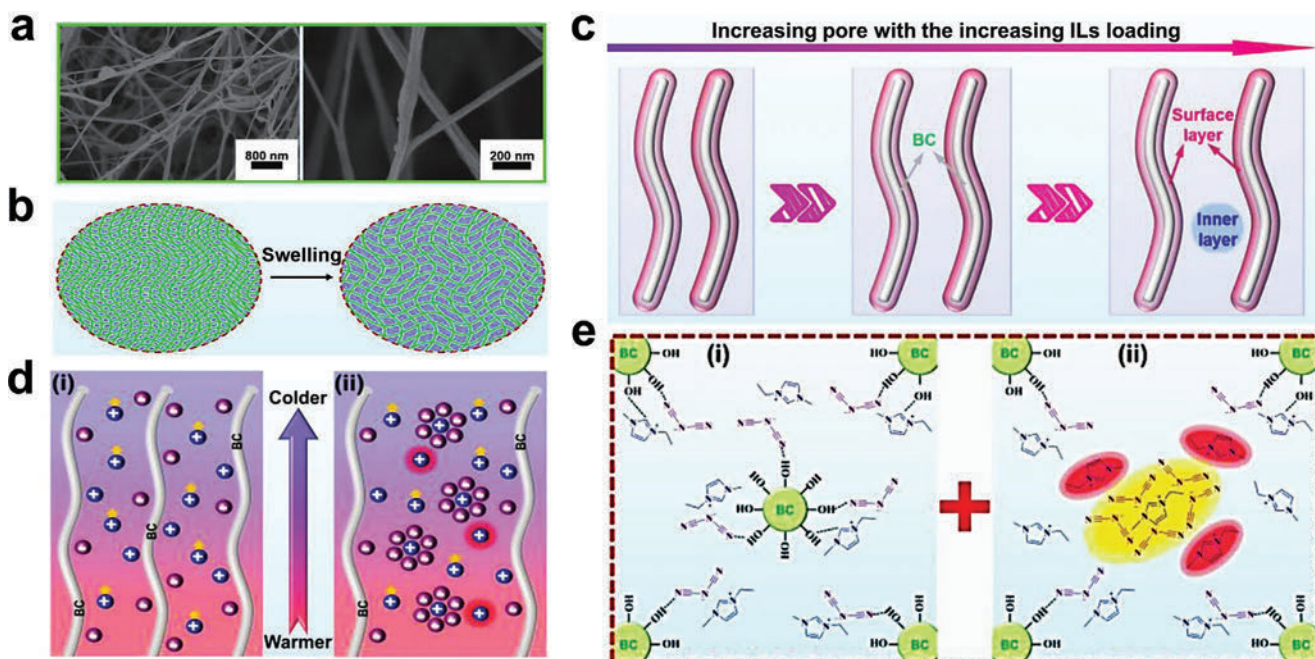of DMSO and DMF. Scanning electron microscopy (SEM) images in Figure 16b,c compare the morphology of the pristine PVDF-HFP/[EMIM:DCA]-50% ($m_{[EMIM:DCA]}:m_{[PVDF-HFP]}$ = 1:1) ionogels and the PVDF-HFP/[EMIM:DCA]-50% ionogels post-treated with 10 wt% ethanol antisolvent. Obviously, antisolvent treatment results in network structures, which provide connecting points near which the grain size is refined. Figure 16d demonstrates the detailed procedure of how the addition of antisolvent refines grain size. i) The polymer chains are under stretched coil-like conformations in the original good solvent (acetone). ii) After evaporating acetone, large size pores are formed due to connection of the stretching conformational polymers, which are filled with ILs. iii) The stretched PVDF-HFP chains entangle into bundles due to the dipole–dipole interaction. Therefore, the thick polymer bunches fold into large grains at the network connection points. iv) Conversely, the stretched polymer chains contract gradually as the antisolvent addition. The formation of the thick polymer bundles is hindered as well. v) As a result, wispy solid networks are assembled by the contracted polymer chains. vi) Grain refinement is fulfilled.

Phase hybridization is an extensively adopted strategy for conducting polymer materials, which shows efficacy in tuning their thermal properties.[138] As shown in **Figure 17**a, the κ of polymers and polymer composites depend on the phonon transport along continuous pathways.[139] The existence of hetero-interfaces will scatter phonon transport pathways and there-fore prohibit thermal transport. Although phonon scattering can happen within a homogeneous phase, such that between the crystalline segment and amorphous segment in semicrystalline polymers, it mainly arises from the phase boundaries in multiphase materials.[140] As exhibited in Figure 17b, phase boundaries, inclusions, and pores can effectively scatter long-wavelength phonons, and a certain fraction of mid-wavelength phonons and short-wavelength phonons depending on their density-of-state.[141] Nanoscale grain boundaries that tend to exist within the homogeneous phases mainly scatter mid-wavelength phonons, as well as short-wavelength phonons. Whereas point defects due to doping, atomic substitution, or vacancies contribute barely to short-wavelength phonon scatterings. Figure 17c provides the SEM images of BC/[EMIM:DCA], BC/[EMIM:TFSI], and BC/[EMIM:BF$_4$] ionogels. Obviously, micrometer-scale phase separation can be observed and certified, where a minimum κ of 0.186 W m^{-1} K^{-1} was obtained.[69]

As i-TE materials are commonly multi-phase compounds with low κ (see Table 2), the optimization of κ has received less attentions. Since i-TE materials cover liquid, quasi solid, and solid multistates, where heat conduction mechanisms are completely different. Specifically, heterogeneous material composition, phase compatibility, fluid convection, and bulk conduction, can synergistically contribute to the κ of i-TE materials.[142] The thermal performance regulation is deeply complex for i-TE materials, which has not been studied maturely till now.

5.2. Incorporation Approach

Modifying interaction relations has shown efficacy in optimizing i-TE performance. In what follows, four kinds of

ADVANCED
SCIENCE NEWS

www.advancedsciencenews.com

ADVANCED
ENERGY
MATERIALS

www.advenergymat.de
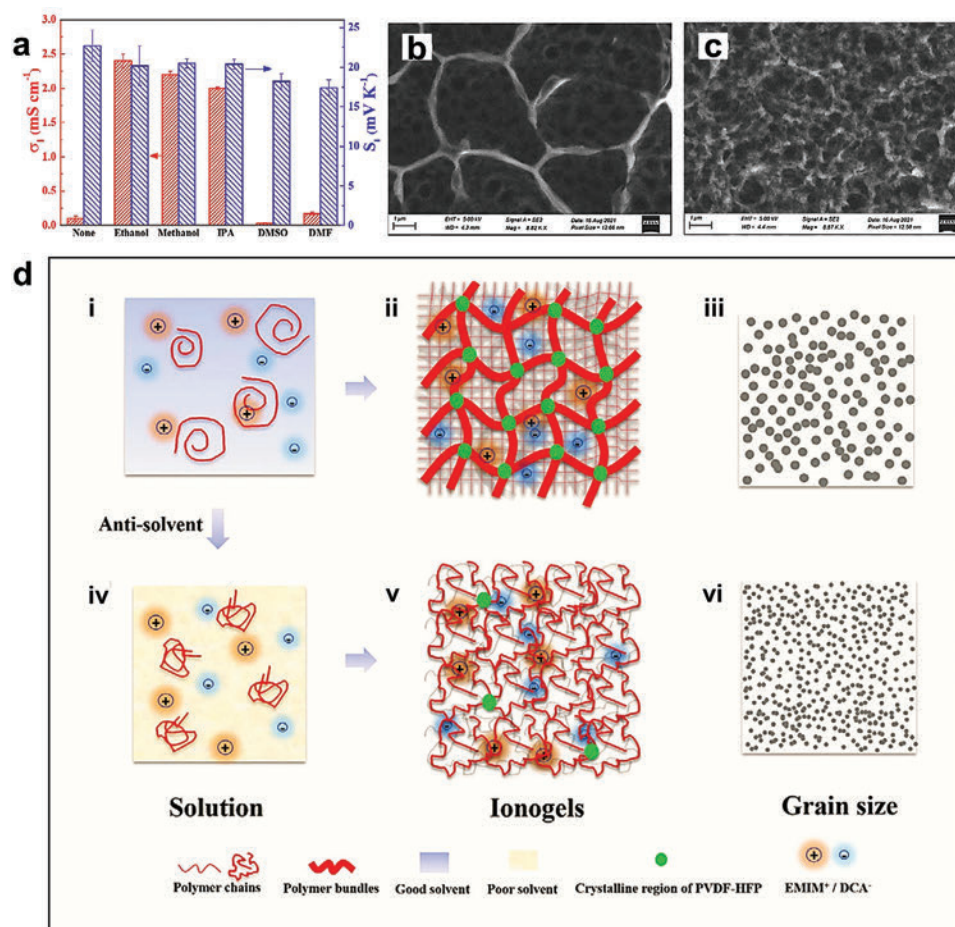
Figure 16. a) *S* and *σ* of the poly(vinylidene fluoride-*co*-hexafluoropropylene) (PVDF-HFP)/[EMIM:DCA]-50% ionogels prepared by adding different antisolvents prior to the ionogel formation. SEM image of the xerogel of b) pristine PVDF-HFP/[EMIM:DCA]-50%, and c) PVDF-HFP/[EMIM:DCA]-50% prepared by adding 10 wt% ethanol. d) Schematic illustration of the crystal formations and the polymer networks of pristine PVDF-HFP/[EMIM:DCA] ionogels and antisolvent treated PVDF-HFP[/EMIM:DCA] ionogels. Reproduced with permission.[19] Copyright 2022, Wiley-VCH.

incorporation strategies are introduced, namely, ion–electrode interaction, ion–matrix interaction, ion–electron combination, and diffusion–redox combination.

5.2.1. Ion–Electrode Interaction

Given the straightforward correlation between i-TE *S* and concentration gradient difference from anions to cations under equilibrium, the adsorption–desorption of ions on the electrode surface plays an important role in generating thermovoltage.[143] As shown in **Figure 18**a, modification of ILs leads to both n-type and p-type i-TE materials with gold sheets as electrodes.[78] As summarized in Figure 18b, with common A4 paper adopted as the substrate, ILs of [OMIM:Ac], [EMIM:Ac], and [OMIM:Cl] behave p-type conductance, while [EMIM:BF$_4$], [EMIM:TFSI], and [OMIM:PF$_6$] exhibit n-type conductance despite of the trivial *S*. A schematic diagram of the adsorption–desorption effects is displayed in Figure 18c: [BF$_4$]$^-$, [TFSI]$^-$, and [PF$_6$]$^-$ are unwieldy anions due to the large radius of F atoms. Thus, the intensive steric hindrance effect is beneficial to the anions desorption from the electrodes.[144] As a result, cations

accumulate in priority around the cold electrode to raise positive *S*. On the contrary, anions of [Ac]$^-$ and [Cl]$^-$ are functional to coordinate with gold electrodes. The binding effect induces more anion aggregations on the electrode surface under equilibrium. In this regard, negative *S* can be generated. By connecting the n-type and p-type units in sequence, a 20-armed device supplies a voltage of 0.8 V at a *ΔT* of 35 °C (Figure 18d). These results confirm that the ion–electrode interaction can not only determine the conductance nature, but also change the magnitude of *S*. Additionally, according to the same i-TE material, the employment of different electrode materials strongly impacts the *S*.[68]

5.2.2. Ion–Matrix Interaction

Ion–matrix interactions have been extensively adopted in optimizing i-TE performance, including the ion–dipole interaction,[94] the ion-coordination interaction,[92] and the hydrogen-bonding interaction.[69] Specifically, ion–matrix interactions can be realized through three pathways.

**ADVANCED
SCIENCE NEWS**

www.advancedsciencenews.com

**ADVANCED
ENERGY
MATERIALS**

www.advenergymat.de
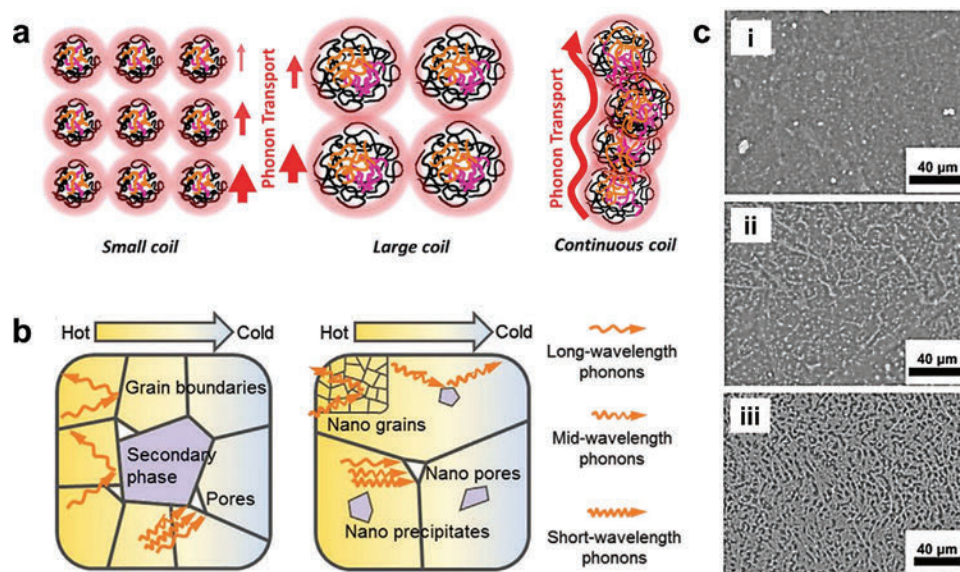
Figure 17. a) Phonon transport envisaging for small, large, and continuous coil polymers. Reproduced with permission.[139] Copyright 2018, Elsevier. b) Comparison of phonon scattering centers between heterogeneous phases and homogeneous phases. Reproduced with permission.[141] Copyright 2020, Wiley-VCH. c) SEM of (i) BC/[EMIM:DCA], (ii) BC/[EMIM:TFSI], and (iii) BC/[EMIM:BF$_4$] ionogels with the same IL loading of 90%. Reproduced with permission.[69] Copyright 2021, Wiley-VCH.

i) Increase the concentration difference between anions and cations. In a PU/[EMIM:DCA] i-TE ionogel where the modified PU chains are functionalized with cationic imidazole side groups, the cationic imidazole groups attract and immobilize [EMIM]$^+$ cations due to the ion–dipole interaction.[94] As a re-sult, a higher thermal diffusion efficiency of [DCA]$^-$ anions can be obtained to generate an impressive S of 34.5 mV K^{-1}, which is 4.4-fold to pure [EMIM:DCA].

ii) Strengthen the ion dissociations. For instance, with add-ing inorganic salts (NaOH or NaCl) into PVA matrix films,
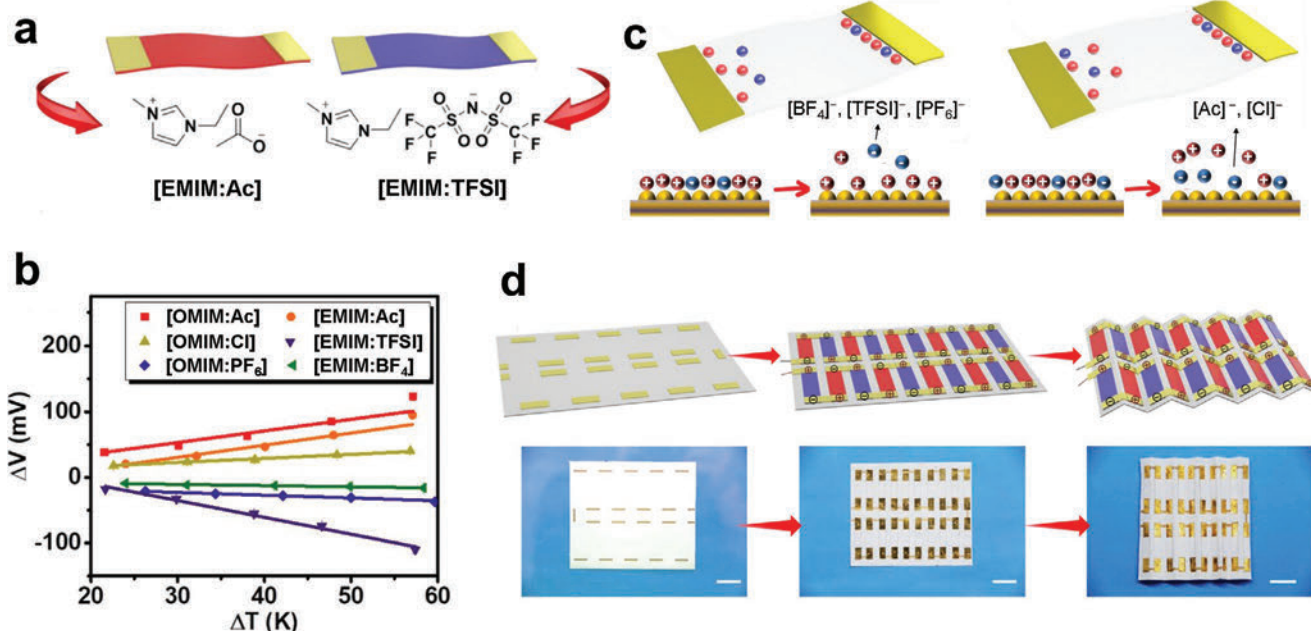
Figure 18. a) Schematic diagram of i-TE modules consisting of gold electrodes, A4 paper matrix, and ILs. b) Thermovoltage of the i-TE modules employing six different kinds of ILs. c) Schematic diagram of the adsorption–desorption effects on both p-type and n-type modules. d) Fabrication and foldability of a 20-armed i-TE device by in-order connection of the p-type and n-type modules. Reproduced with permission.[78] Copyright 2020, American Chemical Society.

2203692 (25 of 45)
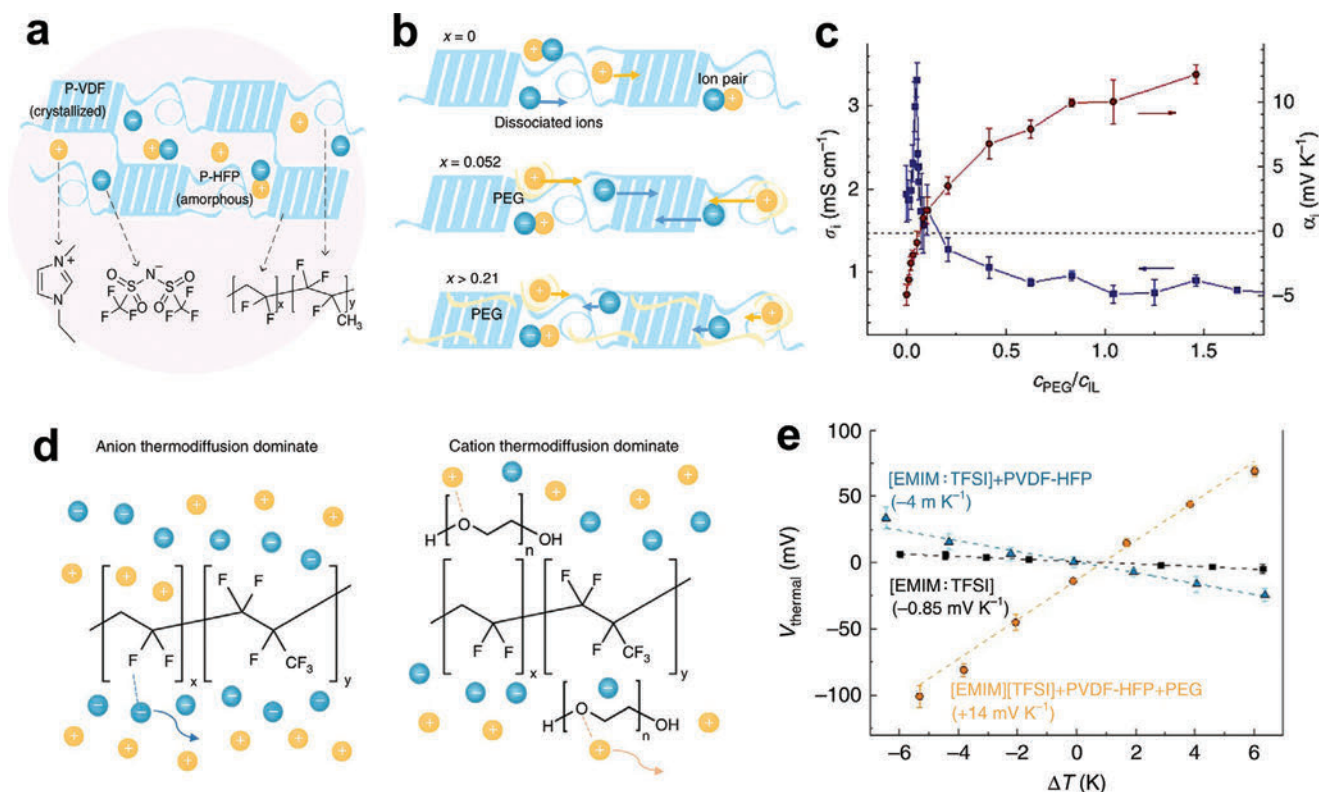
Figure 19. a) Composition and corresponding chemical structures of [EMIM:TFSI]/PVDF-HFP i-TE gels. b) Schematic diagram of the interaction between [EMIM:TFSI], PVDF-HFP, and polyethylene glycol (PEG). c) σ and S of [EMIM:TFSI]/PVDF-HFP/PEG as a function of the molar concentration ratio of c_{PEG}/c_{IL}. d) Schematic diagram of the ion transfer before and after PEG addition. e) $V_{thermal}$ of pure [EMIM:TFSI], [EMIM:TFSI]/PVDF-HFP, and [EMIM:TFSI]/PVDF-HFP/PEG as a function of ΔT. Reproduced with permission.[99] Copyright 2019, Springer Nature.

the abundant hydroxyl groups of PVA coordinate with inorganic salt cations. Such coordination promotes the dissociation of the anion–cation pairs and improves the σ.[92,145] Hydrogen bonding between PVA and the cations can greatly intensifies the concentration gradient of anions in another PVA/NaI i-TE system, in which a record-high ionic S of 52.9 mV K^{-1} was achieved and the ZT value can be calculated to be 5.18.[97]

iii) Achieve p–n conversions. Several works highlighted the p–n conversions in i-TE materials mainly due to ion–matrix interactions.[67,99,102] **Figure 19**a displays the material composition of a [EMIM:TFSI]/PVDF-HFP i-TE gel via chemical structures.[99] As illustrated in Figure 19b, the addition of PEG promotes the dissociation of ILs due to ion-PEG coordination, leading to continuous raise of PEG fraction, which in turn hinders ion transport. As a result, the σ value increases first and decreases afterward, as shown in Figure 19c. As demonstrated in Figure 19d, the matrix of PVDF-HFP interacts with [TFSI]$^-$ to provide anion pathways, resulting in negative S. With increase of PEG fraction, PEG interacts with [EMIm]$^+$ via hydrogen bonding to provide cation pathways. Besides, the [TFSI]$^-$ can be isolated from the PVDF-HFP chains by PEG, synergistically resulting in positive S (Figure 19e). Consequently, an 18-armed [EMIM:TFSI]/PVDF-HFP i-TE device exhibits an outstanding S of 0.333 V K^{-1}.

5.2.3. Ion–Electron Combination

The main shortcoming of i-TE materials is the insufficient σ. Therefore, a strategy of doping e-TE materials (which possess much higher σ) can be expected to compensate for the insufficient i-TE σ.[146] As quantitative prediction of the σ of such an ion–electron combined system is still in controversies, here, we provide a brief discussion at the conceptional level.[22] Taking a ternary hybrid i-TE material composed of PANI, PAAMPSA, and PA system as an example (**Figure 20**a). PANI is a p-type conducting polymer e-TE material employing holes as carriers that have been widely known.[147] PAAMPSA is a polyelectrolyte i-TE material that is structured with H$^+$ protons and SO$_3^{2-}$ functioned groups. PA is an inorganic acid that can replenish ionic carriers in the whole system. The combination of the three species thus reaches a maximum σ of 23.7 mS cm^{-1}, which is much higher than the individual σ of each phase.[104] Another strategy has been reported for the embedding arrangement of graphene oxide (GO) in a PSSH solid electrolyte (Figure 20b–d).[105] By repeatedly dropping–evaporating water solvent, GO tends to align in the way as per Figure 20b, leading to the establishment of continuous channels to foster the vehicular behavior of proton carriers (Figure 20c). As a result, the σ is remarkably increased to ≈115 mS cm^{-1} and its ionic ZT value exceeded twice higher of 0.85 (namely, PSSH containing 3 wt% GO) compared with pure PSS-H (Figure 20d). Besides, similar
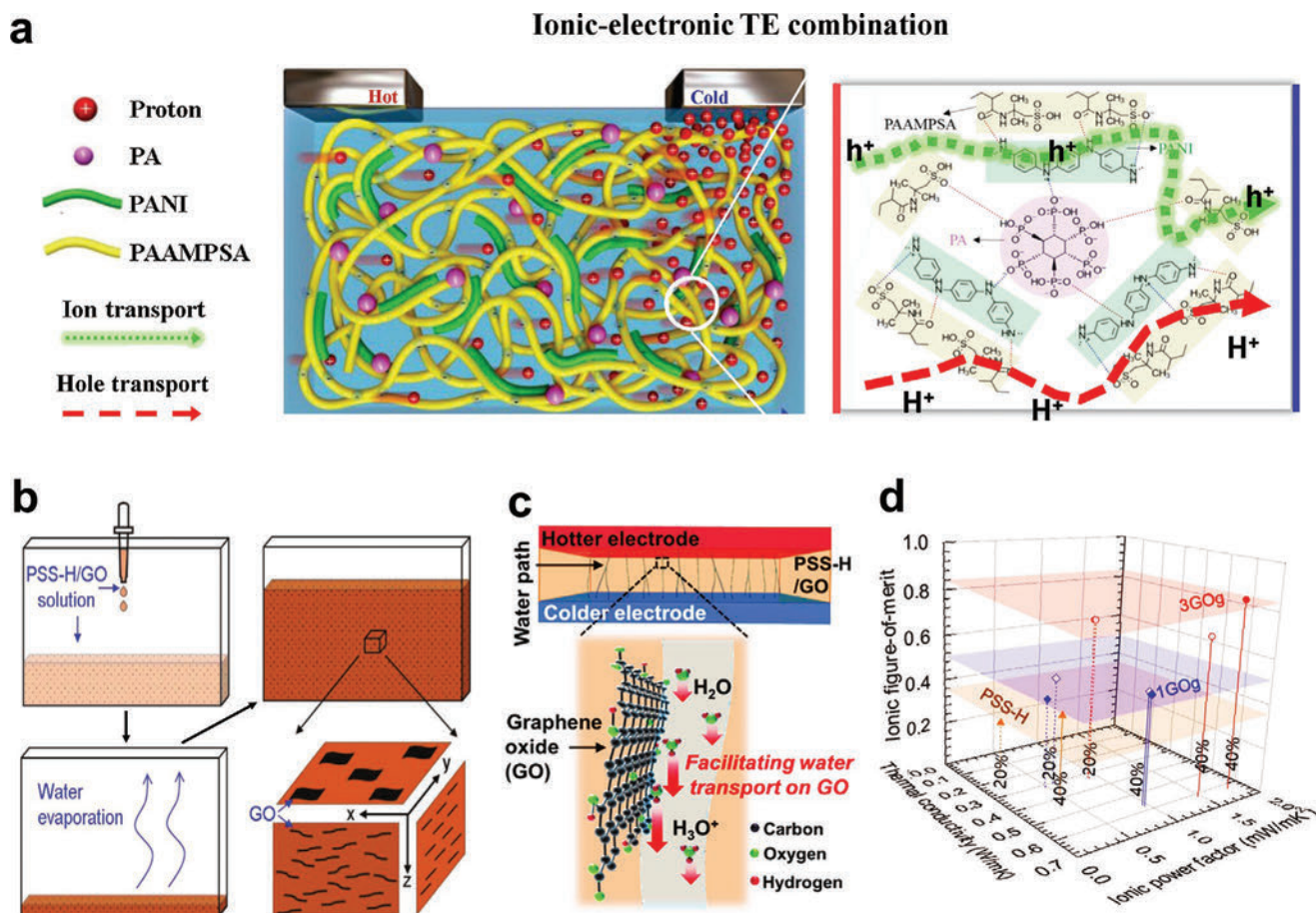
Figure 20. a) Schematic diagram of the composition and carrier pathways of the PANI/PAAMPSA/PA i-TE gels. Reproduced with permission.[104] Copyright 2020, Royal Society of Chemistry. b) Schematic diagram showing the fabrication of the aligned GO/PSSH blending i-TE materials. c) Proton transport pathways provided by aligned GO. d) Stereogram showing ZT, κ, and $S^2\sigma$ for pure PSS-H (orange), PSS-H containing 1 wt% GO (blue), and PSS-H containing 3 wt% GO (red). Reproduced with permission.[105] Copyright 2021, Wiley-VCH. Note: dotted and solid vertical lines represent 20 and 40 wt% water content, and hollow and solid icons indicate pure PSS-H/GO hybrid and PSS-H/GO/hydrogel hybrid, respectively. The synthesis of the hydrogel can be elaborated in the literature.[105]

mixed ionic–electronic conducting effects in polymer/carbon TE materials were reported by other researchers.[148]

5.2.4. Diffusion–Redox Combination

Unlike the ion–electron combination strategy which focuses on optimizing σ, the combination of ion diffusion and redox reactions mainly affects the S.[15,21,81,149] According to the Onsager reciprocal relations,[150] the synergistic S (S_T) can be expressed as the coupling of thermodiffusion and thermogalvanic factors[21]

$$S_T = -\alpha_R + S_{td}(\text{redox couple}) + S_{td}(\text{ions}) + S_{td}(\text{matrix}) \quad (24)$$

where $-\alpha_R$ is the contribution of redox potential, S_{td} (redox couple) is the contribution of the thermodiffusion potential of the redox couples, S_{td} (ions) is the contribution of the thermodiffusion potential of the ionized ions, and S_{td} (matrix) is the contribution of the thermodiffusion potential of the matrix.

Recent efforts prepared a $Fe(CN)^{4-/3-}$/KCl/gelatin i-TE system, as shown in **Figure 21**a.[21] Figure 21b compares the S of the corresponding samples with individual TE effects and diffusion–redox combinations. Presumably, as-prepared $Fe(CN)^{4-/3-}$/KCl/gelatin exhibits an overwhelming S in a range of 12.7–17 mV K^{-1}. The equivalent circuit diagram and fraction contribution to S_T is presented in Figure 21c. The S_T benefits maximally from the thermodiffusion of KCl (62.2%) while the redox potential of $Fe(CN)^{4-/3-}$ occupies a second proportion of 17.9%. Figure 21d–f explains the fundamental of the synergistic effect. At a given ΔT, KCl accumulates at the cold electrode to induce an electric field. This is caused by the thermodiffusion effect and the electric field is directional from the cold electrode to the hot electrode (Figure 21d). Regarding the thermogalvanic effect, oxidation reaction occurs at the hot end and a reduction reaction occurs at the cold end (Figure 21e). As a result, the hot electrode gains electrons to generate a lower chemical potential. The cold electrode loses electrons, and higher chemical potential is attained. Therefore, the thermogalvanic effect of the $Fe(CN)^{4-/3-}$ couple endows the same sign of electric field with
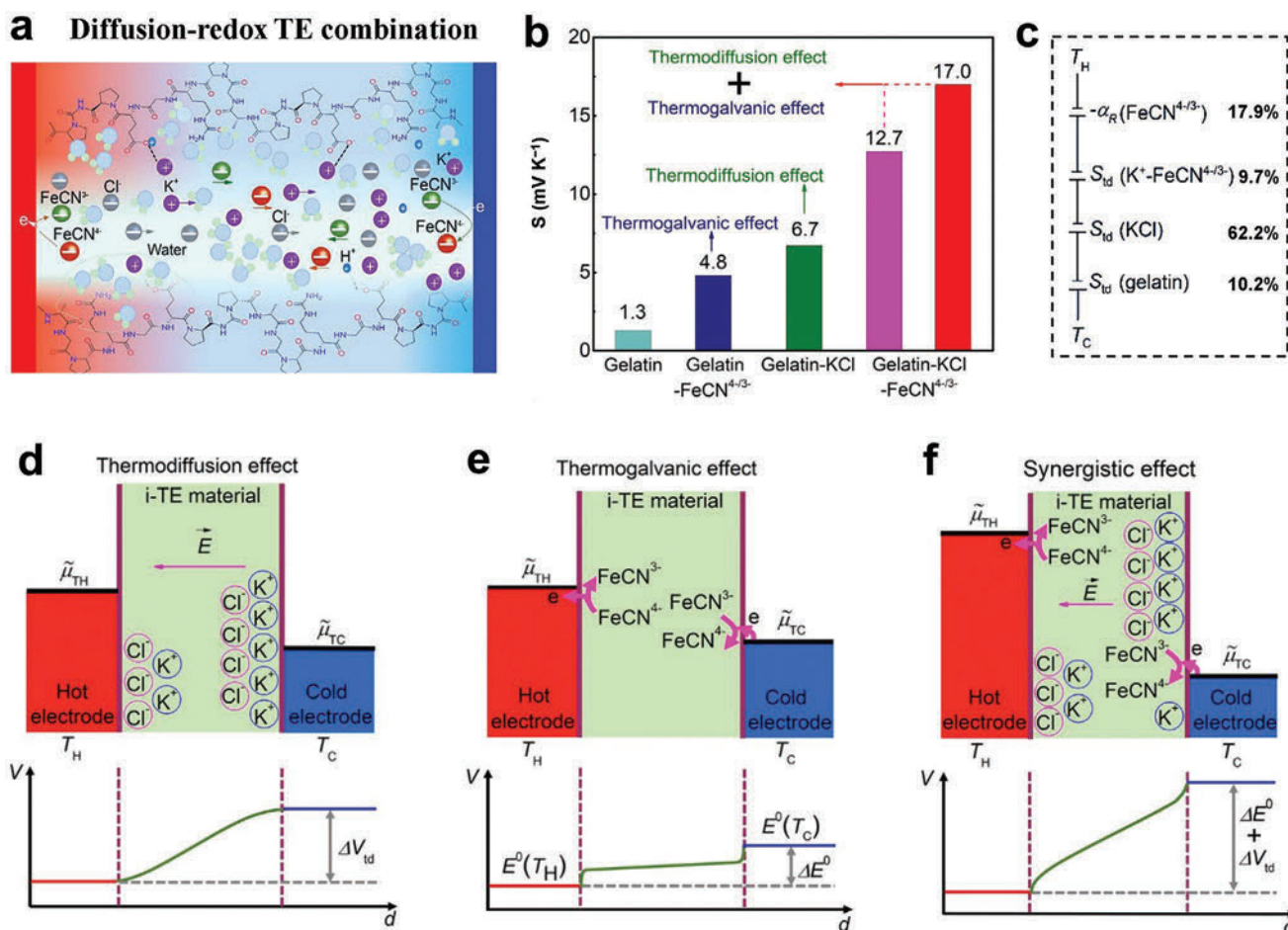
Figure 21. a) Schematic diagram of the thermodiffusion and thermogalvanic i-TE effects of a $Fe(CN)^{4-/3-}$/KCl/gelatin system. b) Comparison of the S of the pure gelatin, gelatin/$Fe(CN)^{4-/3-}$, gelatin/KCl, and gelatin/KCl/$Fe(CN)^{4-/3-}$. c) The equivalent circuit diagram and the fraction contribution of every single part. Chemical potential ($\tilde{\mu}$) diagrams of d) thermodiffusion effect of KCl, e) thermogalvanic effect of $Fe(CN)^{4-/3-}$, and f) synergistic effect of the $Fe(CN)^{4-/3-}$/KCl/gelatin system. Reproduced with permission.[21] Copyright 2020, American Association for the Advancement of Science.

that due to the thermodiffusion of the KCl ions (from the cold electrode to the hot electrode). Therefore, an increase of S can be achieved (Figure 21f).

5.3. Structural Optimization Approach

Structure engineering provides another scheme where i-TE performance can be effectively modified. Currently, structural engineering strategies include constructing ion channel, introducing dual layer structure, and modifying surface morphology, which will be discussed in detail.

5.3.1. Constructing Ion Channel

Artificially constructed ion transport channels can increase ion mobility, which has been verified in natural-wood-prepared cellulose matrix with intrinsically aligned structures as the ion carrier channels.[151] As shown in the XRD spectrum of **Figure 22**a, the delignification treated cellulose exhibits excellent orientation alignments which is responsible for the clean elliptical pattern. When electrolyte consisting of PEO, NaOH, and deionized water is added to the aligned cellulose, the ion transport channels are accordingly constructed, as illustrated in Figure 22b. The hydroxyl-rich PEO chains attached to the cellulose surface serve as an inner layer to promote the dissociation of NaOH. Meanwhile, the ionized OH^- anions from the salt link with plenty of hydroxyl groups via hydrogen bonds. In such a way, selective migration of Na^+ through the cellulose aisles can be realized, leading to an ultrahigh S of 24 mV K^{-1}.[12] Saito et al. also reported a porous polypropylene membrane providing vertical linear channels for ion transfer.[152] He et al. built ion pathways within the intervals of nanoparticle i-TE gels.[20] Moriyasu et al. prepared a slide-ring cross-linked i-TE gel where the ions transport through non-networking regions.[153] These cases imply that ion channel frames can effectively optimize i-TE performance.

5.3.2. Introducing Dual Layer Structure

A dual-layered structure composed of i-TE (PSS^-) and e-TE materials instead of the traditional one-layered mixture is
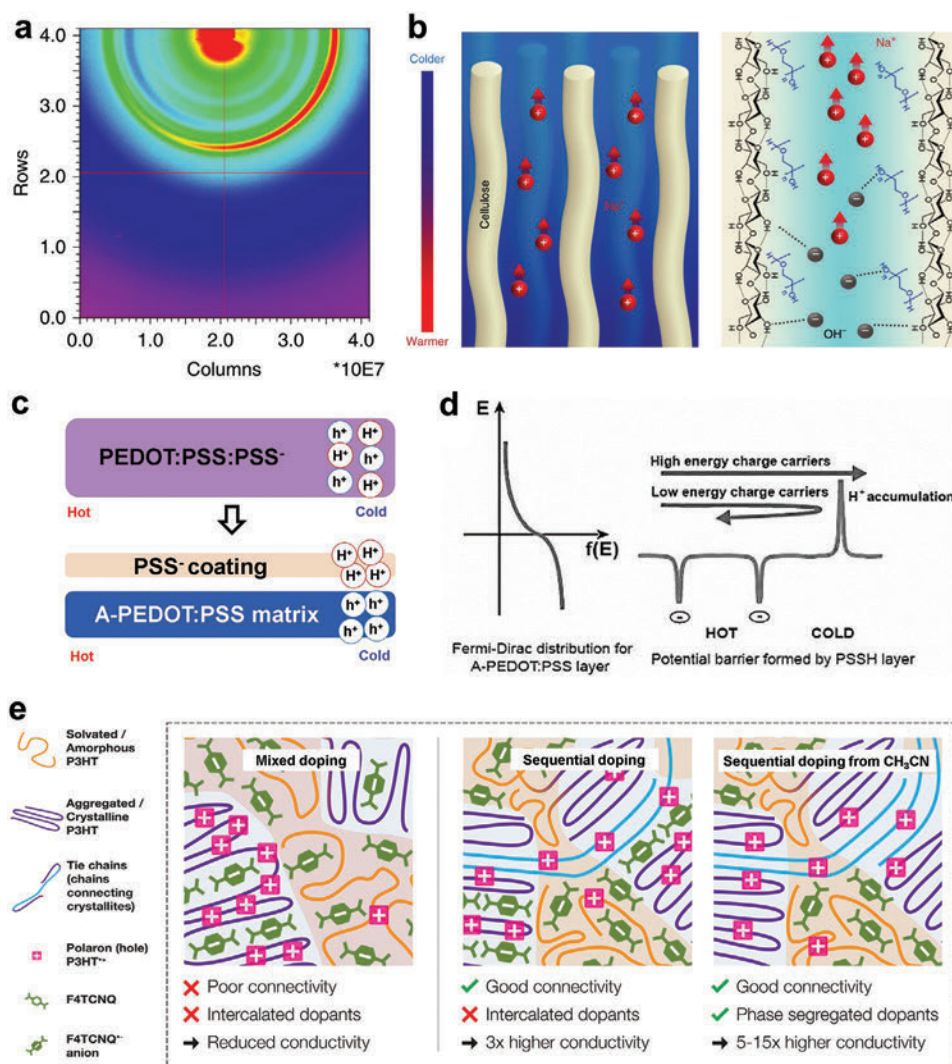
Figure 22. a) XRD pattern of the cellulose film infiltrated with NaOH. b) Schematic diagram of the aligned cellulose with selective ion transport and the corresponding chemical structures. Reproduced with permission.[12] Copyright 2019, Springer Nature. c) Schematic diagram of carrier transports of PEDOT:PSS/PSS⁻ and PSS⁻ coated H_2SO_4 treated PEDOT:PSS (A-PEDOT:PSS) under a given ΔT. d) The demonstration of the energy filtering effects of PSSH/A-PEDOT:PSS (including the Fermi–Dirac distribution and the hole potential barrier at the A-PEDOT:PSS layer surface). Reproduced with permission.[131] Copyright 2018, Royal Society of Chemistry. e) Dopant distribution and corresponding property characteristics of 2,3,5,6-tetrafluoro-7,7,8,8-tetracyanoquinodimethane (F4TCNQ) doped poly(3-hexylthiophene-2,5-diyl) (P3HT) film applying the sequential doping methods. Reproduced with permission.[154] Copyright 2016, Royal Society of Chemistry.

shown in Figure 22c.[131] The H_2SO_4-treated PEDOT:PSS (A-PEDOT:PSS) layer is the major component of the film and the PSSH layer was coated onto the A-PEDOT:PSS matrix as a functional layer. Ideally in this structure, protons flow along the PSS⁻ layer while holes flow along the A-PEDOT:PSS layer. However, as shown in Figure 22d, the accumulated protons in PSSH layer generate a same-sign potential with holes in the A-PEDOT:PSS layer. When the carriers pass through the interface between two layers, low-energy carriers can be filtered. As a result, the energy filtering effect based on the Soret effect is achieved by rational designation. A stable and continuous TE conversion can be obtained, and the measured $S^2\sigma$ of 401 µW m⁻¹ K⁻² is several orders of magnitude higher than that of the monolayered PEDOT:PSS/PSS⁻ under 100% relative humidity.

5.3.3. Modifying Surface Morphology

Extensive results have been reported about the modification of film morphology via sequential doping.[154] For instance, 2,3,5,6-tetrafluoro-7,7,8,8-tetracyanoquinodimethane (F4TCNQ)-doped poly(3-hexylthiophene-2,5-diyl) (P3HT) film, processed by a sequential solution, shows uniform nanoscale morphology and good connection between the amorphous phase and the crystalline phase (Figure 22e). Moreover, the method of selective sequential doping of acetonitrile (CH_3CN) leads to the exclusive distribution of F4TCNQ anions in amorphous domains. In this way, the resultant σ can be improved to 5–15 times higher (see Figure 22e). Although the article is not focused on the i-TE materials and the ionic conductively, we noticed that the ion enrichment occurs by adopting sequential

**ADVANCED
SCIENCE NEWS**

www.advancedsciencenews.com

**ADVANCED
ENERGY
MATERIALS**

www.advenergymat.de

a Encapsulation

Patterned basement → Injection → Full filling

b Printing

Load Resistor

Temperature flow

Norm. power output vs Number of cuts

1 2 3 4 5 6 7 8 9 10

c Melting-cooling

i-TE mixture → **Molten molding** → **Annealing/Quenching**

d Evaporation

Bottom electrodes → Insulate layer → i-TE solutions

Top electrodes ← Evaporation molding

e Drop casting

Composite solution → **Drop casting & annealing** → **Detaching**

Substrate → Composite film / Substrate → Freestanding Composite film

f Spin coating

Dripped ink → **Spin coat & dry** (dry after 1 second) → OR → **Multi-layered**

2203692 (30 of 45)

47

doping, which provides a possible strategy for the ion pathway design. This is likely an inspiring reference for high-performance i-TE materials.

6. Molding

Although the materials design is essential that primarily determines the TE conversion efficiency, the subsequent molding process is also indispensable before TE device fabrications. In most cases, i-TE materials are pre-prepared into solutions and molding methods are analogous to the polymer e-TE materials including printing, drop casting, and spin-coating techniques.[155] Besides, common methods of cooling and evaporation have been applied to shape the raw materials as well.[156] In this section we will briefly introduce these molding methods in order.

6.1. Pretreatment

As has been discussed, i-TE materials can be classified into liquid state, quasi-solid state, and solid state. i) For i-TE liquids, encapsulations are directly applied for containment. ii) For quasi-solid gels, the existence of solvents permits satisfying fluxility and facile molding. Particularly, the chemical reaction of cross-linking often happens during gel forming as a unique process.[156] iii) For solid state polyelectrolytes, solutions are commonly pre-prepared, where solvents can be removed after solution molding.

6.2. Molding Approach

Encapsulation approves the fixation of liquid and fragile i-TEs.[157] As an important part to achieve encapsulation, materials of epoxy resin, organic silicon, glass tube, etc. have been used as the packaging basements to contain i-TE liquids.[158] For instance, by predepositing electrodes and predesigning filling channels in the epoxy resin, ILs can be injected into the reserved channel via a needle tube. After full-filling, the injection cavity is sealed with glue or rubber. The encapsulated liquid i-TE materials are thus obtained for subsequent testing and device assembling, as shown in **Figure 23**a.

Printing process includes screen printing, 3D printing, inkjet printing, etc.[78,90,99] Specifically, screen printing and inkjet printing are suitable for film manufacturing, while 3D printing can yield shaped bulks. In practice, the realization of printing extremely depends on the physical properties of the i-TE inks including melting point (T_m), viscosity, rheological behavior, density, solid particle size, and content.[159] Regarding low T_m i-TE materials, 3D printing can be employed using pure i-TE inks. Whereas for dissolvable i-TE materials, screen printing and inkjet printing can be achieved by preparing i-TE solution inks. As shown in Figure 23b,

appropriately designed i-TE inks can be printed out as a target TE array according to the programmed pattern.[90] Then, a preliminary i-TE device can be obtained after a simple electrode connecting process. The printing technique supports rapid and convenient fabrications, which enables scalable TE engineering at a low cost.

Melting–cooling technique can mold i-TE materials with thermoplastic matrix concisely and efficiently.[160] For example, PEO, PEG, agarose, and gelatin gel are common matrix materials for i-TEs with a low T_m of around 87, −50 to 60, 70, and 25–35 °C, respectively.[161] Notably, all of the above-mentioned T_m are lower than the boiling point of water (100 °C). Therefore, molding at a temperature higher than the matrix T_m cannot damage the component contents of the entire i-TE system containing water. As shown in Figure 23c, after the i-TE system is heated to a complete liquid state and defoamed, the resulted fluid can be poured into a mold with required shapes.[94] Subsequently, both the annealing and quenching process can be employed for frozen settings. Possible postprocessing procedures can be applied afterward according to the material designation.

Evaporation is a low-cost and simple-operated molding technique, where the required equipment can be simplified to merely an oven.[12,69,99] Pre-preparation of dilute solution or cosolution is necessary to provide sufficient fluidity. As shown in Figure 23d, certain molds are required for supporting or clamping the pre-prepared solutions. Then the excess solvent or cosolvent can be evaporated under gas blowing or heating conditions. Herein, the heating process and the corresponding temperature play an important role in the obtained i-TE structure. When the top and bottom electrodes are attached, a facile i-TE device can be obtained.

Drop casting technique has been widely applied in the molding of polyelectrolyte type i-TE materials.[91,102] The methods of drop casting and evaporation are analogous, but the main difference exists where drop casting is more fitness for fabricating films. Furthermore, compared with spin-coating technology (which will be discussed afterward), drop casting technology can maintain the uniformity of solid particles contained i-TE materials. Figure 23e is a typical drop casting progress sketch. First, the i-TE solution is dropped onto the substrate such as silicon wafer, quartz, or release film, which is precleaned by detergent, organic solvents, or plasma.[162] Then vacuum drying at an inert gas atmosphere will be conducted to output aimed casting films. Freestanding i-TE films can be obtained after peeling off from the substrate. On some occasions, the i-TE film deposited substrates can be directly applied to assemble i-TE devices. Nevertheless, both evaporation and drop casting technology are relatively time-consuming due to the long-term drying process.

Spin-coating is another solution-based technique apart from evaporation and drop casting. As spin-coating technology relies on the centrifugal force for drying, the i-TE ink is required to be uniform without possible centrifugal force derived enrichments. As displayed in Figure 23f, i-TE inks are dropped

Figure 23. Schematic diagrams for i-TE molding processes. a) Encapsulation. Reproduced with permission.[68] Copyright 2016, Wiley-VCH. b) Printing. Reproduced with permission.[90] Copyright 2019, Wiley-VCH. c) Melting–cooling. Reproduced with permission.[94] Copyright 2021, American Chemical Society. d) Evaporation. Reproduced with permission.[99] Copyright 2019, Springer Nature. e) Drop casting. Reproduced with permission.[90] Copyright 2019, Wiley-VCH. f) Spin-coating. Reproduced with permission.[164] Copyright 2016, American Chemical Society.

48

**ADVANCED
SCIENCE NEWS**

www.advancedsciencenews.com

**ADVANCED
ENERGY
MATERIALS**

www.advenergymat.de
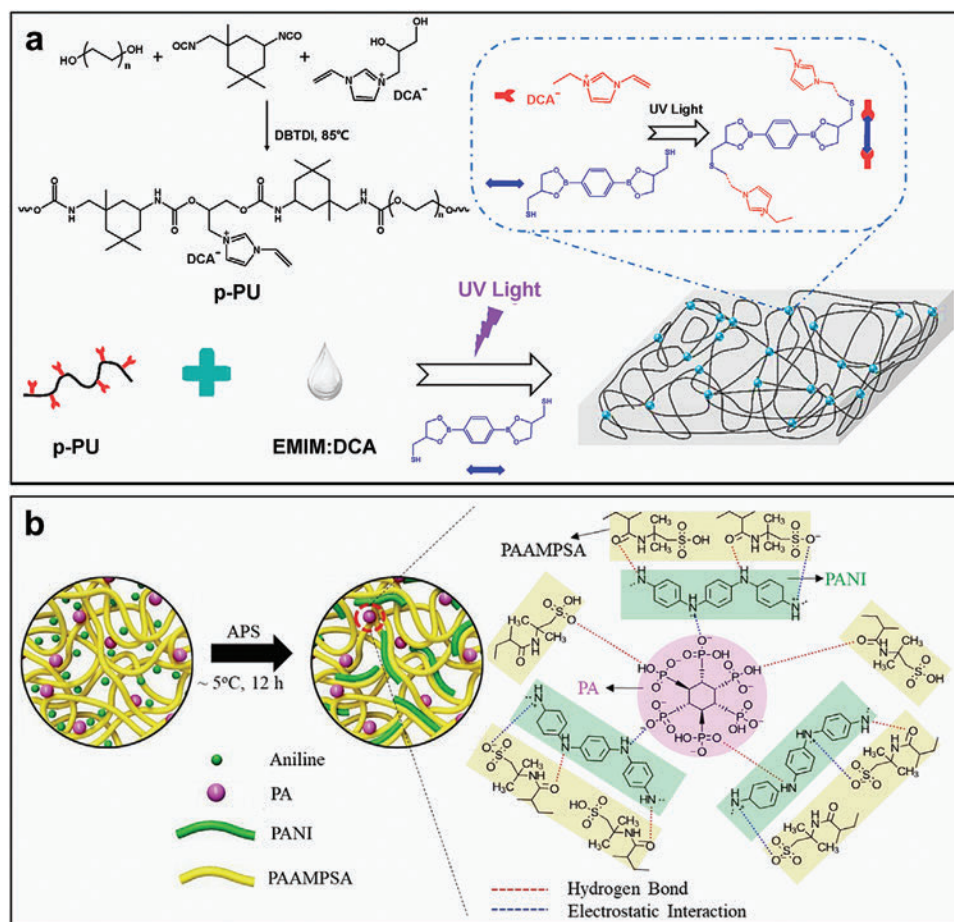
Figure 24. Schematic diagrams of a) preparation routine of cross-linked PU/[EMIM:DCA] ionogel. Reproduced with permission.[94] Copyright 2021, American Chemical Society. b) The physical cross-links consisted of hydrogen bonds and electrostatic interactions within the PANI/PAAMPSA/PA ionogel. Reproduced with permission.[104] Copyright 2020, Royal Society of Chemistry.

to the center of the platform (covered with substrate) with stationary or low speed spinning. Afterward the platform will be rotated rapidly to spread the i-TE drop and shake off the excessive solvents.[163] Layered films can be obtained by repeated spin-coating whereas the amount of layer cannot be indefinitely increased. This is because each spin-coating process will introduce solvent to destroy the layer structure.[19,94,131]

6.3. Potential Chemical Reaction during Molding–Cross-Linking

Unlike common molding processes, some i-TE materials, especially ionogels and hydrogels, exclusive chemical reactions of cross-linking are required to solidify the raw fluid materials. Practically, gels are a kind of network structured materials where polymer chains are cross-linked to each other.[165] The cross-linking process ensures the solid form of the gels, which is also known as cure molding.[166] There are mainly two kinds of cross-linking pathways: via chemical covalent bonds, or via physical supramolecular structures (including van der Waals forces, hydrogen bonds, and ionic bonds).[167]

Figure 24a illustrates the synthesis of homopolymeric polyurethane p-PU.[94] As can be seen, p-PU liner chains were

designed with side groups containing double bonds. Then these double bonds reacted with thiols under UV light where chemical cross-linking forms. During the UV irradiation, ILs were added to the solution, which brings more evenly dispersion. Experimental results verify the conclusion that chemical cross-linking promotes thermal/dimensional stability and prevents the leakage of ILs from the i-TE gels.[94,132] Figure 24b demonstrates an example of multiple physical cross-linked i-TE gels.[104] The whole system contained components of PANI, PAAMPSA, and PA. Abundant amino groups, carbonyl groups, organic acids, and inorganic acids in the system are assembled with hydrogen bonds and electrostatic interactions between each other. As a result, an integral network with regenerative dynamic characteristics was formed as the matrix. In this way, sufficient mechanical strength is endowed.

7. I-TE Device Design and Application

In this section, we examine the feasibility of making i-TE materials into applicable devices, with a highlight on basic design principles, key integration technologies, and performance optimization methods.[168] Specifically, we start with a description

Figure 25. Schematic diagrams of the a) i-TE thermocapacitor, b) i-TE thermocell, c) typical electric double-layer supercapacitor, and d) typical pseudocapacitive capacitor. Reproduced with permission.[26] Copyright 2021, American Association for the Advancement of Science. Reproduced with permission.[172] Copyright 2022, Springer Nature. e) Comparison chart of the normalized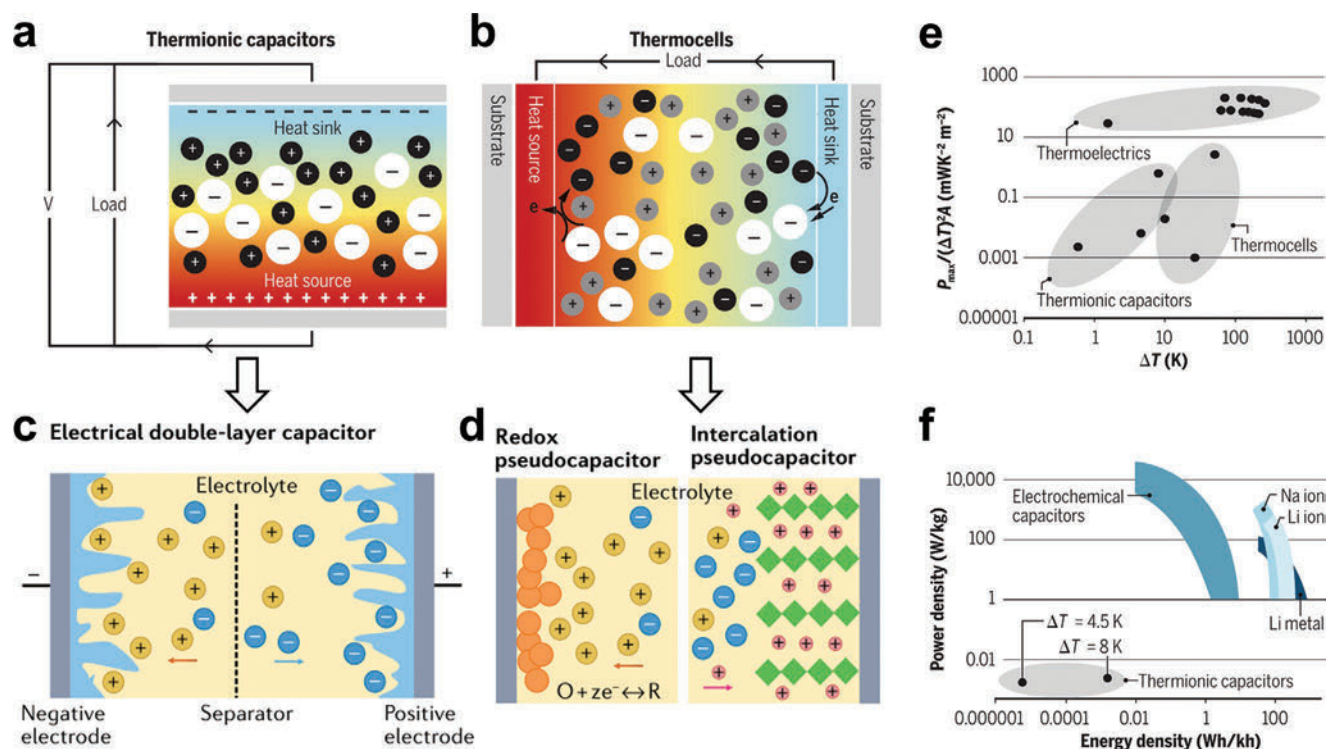 maximum instantaneous power density $P_{max}A^{-1}\Delta T^{-2}$ as a function of ΔT, and f) plots of power density versus energy density. Reproduced with permission.[26] Copyright 2021, American Association for the Advancement of Science.

of comprehensive i-TE device characteristics and unique performance features. To fabricate i-TE modules, the structure and composition of typical devices are discussed. After that, several advanced electrode materials are introduced, which play significant roles in the capacitance of i-TEs. Subsequently, we summarize four prevalent working modes (i-TE capacitor mode based on the thermodiffusion effect, i-TE capacitor mode based on the thermogalvanic effect, i-TE generator mode based on the thermodiffusion effect, and i-TE generator mode based on the thermogalvanic effect) of the i-TE devices on the basis of distinguished power supply curves. In the end, practical examples of state-of-art i-TE capacitors, generators, and sensors are overviewed, respectively.

7.1. Comprehensive Characteristics and Performance Specialness

The most considerable advantage of i-TE materials is the large ionic S, which is commonly more than 50 times higher than that of commercial Bi_2Te_3 ($\approx$190 µV K^{-1}).[101] As a thermal-to-electrical conversion device, this is of great significance in recycling low-grade waste heat. On the one hand, i-TE devices generate higher thermovoltage under unit ΔT. On the other hand, owing to the low κ of i-TE materials, preferable ΔT can be established even across a film thickness of a few tens of micrometers.[99] As a result, i-TE materials are usually featured with a high S/κ ratio which is more than 100 times compared

with that of e-TE materials, making i-TE devices capable for working as high-resolution temperature sensors,[169] e-skin that directly powers the IoT.[170]

As shown in **Figure 25**a,b, although all i-TE devices generally transform ΔT into ΔV under a power generation mode, the detailed working mode of thermodiffusive and thermogalvanic i-TE devices are different, where the former works as intermittent thermocapacitors, while the latter works as continuous thermocells.[26,171] From the electronic capacitance perspective, thermocapacitors are analogous to the electric double-layer supercapacitor, while thermocells are analogous to the pseudocapacitive supercapacitor as shown in Figure 25c,d.[172]

The performance of TE devices is usually evaluated by the parameter of normalized maximum instantaneous power density $P_{max}A^{-1}\Delta T^{-2}$, where P_{max} is the maximum output power and A is the cross-sectional area. Moreover, regular capacitors are assessed by the parameters of power density, which is apportioned performances over a period of time. As shown in Figure 25e, i-TE thermocells and thermocapacitors behave at much lower $P_{max}A^{-1}\Delta T^{-2}$ compared with e-TE devices mainly due to large internal resistances. Whereas Figure 25f indicates that there are significant gaps for i-TE thermocapacitors to be comparable with commercial capacitors and batteries. These comparisons show the great potential of decreasing the internal resistance of i-TE devices. Nevertheless, the inferior energy/power density is roughly tolerable in the case of TE materials are exploited to utilize the waste heat which will otherwise be discarded to the surroundings.[26]

**ADVANCED
SCIENCE NEWS**

www.advancedsciencenews.com

**ADVANCED
ENERGY
MATERIALS**

www.advenergymat.de
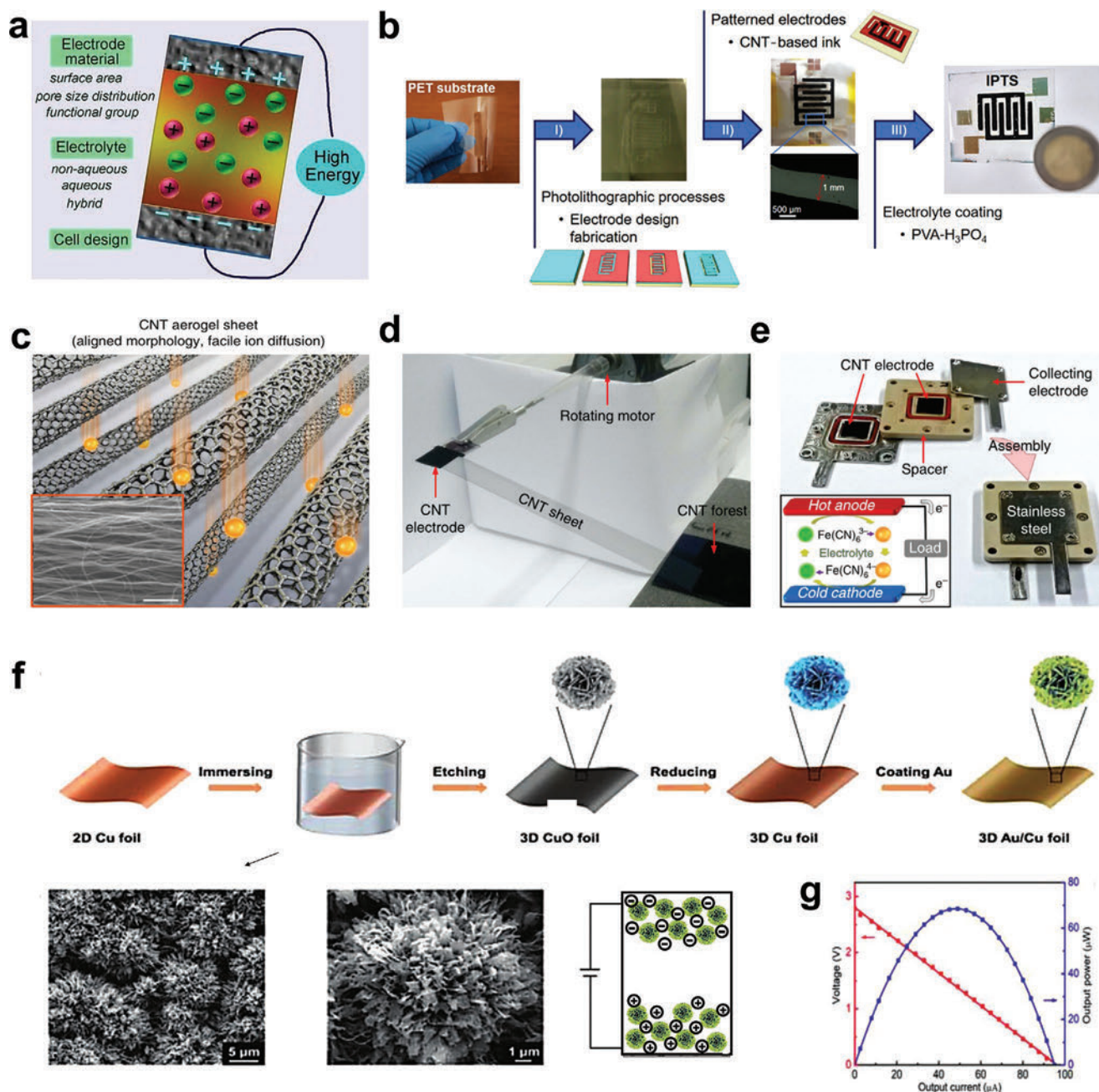
Figure 26. a) Typical i-TE device composition. b) Fabrication of the PVA/H$_3$PO$_4$ i-TE device with MWCNT electrodes: (I) photolithographic process of the designed electrode pattern, (II) electrode fabrication by fulfilling MWCNT inks to the designed pattern, and (III) device fabrication by depositing PVA/H$_3$PO$_4$ gel between two pieces of patterned electrodes. Reproduced with permission.[175] Copyright 2021, American Chemical Society. c) SEM image of the aligned CNT aerogel. d) Process of continuous reeling off CNT aerogel sheets from a CNT forest, and wrapping it around a metal shaft to obtain planar electrodes. e) Photographs of a CNT sandwiched Fe(CN)$_6^{3-}$/Fe(CN)$_6^{4-}$ thermocell with the schematic drawing inset. Reproduced with permission.[176] Copyright 2016, Springer Nature. f) Preparation process and morphology of the 3D hierarchical Au/Cu foil electrodes with microflower-like morphology. g) Voltage and output power as a function of the output current of the installed 24-united i-TE device by harvesting body heat. Reproduced with permission.[160] Copyright 2022, Wiley-VCH.

7.2. Device Composition and High-Performance Electrode Materials

The necessary elements for i-TE devices include electrolyte, electrodes, and supporting substrates, as shown in **Figure 26**a. In addition, appropriate interconnection technology, contact

resistance optimization, device packaging, and wire colloca-tion are also inescapable factors for high-performance i-TE devices.[168c] Electrodes are one of the most prominent com-ponents where the accumulated ions will lay, attach, and deposit. Practically, the electrode behavior directly determines the maximum capacitance and the energy density. State-of-art

electrode materials have drawn intensive interest recently, such as carbon nanotubes, polymer composites, CNT forests, treated metals, and aerogels.[12,70,84c,99,100,173] These promising electrodes are normally made with complicated microstructures to provide large specific surface areas for promoting ion accumulation.[149,174]

As shown in Figure 26b, multiwalled carbon nanotubes (MWCNTs) were employed as the electrodes of a PVA/phosphoric acid (H_3PO_4) i-TE gel-based device with delicately designed electrode patterns.[175] The MWCNT was predissolved as aqueous inks aided by sodium dodecylbenzenesulfonate surfactant, followed by deposited as patterned electrodes. After coating PVA/H_3PO_4 gel to bridge two patterned electrodes, a supercapacitor was successfully prepared, which achieved an energy density of 1.05 mW h cm^{-3}. Figure 26c–e depicts CNT aerogel electrodes and the fabrication of the corresponding device.[176] Aligned nanostructures (Figure 26c) can be obtained by the engineering method of continuous reeling off and wrapping CNT sheets (Figure 26d). The electrode optimization process involved removing low-activity carbon impurities, deposition of catalytic platinum nanoparticles, mechanical compressing to regulate porosity, and the griping of the cylindrical device geometry. The obtained i-TE device (Figure 26e) can generate an output power density of 6.6 W m^{-2} ($\Delta T = 51$ °C), which is 3.95% of the Carnot efficiency. Moreover, the introduction of 3D hierarchical Au/Cu electrodes can greatly increase the electroactive surface area and lower the interface charge transfer resistance.[160] As can be seen in Figure 26f, the double-layer metal electrode with microflower-like morphology contributes to a power density of 8.9 mW m^{-2} K^{-2}, which is six times higher than that of 2D Au/Cu electrode devices. The developed 24-armed i-TE device harvests a remarkable output voltage of 2.8 V and output power of 68 μW at a ΔT of 10 °C) (Figure 26g).

7.3. Device Types and Working Principle

I-TE capacitors based on thermodiffusion effect is the most common situation where the i-TE capacitor works barely following the Soret effect mechanisms. As shown in **Figure 27**a, the exact thermovoltage curve corresponds to the typical four-stage process discussed in Section 4.3. The potential raised from the thermodiffusive ion concentration difference (especially for the second stage in Figure 27a) can be estimated by the Nernst equation as[98]

$$E_{cell} = E_{cell}^0 - \frac{RT}{nF} \ln \frac{c_{hot}}{c_{cold}} \tag{25}$$

where E_{cell} refers to the ion-diffusion derived potential difference (a single species of ion couple), E_{cell}^0 is the standard cell potential of the corresponding ion couple, c_{hot} and c_{cold} are the molar concentrations of the balanced ions at the surface of the hot and cold electrode, R, F, and n are the universal gas constant, Faraday constant, and the ionic charge, respectively. Moreover, we noticed that in this four-stage mode, the countered charge generated in stage III can be accumulated by repeatedly executing the step of heating–charging (stages I and

II). Since in stage I, the accumulated ions at the electrode surface are saturated mainly due to electrostatic repulsion. However in stage II, as the circuit is connected, the counter charges generated within the electrodes can neutralize the ionic charge at the electrode surface. Therefore, if the circuit is disconnected at this time and the ΔT is applied again, additional ions will migrate to the electrode surface and accumulate (a 2nd stage I). Then an expanded counter potential will be generated during the 2nd stage II via continue transporting electrons across the external circuit from the electrodes. This means that repeat operation of stages I and II can expand the capacitance before cooling in stage III. It is a viewpoint of our logical inference according to some analogous literature results which could develop inspirations for future experiments.[18,92]

I-TE generators based on thermodiffusion effect is a simple two-stage process based on the thermodiffusion effect,[51] as illustrated in Figure 27b. Different from e-TE generators, a prior voltage build-up step is required that consumes a certain time. When the external circuit is connected in the following power output step, a gradually decayed power supply occurs. This is principally analogous to stage II of the i-TE capacitor mode in Figure 27a. This type of generator is intermittent, and the resetting of the accumulated ions is demanded after every cycle. Practically, this generator mode is likely to be the capacitor mode in the condition of supplying power while charging (stages I and II).

I-TE capacitors based on thermogalvanic effect also conceive a four-stage process, as exhibited in Figure 27c.[160,177] In stage I, the spontaneous oxidation/reduction reaction occurs initially at the hot end (taking the oxidation reaction as an example here). Therefore, electrons are continuously released to the hot electrode and accumulated to generate open-circuit thermovoltage. The reverse reaction (reduction here) will not take place at the cold electrode. In stage II, the accumulated electrons flow from the hot electrode to the cold electrode across the external circuit. As a result, the reduction reaction is motived at the cold end, which continuously absorbs electrons. The hot-end electrons generated in stage I are thus circulated which triggers potential decay. It is noteworthy that the voltage will not decline to zero as a drain voltage generally maintains. Meanwhile, the oxidized ions gather nearby the hot electrode and the reduced ion clusters enrich around the cold electrode. In the following stage III, the external circuit is disconnected and the ΔT is removed. Besides, the redox couples remain localized surrounding the electrode because of the bulky dimension of ion clusters (such as $Fe(CN)_6^{3-}$/$Fe(CN)_6^{4-}$). As the cold electrode return to ambient temperature, a reverse oxidation reaction is triggered to transfer electrons to the cold electrode. An opposite open-circuit potential is formed gradually as depicted in Figure 27c. Finally, in stage IV, the device can be discharged by connecting to an external circuit. A reverse current generates in this period, which promotes the reverse reaction at the hot electrode surface. The redox couples return to the initial state.

I-TE generators based on thermogalvanic effect is no more than the combination of the above two modes, as shown in Figure 27d. The voltage build-up and power output process are equivalent to stages I and II of i-TE capacitors based on thermogalvanic effect. However, there is an

**ADVANCED
SCIENCE NEWS**

www.advancedsciencenews.com

**ADVANCED
ENERGY
MATERIALS**

www.advenergymat.de
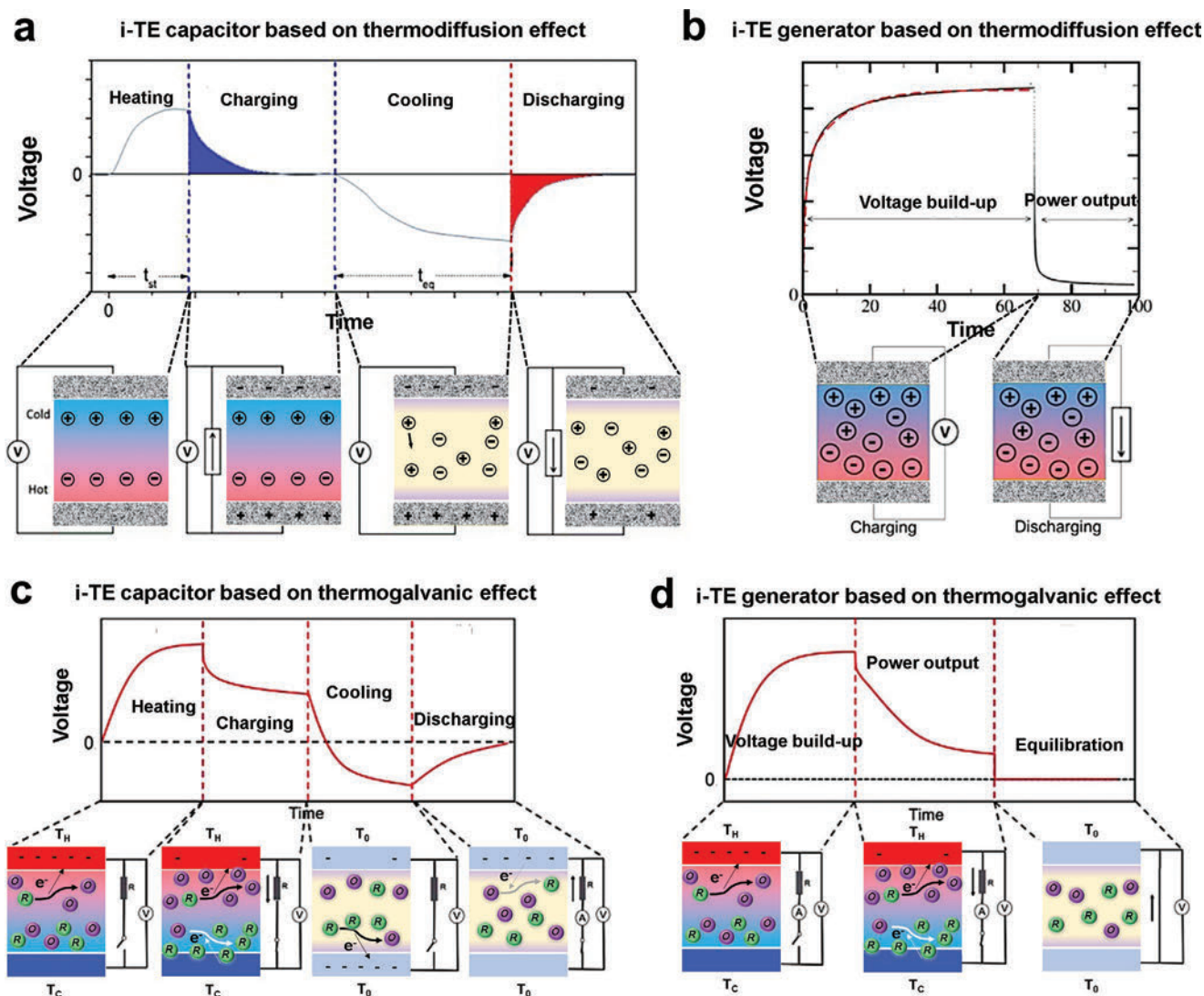
Figure 27. Voltage curve and mechanism of a) i-TE capacitors based on thermodiffusion effect, b) i-TE generators based on thermodiffusion effect, c) i-TE capacitors based on thermogalvanic effect, and d) i-TE generators based on thermogalvanic effect. Reproduced with permission.[80] Copyright 2017, Wiley-VCH.

additional equilibration process where the external circuit is retained and the ΔT is revoked. The redox couples return to the initial state in this stage for repeat–cycle standby. This equals to a waiting step between power supply intervals, generators with rapid self-discharging will provide superior economic benefits.[98]

7.4. Application of I-TE Capacitors

The i-TE devices are highly inadequate compared with traditional e-TE devices. At the same time, the specific device design theory has not been systematically established yet. Current mainstream fabrication strategies for i-TE devices are focused on the consulting of flexible e-TE devices. In the following three sections, we will provide several state-of-art examples of i-TE capacitors, generators, and sensors in order. **Figure 28**a dem-

onstrates an assembled thermobattery, with the top and bottom electrodes being polypyrrole (PPy)-coated graphite sheets, and inner layer being potassium ferricyanide/ferrocyanide [$K_3Fe(CN)_6$/$K_4Fe(CN)_6$] aqueous, which showed an inherent S of around -1.4 mV K^{-1}.[178] Composites of Cu foam/PEG1000 were filled into the bottom layer serving as the thermal storage and preservation module. As a result, the disturbing low-grade ΔT was exceptionally stabilized. An all-day electricity supply was achieved because of the heat reservation in the daytime. Figure 28b shows the working mechanisms in aspects of daytime heating (Model 1) and nighttime cooling (Model 2), respectively. In the daytime, sunlight heat was absorbed by the PPy broadband absorber layer via convention and conduction. Subsequently, the heat was absorbed by continued transferring down through the i-TE layer to the energy storage layer. This further cooled bottom electrode to yield a larger ΔT. While in the nighttime, the stored heat was released to build ΔT with

53
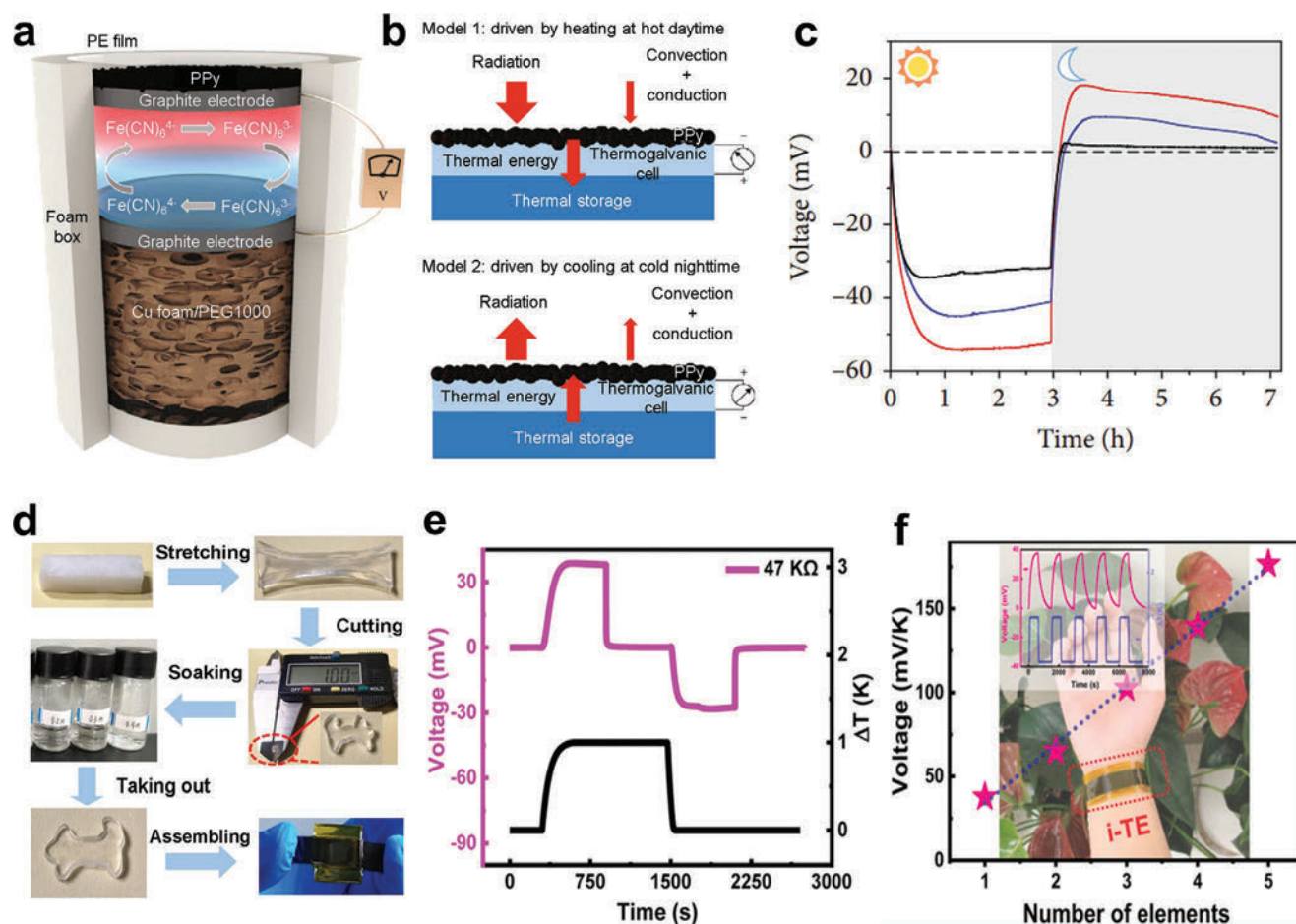
Figure 28. a) Schematic structure of the thermogalvanic i-TE battery designed for all-day energy supply. b) Working principle of the thermogalvanic i-TE battery where model 1 indicates the daytime energy flux and model 2 demonstrates the nighttime energy flux. c) The open-circuit voltage in an all-day long period, black curve for pristine graphite/[$K_3Fe(CN)_6$/$K_4Fe(CN)_6$] battery, blue curve for graphite/[$K_3Fe(CN)_6$/$K_4Fe(CN)_6$]/Cu foam/PEG1000 battery, red curve for PPy/graphite/[$K_3Fe(CN)_6$/$K_4Fe(CN)_6$]/Cu foam/PEG1000 battery. Reproduced with permission.[178] Copyright 2019, American Association for the Advancement of Science. d) Fabrication process of the PVA/HCl hydrogel thermocapacitor unit. e) The four-stage voltage curve of the thermocapacitor with an external load of 47 kΩ. f) The open-circuit voltage of the tandem device with different i-TE elements where every element is cut into an identical dimension of $8 \times 8 \times 1$ mm. Reproduced with permission.[179] Copyright 2022, American Chemical Society.

an opposite sign, which sustainably powered the battery. As can be seen, the maximum device voltage reached −54.2 mV in the daytime and 18.2 mV in the nighttime (Figure 28c). The comparative experiment of innocent graphite/[$K_3Fe(CN)_6$/$K_4Fe(CN)_6$] thermobattery exhibited inferior daytime voltage of −34.1 mV and scarce nighttime voltage. Such a strategy indicates a proof-of-concept module to recycle TE conversion for all-day electricity furnishing.

As depicted in Figure 28d, a PVA/HCl hydrogel thermocapacitor was fabricated by the designed process, which introduced ion channels to optimize TE performance.[179] In brief, the freeze-thawed PVA hydrogel was stretched repeatedly at room temperature to induce directed crystallization. Then the hydrogel was cut into the desired shape and soaked into the HCl solution along the stretching direction. After that, the PVA hydrogel was fully swollen with HCl filled in the gaps within aligned crystals, which was exactly the ion transport pattern. By installing and encapsulating the prepared i-TE hydrogel, a bracelet-like device was obtained. Figure 28e shows the voltage

curve of the i-TE device applying under the capacitor mode with an external load of 47 kΩ. Finally, this work achieved a superior S of 176.58 mV K^{-1} just employing five tandem pieces of $8 \times 8 \times 1$ mm squired i-TE hydrogels (Figure 28f).

7.5. Application of I-TE Generators

Figure 29a shows a wearable i-TE generator fabricated through coating PEDOT:PSS/DMSO/[EMIM:DCA] (see Figure 29b) on fabrics.[180] A continuous 8.78 μm ultrathin TE layer was formed on the surface of the cotton yarn, in contrast to the pristine PEDOT:PSS penetrated yarn which resulted in discontinuous structures. This is closely related to the higher viscosity and surface tension of the PEDOT:PSS/DMSO/[EMIM:DCA] composite solution. The yarn fibers were inaccessible to be wetted at the surface and penetrated the bulk. The surface-coated yarn showed significantly enhanced flexibility compared with pristine PEDOT:PSS. Besides, the maximum $S^2\sigma$ was optimized
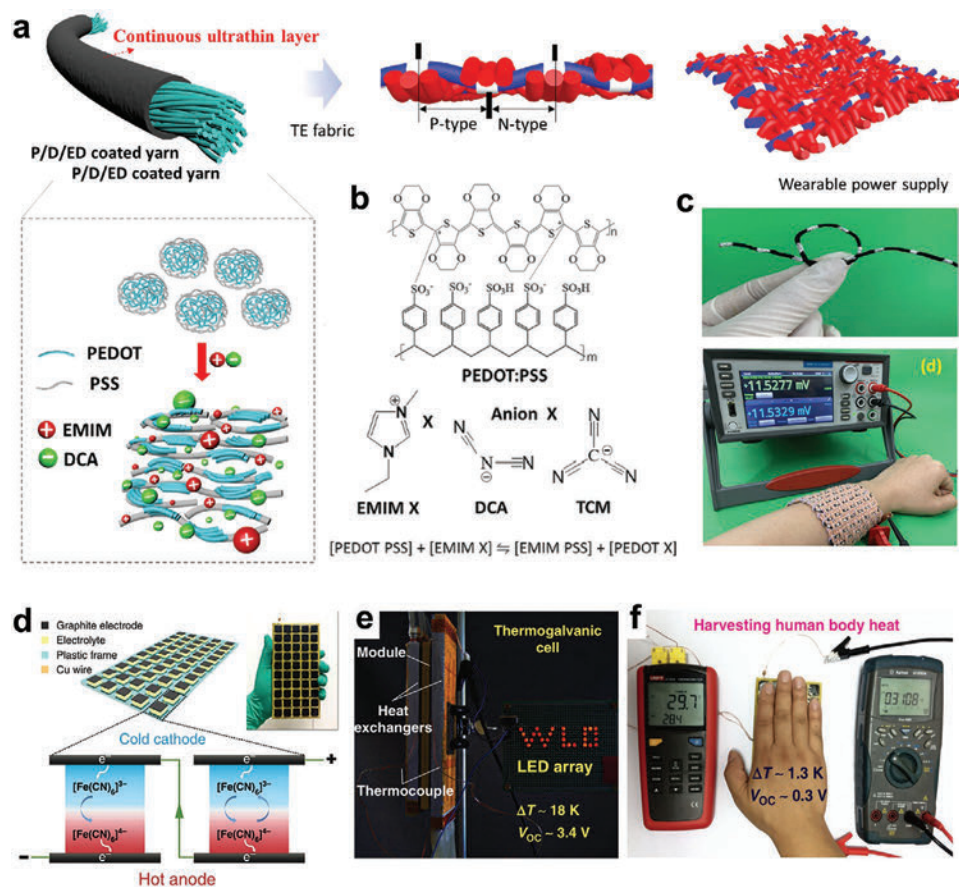
Figure 29. a) Schematic diagram of the fabrication and structure of the PEDOT:PSS/DMSO/[EMIM:DCA] (P/D/ED)-coated yarn. b) Chemical structures and interactions between PEDOT:PSS and [EMIM:DCA]. c) Photographs of the flexible P/D/ED-coated long yarn fabric and the voltage generated by the weft TE wristband harvesting body heat. Reproduced with permission.[180] Copyright 2021, American Chemical Society. d) Schematic diagram and photograph of the 50-unit integrated i-TE module. e) Photograph of the i-TE thermogenerator directly lights on an array of 29 red LED lamp beads (the module was sandwiched by two aluminum heat pipe exchangers with cold and hot water controlled at ≈278 and 333 K, respectively). f) Photograph of an i-TE generator attached to human body, with the temperature and open-circuit voltage were measured by a thermometer (left) and a multimeter (right), respectively. Reproduced with permission.[34] Copyright 2018, Springer Nature.

to 24.7 µW m^{-1} K^{-2} in contrast to 0.00684 µW m^{-1} K^{-2} of pristine PEDOT:PSS. By preparing a 2 m long coated yarn as the weft yarn and pristine cotton yarn as the warp yarn, a flexible 15 cm × 6.5 cm squired TE wrist containing 140 TE units was weaved (Figure 29c). The output power density reached 136.1 mW m^{-2} under a ΔT of 40.8 K. It is worth mentioning that although the addition of ILs induced PSS amount elimination, there are also ion/electron synergistic effects.[181]

Another instance of i-TE generator can be referred to Figure 29d,e.[34] The chaotropic cations guanidine chloride (GdmCl) and highly soluble urea enhanced [Fe(CN)$_6$$^{4-}$/Fe(CN)$_6$$^{3-}$] electrolytes were employed to fabricate the i-TE material. A thermogalvanic i-TE module including 50 units was fabricated by utilizing a polyamide frame containing 50 holes with sizes of 10 × 10 × 5 mm^3 (Figure 29d). Then the prepared electrolyte was injected into the holes and sandwiched by two pieces of graphite electrodes. Finally, all these units were connected in series with Cu wires and sealed by epoxy resin glues. The as-assembled generator module was able to generate an open-circuit voltage of 3.4 V and a short-circuit current of 1.2 mA at a low-grade ΔT of 18 K. An LED array can be directly

lighted on (Figure 29e). When harvesting heat from human skin, a practically considerable voltage over 0.3 V was stably transformed by a faint ΔT of 1.3 K, as shown in Figure 29f.

7.6. Application of I-TE Sensors

Traditional thermosensors such as thermopiles are composed of inorganic alloys based on the e-TE effect. However, there are still straits of insufficient thermovoltage, material brittleness, and large-scale production obstacles. These drawbacks of traditional TE sensors restrict the detection limits and sensitivities. Recently, i-TE devices have been proposed as TE detectors owing to the giant ionic S values, high flexibility, and scale-up feasibility.

Figure 30a,b illustrates a TE paper chip that is designed for remote alarming of early-stage forest fires.[78] After collecting the signal of ΔT, the telecommunication signal is transferred through a loop of signal conversion module, signal acquisition module, transmitter, and receiver in sequence, as shown in Figure 30a. The whole system achieved signal transformation

**ADVANCED
SCIENCE NEWS**

www.advancedsciencenews.com

**ADVANCED
ENERGY
MATERIALS**

www.advenergymat.de
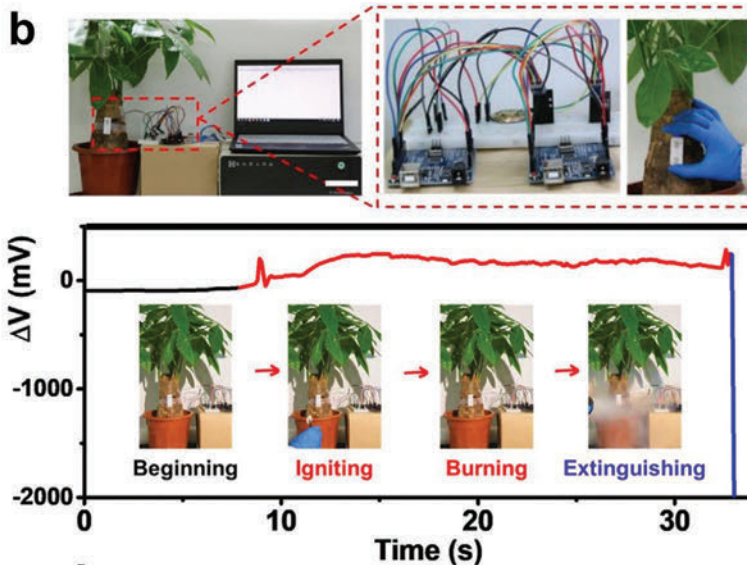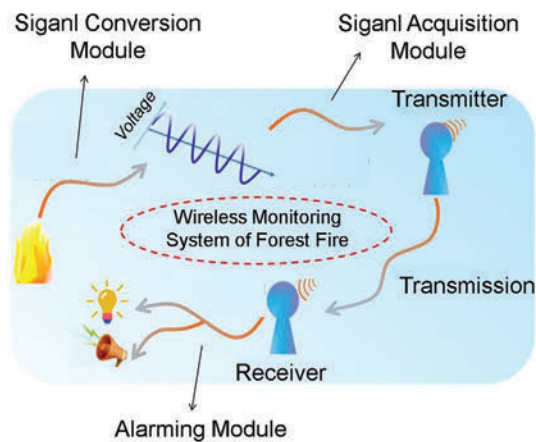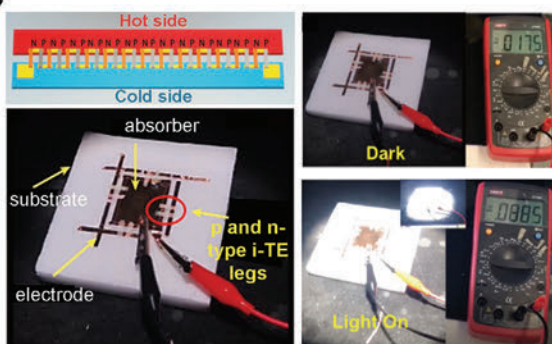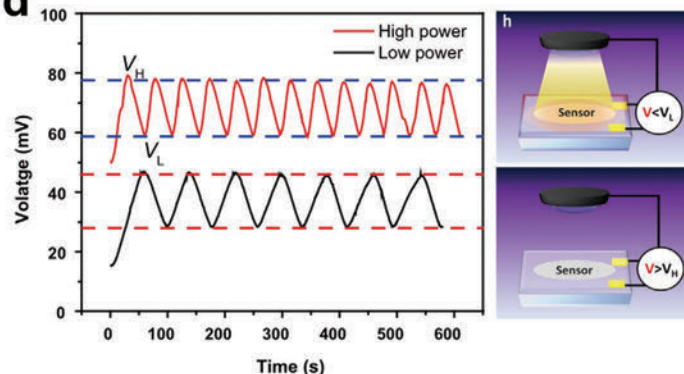
Figure 30. a) Schematic diagram of the communication system of the wireless remote fire alarm monitor. b) Images of the wireless remote fire alarm monitor and the offhand thermovoltage evolution in the process from the initial fire to the extinguishing. Reproduced with permission.[78] Copyright 2020, American Chemical Society. c) Structure, composition, and real-time response of the i-TE thermal sensor. d) Thermovoltage performance of the light-induced thermal sensor with corresponding demonstrations of the automatic lamp controlling. Reproduced with permission.[182] Copyright 2022, Springer Nature.

without relying on an additional power source, being low-cost (≈$0.4) and environment-friendly (paper matrix). As shown in Figure 30b, the TE paper chip can be bent freely into desirable shapes to fit the tree trunk. Once a burning fire source approached the trunk, ΔT would be established. Such a signal was grasped by the i-TE alarm module to generate a rapid sharped voltage signal. Upon the voltage reached the programmed threshold voltage, the alarming circuit was triggered with a flashing red LED. Simultaneously, the loudspeaker started broadcasting. At last, the fire was experimentally extinguished, which led to quieting of the voltage signal. This work makes a proof of concept that i-TE sensors can be applied for wireless real-time detections of abnormal temperature change.

Another interest i-TE research was reported where the light-derived heat change was monitored (Figure 30c,d).[182] All-solid-state i-TE units of p-type PVDF-HFP/NaTFSI/propylene carbonate (PhNP) and n-type tris(pentafluorophenyl)borane incorporated PhNP (T-PhNP) were prepared. The S values were measured as +20 and −6 mV K$^{−1}$, respectively. A 13-leg p–n connected device generated a superior voltage of 2.6 V under a ΔT

of 10 K. In these regards, a self-powered 4-leg sensor was developed, which induced the lamp on/off by waved output voltages. By further connecting the sensor to a computer program, the automatic control of the lamp was achieved (Figure 30d). Specifically, during the light-on periods, the light-derived heat was absorbed to generate voltage. Once the voltage attained the upper stated limit, the light was automatically turned off via a designed electric circuit. Subsequently, the device surface was cooled down because the voltage drops accordingly. Once the voltage dropped to the lower stated limit, the light was automatically turned on. Presumably, the constant on–off cycle of the lamp appeared where higher lighting power promoted more rapid responses, as shown in Figure 30d. This will offer great promise in heat detection, power supply, gating elements.[183]

8. Summary and Outlook

Last decade has witnessed the rapid development of i-TEs. Compared to traditional e-TE materials, the most significant

ADVANCED
SCIENCE NEWS
www.advancedsciencenews.com

ADVANCED
ENERGY
MATERIALS
www.advenergymat.de
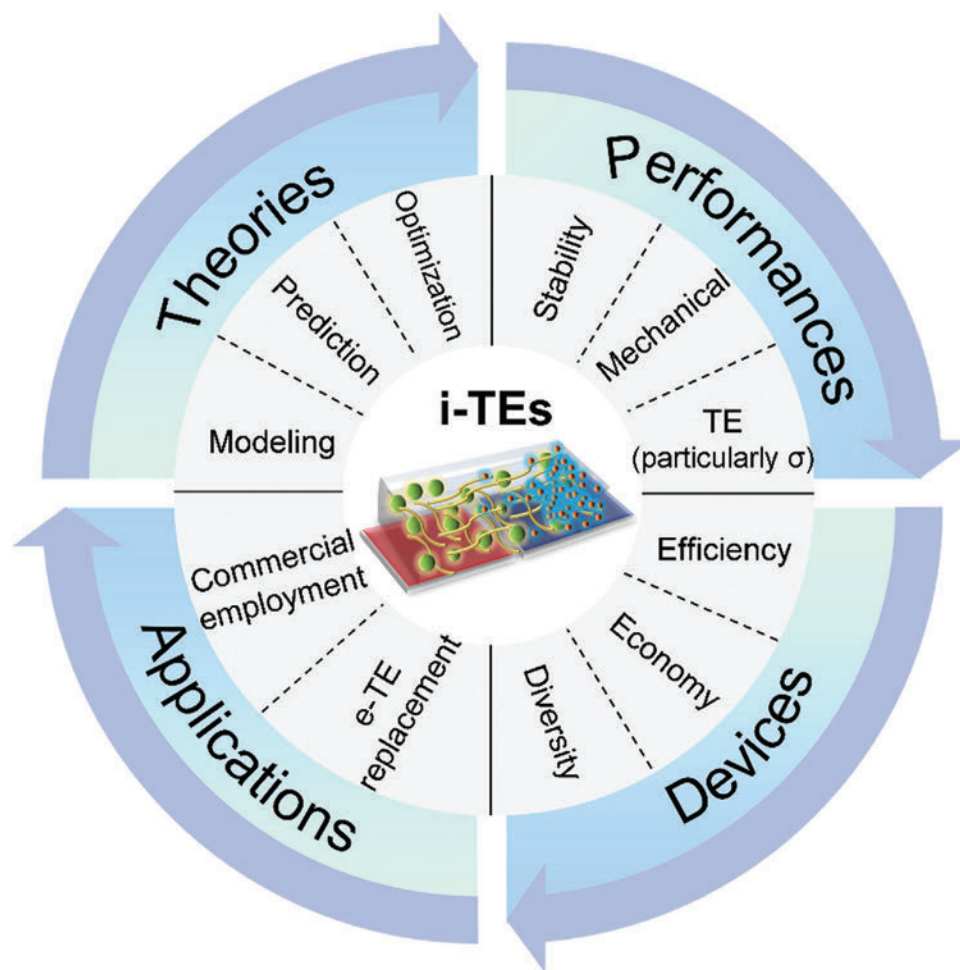
Figure 31. Prospects of i-TE technologies. Reproduced with permission.[182] Copyright 2022, Springer Nature.

characteristic of i-TE materials is their ultrahigh S, which is highly desirable for collecting and cycling low-grade waste heat. I-TE materials are also flexible, economic, and eco-friendly. Compared with e-TE device, an additional thermal-powered capacitor mode is endowed in i-TE devices, which can be therefore used for continuously supplying energy in the condition of intermittent heat sources.

Despite of grand progresses, research on i-TEs is still in its infant stage, while in-depth understandings are still urgently required. Several main research gaps are hindering performance optimizations and practical applications. First, it is controversial to directly equate or compare i-TE parameters to e-TE parameters, which are derived from the electron/phonon transport characteristics in a single homogeneous material. In fact, i-TE effect is based on the accumulated ion concentration difference is determined by the whole system as well as the interaction between every single component. Second, i-TE materials are suffering from inferior σ because of the addition of nonconductive components. Besides, the dissociation and transfer of ions are also more time-consuming than electrons. The insufficient σ degrades the ultimate i-TE performance despite the ultrahigh S and normally low κ. Third, the i-TE performance is relatively unstable. On the one hand, ionic transport is sensitive

to the external environment, especially variation of temperature and humidity. On the other hand, the solvents will inevitably evaporate as time passed, which impedes long-term services. Although it can be minimized by replenishing hygroscopic agents or restricting the vapor pressures, the vaporization cannot be completely prevented. Last but not the least, there are risks of dissipation and leakage to the IL components in the process of device assembly and application. In terms of liquid state and quasi-solid state i-TE materials, the device fabrication engineering should consider encapsulation strategies.

In these regards, we summarize several prospects as below (**Figure 31**).

i) Further shaping of i-TE theories. The exploration of novel TE materials is supported by appropriate theoretical guidance. However, the theoretical fundamentals of i-TE systems are completely different from e-TE fundamentals, which have been relatively maturely established. To predict the performance and design advanced i-TE systems, future research on i-TE theories is in urgent demand. The critical research directions include the digital modeling of the i-TE program, the logical prediction formula deduction, and the systematization of performance optimization philosophies.

**ADVANCED
SCIENCE NEWS**

www.advancedsciencenews.com

**ADVANCED
ENERGY
MATERIALS**

www.advenergymat.de

ii) Improvement of i-TE performances. Currently, high-performance i-TE materials are still under development. The promising designation targets involve the discovery of novel n-type and p-type i-TE systems, the balance between the TE and the mechanical behaviors (e.g., flexibility, self-healing ability, stretchability, etc.), and the enhancement of material stability. Herein, the improvement of σ values is the key point for optimizing TE behaviors. The combination of i-TE materials and other advanced TE components is another enlightenment that is an effective way to tap the performance potential.

iii) Optimization of i-TE devices. Irrespective of serving as capacitors, generators, and sensors, high-efficiency of i-TE devices is prominent. Insightful understanding surrounding the high-efficient device, the large-scale feasibility, the low-cost material innovation, the creation of novel battery architecture, the material flittering for different application scenarios, and the organization of biocompatible/wearable human body electronics are needed. Additional efforts should be paid to companion research of the minimization of contact resistance and the fabrication/functional modification of electrode materials as well.

iv) Extending practical applications. Unlike the commercialized e-TE materials, there have been technology gaps between experimental development and the practical application of i-TE systems. As the i-TE materials are lavish and interlock plenty of disciplines, the practical application of i-TE materials will also validate their prospects as a next-generation TE solution.

## Conflict of Interest

The authors declare no conflict of interest.

[1] a) Y. Zhang, Q. Zeng, Y. Wu, J. Wu, S. Yuan, D. Tan, C. Hu, X. Wang, *Nano-Micro Lett.* **2020**, *12*, 175; b) S. Chu, A. Majumdar, *Nature* **2012**, *488*, 294.

[2] a) X.-L. Shi, J. Zou, Z.-G. Chen, *Chem. Rev.* **2020**, *120*, 7399; b) J. M. Ding, W. R. Zhao, W. L. Jin, C.-A. Di, D. B. Zhu, *Adv. Funct. Mater.* **2021**, *31*, 2010695; c) X. Shi, L. Chen, *Nat. Mater.* **2016**, *15*, 691; d) Y. Xiao, L. D. Zhao, *Science* **2020**, *367*, 1196; e) D. Beretta, N. Neophytou, J. M. Hodges, M. G. Kanatzidis, D. Narducci, M. Martin- Gonzalez, M. Beekman, B. Balke, G. Cerretti, W. Tremel, A. Zevalkink, A. I. Hofmann, C. Müller, B. Dörling,

M. Campoy-Quiles, M. Caironi, *Mater. Sci. Eng., R* **2019**, *138*, 100501.

[3] a) M. Bharti, A. Singh, S. Samanta, D. K. Aswal, *Prog. Mater. Sci.* **2018**, *93*, 270; b) S. Xu, X.-L. Shi, M. Dargusch, C. Di, J. Zou, Z.-G. Chen, *Prog. Mater. Sci.* **2021**, *121*, 100840; c) A. Mehdizadeh Dehkordi, M. Zebarjadi, J. He, T. M. Tritt, *Mater. Sci. Eng., R* **2015**, *97*, 1.

[4] R. A. Kishore, A. Nozariasbmarz, B. Poudel, M. Sanghadasa, S. Priya, *Nat. Commun.* **2019**, *10*, 1765.

[5] D. Beretta, A. Perego, G. Lanzani, M. Caironi, *Sustainable Energy Fuels* **2017**, *1*, 174.

[6] a) G. Zuo, Z. Li, E. Wang, M. Kemerink, *Adv. Electron. Mater.* **2018**, *4*, 1700501; b) L. Yang, Z.-G. Chen, M. S. Dargusch, J. Zou, *Adv. Electron. Mater.* **2018**, *8*, 1701797.

[7] R. Kita, P. Polyakov, S. Wiegand, *Macromolecules* **2007**, *40*, 1638.

[8] S. Scott, T. Driesner, P. Weis, *Nat. Commun.* **2015**, *6*, 7837.

[9] Z. Wang, S. Yun, H. Xu, C. Wang, Y. Zhang, J. Chen, B. Jia, *Bioresour. Technol.* **2019**, *286*, 121394.

[10] S. Zhang, C. Chen, Y. Zhou, Y. Qian, J. Ye, S. Xiong, Y. Zhao, X. Zhang, *ACS Appl. Mater. Interfaces* **2018**, *10*, 23048.

[11] H. J. Tyrrell, D. A. Taylor, C. M. Williams, *Nature* **1956**, *177*, 668.

[12] T. Li, X. Zhang, S. D. Lacey, R. Mi, X. Zhao, F. Jiang, J. Song, Z. Liu, G. Chen, J. Dai, Y. Yao, S. Das, R. Yang, R. M. Briber, L. Hu, *Nat. Mater.* **2019**, *18*, 608.

[13] a) Y. Li, Y. Yang, X. Liu, Y. Yang, Y. Wu, L. Han, Q. Han, *Colloids Surf., A* **2022**, *648*, 129254; b) Y. Chen, C. Shi, J. Zhang, Y. Dai, Y. Su, B. Liao, M. Zhang, X. Tao, W. Zeng, *Energy Technol.* **2022**, *10*, 2200070.

[14] H. Cheng, X. He, Z. Fan, J. Ouyang, *Adv. Energy Mater.* **2019**, *9*, 1901085.

[15] T. J. Abraham, D. R. MacFarlane, J. M. Pringle, *Energy Environ. Sci.* **2013**, *6*, 2639.

[16] S. L. Kim, J.-H. Hsu, C. Yu, *Org. Electron.* **2018**, *54*, 231.

[17] H. Wang, J. H. Hsu, S. I. Yi, S. L. Kim, K. Choi, G. Yang, C. Yu, *Adv. Mater.* **2015**, *27*, 6855.

[18] B. Kim, J. Na, H. Lim, Y. Kim, J. Kim, E. Kim, *Adv. Funct. Mater.* **2019**, *29*, 1807549.

[19] Z. Liu, H. Cheng, H. He, J. Li, J. Ouyang, *Adv. Funct. Mater.* **2021**, *32*, 2109772.

[20] X. He, H. Cheng, S. Yue, J. Ouyang, *J. Mater. Chem. A* **2020**, *8*, 10813.

[21] C. G. Han, X. Qian, Q. Li, B. Deng, W. Liu, *Science* **2020**, *368*, 1091.

[22] B. Kim, J. U. Hwang, E. Kim, *Energy Environ. Sci.* **2020**, *13*, 859.

[23] a) M. Massetti, F. Jiao, A. J. Ferguson, D. Zhao, K. Wijeratne, A. Wurger, J. L. Blackburn, X. Crispin, S. Fabiano, *Chem. Rev.* **2021**, *121*, 12465; b) M. F. Dupont, D. R. MacFarlane, J. M. Pringle, *Chem. Commun.* **2017**, *53*, 6288; c) M. Li, M. Hong, M. Dargusch, J. Zou, Z.-G. Chen, *Trends Chem.* **2021**, *3*, 561.

[24] Y. Jia, Q. Jiang, H. Sun, P. Liu, D. Hu, Y. Pei, W. Liu, X. Crispin, S. Fabiano, Y. Ma, Y. Cao, *Adv. Mater.* **2021**, *33*, 2102990.

[25] J. Chipman, *J. Am. Chem. Soc.* **1926**, *48*, 2577.

[26] X. Shi, J. He, *Science* **2021**, *371*, 343.

[27] a) C. Soret, *Arch. Sci. Phys. Nat.* **1879**, *2*, 48; b) C. Ludwig, *Sitzber. Akad. Wiss. Wien, Math-naturw, Kl.* **1856**, *20*, 539.

[28] E. Laux, S. Uhl, T. Journot, J. Brossard, L. Jeandupeux, H. Keppner, *J. Electron. Mater.* **2016**, *45*, 3383.

[29] X. Wu, N. Gao, H. Jia, Y. Wang, *Chem. - Asian J.* **2021**, *16*, 129.

[30] M. Li, L. Dai, Y. Hu, *ACS Energy Lett.* **2022**, *7*, 3204.

[31] H. Zhu, C. Xiao, Y. Xie, *Adv. Mater.* **2018**, *30*, 1802000.

[32] a) A. Al-zubaidi, X. Ji, J. Yu, *Sustainable Energy Fuels* **2017**, *1*, 1457; b) C. Cheng, Y. Dai, J. Yu, C. Liu, S. Wang, S. P. Feng, M. Ni, *Energy Fuels* **2021**, *35*, 161.

[33] M. A. M. Hasan, H. Wu, Y. Yang, *J. Mater. Chem. A* **2021**, *9*, 19116.

[34] J. Duan, G. Feng, B. Yu, J. Li, M. Chen, P. Yang, J. Feng, K. Liu, J. Zhou, *Nat. Commun.* **2018**, *9*, 5146.

ADVANCED
SCIENCE NEWS

www.advancedsciencenews.com

ADVANCED
ENERGY
MATERIALS

www.advenergymat.de

[35] T. Kim, J. S. Lee, G. Lee, H. Yoon, J. Yoon, T. J. Kang, Y. H. Kim, *Nano Energy* **2017**, *31*, 160.

[36] a) A. Würger, *Phys. Rev. Lett.* **2008**, *101*, 108302; b) S. A. Putnam, D. G. Cahill, *Langmuir* **2005**, *21*, 5317; c) K. A. Eslahian, A. Majee, M. Maskos, A. Würger, *Soft Matter* **2014**, *10*, 1931; d) D. Vigolo, S. Buzzaccaro, R. Piazza, *Langmuir* **2010**, *26*, 7792; e) M. Reichl, M. Herzog, A. Götz, D. Braun, *Phys. Rev. Lett.* **2014**, *112*, 198101.

[37] a) M. Eslamian, F. Sabzi, M. Z. Saghir, *Phys. Chem. Chem. Phys.* **2010**, *12*, 13835; b) A. Sosnowska, E. Laux, H. Keppner, T. Puzyn, M. Bobrowski, *J. Mol. Liq.* **2020**, *316*, 113871; c) W. Zhang, J. Zhang, X. Liu, H. Li, Y. Guo, C. Geng, Y. Tao, Q.-H. Yang, *Adv. Funct. Mater.* **2022**, *32*, 2201205; d) F. Chen, *Curr. Opin. Electrochem.* **2022**, *35*, 101086; e) A. Boruń, *J. Mol. Liq.* **2019**, *276*, 214; f) A. Kumar, V. P. Mohandas, V. R. K. S. Susarla, P. K. Ghosh, *J. Solution Chem.* **2004**, *33*, 995; g) K. Dong, X. Liu, H. Dong, X. Zhang, S. Zhang, *Chem. Rev.* **2017**, *117*, 6636; h) M. Meot-Ner, *Chem. Rev.* **2005**, *105*, 213.

[38] a) L. Onsager, *Phys. Rev.* **1931**, *38*, 2265; b) L. Onsager, *Phys. Rev.* **1931**, *37*, 405.

[39] J. N. Agar, J. C. R. Turner, *Proc. R. Soc. A* **1960**, *255*, 307.

[40] A. Würger, *Phys. Rev. Res.* **2020**, *2*, 042030(R).

[41] B. E. Conway, E. Ayranci, *J. Solution Chem.* **1999**, *28*, 163.

[42] J. Meixner, S. R. De Groot, P. Mazur, North-Holland Publishing Company, Amsterdam **1962**.

[43] A. Würger, *Rep. Prog. Phys.* **2010**, *73*, 126601.

[44] E. D. Eastman, *J. Am. Chem. Soc.* **1926**, *48*, 1482.

[45] M. Born, *Z. Phys.* **1920**, *1*, 45.

[46] a) M. Bonetti, S. Nakamae, M. Roger, P. Guenoun, *J. Chem. Phys.* **2011**, *134*, 114513; b) E. D. Eastman, *J. Am. Chem. Soc.* **1928**, *50*, 283.

[47] J. Y. Cho, Y. S. Lim, S. M. Choi, K. H. Kim, W. S. Seo, H. H. Park, *J. Electron. Mater.* **2011**, *40*, 1024.

[48] Z. Lei, B. Chen, C. Li, H. Liu, *Chem. Rev.* **2008**, *108*, 1419.

[49] J. N. Agar, C. Y. Mou, J. L. Lin, *J. Phys. Chem.* **1989**, *93*, 2079.

[50] J. Morthomas, A. Würger, *Eur. Phys. J. E* **2008**, *27*, 425.

[51] D. Zhao, A. Würger, X. Crispin, *J. Energy Chem.* **2021**, *61*, 88.

[52] J. M. Rubi, S. Kjelstrup, *J. Phys. Chem. B* **2003**, *107*, 13471.

[53] X. Qian, J. Shin, Y. Tu, J. H. Zhang, G. Chen, *Phys. Chem. Chem. Phys.* **2021**, *23*, 22501.

[54] a) A. Campero, J. A. Díaz Ponce, *ACS Omega* **2020**, *5*, 12046; b) X. Ji, X. Liu, M. Li, S. Shao, J. Chang, J. Du, X. Ma, X. Feng, L. Zhu, X. Yu, W. Hu, *J. Chem. Educ.* **2021**, *98*, 3019.

[55] a) Y. Matsubara, D. C. Grills, Y. Koide, *ACS Omega* **2016**, *1*, 1393; b) P. Zhang, Y. Zhao, X. Zhang, *Chem. Soc. Rev.* **2018**, *47*, 2921.

[56] a) M. T. Agne, R. Hanus, G. J. Snyder, *Energy Environ. Sci.* **2018**, *11*, 609; b) R. Hanus, J. George, M. Wood, A. Bonkowski, Y. Cheng, D. L. Abernathy, M. E. Manley, G. Hautier, G. J. Snyder, R. P. Hermann, *Mater. Today Phys.* **2021**, *18*, 100344.

[57] a) H. Liu, X. Shi, F. Xu, L. Zhang, W. Zhang, L. Chen, Q. Li, C. Uher, T. Day, G. J. Snyder, *Nat. Mater.* **2012**, *11*, 422; b) B. Li, H. Wang, Y. Kawakita, Q. Zhang, M. Feygenson, H. L. Yu, D. Wu, K. Ohara, T. Kikuchi, T. Shibata, T. Yamada, X. K. Ning, Y. Chen, J. Q. He, D. Vaknin, R. Q. Wu, K. Nakajima, M. G. Kanatzidis, *Nat. Mater.* **2018**, *17*, 226.

[58] E. S. Toberer, A. Zevalkink, G. J. Snyder, *J. Mater. Chem.* **2011**, *21*, 15843.

[59] S. Lin, W. Li, Y. Pei, *Mater. Today* **2021**, *48*, 198.

[60] a) T. Bernges, T. Böger, O. Maus, P. S. Till, M. T. Agne, W. G. Zeier, *ACS Mater. Lett.* **2022**, *4*, 2491; b) T. Bernges, R. Hanus, B. Wankmiller, K. Imasato, S. Lin, M. Ghidiu, M. Peterlechner, S. Graham, G. Hautier, Y. Pei, M. R. Hansen, G. Wilde, G. J. Snyder, J. George, M. T. Agne, W. G. Zeier, *Adv. Energy Mater.* **2022**, *12*, 2200717.

[61] a) H. Zhou, Z.-Y. Ong, G. Zhang, Y.-W. Zhang, *Nanoscale* **2022**, *14*, 9209; b) J. T. Gaskins, G. Kotsonis, A. Giri, S. Ju, A. Rohskopf, Y. Wang, T. Bai, E. Sachet, C. T. Shelton, Z. Liu, Z. Cheng, B. M. Foley, S. Graham, T. Luo, A. Henry, M. S. Goorsky, J. Shiomi, J.-P. Maria, P. E. Hopkins, *Nano Lett.* **2018**, *18*, 7469.

[62] a) G. Tan, S. Hao, R. Hanus, X. Zhang, S. Anand, T. P. Bailey, A. Rettie, X. Su, C. Uher, V. P. Dravid, *ACS Energy Lett.* **2018**, *3*, 705; b) R. Hanus, R. Gurunathan, L. Lindsay, M. T. Agne, J. Shi, S. Graham, G. Jeffrey Snyder, *Appl. Phys. Rev.* **2021**, *8*, 031311.

[63] A. Würger, *Phys. Rev. Lett.* **2021**, *126*, 068001.

[64] a) A. W. Omta, M. F. Kropman, S. Woutersen, H. J. Bakker, *J. Chem. Phys.* **2003**, *119*, 12457; b) Y. Marcus, *Pure Appl. Chem.* **2009**, *62*, 899.

[65] D. Song, C. Chi, M. An, Y. Du, W. Ma, K. Wang, X. Zhang, *Cell Rep. Phys. Sci.* **2022**, *3*, 101018.

[66] S.-M. Chen, H.-L. Gao, X.-H. Sun, Z.-Y. Ma, T. Ma, J. Xia, Y.-B. Zhu, R. Zhao, H.-B. Yao, H.-A. Wu, S.-H. Yu, *Matter* **2019**, *1*, 412.

[67] J. Duan, B. Yu, K. Liu, J. Li, P. Yang, W. Xie, G. Xue, R. Liu, H. Wang, J. Zhou, *Nano Energy* **2019**, *57*, 473.

[68] H. Jia, X. Tao, Y. Wang, *Adv. Electron. Mater.* **2016**, *2*, 1600136.

[69] K. Liu, J. Lv, G. Fan, B. Wang, Z. Mao, X. Sui, X. Feng, *Adv. Funct. Mater.* **2021**, *32*, 2107105.

[70] W. B. Chang, C. M. Evans, B. C. Popere, B. M. Russ, J. Liu, J. Newman, R. A. Segalman, *ACS Macro Lett.* **2016**, *5*, 94.

[71] L. Li, W. D. Liu, Q. Liu, Z. G. Chen, *Adv. Funct. Mater.* **2022**, *32*, 2200548.

[72] Y. Yu, J. Nassar, C. Xu, J. Min, W. Gao, *Sci. Rob.* **2020**, *5*, 7946.

[73] Y. Wang, L. Yang, X.-L. Shi, X. Shi, L. Chen, M. S. Dargusch, J. Zou, Z.-G. Chen, *Adv. Mater.* **2019**, *31*, 1807916.

[74] Y. Liu, H. Zhou, W. Zhou, S. Meng, C. Qi, Z. Liu, T. Kong, *Adv. Energy Mater.* **2021**, *11*, 2101329.

[75] a) M. Anouti, J. Jacquemin, P. Porion, *J. Phys. Chem. B* **2012**, *116*, 4228; b) J. Vila, P. Ginés, E. Rilo, O. Cabeza, L. M. Varela, *Fluid Phase Equilib.* **2006**, *247*, 32.

[76] E. Laux, L. Jeandupeux, S. Uhl, H. Keppner, P. Pérez López, P. Sanglard, E. Vanoli, R. Marti, *Mater. Today Phys.* **2019**, *8*, 672.

[77] a) H. Cheng, Q. Le, Z. Liu, Q. Qian, Y. Zhao, J. Ouyang, *J. Mater. Chem. C* **2022**, *10*, 433; b) P. Pérez, S. Uhl, E. Laux, P. Sanglard, R. Marti, H. Keppner, E. Vanoli, *Mater. Today Phys.* **2018**, *5*, 10298.

[78] X. Wu, N. Gao, X. Zheng, X. Tao, Y. He, Z. Liu, Y. Wang, *ACS Appl. Mater. Interfaces* **2020**, *12*, 27691.

[79] a) E. N. Durmaz, S. Sahin, E. Virga, S. de Beer, L. C. P. M. de Smet, W. M. de Vos, *ACS Appl. Polym. Mater.* **2021**, *3*, 4347; b) B. Yang, G. Portale, *Colloid Polym. Sci.* **2021**, *299*, 465.

[80] H. Wang, D. Zhao, Z. U. Khan, S. Puzinas, M. P. Jonsson, M. Berggren, X. Crispin, *Adv. Electron Mater.* **2017**, *3*, 1700013.

[81] A. Sohn, C. Yu, *Mater. Today Phys.* **2021**, *19*, 100433.

[82] a) A. Yang, F. Yan, *ACS Appl. Electron Mater.* **2021**, *3*, 53; b) A. Shukla, T. P. Kumar, *Isr. J. Chem.* **2020**, *61*, 120.

[83] a) H. Zhou, T. Yamada, N. Kimizuka, *J. Am. Chem. Soc.* **2016**, *138*, 10502; b) J. H. Kim, Y. Han, G. Shin, J. G. Jeon, H. J. Kim, B. J. So, S. Yun, T. J. Kang, *ACS Appl. Energy Mater.* **2022**, *5*, 13053; c) Y. Liu, H. Wang, P. C. Sherrell, L. Liu, Y. Wang, J. Chen, *Adv. Sci.* **2021**, *8*, 2100669.

[84] a) G. Wu, Y. Xue, L. Wang, X. Wang, G. Chen, *J. Mater. Chem. A* **2018**, *6*, 3376; b) T. J. Abraham, D. R. Macfarlane, J. M. Pringle, *Chem. Comm.* **2011**, *47*, 6260; c) P. Yang, K. Liu, Q. Chen, X. Mo, Y. Zhou, S. Li, G. Feng, J. Zhou, *Angew. Chem., Int. Ed.* **2016**, *55*, 12050; d) T. J. Kang, S. Fang, M. E. Kozlov, C. S. Haines, N. Li, Y. H. Kim, Y. Chen, R. H. Baughman, *Adv. Funct. Mater.* **2012**, *22*, 477; e) E. Nightingale, *Biochim. Biophys. Acta* **1959**, *63*, 566; f) Burrows, Brian, *J. Electrochem. Soc.* **1976**, *123*, 154.

[85] A. J. deBethune, T. S. Licht, N. Swendeman, *J. Electrochem. Soc.* **1959**, *106*, 616.

59

**ADVANCED
SCIENCE NEWS**

www.advancedsciencenews.com

**ADVANCED
ENERGY
MATERIALS**

www.advenergymat.de

[86] R. Hu, B. A. Cola, N. Haram, J. N. Barisci, S. Lee, S. Stoughton, G. Wallace, C. Too, M. Thomas, A. Gestos, *Nano Lett.* **2010**, *10*, 838.

[87] E. H. Anari, M. Romano, W. X. Teh, J. J. Black, E. Jiang, J. Chen, T. Q. To, J. Panchompoo, L. Aldous, *Chem. Commun.* **2016**, *52*, 745.

[88] V. Zinovyeva, S. Nakamae, M. Bonetti, M. Roger, *ChemElectroChem* **2014**, *1*, 426.

[89] T. Zhu, C. Jiang, M. Wang, C. Zhu, N. Zhao, J. Xu, *Adv. Funct. Mater.* **2021**, *31*, 2102433.

[90] S. Kee, M. A. Haque, D. Corzo, H. N. Alshareef, D. Baran, *Adv. Funct. Mater.* **2019**, *29*, 1905426.

[91] Y. Zhao, H. Cheng, Y. Li, J. Rao, S. Yue, Q. Le, Q. Qian, Z. Liu, J. Ouyang, *J. Mater. Chem. A* **2022**, *10*, 4222.

[92] B. Chen, Q. Chen, S. Xiao, J. Feng, X. Zhang, T. Wang, *Sci. Adv.* **2021**, *7*, 7233.

[93] F. Jiao, A. Naderi, D. Zhao, J. Schlueter, M. Shahi, J. Sundström, H. Granberg, J. Edberg, U. Ail, J. Brill, T. Lindström, M. Berggren, X. Crispin, *J. Mater. Chem. A* **2017**, *5*, 16883.

[94] J. Xu, H. Wang, X. Du, X. Cheng, Z. Du, H. Wang, *ACS Appl. Mater. Interfaces* **2021**, *13*, 20427.

[95] M. Dietzel, S. Hardt, *Phys. Rev. Lett.* **2016**, *116*, 225901.

[96] J. Le Bideau, L. Viau, A. Vioux, *Chem. Soc. Rev.* **2011**, *40*, 907.

[97] Y. He, Q. Zhang, H. Cheng, Y. Liu, Y. Shu, Y. Geng, Y. Zheng, B. Qin, Y. Zhou, S. Chen, J. Li, M. Li, G. O. Odunmbaku, C. Li, T. Shumilova, J. Ouyang, K. Sun, *J. Phys. Chem. Lett.* **2022**, *13*, 4621.

[98] S. L. Kim, H. T. Lin, C. Yu, *Adv. Energy Mater.* **2016**, *6*, 1600546.

[99] D. Zhao, A. Martinelli, A. Willfahrt, T. Fischer, D. Bernin, Z. U. Khan, M. Shahi, J. Brill, M. P. Jonsson, S. Fabiano, X. Crispin, *Nat. Commun.* **2019**, *10*, 1093.

[100] S. L. Kim, J.-H. Hsu, C. Yu, *Nano Energy* **2018**, *48*, 582.

[101] D. Zhao, H. Wang, Z. U. Khan, J. C. Chen, R. Gabrielsson, M. P. Jonsson, M. Berggren, X. Crispin, *Energy Environ. Sci.* **2016**, *9*, 1450.

[102] Y. Fang, H. Cheng, H. He, S. Wang, J. Li, S. Yue, L. Zhang, Z. Du, J. Ouyang, *Adv. Funct. Mater.* **2020**, *30*, 2004699.

[103] W. Zhao, T. Sun, Y. Zheng, Q. Zhang, A. Huang, L. Wang, W. Jiang, *Adv. Sci.* **2022**, *9*, 2201075.

[104] Z. A. Akbar, J.-W. Jeon, S.-Y. Jang, *Energy Environ. Sci.* **2020**, *13*, 2915.

[105] M. Jeong, J. Noh, M. Z. Islam, K. Kim, A. Sohn, W. Kim, C. Yu, *Adv. Funct. Mater.* **2021**, *31*, 2011016.

[106] W. Gao, Z. Lei, W. Chen, Y. Chen, *ACS Nano* **2022**, *16*, 8347.

[107] a) J. K. G. Dhont, S. Wiegand, S. Duhr, D. Braun, *Langmuir* **2007**, *23*, 1674; b) G. Qian, Z. Li, R. Huang, J. Chen, X. Yu, *Energy Rep.* **2021**, *7*, 4895.

[108] M. Scholer, S. Matsukiyo, *Ann. Geophys.* **2004**, *22*, 2345.

[109] a) X. Yang, C. Wang, R. Lu, Y. Shen, H. Zhao, J. Li, R. Li, L. Zhang, H. Chen, T. Zhang, X. Zheng, *Nano Energy* **2022**, *101*, 107553; b) Q. Zhang, Y. Sun, W. Xu, D. Zhu, *Adv. Mater.* **2014**, *26*, 6829.

[110] S. Inceoglu, A. A. Rojas, D. Devaux, X. C. Chen, G. M. Stone, N. P. Balsara, *ACS Macro Lett.* **2014**, *3*, 510.

[111] B.-A. Mei, O. Munteshari, J. Lau, B. Dunn, L. Pilon, *J. Phys. Chem. C* **2018**, *122*, 194.

[112] H. Wang, U. Ail, R. Gabrielsson, M. Berggren, X. Crispin, *Adv. Energy Mater.* **2015**, *5*, 1500044.

[113] a) S. Verma, B. Padha, S. Arya, *ACS Appl. Energy Mater.* **2022**, *5*, 9090; b) G. L. Grocke, B. X. Dong, A. D. Taggart, A. B. F. Martinson, J. Niklas, O. G. Poluektov, J. W. Strzalka, S. N. Patel, *ACS Polym. Au* **2022**, *2*, 275.

[114] a) M. Sezen-Edmonds, A. M. Glaudell, W. B. Chang, R. A. Segalman, M. L. Chabinyc, Y.-L. Loo, *J. Phys. Chem. C* **2021**, *125*, 12289; b) M. Chen, Y. Wang, W. Ma, Y. Huang, Z. Zhao, *ACS Appl. Mater. Interfaces* **2020**, *12*, 28510; c) I. H. Sajid, N. Aslfattahi, M. F. Mohd Sabri, S. M. Said, R. Saidur, M. F. Mohd Salleh,

N. N. Nik Ghazali, S. W. Hasan, *Electrochim. Acta* **2019**, *320*, 134575.

[115] a) A. Sheskin, T. Schwarz, Y. Yu, S. Zhang, L. Abdellaoui, B. Gault, O. Cojocaru-Mirédin, C. Scheu, D. Raabe, M. Wuttig, Y. Amouyal, *ACS Appl. Mater. Interfaces* **2018**, *10*, 38994; b) M. R. Burton, C. A. Boyle, T. Liu, J. McGettrick, I. Nandhakumar, O. Fenwick, M. J. Carnie, *ACS Appl. Mater. Interfaces* **2020**, *12*, 28232.

[116] W. Zhao, J. Ding, Y. Zou, C. A. Di, D. Zhu, *Chem. Soc. Rev.* **2020**, *49*, 7210.

[117] a) N. Mateeva, H. Niculescu, J. Schlenoff, L. R. Testardi, *J. Appl. Phys.* **1998**, *83*, 3111; b) C. Wood, *Rep. Prog. Phys.* **1988**, *51*, 459.

[118] a) S. Fleischmann, J. B. Mitchell, R. Wang, C. Zhan, D.-e. Jiang, V. Presser, V. Augustyn, *Chem. Rev.* **2020**, *120*, 6738; b) H. Mahon, D. O'Connor, D. Friedrich, B. Hughes, *Energy* **2022**, *239*, 122207; c) P. Rohland, E. Schröter, O. Nolte, G. R. Newkome, M. D. Hager, U. S. Schubert, *Prog. Polym. Sci.* **2022**, *125*, 101474; d) W. Zhang, P. Feng, J. Chen, Z. Sun, B. Zhao, *Prog. Polym. Sci.* **2019**, *88*, 220; e) J. Wei, L. Zhu, *Prog. Polym. Sci.* **2020**, *106*, 101254.

[119] A. Härtel, M. Janssen, D. Weingarth, V. Presser, R. van Roij, *Energy Environ. Sci.* **2015**, *8*, 2396.

[120] a) C. S. Kim, H. M. Yang, J. Lee, G. S. Lee, H. Choi, Y. J. Kim, S. H. Lim, S. H. Cho, B. J. Cho, *ACS Energy Lett.* **2018**, *3*, 501; b) M. N. Hasan, N. Nayan, M. Nafea, A. G. A. Muthalif, M. S. Mohamed Ali, *Energy* **2022**, *259*, 125032; c) G. Prunet, F. Pawula, G. Fleury, E. Cloutet, A. J. Robinson, G. Hadziioannou, A. Pakdel, *Mater. Today Phys.* **2021**, *18*, 100402.

[121] a) W. Gao, Z. Lei, C. Zhang, X. Liu, Y. Chen, *Adv. Funct. Mater.* **2021**, *31*, 2104071; b) J. Chen, C. Shi, L. Wu, Y. Deng, Y. Wang, L. Zhang, Q. Zhang, F. Peng, X.-M. Tao, M. Zhang, W. Zeng, *ACS Appl. Mater. Interfaces* **2022**, *14*, 34714; c) V. Arumugam, M. Naresh, R. Sanjeevi, *J. Biosci.* **1994**, *19*, 307; d) A. Chortos, Z. Bao, *Mater. Today* **2014**, *17*, 321.

[122] a) N. Tanaka, *Polymer* **1978**, *19*, 770; b) D. Cangialosi, A. Alegría, J. Colmenero, *Prog. Polym. Sci.* **2016**, *54–55*, 128; c) M. Philipp, C. Nies, M. Ostermeyer, W. Possart, J. K. Krüger, *Soft Matter* **2018**, *14*, 3601.

[123] a) D. Ji, T. Li, W. Hu, H. Fuchs, *Adv. Mater.* **2019**, *31*, 1806070; b) M. Ibanez, Z. Luo, A. Genc, L. Piveteau, S. Ortega, D. Cadavid, O. Dobrozhan, Y. Liu, M. Nachtegaal, M. Zebarjadi, J. Arbiol, M. V. Kovalenko, A. Cabot, *Nat. Commun.* **2016**, *7*, 10766.

[124] Z. Lei, W. Gao, P. Wu, *Joule* **2021**, *5*, 2211.

[125] a) J. Li, C. Dong, J. Hu, J. Liu, Y. Liu, *ACS Appl. Electron. Mater.* **2021**, *3*, 3641; b) H. Sadeghi, S. Sangtarash, C. J. Lambert, *Nano Lett.* **2015**, *15*, 7467; c) M. Zeng, D. Zavanelli, J. Chen, M. Saeidi-Javash, Y. Du, S. LeBlanc, G. J. Snyder, Y. Zhang, *Chem. Soc. Rev.* **2022**, *51*, 485.

[126] a) Z. Li, Y. Lu, Q. Su, M. Wu, X. Que, H. Liu, *ACS Appl. Mater. Interfaces* **2022**, *14*, 5402; b) L. Zhang, K. Jia, J. Wang, J. Zhao, J. Tang, J. Hu, *Mater. Horiz.* **2022**, *9*, 1911; c) Z. Yu, P. Wu, *Mater. Horiz.* **2021**, *8*, 2057.

[127] a) F. Ni, P. Xiao, C. Zhang, W. Zhou, D. Liu, S. W. Kuo, T. Chen, *Adv. Mater.* **2021**, *33*, 2103937; b) J. Mo, Y. Dai, C. Zhang, Y. Zhou, W. Li, Y. Song, C. Wu, Z. Wang, *Mater. Horiz.* **2021**, *8*, 3409; c) Q. Pang, H. Hu, H. Zhang, B. Qiao, L. Ma, *ACS Appl. Mater. Interfaces* **2022**, *14*, 26536.

[128] D. Gan, T. Shuai, X. Wang, Z. Huang, F. Ren, L. Fang, K. Wang, C. Xie, X. Lu, *Nanomicro Lett.* **2020**, *12*, 169.

[129] a) R. Freer, A. V. Powell, *J. Mater. Chem. C* **2020**, *8*, 441; b) W. Shi, D. Wang, Z. Shuai, *Adv. Electron. Mater.* **2019**, *5*, 1800882; c) J. Yang, H.-L. Yip, A. K.-Y. Jen, *Adv. Energy Mater.* **2013**, *3*, 549.

[130] a) Z. Huang, Y. Zhang, H. Wu, S. J. Pennycook, L.-D. Zhao, *ACS Appl. Energy Mater.* **2019**, *2*, 8236; b) J. Zeng, X. He, S.-J. Liang, E. Liu, Y. Sun, C. Pan, Y. Wang, T. Cao, X. Liu, L. Zhang, S. Yan, G. Su, Z. Wang, K. Watanabe, T. Taniguchi, D. J. Singh, L. Zhang, F. Miao, *Nano Lett.* **2018**, *18*, 7538.

60

**ADVANCED
SCIENCE NEWS**

www.advancedsciencenews.com

**ADVANCED
ENERGY
MATERIALS**

www.advenergymat.de

[131] X. Guan, H. Cheng, J. Ouyang, *J. Mater. Chem. A* **2018**, *6*, 19347.

[132] I. H. Sajid, M. F. M. Sabri, S. M. Said, M. F. M. Salleh, N. N. N. Ghazali, R. Saidur, B. Subramaniam, S. W. Hasan, H. A. Jaffery, *Energy Convers. Manage.* **2019**, *198*, 111813.

[133] E. Helfand, J. G. Kirkwood, *J. Chem. Phys.* **1960**, *32*, 857.

[134] a) R. Kroon, D. A. Mengistie, D. Kiefer, J. Hynynen, J. D. Ryan, L. Yu, C. Müller, *Chem. Soc. Rev.* **2016**, *45*, 6147; b) Y. Yang, H. Deng, Q. Fu, *Mater. Chem. Front.* **2020**, *4*, 3130.

[135] a) S. Kim, M. M. Mench, *J. Electrochem. Soc.* **2009**, *156*, B353; b) M. Tasaka, T. Mizuta, O. Sekiguchi, *J. Membr. Sci.* **1990**, *54*, 191; c) J. P. G. Villaluenga, B. Seoane, V. M. Barragán, C. Ruiz-Bauzá, *J. Membr. Sci.* **2006**, *274*, 116.

[136] H. Kim, S. Yang, S. R. Rao, S. Narayanan, E. A. Kapustin, H. Furukawa, A. S. Umans, U. M. Yaghi, E. N. Wang, *Science* **2017**, *358*, 430.

[137] a) B. G. Sumpter, D. W. Noid, M. D. Barnes, *Polymer* **2003**, *44*, 4389; b) J. Yang, H. Zhang, Q. Zhou, H. Qu, T. Dong, M. Zhang, B. Tang, J. Zhang, G. Cui, *ACS Appl. Mater. Interfaces* **2019**, *11*, 17109; c) T. Gaillard, M. George, E. Gastaldi, F. Nallet, P. Fabre, *Soft Matter* **2019**, *15*, 8302.

[138] a) Z. Li, J.-F. Dong, F.-H. Sun, S. Hirono, J.-F. Li, *Chem. Mater.* **2017**, *29*, 7378; b) P.-A. Zong, J. Liang, P. Zhang, C. Wan, Y. Wang, K. Koumoto, *ACS Appl. Energy Mater.* **2020**, *3*, 2224; c) X. Jiang, J. Hoffman, C. C. Stoumpos, M. G. Kanatzidis, E. Harel, *ACS Energy Lett.* **2019**, *4*, 1741.

[139] C. Huang, X. Qian, R. Yang, *Mater. Sci. Eng., R* **2018**, *132*, 1.

[140] a) Q. Long, J. Xin, S. Li, A. Basit, S. Li, A. Luo, T. Xu, B. Xiao, J. Yang, Q. Jiang, X. Han, *ACS Appl. Energy Mater.* **2019**, *2*, 7490; b) S. Li, Z. Huang, W. Zhao, J. Luo, Y. Xiao, F. Pan, R. Wang, *ACS Appl. Mater. Interfaces* **2021**, *13*, 51018; c) D. Tan, J. Zhao, C. Gao, H. Wang, G. Chen, D. Shi, *ACS Appl. Mater. Interfaces* **2017**, *9*, 21820; d) Y. Zheng, T. J. Slade, L. Hu, X. Y. Tan, Y. Luo, Z.-Z. Luo, J. Xu, Q. Yan, M. G. Kanatzidis, *Chem. Soc. Rev.* **2021**, *50*, 9022.

[141] W. D. Liu, L. Yang, Z. G. Chen, J. Zou, *Adv. Mater.* **2020**, *32*, 1905703.

[142] a) C. Liu, D.-L. Shan, Z.-H. Shen, G.-K. Ren, W. Yue, Z.-F. Zhou, J.-Y. Li, D. Yi, J.-L. Lan, L.-Q. Chen, G. J. Snyder, Y.-H. Lin, C.-W. Nan, *Nano Energy* **2021**, *89*, 106380; b) Y. Sargolzaeiaval, V. Padmanabhan Ramesh, T. V. Neumann, V. Misra, D. Vashaee, M. D. Dickey, M. C. Öztürk, *Appl. Energy* **2020**, *262*, 114370; c) S. J. Kim, J. H. We, B. J. Cho, *Energy Environ. Sci.* **2014**, *7*, 1959; d) V. Padmanabhan Ramesh, Y. Sargolzaeiaval, T. Neumann, V. Misra, D. Vashaee, M. D. Dickey, M. C. Ozturk, *npj Flexible Electron.* **2021**, *5*, 5.

[143] S. Horike, Q. Wei, K. Kirihara, M. Mukaida, T. Sasaki, Y. Koshiba, T. Fukushima, K. Ishida, *ACS Appl. Mater. Interfaces* **2020**, *12*, 43674.

[144] a) X. Yang, G. Zhou, W.-Y. Wong, *Chem. Soc. Rev.* **2015**, *44*, 8484; b) A. X. Wu, J. A. Drayton, K. M. Rodriguez, Q. Qian, S. Lin, Z. P. Smith, *Macromolecules* **2020**, *53*, 5085.

[145] a) R. Wang, L. Mu, Y. Bao, H. Lin, T. Ji, Y. Shi, J. Zhu, W. Wu, *Adv. Mater.* **2020**, *32*, 2002878; b) K. K. Kiran, M. Ravi, Y. Pavani, S. Bhavani, A. K. Sharma, V. V. R. Narasimha Rao, *J. Non-Cryst. Solids* **2012**, *358*, 3205.

[146] a) W. Zhou, Q. Fan, Q. Zhang, L. Cai, K. Li, X. Gu, F. Yang, N. Zhang, Y. Wang, H. Liu, *Nat. Commun.* **2017**, *8*, 14886; b) Y. Wang, M. Hong, W. Liu, X. L. Shi, Z. G. Chen, *Chem. Eng. J.* **2020**, *397*, 125360; c) Z. Fan, P. Li, D. Du, J. Ouyang, *Adv. Energy Mater.* **2017**, *7*, 1602116.

[147] a) H. Yan, N. Sada, N. Toshima, *J. Therm. Anal. Calorim.* **2002**, *69*, 881; b) L. Wang, Q. Yao, H. Bi, F. Huang, Q. Wang, L. Chen, *J. Mater. Chem. A* **2014**, *2*, 11107.

[148] K. Choi, S. L. Kim, S. I. Yi, J. H. Hsu, C. Yu, *ACS Appl. Mater. Interfaces* **2018**, *10*, 23891.

[149] H. Im, H. G. Moon, J. S. Lee, I. Y. Chung, T. J. Kang, Y. H. Kim, *Nano Res.* **2014**, *7*, 443.

[150] H. B. Callen, *Phys. Rev.* **1948**, *73*, 1349.

[151] K. Chen, L. Yao, B. Su, *J. Am. Chem. Soc.* **2019**, *141*, 8608.

[152] a) Y. Saito, S. Takeda, S. Yamagami, J. Nakadate, T. Sasaki, T. Cho, *J. Phys. Chem. C* **2018**, *122*, 18311; b) Y. Saito, *Membranes* **2021**, *11*, 277.

[153] T. Moriyasu, T. Sakamoto, N. Sugihara, Y. Sasa, Y. Ota, T. Shimomura, Y. Sakai, K. Ito, *Polymer* **2013**, *54*, 1490.

[154] I. E. Jacobs, E. W. Aasen, J. L. Oliveira, T. N. Fonseca, J. D. Roehling, J. Li, G. Zhang, M. P. Augustine, M. Mascal, A. J. Moulé, *J. Mater. Chem. C* **2016**, *4*, 3454.

[155] a) H. Yuk, B. Lu, S. Lin, K. Qu, J. Xu, J. Luo, X. Zhao, *Nat. Commun.* **2020**, *11*, 1604; b) S. Xu, M. Hong, X.-L. Shi, Y. Wang, L. Ge, Y. Bai, L. Wang, M. Dargusch, J. Zou, Z.-G. Chen, *Chem. Mater.* **2019**, *31*, 5238; c) M. Pichumani, P. Bagheri, K. M. Poduska, W. González-Viñas, A. Yethiraj, *Soft Matter* **2013**, *9*, 3220.

[156] a) J. Wu, G. Xia, S. Li, L. Wang, J. Ma, *Ind. Eng. Chem. Res.* **2020**, *59*, 22509; b) S. Guo, K. Zhao, Z. Feng, Y. Hou, H. Li, J. Zhao, Y. Tian, H. Song, *Appl. Surf. Sci.* **2018**, *455*, 599.

[157] a) F. Schüth, *Chem. Mater.* **2014**, *26*, 423; b) M. Giannouli, V. M. Drakonakis, A. Savva, P. Eleftheriou, G. Florides, S. A. Choulis, *ChemPhysChem* **2015**, *16*, 1134.

[158] a) F. Ahangaran, A. H. Navarchian, F. Picchioni, *J. Appl. Polym. Sci.* **2019**, *136*, 48039; b) S. Karumuri, S. Hiziroglu, A. K. Kalkan, *ACS Appl. Mater. Interfaces* **2015**, *7*, 6596; c) J. Zhu, X. Wang, X. Wang, Y. Lei, Y. Li, *Compos. Sci. Technol.* **2021**, *214*, 108960; d) K. Zhu, Y. Yu, Y. Cheng, C. Tian, G. Zhao, Y. Zhao, *ACS Appl. Mater. Interfaces* **2019**, *11*, 4826; e) M. Darbandi, W. Lu, J. Fang, T. Nann, *Langmuir* **2006**, *22*, 4371.

[159] a) D. Tian, Y. Song, L. Jiang, *Chem. Soc. Rev.* **2013**, *42*, 5184; b) H. Yuk, X. Zhao, *Adv. Mater.* **2018**, *30*, 1704028.

[160] Y. Li, Q. Li, X. Zhang, B. Deng, C. Han, W. Liu, *Adv. Energy Mater.* **2022**, *12*, 2103666.

[161] a) M. A. Johnson, J. Iyer, P. T. Hammond, *Macromolecules* **2004**, *37*, 2490; b) T. J. Trivedi, D. N. Srivastava, R. D. Rogers, A. Kumar, *Green Chem.* **2012**, *14*, 2831; c) F. Bode, M. A. da Silva, P. Smith, C. D. Lorenz, S. McCullen, M. M. Stevens, C. A. Dreiss, *Soft Matter* **2013**, *9*, 6986.

[162] Z. Li, G. Ma, R. Ge, F. Qin, X. Dong, W. Meng, T. Liu, J. Tong, F. Jiang, Y. Zhou, K. Li, X. Min, K. Huo, Y. Zhou, *Angew. Chem., Int. Ed.* **2016**, *55*, 979.

[163] Y. Son, A. Liao, R. L. Peterson, *J. Mater. Chem. C* **2017**, *5*, 8071.

[164] V. Chernikova, O. Shekhah, M. Eddaoudi, *ACS Appl. Mater. Interfaces* **2016**, *8*, 20459.

[165] a) Y. Huang, I. Szleifer, N. A. Peppas, *Macromolecules* **2002**, *35*, 1373; b) T. Yamakado, S. Saito, *J. Am. Chem. Soc.* **2022**, *144*, 2804.

[166] Y. Tan, Z.-B. Shao, X.-F. Chen, J.-W. Long, L. Chen, Y.-Z. Wang, *ACS Appl. Mater. Interfaces* **2015**, *7*, 17919.

[167] a) Y. P. Neo, C. O. Perera, M. K. Nieuwoudt, Z. Zujovic, J. Jin, S. Ray, M. Gizdavic-Nikolaidis, *J. Agric. Food Chem.* **2014**, *62*, 5163; b) M. Yang, S. Li, S. Zhang, B. Gao, Z. Tong, D. Cheng, D. Chen, R. Huang, Y. Yang, *J. Mater. Chem. A* **2022**, *10*, 18834; c) K. Li, T. Ping, H. Zhang, J. Zhang, J. Cheng, F. Gao, *RSC Adv.* **2021**, *11*, 3740.

[168] a) J. S. Teixeira, R. S. Costa, A. L. Pires, A. M. Pereira, C. Pereira, *Dalton Trans.* **2021**, *50*, 9983; b) Z. Wu, S. Zhang, Z. Liu, E. Mu, Z. Hu, *Nano Energy* **2022**, *91*, 106692; c) T. Cao, X.-L. Shi, Z.-G. Chen, *Prog. Mater. Sci.* **2023**, *131*, 101003.

[169] a) R. Lin, H. J. Kim, S. Achavananthadith, S. A. Kurt, S. C. C. Tan, H. Yao, B. C. K. Tee, J. K.-W. Lee, J. S. Ho, *Nat. Commun.* **2020**, *11*, 444; b) S. Mannsfeld, B. Tee, R. Stoltenberg, C. Chen, S. Barman, B. Muir, A. Sokolov, C. Reese, Z. Bao, *Nat. Mater.* **2010**, *9*, 859; c) J. Huang, J. Zhou, Y. Luo, G. Yan, H. Duan, *ACS Appl.*

ADVANCED
SCIENCE NEWS

www.advancedsciencenews.com

ADVANCED
ENERGY
MATERIALS

www.advenergymat.de

Mater. Interfaces **2020**, *12*, 43009; d) C. Zhang, J. Chen, W. Xuan, S. Huang, B. You, W. Li, L. Sun, H. Jin, X. Wang, S. Dong, *Nat. Commun.* **2020**, *11*, 58.

[170] a) H. Huang, L. Tao, F. Liu, L. Ji, Y. Hu, M. C. Cheng, P. Y. Chen, D. Akinwande, *Microsyst. Technol.* **2016**, *2*, 9; b) A. Aslam, U. Mehmood, M. H. Arshad, A. Ishfaq, M. Sufyan, *Sol. Energy* **2020**, *207*, 874; c) A. Saleem, H. Najam, J. Ju, L. Kyung-Geun, *Sensors* **2016**, *16*, 460; d) T. C. Huang, Y. G. Leu, C. W. Huang, *Energy* **2017**, *133*, 879.

[171] a) J. Wu, J. J. Black, L. Aldous, *Electrochim. Acta* **2017**, *225*, 482; b) L. Zhang, T. Kim, N. Li, T. J. Kang, J. Chen, J. M. Pringle, M. Zhang, A. H. Kazim, S. Fang, C. Haines, D. Al-Masri, B. A. Cola, J. M. Razal, J. Di, S. Beirne, D. R. MacFarlane, A. Gonzalez-Martin, S. Mathew, Y. H. Kim, G. Wallace, R. H. Baughman, *Adv. Mater.* **2017**, *29*, 1605652.

[172] R. Liu, Z. L. Wang, K. Fukuda, T. Someya, *Nat. Rev. Mater.* **2022**, *7*, 870.

[173] A. M. Abdul Mageeth, S. Park, M. Jeong, W. Kim, C. Yu, *Appl. Energy* **2020**, *268*, 114975.

[174] G. Li, D. Dong, G. Hong, L. Yan, X. Zhang, W. Song, *Adv. Mater.* **2019**, *31*, 1901403.

[175] A. L. Pires, R. S. Costa, C. Pereira, A. M. Pereira, *ACS Appl. Electron. Mater.* **2021**, *3*, 696.

[176] H. Im, T. Kim, H. Song, J. Choi, J. S. Park, R. Ovalle-Robles, H. D. Yang, K. D. Kihm, R. H. Baughman, H. H. Lee, T. J. Kang, Y. H. Kim, *Nat. Commun.* **2016**, *7*, 10600.

[177] A. Kundu, T. S. Fisher, *Electrochim. Acta* **2018**, *281*, 357.

[178] B. Yu, J. Duan, J. Li, W. Xie, H. Jin, R. Liu, H. Wang, L. Huang, B. Hu, J. Zhou, *Research* **2019**, *1*, 2460953.

[179] Q. Chen, B. Chen, S. Xiao, J. Feng, J. Yang, Q. Yue, X. Zhang, T. Wang, *ACS Appl. Mater. Interfaces* **2022**, *14*, 19304.

[180] M. Li, F. Zeng, M. Luo, X. Qing, W. Wang, Y. Lu, W. Zhong, L. Yang, Q. Liu, Y. Wang, J. Luo, D. Wang, *ACS Appl. Mater. Interfaces* **2021**, *13*, 50430.

[181] M. Du, X. Chen, K. Zhang, *ACS Appl. Energy Mater.* **2021**, *4*, 4070.

[182] C. Chi, M. An, X. Qi, Y. Li, R. Zhang, G. Liu, C. Lin, H. Huang, H. Dang, B. Demir, Y. Wang, W. Ma, B. Huang, X. Zhang, *Nat. Commun.* **2022**, *13*, 221.

[183] E. Miyako, H. Nagata, R. Funahashi, K. Hirano, T. Hirotsu, *ChemSusChem* **2009**, *2*, 419.
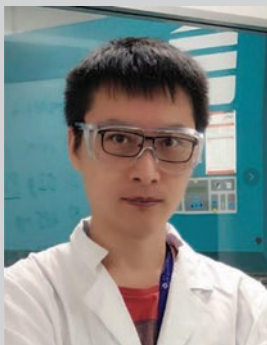
Xiao-Lei Shi is currently a Research Fellow at Queensland University of Technology. He received his Ph.D. degree in 2019 from the University of Queensland under the supervision of Prof. Zhi-Gang Chen with a research focus on the development of high-performance thermoelectrics and underlying physics and chemistry.

Zhi-Gang Chen is currently a Capacity Building Professor of Energy Materials in Queensland University of Technology (QUT). He received his Ph.D. in materials science and engineering from the Institute of Metal Research, Chinese Academy of Science, in 2008. His research concentrates on smart functional materials for thermoelectrics and nanoelectronics from synthesizing materials to understanding their underlying physics and chemistry.

62

2.3. Flexible thermoelectric device constructions and applications

As TE materials are steadily discovered and developed, basic design principles, key integration technologies and characterization methods of TE generators (TEGs) are correspondingly promoted as well (Bell, 2008; Hamid Elsheikh et al., 2014; Majumdar, 2009). Specifically, flexible TEGs can be achieved by (i) well design of the integrated inorganic rigid TE materials and (ii) directly assembling of FTE materials.

2.3.1. Rigid material based flexible thermoelectric devices

Generally, the inorganic bulk material based flexible TEGs are composed of integrated rigid units stacked side by side through flexible bridges and substates (**Figure 2.10**) (Russ, Glaudell, Urban, Chabinyc, & Segalman, 2016; Q. H. Zhang et al., 2016). The thermal voltage generated by each unit can be series-connected to considerable output voltage, providing power for small-scale electronic devices or batteries. As can be seen from the enlarged view of **Figure 2.10b**, TE elements are n-type and p-type units in series. Electrons transport to the cold end under temperature difference in terms of n-type legs, while holes spread to the cold end driven by the for p-type legs. Therefore, the electric circuit is built to generate current. After weaving, graphing, or laminating onto flexible substrates, the flexible bending or stretching can be achieved.
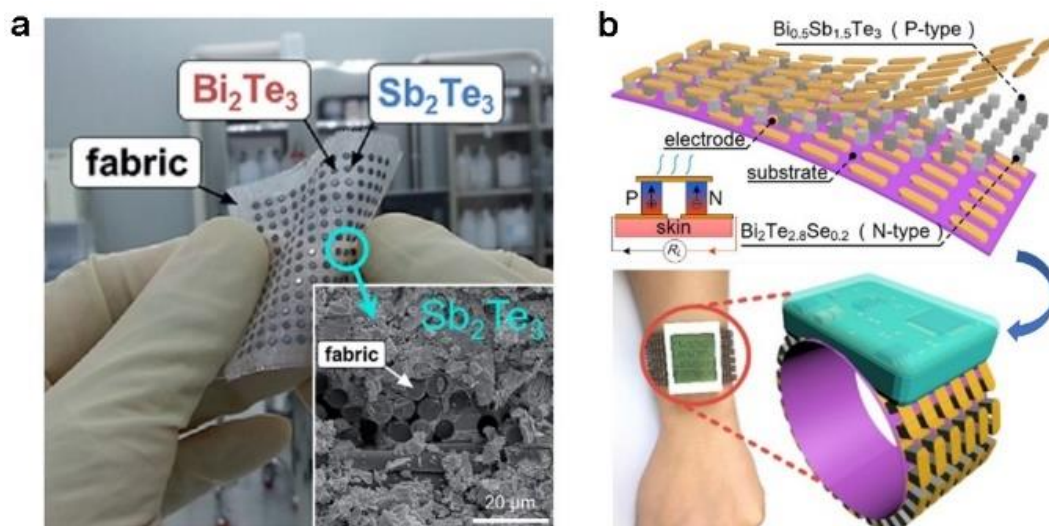
Figure 2.10. Schematic diagram of rigid material based flexible thermoelectric device structure. (a) A 40 mm × 40mm glass fabric with Bi_2Te_3 and Sb_2Te_3 dots as thermoelectric legs, (b) A wristwatch using p-type $Bi_{0.5}Sb_{1.5}Te_3$ and n-type $Bi_2Te_{2.8}Se_{0.2}$ as thermoelectric legs and polyimide as the flexible substrate (Russ et al., 2016; Q. H. Zhang et al., 2016).

2.3.2. Flexible material based flexible thermoelectric devices

Considering inorganic rigid materials integration is cumbersome, flexible material-based TEGs can be processed by facile molding. On the first hand, there are plenty basic connection methods as shown in **Figure 2.11**. As can be seen, p-n series modules (Yimeng Sun et al., 2012), as well as high-density integrated single p (or single n) series modules can be prepared on flexible substrates to achieve large voltage output (Weber et al., 2006). Moreover, the molding process are diversified from solution printing, inkjet printing, to computer monitored etching, *etc.* (J. A. Lee et al., 2016). As a result, 1D fiber-like, 2D film-like, and 3D bulk-like flexible TEGs can be prepared on the basis of flexible fundamental materials. Notably, the integrated flexible material-based TEGs can directly be applied with raw materials, whereas flexible substrates are essential for well-designed rigid material-based TEGs.
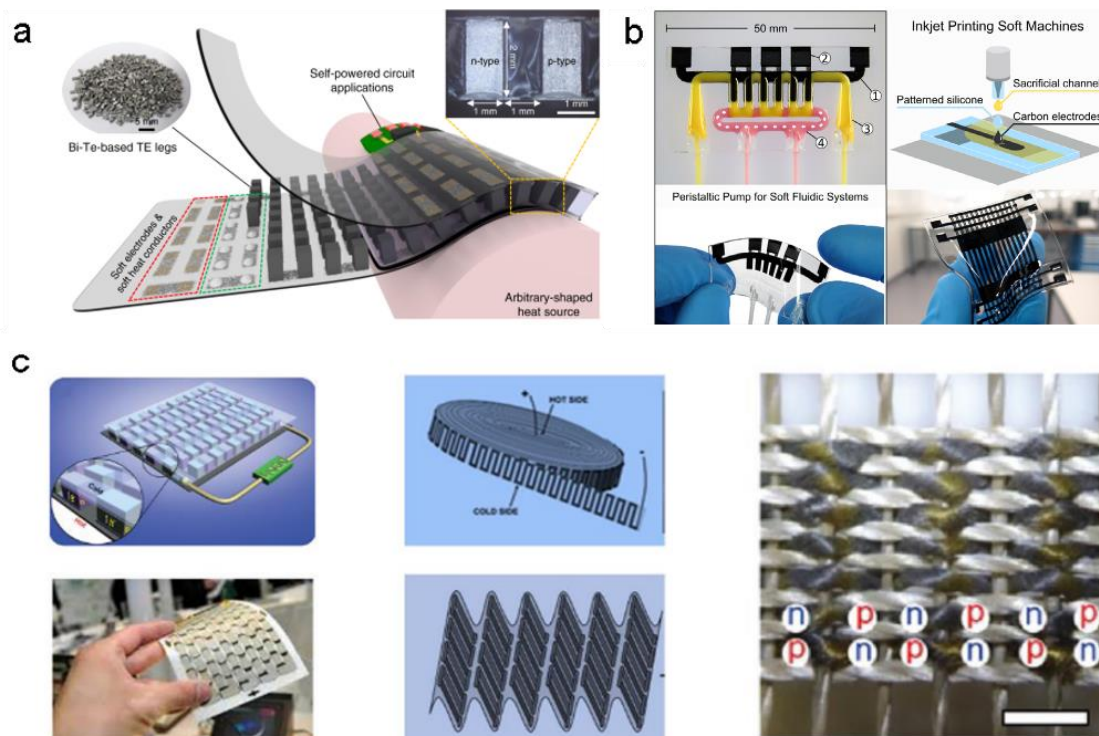
Figure 2.11. (a) Basic connection method of integrated devices (B. Lee et al., 2020), (b) solution processing technology (Schlatter, Grasso, Rosset, & Shea, 2020), (c) high-density integrated devices (J. A. Lee et al., 2016; Yimeng Sun et al., 2012).

2.3.3. Typical applications of flexible thermoelectric devices

The most typical application of TE power generation device is the radioisotope TEGs employed as a space power source, as demonstrated in **Figure 2.12a** (Telkes, 2004; Vedernikov & Iordanishvili, 1998). The power provided by three radioisotope TEGs on

the Voyager launched by NASA in 1977 can be maintained until now. Besides, the radioisotope TEGs carried by Apollo 12-17 were left on the surface of the moon to provide power for scientific research experiments. In 1950s, a ring-like TEG based on a ZnSb/Constantan thermocouple was commercialized (the Soviet Union), which utilized the kerosene lamp heat to power the radio receiver (**Figure 2.12b**). In 1998, Seiko Corporation (Japan) launched the first thermoelectric watch "THERMIC" powered by the temperature difference between human body and the ambient. In 2003, BMW developed a TEG that took advantage of the automobile waste heat to generate electricity, where the obtained power can reach 80 W (Liebl et al., 2009). By 2011, the generated power has been greatly increased to 600 W (**Figure 2.12c**).
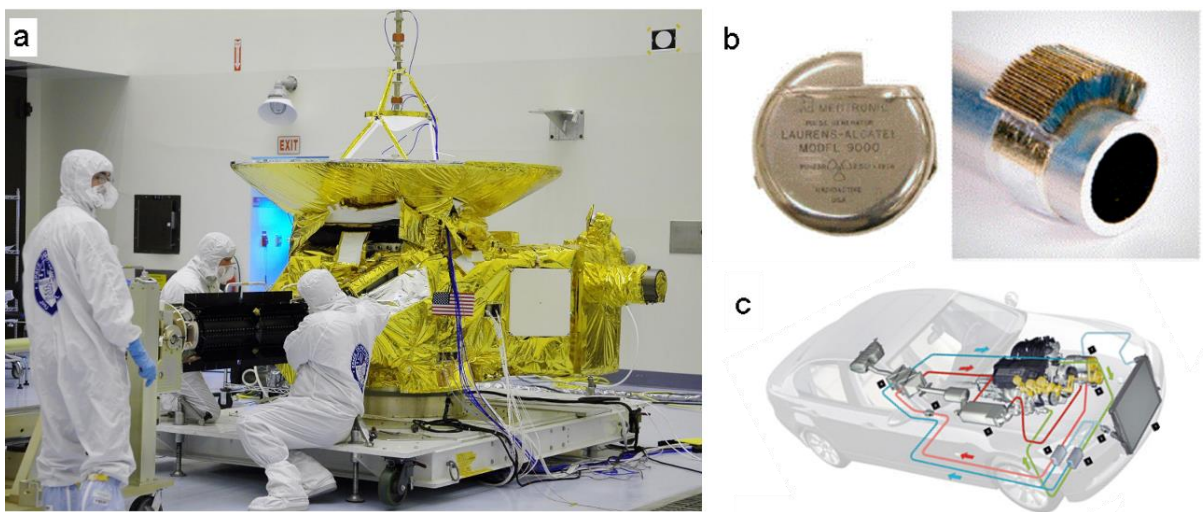
Figure 2.12. (a) Radioisotope thermoelectric devices applied in the aircraft (Telkes, 2004; Vedernikov & Iordanishvili, 1998), (b) a ring-like thermoelectric generator based on a ZnSb/Constantan thermocouple, (c) automotive waste heat recovery generators by BMW.

CHAPTER 3: METHODOLOGIES

In this project, both graphite-based solid film and carbon-incorporated ionogel quasi-solid film will be prepared and optimized. Therefore, this section summarizes the fabrication and characterization methods to achieve the experimental works.

3.1. Synthesis methods

3.1.1. Preparation of graphite-based composites

Graphite composite films can be typically prepared by the hot-pressing procedure. The entire process is simple and rapid which can be logically industrialized scale-up. Firstly, designed compound powders were fully dried in an oven. After completely removing the moisture, the compound powders were mechanically mixed evenly in a blade shredder. Subsequently, we evenly and smoothly spread the powders in a stainless steel module, and placed the module between the upper and lower plates of a flat vulcanizer (**Figure 3.1**). Hot pressing conditions are set with individual temperature, pressure, and maintaining time, which will be revealed in the corresponding publications. The thicknesses of all obtained thin films can be regulated by controlling the powder amounts.

Figure 3.1. Images of flat vulcanizer. (a) Laboratorial and (b) industrial facilities.

3.1.2. Preparation of ionic liquid-incorporated carbon films

Firstly, EG pre-treated with IL. [EMIM:DCA] is diluted in anhydrous methanol with a mass ratio of 1:1, then the dissolved solution is sprayed through a sprinkling can under ultrasonic dispersion, following the principle of multiple-low-dose. The treated EG particles are dried for subsequent use in an oven under 378K for 1 hour. Afterward, a flat vulcanizer is employed for the hot-press molding of the hybrid films. Dried raw powders and modified EG can be physically mixed in proportion via a blade blender

for 5 minutes. Uniformly blended particles are subsequently hot-pressed in a grooved stainless steel plate with designed temperature program. The molding pressure is maintained at 12 MPa, and the fabricated film thicknesses are adjusted to ~0.1 mm.

3.1.3. Preparation of carbon-incorporated ionogels

The ionogels were obtained by free radical polymerization. Acrylamide (AM) is selected as the basic monomers of the hydrogel. Moreover, water soluble ionic liquid and graphene oxide (GO) were added to enhance the TE performance. As a result, TE ionogels combined the excellent flexibility from the ionogel, relatively high σ from GO, and the super pioneeried S from the ionic liquid. Specific procedures are as follows: we firstly weighed a certain mass of AM, GO, ionic liquid, water, and initiator ammonium persulfate (APS), where the mass of APS is around 1% of the total mass of monomers. Then the mixture was ultrasonic stirred under ice-water bath for 30 minutes to prepare an aqueous solution with the designed concentration. After blowing nitrogen for 10 minutes to remove oxygen in the system, the suspension solution was poured into a mold and cured at the temperature of 330 K for 12 hours, followed by annealing at 383 K for 5 hours.

3.2. Characterization methods

The conductivity (σ), thermal conductivity (κ) and ZT were studied to measure TE properties of the materials. Besides, structure, crystallization, and mechanical properties, *etc.* were confirmed by Raman spectroscopy, X-ray diffraction (XRD), X-ray photoemission spectroscopy (XPS), and universal tensile testing machine. Scanning electron microscopy (SEM) equipped with an energy dispersive X-ray spectrometer (EDS) were utilized to analyse the element compositions and morphologies.

3.2.1. Raman spectrometer

Raman spectroscopy is based on the Raman scattering effect (**Figure 3.2**) (X. Zhang, Tan, Wu, Shi, & Tan, 2016). It is a typical carbon material characterization method by analysing the scattering spectra with different frequencies of incident light. Information on molecular vibrations and rotations can be obtained, reflecting the structure of tested

materials. Raman analysis is commonly used for the qualitative analyse of crystalline materials.
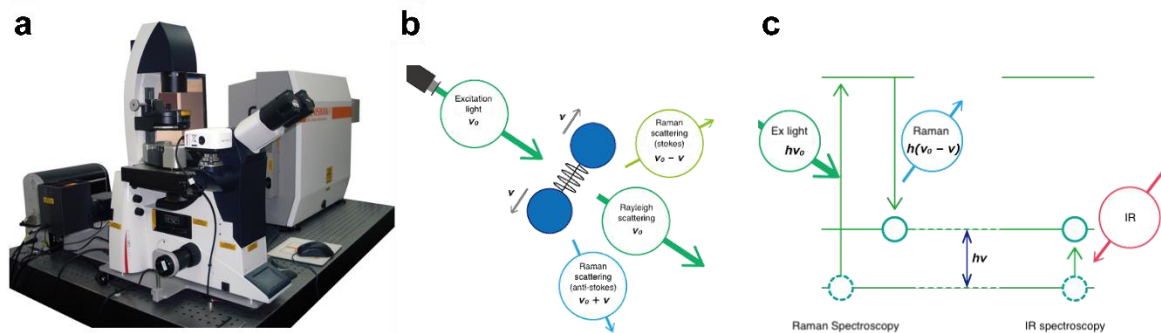
Figure 3.2. (a) Image, (b) diagrammatic principle, and (c) vibration energy level mechanism of Raman microscopy.

3.2.2. XRD diffractometer

Phase analysis is the major function of XRD, especially for inorganic materials (Cole, 2004). XRD technology can be used for both qualitative analysis and quantitative analysis (**Figure 3.3**). By comparing the measured lattice plane location and diffraction intensity of the material with the standard spectrum, qualitative analysis can be achieved. By recording and comparing the intensity of the diffraction pattern, the content of each phase can be determined. XRD has been widely used to measure the crystallization parameters of TE materials.
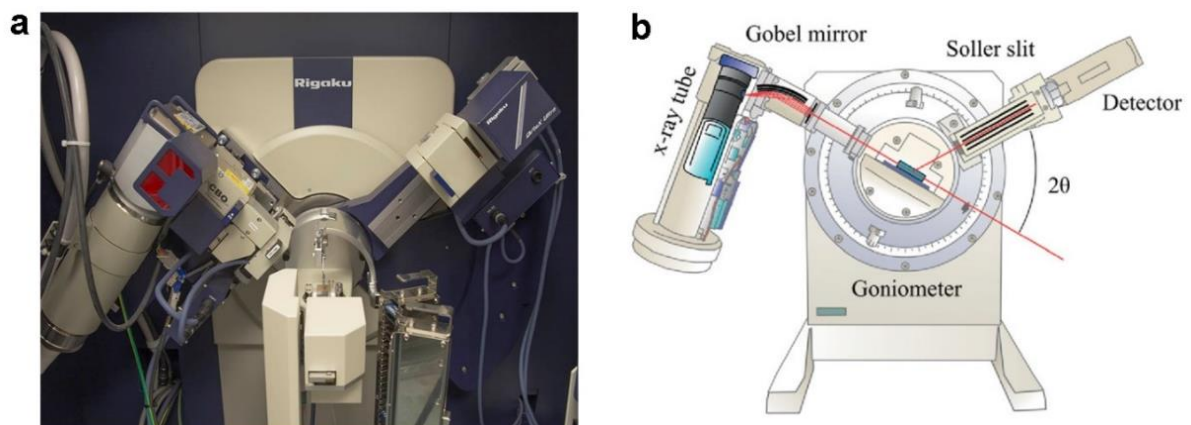
Figure 3.3. (a) Image and (b) diagrammatic principle of XRD diffractometer.

3.2.3. XPS spectrometer

XPS provides information on the molecular structures, atomic valence states, element composition and content, chemical state, and chemical bonds (**Figure 3.4**) (Seah, 1980). XPS technology is benefited from no pollution, fast speed, and high

measurement accuracy, but the stability of organic and polymer materials should be considered initially to prevent X-ray damage. Meanwhile, scientific sample preparations can also effectively avoid signal artifacts, such as polishing, grinding, and argon ion etching of samples, *etc.* Notably, samples with inherent fluorescence are not suitable for XPS detection.
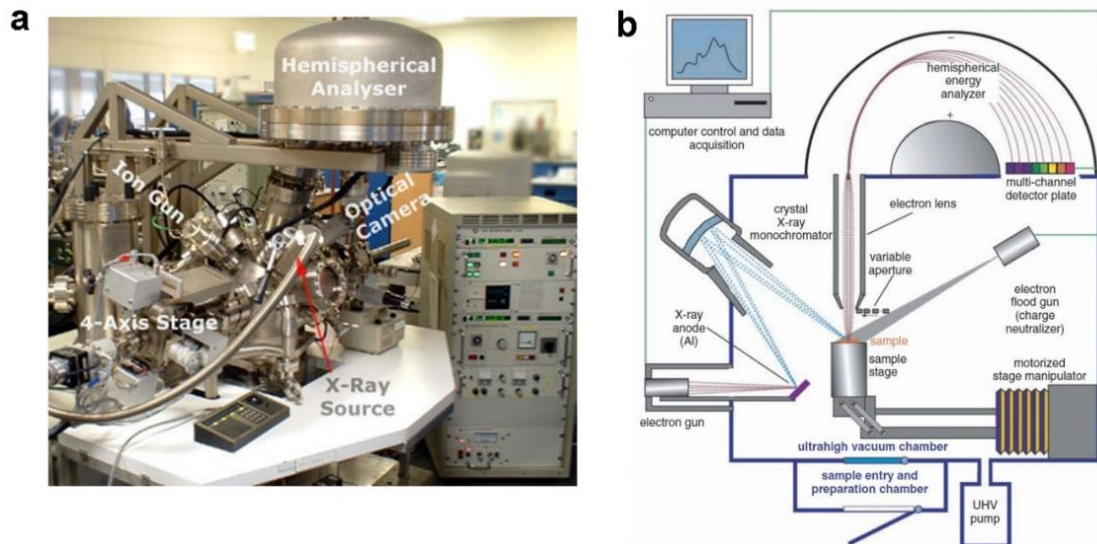
Figure 3.4. (a) Image and (b) diagrammatic principle of XPS spectrometer.

3.2.4. SEM image

SEM characterizes the microscopic morphology of samples through the laser excitation, information collection, amplified, and re-imaged (**Figure 3.5**) (Narayan & Subramaniam, 2015). The resolution can reach 1 nm, the magnification can reach 300,000 times. SEM observation depth and field of the view is large, whereas the three-dimensional imaging is optional. Additionally, the combination of SEM and EDS can be used to map the material composition in certain micro-level regions.
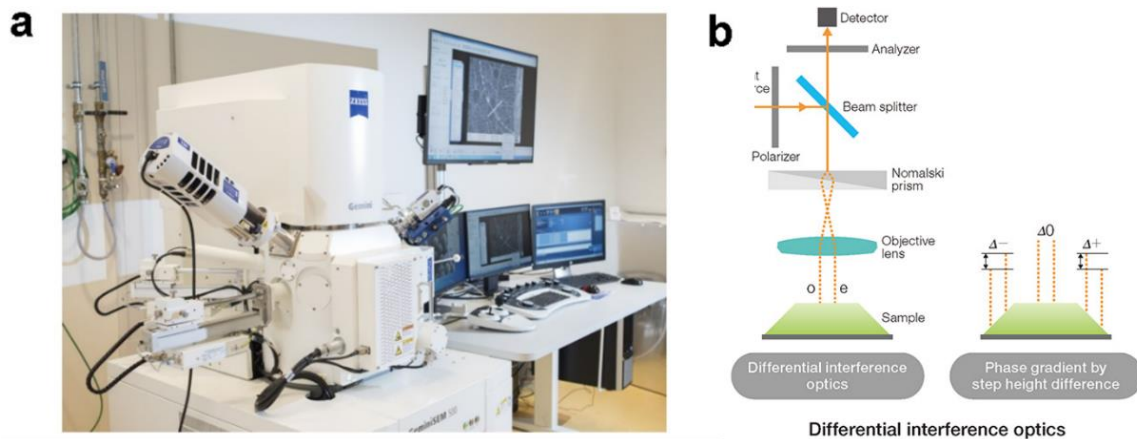
Figure 3.5. (a) Image and (b) diagrammatic principle of SEM spectrometer.

3.2.5. Tensile properties

Universal tensile testing machine has been generally applied for the tensile, compression, bending, tearing, 90° peeling, 180° peeling, shearing, adhesion, pull-out force, and elongation characterization of both inorganic mental and organic polymers (**Figure 3.6**). In this project, we employed a high-precision laboratory equipment to characterize the tensile performance of as-prepared samples.
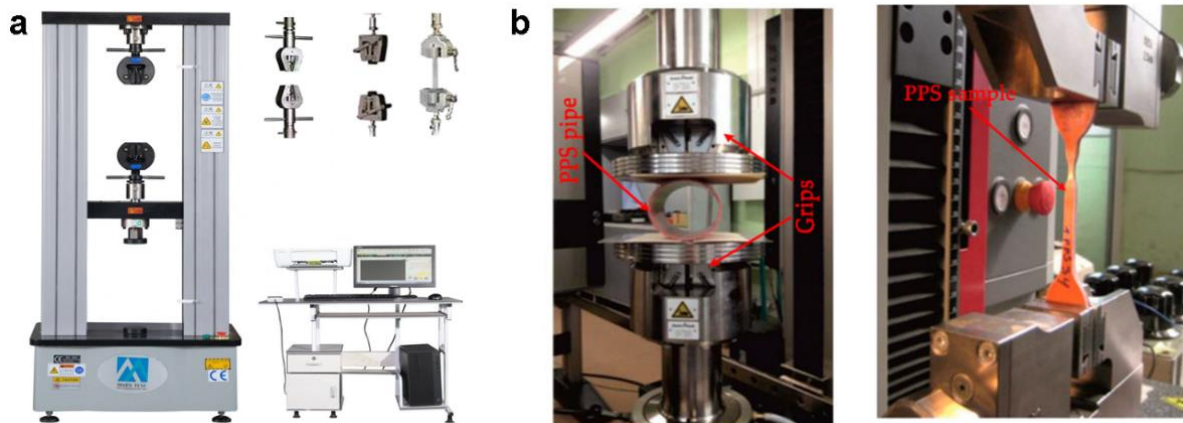
Figure 3.6. Image of (a) universal tensile testing machine and (b) the specimen testing process (Vidinejevs, Chatys, Aniskevich, & Jamroziak, 2021).

3.2.6. TE properties

By testing the I/V curve at two ends of the material, the electrical resistance can be calculated. Then the σ of the TE material can be calculated *via* calculation with the material thickness and cross-sectional area. The "four probe" method can effectively eliminate the contact resistance between the TE material and the electrode, which is the most used method in the field of TE technology.

During the detection of S, aimed materials are usually installed with a heating unit at one end and a cooling unit at the other end to creating a temperature difference. In a circuit without external voltage applied, the generated voltage difference (ΔV) will be recorded by the instrument. Specifically, the measured S is described as $S = \Delta V/\Delta T$. In this project, we employed a commercial instrument SBA 458 to characterize the σ and S of as-prepared samples (**Figure 3.7a-b**). For inorganic TE materials, thermal diffusivity coefficient D can be measured by the laser flash diffusivity apparatus. In this project, we employed a commercial instrument LFA 457 to characterize the D of as-prepared samples (**Figure 3.7c-d**). Besides, the specific heat capacity C_p should be characterized by the differential scanning calorimetry (DSC) and density ρ can be

measured by applying Archimedes law simultaneously. As a result, κ can be calculated by the formula $\kappa = D \times C_p \times \rho$.
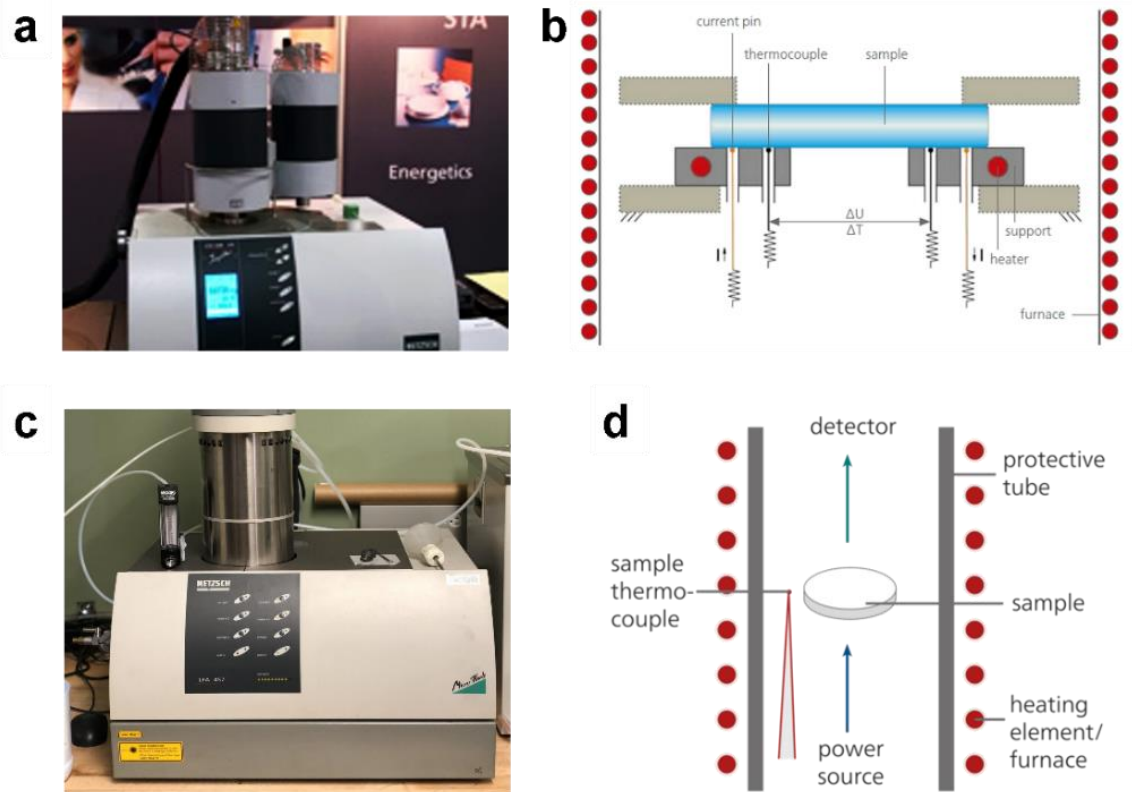
Figure 3.7. (a) Image and (b) diagrammatic principle of SBA 458, (c) image and (d) diagrammatic principle of LFA 457.

CHAPTER 4: PAPER 2 – CHEAP, LARGE-SCALE, AND HIGH-PERFORMANCE GRAPHITE-BASED FLEXIBLE THERMOELECTRIC MATERIALS AND DEVICES WITH SUPERNORMAL INDUSTRY FEASIBILITY

4.1.   Introduction

In this study, we developed super-large 25×20 cm^2 commercial-graphite produced p-type composite films. For the optimal blended specimen, namely EG$_3$-GIC2$_7$, high σ of 1089 S cm^{-1}, S of 28.2 µV K^{-1}, and PF of 87 µW m^{-1} K^{-2} are obtained at room temperature. The entire procedure of preparation needs only 10 minutes and ten pieces of batch outputs produced by industrial equipment are presented in this work as a model. Record high cost-effectiveness of 7250 µW g m^{-1} K^{-2} $\$^{-1}$ has been achieved, which is ahead of the existing p-type TE materials. Moreover, two types of flexible TEGs adapt to different application scenarios are installed based on such novel composite. An output open-circuit voltage of 3.70 mV (ΔT = 3.9 K) is achieved using human wrist as the heat source, and 1.33 mV (ΔT = 1.6 K) is achieved soaking in the river water as the cold source.

4.2.   Published paper

4.3. Links and implications

This study is published in the journal of ACS Applied Materials & Interfaces at the website of https://pubs.acs.org/doi/10.1021/acsami.1c24649. Based on this work, a facile one step hot-pressing method has been established to guide the next study during the fabrication process. Besides, we are also inspired from this work, that further doping modification of such kind of industrial feasible composite films is under demand. High-performance n-type industrial feasible carbon-based TE films are urgently needed to be discovered.

CHAPTER 5: PAPER 3 – ULTRAFAST AND COST-EFFECTIVE FABRICATION OF HIGH-PERFORMANCE CARBON-BASED FLEXIBLE THERMOELECTRIC HYDRID FILMS AND THEIR DEVICES

5.1. Introduction

In this work, we develop an ultrafast and cost-effective n-type carbon-based hybrid film, which consists of ionic liquid/phenolic resin/carbon fiber/expanded graphite. One fabrication cycle costs no more than 15 minutes. We found that the expanded graphite as the major component enables high flexibility and the introduction of phenolic resin and carbon fiber enhances the shear resistance and toughness of the film, while the ion-induced carrier migration contributes to a *PF* of 38.7 μW m^{-1} K^{-2} at 500 K. After the comparison based on the ratios between *PF* with fabrication time and cost among the current conventional carbon-based TE composites, our hybrid films show the best cost-effective. Besides, a flexible TE device, assembled by the as-designed hybrid films, shows a maximum *η* of 79.3 nW cm^{-2} at a temperature difference of 20 K. This work paves a new way to fabricate cost-effective and high-performance carbon-based n-type TE hybrids with promising application potential.

5.2. Published paper

5.3. Links and implications

This study is published in the journal of ACS Applied Materials & Interfaces at the website of https://doi.org/10.1021/acsami.3c05226. Based on this work, ionic liquids and carbon materials are combined to fabricate FTE material, where their advantages are synergized. However, ionogel TE materials are recently reported to behave superior S values, showing great promise in the TE family. This study inspires us to design a novel carbon material hybrid ionogel, where the advanced S from ionogel and the outstanding σ from carbon material may be integrated to achieve breakthroughs in TE performance.

CHAPTER 6: PAPER 4 – STABLE, SELF-HEALABLE, AND HIGH-PERFORMANCE GRAPHENE-OXIDE-MODIFIED FLEXIBLE IONOGEL THERMOELECTRIC FILMS AND THEIR DEVICES

6.1. Introduction

In this work, we developed a graphene oxide blended polyacrylamide ionic thermoelectric film with high stability, competitive thermoelectric performance, and outstanding flexibilities. Specifically, excellent S of -76.7 mV K^{-1} and ZT of 0.086 are achieved by the optimized sample, namely PAM$_{0.3}$-BMIM:Cl$_{0.6}$-GO$_1$, at 0% humidity and 383 K. At the same time, the as-prepared film is stable after depositing in air for 7 days. Moreover, the tensile strength, elongation at break, Young's module, toughness, and flexibility reach 219.7 kPa, 389 %, 84.1 kPa, 0.4 MJ m^{-3}, and 180° bending respectively. Based on the high thermoelectric and mechanical performance, we fabricated a 9-leg miniaturized (25x25 mm^2) flexible device via an in-site integration strategy. Superior output voltage of 205 mV is generated under a small temperature difference of 5.7 K.

6.2. Published paper

Stable, Self-Healable, and High-Performance Graphene-Oxide-Modified Flexible Ionogel Thermoelectric Films and Their Devices

Shuai Sun,[1,2] Xiao-Lei Shi,[2]* Wanyu Lyu,[2] Min Hong,[1] Wenyi Chen,[2,3] Meng Li,[2] Tianyi Cao,[2] Boxuan Hu,[2] Qingfeng Liu,[4] and Zhi-Gang Chen[1,2]*

[1]Centre for Future Materials, University of Southern Queensland, Springfield Central, Queensland 4300, Australia;

[2]School of Chemistry and Physics and Center for Materials Science, Queensland University of Technology, Brisbane City QLD 4000, Australia;

[3]School of Mechanical and Mining Engineering, The University of Queensland, Brisbane, Queensland 4072, Australia;

[4]State Key Laboratory of Materials Oriented Chemistry Engineering, College of Chemistry Engineering, Nanjing Tech University, Nanjing 211800, China;

* E-mail address: xiaolei.shi@qut.edu.au (XLS); zhigang.chen@qut.edu.au (ZGC)

Abstract

Ionic thermoelectric materials have attracted increasing attention due to their high flexibility and Seebeck coefficient. However, they are still suffering insufficient thermoelectric performance and require strict encapsulation processes for practical applications. In order to achieve ionic thermoelectric materials with simultaneously high stability, flexibility, and thermoelectric performance, in this work, we design a novel acrylamide ionogel modified with graphene oxide (GO). Detailed structural characterizations confirm the good dispersion of GO particles in the ionogel structure, enabling the achievement of a high power factor of 85.9 μW m^{-1} K^{-2} and a promising *ZT* value of 0.086, both reaching world-leading levels. Additionally, the as-prepared ionic thermoelectric thin film demonstrate excellent flexibility, stretchability, and self-adhesiveness. The thermoelectric performance of the as-fabricated film remain highly stable even after 7 days of static exposure to air. Furthermore, we prepare and utilize an integrated device based on these ionogel films, which can generate an outstanding thermoelectric potential of up to 205 mV under a low temperature difference of only 5.7 K. This work contributes to the further optimization of ionic thermoelectric materials and devices, promising significant advancements in the research of long-term, high-performance ionic thermoelectric materials.

Keywords: ionic thermoelectric; graphene oxide; flexibility; stability; device

1. Introduction

Thermoelectric materials and devices play a significant role in the development of clean energy by converting waste heat into electrical energy.[1-5] Generally, the performance of thermoelectric devices largely depends on the properties of the thermoelectric materials. Therefore, significant improvements in the performance of thermoelectric materials are required to enhance the output voltage and thermoelectric conversion efficiency of their devices.[6-8] Currently, the performance of thermoelectric materials remains a key factor limiting the practical application of thermoelectric devices, especially for flexible thermoelectric generators and coolers. The dimensionless figure-of-merit ZT is used to evaluate the thermoelectric performance of these materials, defined as $ZT = S^2\sigma T/\kappa$, where the power factor $S^2\sigma$ is composed of Seebeck coefficient S and electrical conductivity σ, T is the absolute temperature (K), and κ is the thermal conductivity. Currently, there are three common types of thermoelectric materials: semiconductor alloys with high ZT but low flexibility,[9-11] organic polymers and small molecules that exhibit high flexibility and low κ but relatively poor S,[12-14] and carbon-based materials with high σ and flexibility but low S and high κ.[15-17] Furthermore, the combination of these materials as composites is also widely studied to achieve comprehensive high performance.[18-20]

Recently, ionic thermoelectric materials have emerged as a new class of thermoelectric materials based on the Soret effect or thermochemical reactions.[21-23] The most important characteristic of ionic thermoelectric materials is their outstanding S, which is typically on the magnitude of millivolts per Kelvin (mV K^{-1}), approximately 10~100 times higher than that of traditional thermoelectric materials.[24-26] Additionally, ionic thermoelectric materials possess excellent flexibility and stretchability, making them considered as thermoelectric materials with practical application potential.[27-28] They can be utilized in flexible thermoelectric devices to harness power from irregular heat sources. In most cases, ionic thermoelectric materials are composed of various functional components. Among them, the ionic donor is the most important, providing ion carriers such as ionic liquids, polyelectrolytes, and so on.[29-30] Meanwhile, the framework matrix is typically an organic

polymer, such as bacterial cellulose, gelatin, *etc*.[31-33] Additionally, organic solvents and water are used to facilitate ion migration and gel swelling.[34-35] However, a major drawback arising from this is instability, specifically the non-uniformity of solvents over an extended period. For instance, in unsealed ion gel/water gel-based ionic thermoelectric materials, both flexibility and thermoelectric performance (particularly σ) may experience degradation within several hours.[23, 36-38] Moreover, the larger volume and higher transfer entropy of ion carriers can also lead to a decrease in σ.[26] With some recent advancements in ionic thermoelectric research, several preliminary strategies have been developed to overcome this challenge. For example, a ternary hybrid of poly(2-acrylamido-2-methyl-1-propanesulfonic acid) (PAAMPSA)/phytic acid (PA)/polyaniline (PANI) exhibited excellent σ of 256.0 mS cm^{-1} at 90 % relative humidity.[27] By combining the ion conductivity of PAAMPSA/PA with the electronic conductivity of PANI, σ was improved by 33 % compared to the original PAAMPSA/PA. However, most strategies aimed at promoting ion concentration/mobility still remain highly sensitive to humidity or solvent composition. The acid gradient of PA is also limited in the fabrication of electronic skin devices.

Carbon-based materials exhibit significant potential in the field of flexible thermoelectrics.[39] They possess high intrinsic σ, which theoretically can compensate for the lower σ of ionic thermoelectric materials.[40-41] However, achieving uniform dispersion of inorganic carbon-based particles within organic-based ionic thermoelectric materials is still challenging.[42-44] Therefore, one of the aims is to achieve a continuous carbon phase to improve the overall σ, which is difficult to accomplish with particle-level dispersion.[45-46] However, because water may be an essential component of the ionic thermoelectric system, we have noticed that graphene oxide (GO) exhibits high water solubility.[47-48] Although the intrinsic σ of GO (a few mS cm^{-1}) is not as high as graphene and carbon nanotubes, it still falls within the same magnitude as that of ionic thermoelectric materials.[49-50] This provides a new approach for designing ionic thermoelectric materials with high stability and high thermoelectric performance.

Therefore, in this work, we developed a GO-blended polyacrylamide (PAM) ionic thermoelectric thin film that simultaneously exhibits high stability, competitive thermoelectric performance, and excellent flexibility. **Figure 1a** illustrates the fabrication process of the film, from which the raw materials include acrylamide (AM), 1-butyl-3-methylimidazolium chloride (BMIM:Cl), initiator ammonium persulfate (APS), and crosslinker N,N'-methylenebisacrylamide (MBA) in a mixed solution. The initiator is crucial for the dispersion of GO, while the crosslinker is essential for the mechanical properties of the prepared film. In terms of the fabrication, we added the GO solution to the pre-prepared solution and subjected it to ultrasonic dispersion in an ice-water bath. The ice-water bath is critical for the well dispersion of GO. After the synthesis of the ion gel by free-radical polymerization at 333 K, the film material was annealed for 5 hours at 383 K, which is vital for the stability of the prepared film. The optimized film sample (PAM$_{0.3}$-BMIM:Cl$_{0.6}$-GO$_1$) achieved an outstanding S value of -76.7 mV K^{-1} and a promising ZT of 0.086 at 0 % humidity and 383 K, surpassing most reported ionic thermoelectric materials, as indicated by **Figures 1b-c**.[29, 51-58] Additionally, the as-prepared film exhibited exceptional stability even after 7 days of exposure in the air. Furthermore, the tensile strength, elongation at break, Young's modulus, toughness, and flexibility of the as-prepared film reached 219.7 kPa, 389 %, 84.1 kPa, 0.4 MJ m^{-3}, and 180° bending, respectively, ranking among the top in existing ionic thermoelectric materials.[51, 59-60] Based on its high thermoelectric and mechanical properties, we manufactured a 25×25 mm^2 flexible device with 9 legs through an integration strategy. It can generate an outstanding output voltage V of 205 mV under a small temperature difference ΔT of only 5.7 K. This design is crucial for advancing the research on ionic flexible thermoelectric materials and devices.
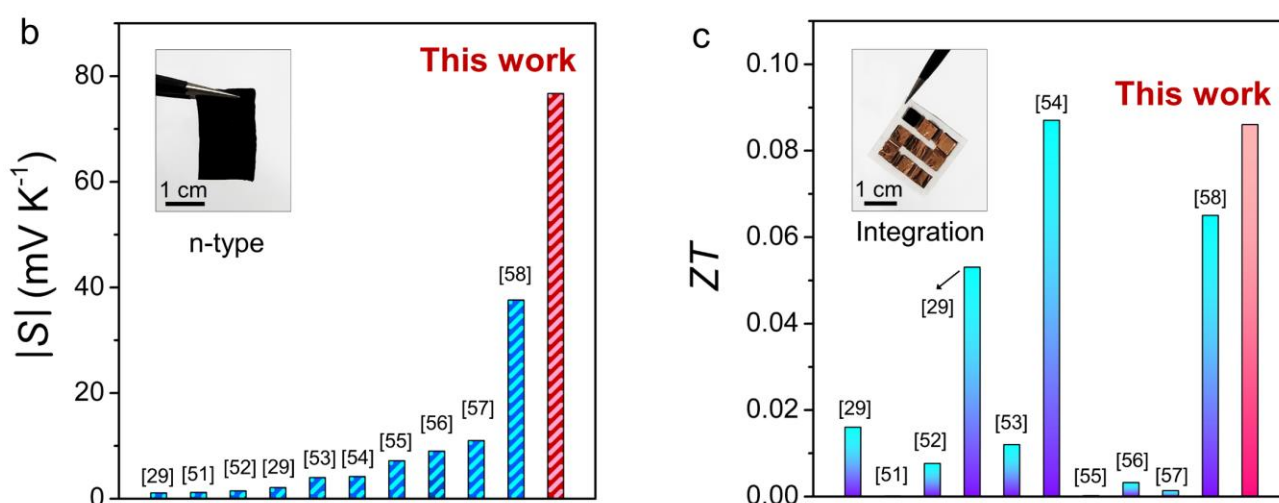
Figure 1. Illustration of the fabrication process of PAM$_{0.3}$-BMIM:Cl$_{0.6}$-GO$_x$ ionic thermoelectric films and their competitive thermoelectric performance. (**a**) Schematic diagram illustrating the raw materials, fabrication process, and components of the PAM$_{0.3}$-BMIM:Cl$_{0.6}$-GO$_x$ ionic thermoelectric film. Here PAM is abbreviated from polyacrylamide, BMIM:Cl is abbreviated from 1-butyl-3-methylimidazolium chloride, and GO is abbreviated from graphene oxide. Comparison of the optimized (**b**) Seebeck coefficient S and (**c**) dimensionless figure-of-merit ZT values between PAM$_{0.3}$-BMIM:Cl$_{0.6}$-GO$_1$ developed in this work and previously reported flexible ionic thermoelectric materials.[29, 51-58] Inserted: photos of as-prepared (**b**) PAM$_{0.3}$-BMIM:Cl$_{0.6}$-GO$_1$ film and (**c**) thermoelectric device, respectively.

2. Results and Discussion

We first analyzed the thermoelectric performance and stability of $PAM_{0.3}$-$BMIM:Cl_{0.6}$-GO_x (subscripts represent the mass ratio of PAM, BMIM:Cl, and GO) to find the optimal composition (x value). Among them, the optimal composition of $PAM_{0.3}$-$BMIM:Cl_{0.6}$ is fixed with a ratio of 1:2 (0.3:0.6) as it exhibits the best thermoelectric performance. Theoretically, the higher the proportion of the BMIM:Cl ionic liquid, the better the thermoelectric performance. However, the ratio of 1:2 ($PAM_{0.3}$-$BMIM:Cl_{0.6}$) represents an upper limit, as exceeding this ratio would make it difficult to stably incorporate a larger amount of BMIM within the film. **Figure 2a** compares room-temperature σ and S. With increasing the x value, σ was increased from 10.7 mS m^{-1} to 26.3 mS m^{-1}, and S was decreased from -33.8 mV K^{-1} to -30.1 mV K^{-1}. It has been reported that pure GO has a typical σ value of >50 mS m^{-1}.[49-50, 61] Therefore, after mixing with GO, both ions and electronic charge carriers contribute to optimized σ. Moreover, it is known that the σ of ionic thermoelectric materials is highly sensitive to humidity, and high humidity is necessary for high σ performance.[26, 62] In this work, σ testing was conducted under a high-vacuum environment, which can be considered as 0 % humidity. Therefore, achieving a σ as high as 26.3 mS m^{-1} under such conditions is highly promising. Furthermore, increasing the GO content leads to a slight decrease in S. On one hand, well-dispersed GO can slightly impede the transport of ion charge carriers; on the other hand, the interaction between GO and EMIM$^+$ plays an important role in promoting the balance of EMIM$^+$ and Cl$^-$ concentration gradients, enhancing S.[63] The slight decrease in S is likely a result of the combined effects of these two factors. Additionally, it should be noted that $PAM_{0.3}$-$BMIM:Cl_{0.6}$-GO_x is an n-type thermoelectric material. The $S^2\sigma$ results are plotted in **Figure 2b**, where it can be observed that with increasing the GO content, $S^2\sigma$ was increased. Although the increase in $S^2\sigma$ becomes slower after the GO content reaches 0.8, the optimal value is still achieved with $PAM_{0.3}$-$BMIM:Cl_{0.6}$-GO_1, corresponding to 23.8 μW m^{-1} K^{-2}.

In the preparation process of $PAM_{0.3}$-$BMIM:Cl_{0.6}$-GO_x, we employed an annealing process to remove uneven H_2O components and validate its stability. To assess the efficiency, we compared the

σ, S, and $S^2\sigma$ of the non-annealed film, the annealed film (final product of this work), the self-healed film (defined as cutting the annealed $PAM_{0.3}$-$BMIM{:}Cl_{0.6}$-GO_1 film into two pieces and separating from each other, and reattaching the two pieces again by the self-adhesivity at room temperature), and the annealed film left in the air for 7 days, as shown in **Figures 2c-d**. Preliminarily, it can be observed that the annealing process resulted in a decrease in σ but an increase in S and in turn an increase in $S^2\sigma$ for the as-prepared $PAM_{0.3}$-$BMIM{:}Cl_{0.6}$-GO_1. However, the high σ of non-annealed $PAM_{0.3}$-$BMIM{:}Cl_{0.6}$-GO_1 most originated from the $BMIM{:}Cl$ dissolved in H_2O. Additionally, the thermoelectric performance of the as-prepared $PAM_{0.3}$-$BMIM{:}Cl_{0.6}$-GO_1 was highly stable. Long-term stability remains one of the key challenges for quasi-solid-state (hydrogel and ionogel) thermoelectric materials.[64-65] After self-healing, the $S^2\sigma$ was changed from 23.8 µW m^{-1} K^{-2} to 27.8 µW m^{-1} K^{-2}, and after being placed in the air for 7 days, the $S^2\sigma$ remained at 24.0 µW m^{-1} K^{-2}. Such performance was well-maintained, which holds significant importance for the practical application of ionic thermoelectric materials and devices.

To validate the thermal stability of the as-prepared $PAM_{0.3}$-$BMIM{:}Cl_{0.6}$-GO_1, we performed thermogravimetric analysis (TGA) and differential scanning calorimetry (DSC) tests, and the results are shown in **Figures 2e-f**. **Figure 2e** reveals three stages of mass loss: firstly, water (H_2O) evaporated in the temperature range of 300~480 K; secondly, $BMIM{:}Cl$ evaporated in the range of 530~620 K; and finally, the degradation of $PAM_{0.3}$-$BMIM{:}Cl_{0.6}$-GO_1 ionogel started at around 650~750 K. Since the sample was annealed at 383 K for 5 hours, the H_2O component should be saturated absorption from the air, accounting for 21 wt.%. For comparison, the TGA curve of non-annealed $PAM_{0.3}$-$BMIM{:}Cl_{0.6}$-GO_1 is shown in **Figure S1**, where the H_2O proportion was increased to 48 wt.%. However, the absorption of H_2O in the air is inevitable for the hydrophilic PAM component, and theoretically, it would not affect the high-vacuum thermoelectric performance discussed in this work. In **Figure 2f**, the DSC curve of $PAM_{0.3}$-$BMIM{:}Cl_{0.6}$-GO_1 displays the glass transition temperature T_g of the PAM component to be ~418 K. Furthermore, the irregular exothermic peak after 520 K is attributed to the

evaporation of BMIM:Cl, consistent with the second mass loss observed in **Figure 2e**.

Considering the study of the temperature resistance of the ionic thermoelectric thin film and its potential application in high-temperature scenarios, we investigated the thermoelectric performance of the as-prepared $PAM_{0.3}$-$BMIM:Cl_{0.6}$-GO_1 in the temperature range of 298-383 K, as shown in **Figures 2g-i**. Before 353 K, with increasing the temperature, σ was decreased while S was increased, as depicted in **Figure 2g**. However, when the temperature reaches 383 K, both σ and S were increased due to the enhanced charge carrier mobility conferred by the PAM in the near-elastic state. Additionally, polymer-based ionogel materials typically exhibit low κ.[26] Moreover, the annealing process reduces the liquid content of the as-prepared $PAM_{0.3}$-$BMIM:Cl_{0.6}$-GO_1, limiting convective heat transfer. As a result, the κ value ranges from 0.33 to 0.42 W m^{-1} K^{-1} in the temperature range of 298~383 K. Consequently, the $S^2\sigma$ of the prepared $PAM_{0.3}$-$BMIM:Cl_{0.6}$-GO_1 reaches 85.9 μW m^{-1} K^{-2} at 383 K with a ZT of 0.086. Such temperatures can be widely obtained from industrial circulating cooling water in practical applications.
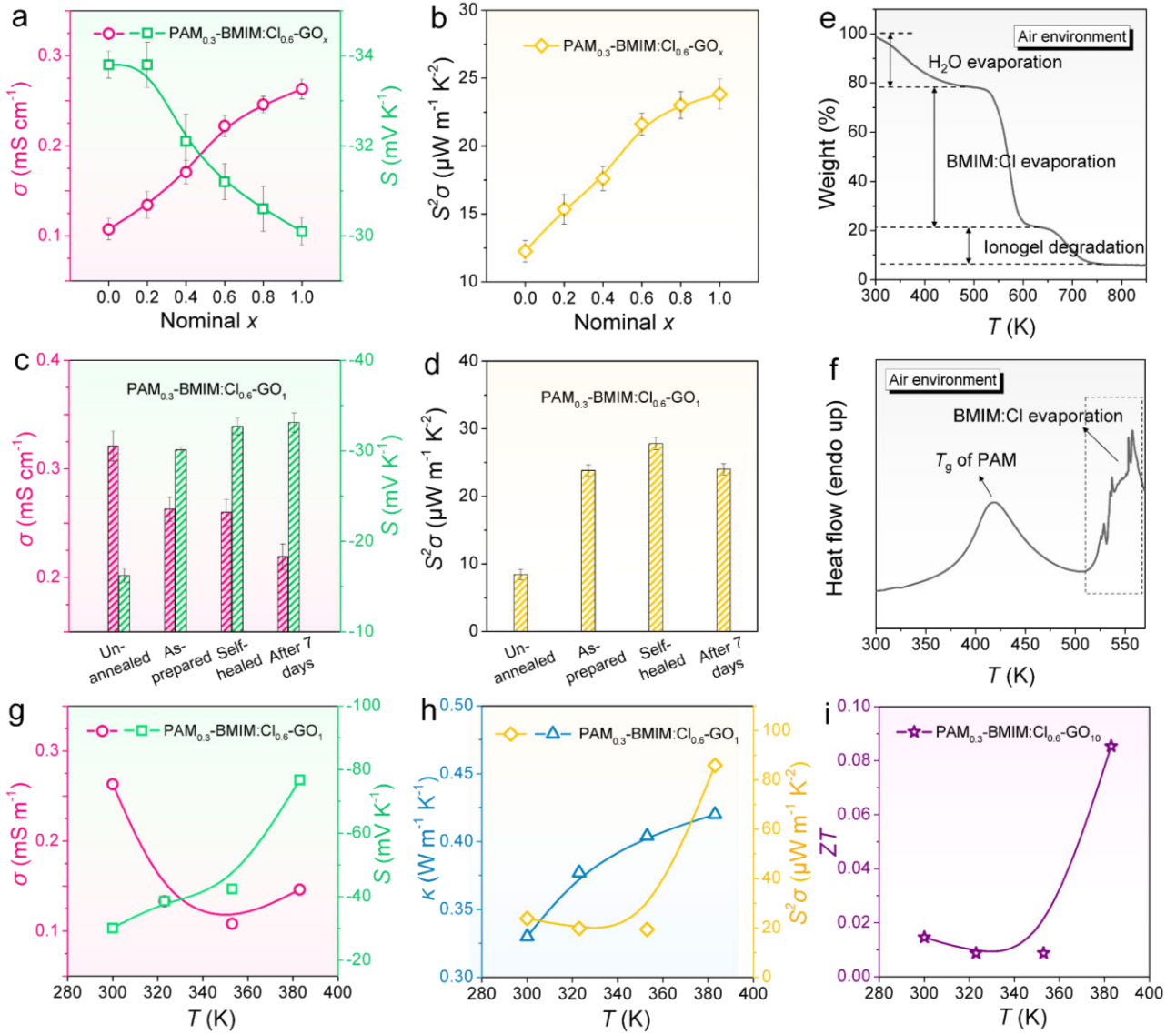
Figure 2. Thermoelectric performance and stability of PAM$_{0.3}$-BMIM:Cl$_{0.6}$-GO$_x$ films with different x values and working temperatures. Room-temperature (**a**) electrical conductivity σ and S, and (**b**) power factor $S^2\sigma$ of PAM$_{0.3}$-BMIM:Cl$_{0.6}$-GO$_x$ ($x = 0$, 0.2, 0.4, 0.6, 0.8, and 1). Room-temperature (**c**) σ and S, and (**d**) $S^2\sigma$ of PAM$_{0.3}$-BMIM:Cl$_{0.6}$-GO$_1$ films for unannealed, as-prepared, self-healed, and 7-days exposed in the air. (**e**) Thermogravimetric analysis (TGA) and (**f**) differential scanning calorimetry (DSC) curves of PAM$_{0.3}$-BMIM:Cl$_{0.6}$-GO$_1$ film in the air environment. Temperature-dependent (298~383 K) (**g**) σ and S, (**h**) $S^2\sigma$ and thermal conductivity κ, and (**i**) ZT of PAM$_{0.3}$-BMIM:Cl$_{0.6}$-GO$_1$.

Since $PAM_{0.3}$-$BMIM:Cl_{0.6}$-GO_x is a ternary hybrid material, we utilized Fourier-transform infrared reflectance (FT-IR), X-ray diffraction (XRD), Raman spectroscopy, and X-ray photoelectron spectroscopy (XPS) to study the different components within the film and their interactions. During the preparation process, PAM was synthesized *via* free-radical polymerization at 333 K (**Figure 1a**). To validate the polymerization efficiency, the FT-IR results of the original GO, $PAM_{0.3}$-$BMIM:Cl_{0.6}$ film, $PAM_{0.3}$-$BMIM:Cl_{0.6}$-$GO_{0.4}$ film, annealed $PAM_{0.3}$-$BMIM:Cl_{0.6}$-GO_1 film (final product in this work), and non-annealed $PAM_{0.3}$-$BMIM:Cl_{0.6}$-GO_1 film are shown in **Figure 3a**. From the spectra, the four film samples exhibit similar peak characteristics, consistent with typical PAM spectra. The single peaks observed around 3360 cm^{-1} and 1660 cm^{-1} can be attributed to the stretching vibrations of N-H and C=O in PAM.[66] Besides, peaks at 1570 cm^{-1} and 1455 cm^{-1} are attributed to the stretching vibrations of C=N and bending vibration of C=H from BMIM:Cl components.[67] Therefore, the introduction of BMIM:Cl and GO did not disrupt the synthesis of PAM. Additionally, the structure of BMIM:Cl in the ternary hybrid $PAM_{0.3}$-$BMIM:Cl_{0.6}$-GO_x remained intact. Here, with the addition of GO, a new peak appeared at 2140 cm^{-1}. This is likely attributed to the conjugation effect between the imidazole ring and GO.[68-69]

Due to the extremely low content of pure GO (*e.g.*, ~0.22 wt.% relative to the total mass of $PAM_{0.3}$-$BMIM:Cl_{0.6}$-GO_1), we employed XRD to characterize the state of GO. As shown in **Figure 3b**, the original GO, $PAM_{0.3}$-$BMIM:Cl_{0.6}$-$GO_{0.4}$, and annealed $PAM_{0.3}$-$BMIM:Cl_{0.6}$-GO_1 exhibit broad peaks at around 16.8°, while the original $PAM_{0.3}$-$BMIM:Cl_{0.6}$ as an amorphous polymer material does not show any distinct crystalline peaks.[70] The consistent peak positions of the original GO, $PAM_{0.3}$-$BMIM:Cl_{0.6}$-$GO_{0.4}$, and annealed $PAM_{0.3}$-$BMIM:Cl_{0.6}$-GO_1 indicate good preservation of the hybridized crystalline phase and interlayer spacing. Interestingly, the characteristic peaks related to GO diffraction disappear in the non-annealed $PAM_{0.3}$-$BMIM:Cl_{0.6}$-GO_1, suggesting that the presence of H_2O impedes the crystallinity of GO. This is further supported by the Raman spectra shown in **Figure 3c**, where the appearance of the characteristic G and D bands with increasing GO content

indicates a physical blending.[71-72] However, Raman absorption is blocked by highly flowable H_2O regarding unannealed $PAM_{0.3}$-BMIM:$Cl_{0.6}$-GO_1.

To investigate the elemental composition and valency states, the XPS spectra are shown in **Figure 3d−f**. According to the peaks of Cl2s (194.0 eV) and Cl2p (264.9 eV) (**Figure 3d** and **Table S1**),[73-74] the BMIM:Cl components are successfully introduced into the as-prepared $PAM_{0.3}$-BMIM:$Cl_{0.6}$-GO_x. However, despite the fact that the binding energy of Cl2p keeps constant for $PAM_{0.3}$-BMIM:$Cl_{0.6}$ and as-prepared $PAM_{0.3}$-BMIM:$Cl_{0.6}$-GO_1 (**Figure 3e**), a blue shift phenomenon can be observed for the N1s peak of $PAM_{0.3}$-BMIM:$Cl_{0.6}$-GO_1 compared with $PAM_{0.3}$-BMIM:$Cl_{0.6}$ (**Figure 3f**).[75] Considering that the Cl element is only presented in the BMIM:Cl component and the N element is presented in both the PAM and BMIM:Cl components, it can be confirmed that there is a binding interaction between GO and both BMIM$^+$ and PAM amino groups. Additionally, the presence of N in the original GO film is attributed to the oxygen functional groups.
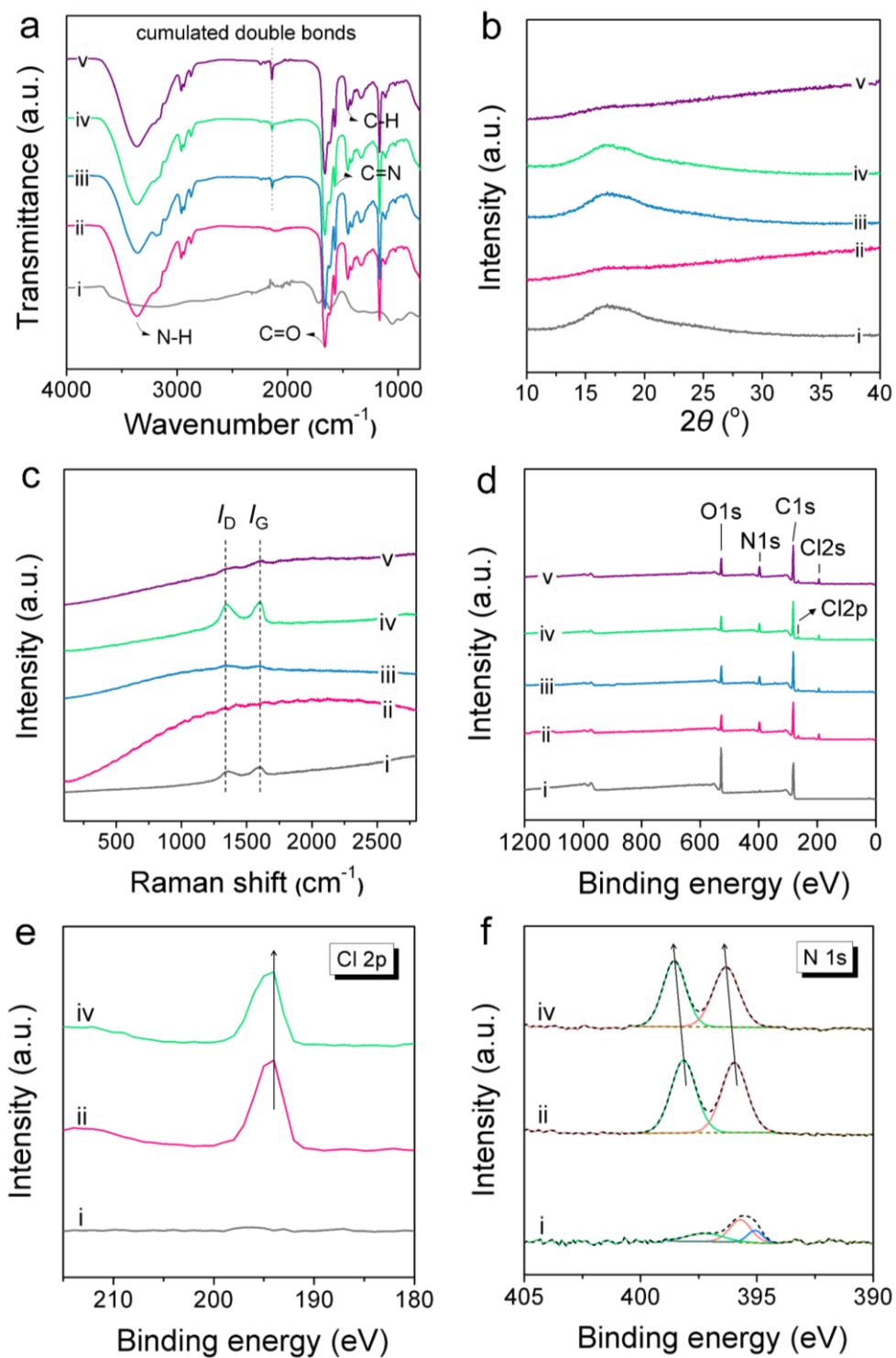
Figure 3. Characterizations of structure and atom binding information of i) pristine GO, ii) PAM$_{0.3}$-BMIM:Cl$_{0.6}$, iii) PAM$_{0.3}$-BMIM:Cl$_{0.6}$-GO$_{0.4}$, iv) annealed PAM$_{0.3}$-BMIM:Cl$_{0.6}$-GO$_1$ (final product in this work), and v) unannealed PAM$_{0.3}$-BMIM:Cl$_{0.6}$-GO$_1$. (**a**) Attenuated total reflectance Fourier transform infrared reflection (ATR-FTIR) spectra. (**b**) X-ray diffraction (XRD)

110

pattern. (**c**) Raman pattern. (**d**) X-ray photoelectron spectroscopy (XPS) patterns with broad range. (**e**) Corresponding magnified Cl2p patterns. (**f**) Corresponding magnified N1s patterns.

To assess the dispersion of GO, we conducted scanning electron microscopy (SEM) and energy-dispersive X-ray spectroscopy (EDS) tests, and the results are presented in **Figure 4**. Due to the annealing process, the surface of the $PAM_{0.3}$-$BMIM:Cl_{0.6}$-GO_1 film exhibits uniform micro-wrinkles (**Figure 4a**). However, the width of the wrinkles is approximately 1 μm (**Figure 4b**), which is sufficiently narrow and does not affect the overall morphology of the film. Furthermore, the backscattered electron (BSE) imaging mode shown in **Figure 4c** confirms the uniform dispersion of the PAM, BMIM:Cl, and GO components.[76-77] The EDS results in **Figures 4d-e** demonstrate the uniform distribution of C, N, O, and Cl elements. The elemental spectrum in **Figure 4f** provides the specific ratios of N, O, and Cl (Pt is the coating material used for SEM sample preparation). For comparison, the corresponding elemental mapping and ratio information of the film after 7 days are shown in **Figure S2**. The uniform elemental distribution and unchanged elemental ratios confirm the exceptional stability of the prepared $PAM_{0.3}$-$BMIM:Cl_{0.6}$-GO_1 film.
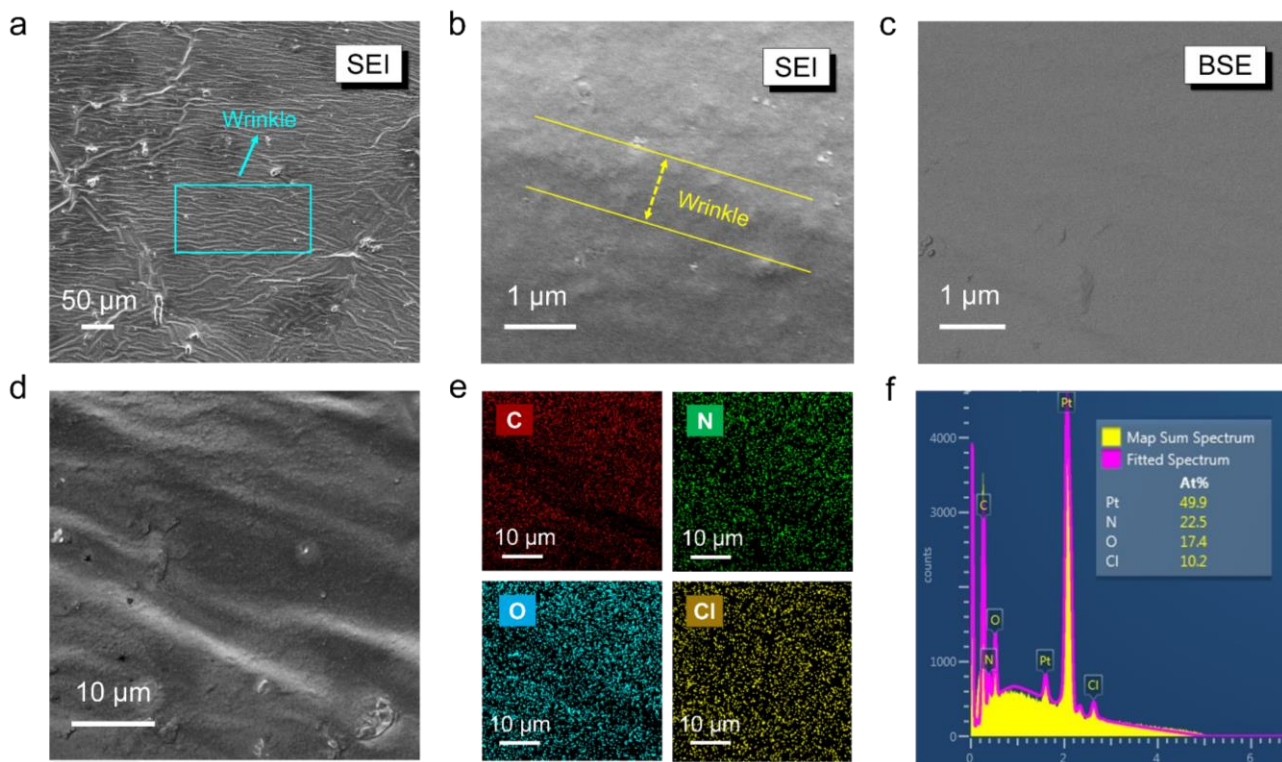
Figure 4. Characterizations of surface morphology and element distributions of as-prepared PAM$_{0.3}$-BMIM:Cl$_{0.6}$-GO$_1$ film. Scanning electron microscopy (SEM) images of PAM$_{0.3}$-BMIM:Cl$_{0.6}$-GO$_1$ with (**a**) low- and (**b**) high-magnification secondary electron imaging (SEI) modes, (**c**) high-magnification backscattered electron imaging (BSE) mode. (**d**) SEM image, (**e**) corresponding X-ray spectroscopy (EDS) mapping images for C, N, O, and Cl elements, and (**f**) corresponding EDS element spectra of a random area of PAM$_{0.3}$-BMIM:Cl$_{0.6}$-GO$_1$.

The mechanical properties, especially flexibility, are crucial for the practical applications of thermoelectric films. To study the mechanical performance, the tensile curves of the PAM$_{0.3}$-BMIM:Cl$_{0.6}$-GO$_1$ film before and after annealing are shown in **Figure 5a**. Compared to the non-annealed film, the annealed film as the final product exhibits a 103 % increase in tensile strength, while the fracture elongation remains nearly unchanged. The inset demonstrates that a lemon weighing 1.2 N can be supported by the film with a dimension of 20×5×1 mm³. Furthermore, we conducted repeated tensile tests for 5 cycles using recovered fractured film segments (randomly selected from fractured

112

samples). As shown in **Figure 5b**, with increasing test cycles, although the tensile performance was decreased, the prepared film still demonstrates potential for repeated use. Overall, the mechanical properties of the film, including 219.7 kPa tensile strength, 389 % fracture elongation, 84.1 kPa Young's modulus, 0.4 MJ m^{-3} toughness, and 180° bending angle, are all highly competitive among reported ionic thermoelectric films (**Figure 5c** and **Table S2**).[51, 59-60] The photographs of the original, curled, and stretched $PAM_{0.3}$-$BMIM:Cl_{0.6}$-GO_1 film in the air (**Figure 5d**) and on the ice (**Figure 5e**) provide visual evidence of the high flexibility. Additionally, our film exhibits suitable self-adhesiveness. After bonding, plastics, metals, and wood can be suspended using a film measuring $20\times5\times1$ mm³ under a load of 500 N (**Figure 5f**). The self-adhesive property is highly advantageous for device fabrication as electrode materials can be directly adhered to the film.
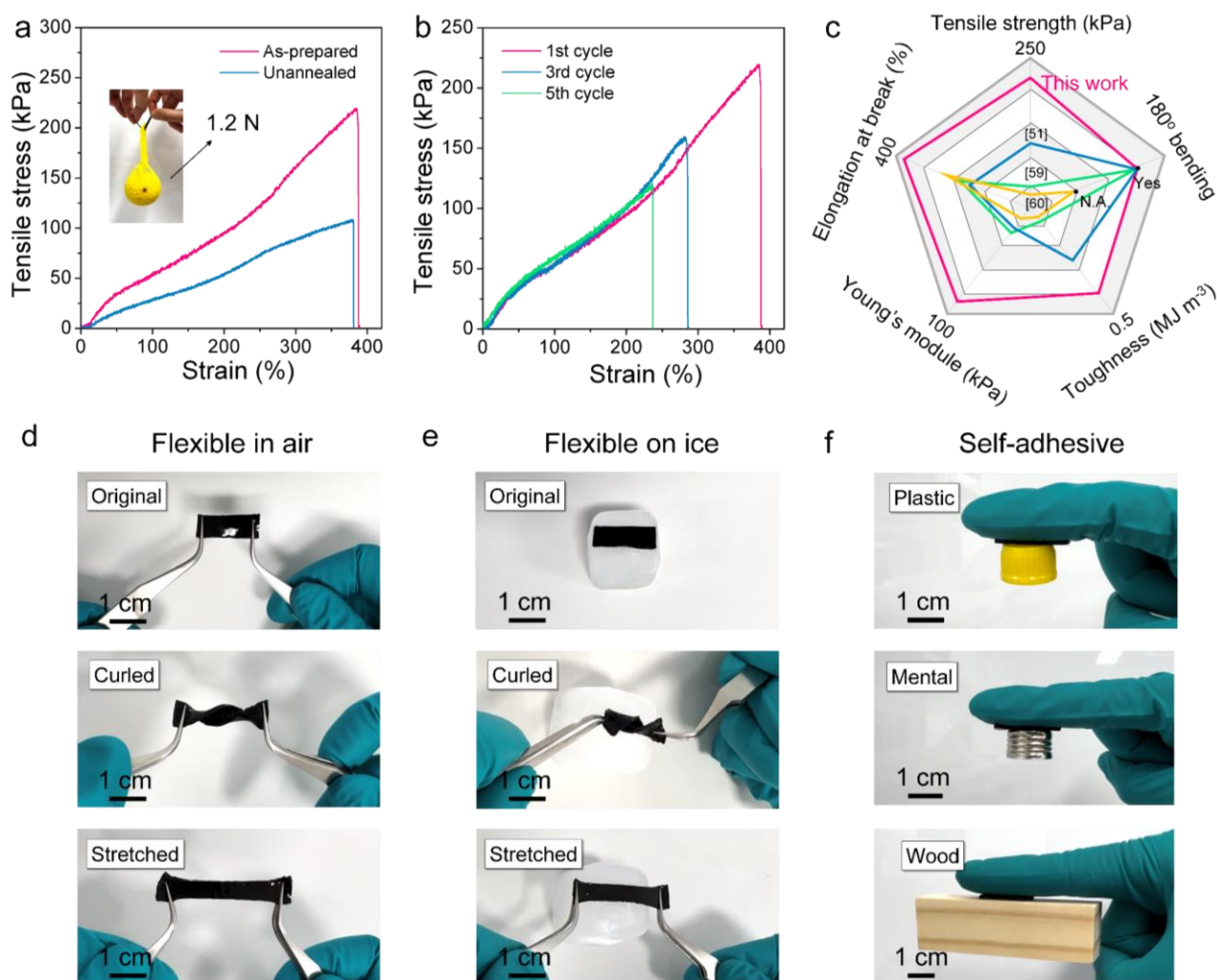
Figure 5. Characterizations of mechanical properties and flexibilities of PAM$_{0.3}$-BMIM:Cl$_{0.6}$-GO$_1$ films. Tensile curves of (**a**) as-prepared and unannealed PAM$_{0.3}$-BMIM:Cl$_{0.6}$-GO$_1$ films, the inserted image shows a $20 \times 5 \times 1$ mm^3 film (as-prepared PAM$_{0.3}$-BMIM:Cl$_{0.6}$-GO$_1$) lifting a 1.2 N weighted lemon, (**b**) as-prepared PAM$_{0.3}$-BMIM:Cl$_{0.6}$-GO$_1$ films at the 1st, 3rd, and 5th testing cycle, respectively. (**c**) Comparison of the tensile strength, elongation at break, Young's module, toughness, and 180° bending angle between as-prepared PAM$_{0.3}$-BMIM:Cl$_{0.6}$-GO$_1$ film and reported ionic thermoelectric films reported in literature.[51, 59-60] Images showing the original, curled, and stretched state of as-prepared PAM$_{0.3}$-BMIM:Cl$_{0.6}$-GO$_1$ film (**d**) in the air and (**e**) on the ice. (**f**) Images showing the self-adhesivity of PAM$_{0.3}$-BMIM:Cl$_{0.6}$-GO$_1$ film slinging plastic, metal, and wood under 500 N.

Based on the high thermoelectric performance, flexibility, stability, self-healing, and self-adhesive features of the as-prepared PAM$_{0.3}$-BMIM:Cl$_{0.6}$-GO$_1$ film, we devised a method for integrating small-sized flexible thermoelectric devices. As shown in **Figure 6a**, a liquid mixed solution containing AM, BMIM:Cl, GO, initiator, and cross-linker was dispensed onto a 1 mm-thick custom-made organosilicon film. After curing and annealing processes, a 9-leg device was integrated. Subsequently, copper foil electrodes were directly adhered to the surface of PAM$_{0.3}$-BMIM:Cl$_{0.6}$-GO$_1$ through end-to-end connections. Finally, two pieces of polyimide tape were used as encapsulation layers, resulting in a π-shaped flexible thermoelectric device.[78] The fabricated flexible device is semi-transparent (**Figure 6b**), and the overall device size (25×25 millimeters) has been miniaturized to approach the size of a coin (**Figure 6c**). During the device application process, a heat plate is used to provide a thermal source at ~383 K, this is because the optimized thermoelectric performance is located at this temperature, as shown in **Figure 2i**. Once the heat plate temperature was determined, we placed the pre-connected device on it. After stabilization, the cold-side temperature (359.3 K) and hot-side temperature (365 K) of the device are confirmed using an infrared thermal camera, as shown in **Figure 6d.** As a result, an output voltage V of 205 mV can be generated with a temperature difference ΔT of

5.7 K. This level of performance is suitable for low-grade wearable microgenerators and electronic skin applications.
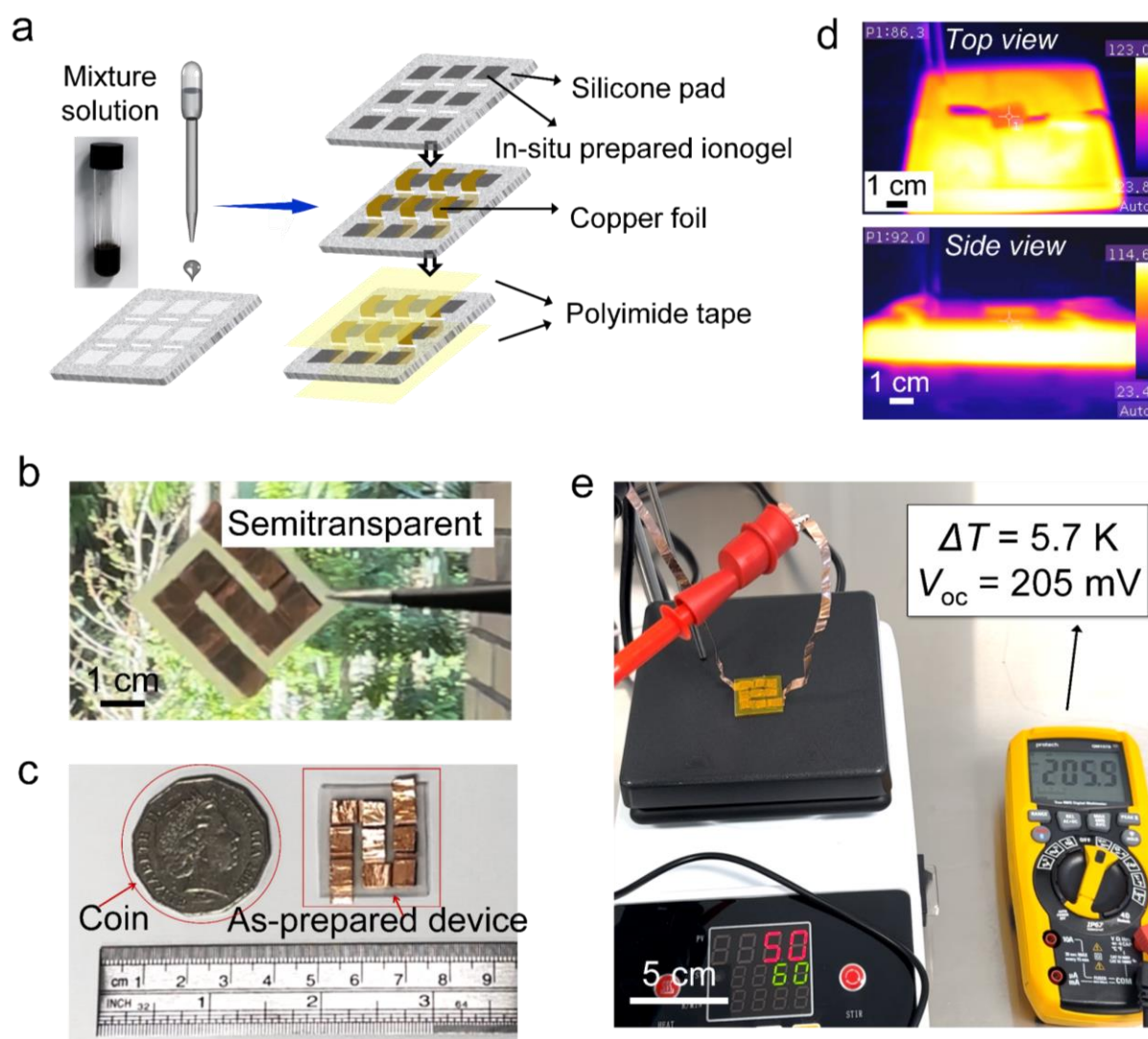
Figure 6. Preparation and the output performance of PAM$_{0.3}$-BMIM:Cl$_{0.6}$-GO$_1$ based thermoelectric device. (**a**) Schematic diagram of the integration, physical connection, and structure of the device. (**b**) Photo of the connected 9-leg 25×25 mm^2 flexible device and its semitransparent outlook. (**c**) Photo compared the miniaturized size of the prepared device and a coin. (**d**) Infrared thermal images of the device applied on a heated plate showing the top-site temperature of 359.3 K (top) and the bottom-site temperature 365 K (bottom) of the device. The images were taken after temperature stabilizations. (**e**) Images showing the corresponding output voltage V of 205 mV of the device where the temperature difference ΔT is 5.7 K.

3. Conclusion

In this study, we successfully develop a novel ionic thermoelectric film with high flexibility, high stability, and high thermoelectric performance, composed of carbon-based materials (RO), ionic liquid, and cross-linked polymer. The film exhibits excellent thermoelectric properties at 383 K, with a S value of -76.7 mV K^{-1}, $S^2\sigma$ value of 85.9 μW m^{-1} K^{-2}, and ZT value of 0.086, which are highly competitive compared to existing ion thermoelectric materials. Additionally, the film demonstrates outstanding mechanical properties, including a tensile strength of 219.7 kPa, elongation at break of 389 %, Young's modulus of 84.1 kPa, toughness of 0.4 MJ m^{-3}, and flexibility to bend at 180°. Importantly, the film maintains its excellent thermoelectric and mechanical performance even after being placed in the air for 7 days. Based on these remarkable properties, we successfully fabricate a miniature 9-legged flexible thermoelectric device with dimensions of 25×25 mm^2, achieving a high V of 205 mV at a low ΔT of only 5.7 K. This work provides a promising and novel approach for the long-term design of high-performance ion thermoelectric materials and easily integrable flexible devices.

4. Experimental Section

The experimental details are provided in the Supporting Information.

Asadi for providing help to accomplish this work.

Appendix A. Supplementary material

Supplementary data associated with this article can be found in the online version at XXXX.

References

(1) Shi, X.; Chen, L. Thermoelectric Materials Step Up. *Nat. Mater.* **2016**, *15*, 691-692.

(2) Xiao, Y.; Zhao, L.-D. Seeking New, Highly Effective Thermoelectrics. *Science* **2020**, *367*, 1196.

(3) Roychowdhury, S.; Ghosh, T.; Arora, R.; Samanta, M.; Xie, L.; Singh Niraj, K.; Soni, A.; He, J.; Waghmare Umesh, V.; Biswas, K. Enhanced atomic ordering leads to high thermoelectric performance in AgSbTe$_2$. *Science* **2021**, *371*, 722-727.

(4) Yang, Q.; Yang, S.; Qiu, P.; Peng, L.; Wei, T.-R.; Zhang, Z.; Shi, X.; Chen, L. Flexible thermoelectrics based on ductile semiconductors. *Science* **2022**, *377*, 854-858.

(5) Han, W. B.; Heo, S.-Y.; Kim, D.; Yang, S. M.; Ko, G.-J.; Lee, G. J.; Kim, D.-J.; Rajaram, K.; Lee, J. H.; Shin, J.-W.; Jang, T.-M.; Han, S.; Kang, H.; Lim, J. H.; Kim, D. H.; Kim, S. H.; Song, Y. M.; Hwang, S.-W. Zebra-inspired stretchable, biodegradable radiation modulator for all-day sustainable energy harvesters. *Sci. Adv. 9*, eadf5883.

(6) Soleimani, Z.; Zoras, S.; Ceranic, B.; Cui, Y.; Shahzad, S. A comprehensive review on the output voltage/power of wearable thermoelectric generators concerning their geometry and thermoelectric materials. *Nano Energy* **2021**, *89*, 106325.

(7) Kim, S.-W.; Kim, J.-K.; Park, J. Y.; Mun, J.; Jung, S.; Yang, S. E.; Lee, G.; Lee, P. S.; Song, H.-C.;

Yang, C.; Park, H. S.; Son, J. S.; Baik, J. M. Boosted Output Voltage of BiSbTe-Based Thermoelectric Generators *via* Coupled Effect between Thermoelectric Carriers and Triboelectric Charges. *Adv. Energy Mater.* **2023**, *13*, 2202987.

(8) Zhu, H.; He, R.; Mao, J.; Zhu, Q.; Li, C.; Sun, J.; Ren, W.; Wang, Y.; Liu, Z.; Tang, Z.; Sotnikov, A.; Wang, Z.; Broido, D.; Singh, D. J.; Chen, G.; Nielsch, K.; Ren, Z. Discovery of ZrCoBi based half Heuslers with high thermoelectric conversion efficiency. *Nat. Commun.* **2018**, *9*, 2497.

(9) Shi, X.-L.; Zou, J.; Chen, Z.-G. Advanced Thermoelectric Design: From Materials and Structures to Devices. *Chem. Rev.* **2020**, *120*, 7399-7515.

(10) Sui, J.; Li, J.; He, J.; Pei, Y.-L.; Berardan, D.; Wu, H.; Dragoe, N.; Cai, W.; Zhao, L.-D. Texturation Boosts the Thermoelectric Performance of BiCuSeO Oxyselenides. *Energy Environ. Sci.* **2013**, *6*, 2916-2920.

(11) Burton, M. R.; Mehraban, S.; Beynon, D.; McGettrick, J.; Watson, T.; Lavery, N. P.; Carnie, M. J. 3D Printed SnSe Thermoelectric Generators with High Figure of Merit. *Adv. Energy Mater.* **2019**, *9*, 1900201.

(12) Hasan, M. N.; Nafea, M.; Nayan, N.; Mohamed Ali, M. S. Thermoelectric Generator: Materials and Applications in Wearable Health Monitoring Sensors and Internet of Things Devices. *Adv. Mater. Technol.* **2022**, *7*, 2101203.

(13) Wang, Y.; Yang, L.; Shi, X.; Shi, X.; Chen, L.; Dargusch, M.; Zou, J.; Chen, Z.-G. Flexible Thermoelectric Materials and Generators: Challenges and Innovations. *Adv. Mater.* **2019**, *31*, 1807916.

(14) Cao, T.; Shi, X.-L.; Chen, Z.-G. Advances in the design and assembly of flexible thermoelectric device. *Prog. Mater. Sci.* **2023**, *131*, 101003.

(15) Blackburn, J. L.; Ferguson, A. J.; Cho, C.; Grunlan, J. C. Carbon-Nanotube-Based Thermoelectric

Materials and Devices. *Adv. Mater.* **2018**, *30*, 1704386.

(16) Meng, C.; Liu, C.; Fan, S. A Promising Approach to Enhanced Thermoelectric Properties Using Carbon Nanotube Networks. *Adv. Mater.* **2010**, *22*, 535-539.

(17) Komatsu, N.; Ichinose, Y.; Dewey, O. S.; Taylor, L. W.; Trafford, M. A.; Yomogida, Y.; Wehmeyer, G.; Pasquali, M.; Yanagi, K.; Kono, J. Macroscopic weavable fibers of carbon nanotubes with giant thermoelectric power factor. *Nat. Commun.* **2021**, *12*, 4931.

(18) Yusupov, K.; Vomiero, A. Polymer-Based Low-Temperature Thermoelectric Composites. *Adv. Funct. Mater.* **2020**, *30*, 2002015.

(19) Bounioux, C.; Díaz-Chao, P.; Campoy-Quiles, M.; Martín-González, M. S.; Goñi, A. R.; Yerushalmi-Rozen, R.; Müller, C. Thermoelectric Composites of Poly(3-hexylthiophene) and Carbon Nanotubes with a Large Power Factor. *Energy Environ. Sci.* **2013**, *6*, 918-925.

(20) Wu, G.; Zhang, Z.-G.; Li, Y.; Gao, C.; Wang, X.; Chen, G. Exploring High-Performance n-Type Thermoelectric Composites Using Amino-Substituted Rylene Dimides and Carbon Nanotubes. *ACS Nano* **2017**, *11*, 5746-5752.

(21) Chen, B.; Chen, Q.; Xiao, S.; Feng, J.; Zhang, X.; Wang, T. Giant negative thermopower of ionic hydrogel by synergistic coordination and hydration interactions. *Sci. Adv. 7*, eabi7233.

(22) Chi, C.; An, M.; Qi, X.; Li, Y.; Zhang, R.; Liu, G.; Lin, C.; Huang, H.; Dang, H.; Demir, B.; Wang, Y.; Ma, W.; Huang, B.; Zhang, X. Selectively tuning ionic thermopower in all-solid-state flexible polymer composites for thermal sensing. *Nat. Commun.* **2022**, *13*, 221.

(23) Le Bideau, J.; Viau, L.; Vioux, A. Ionogels, ionic liquid based hybrid materials. *Chem. Soc. Rev.* **2011**, *40*, 907-925.

(24) Liu, Z.; Cheng, H.; He, H.; Li, J.; Ouyang, J. Significant Enhancement in the Thermoelectric

Properties of Ionogels through Solid Network Engineering. *Adv. Funct. Mater.* **2022**, *32*, 2109772.

(25) Wang, H.; Ail, U.; Gabrielsson, R.; Berggren, M.; Crispin, X. Ionic Seebeck Effect in Conducting Polymers. *Adv. Energy Mater.* **2015**, *5*, 1500044.

(26) Sun, S.; Li, M.; Shi, X.-L.; Chen, Z.-G. Advances in Ionic Thermoelectrics: From Materials to Devices. *Adv. Energy Mater.* **2023**, *13*, 2203692.

(27) Akbar, Z. A.; Jeon, J.-W.; Jang, S.-Y. Intrinsically self-healable, stretchable thermoelectric materials with a large ionic Seebeck effect. *Energy Environ. Sci.* **2020**, *13*, 2915-2923.

(28) Lei, Z.; Gao, W.; Wu, P. Double-network thermocells with extraordinary toughness and boosted power density for continuous heat harvesting. *Joule* **2021**, *5*, 2211-2222.

(29) Chang, W. B.; Evans, C. M.; Popere, B. C.; Russ, B. M.; Liu, J.; Newman, J.; Segalman, R. A. Harvesting Waste Heat in Unipolar Ion Conducting Polymers. *ACS Macro Letters* **2016**, *5*, 94-98.

(30) Fang, Y.; Cheng, H.; He, H.; Wang, S.; Li, J.; Yue, S.; Zhang, L.; Du, Z.; Ouyang, J. Stretchable and Transparent Ionogels with High Thermoelectric Properties. *Adv. Funct. Mater.* **2020**, *30*, 2004699.

(31) Li, T.; Zhang, X.; Lacey, S. D.; Mi, R.; Zhao, X.; Jiang, F.; Song, J.; Liu, Z.; Chen, G.; Dai, J.; Yao, Y.; Das, S.; Yang, R.; Briber, R. M.; Hu, L. Cellulose ionic conductors with high differential thermal voltage for low-grade heat harvesting. *Nat. Mater.* **2019**, *18*, 608-613.

(32) Cheng, H.; He, X.; Fan, Z.; Ouyang, J. Flexible Quasi-Solid State Ionogels with Remarkable Seebeck Coefficient and High Thermoelectric Properties. *Adv. Energy Mater.* **2019**, *9*, 1901085.

(33) Han, C.-G.; Qian, X.; Li, Q.; Deng, B.; Zhu, Y.; Han, Z.; Zhang, W.; Wang, W.; Feng, S.-P.; Chen, G.; Liu, W. Giant Thermopower of Ionic Gelatin near Room Temperature. *Science* **2020**, *368*, 1091-1098.

(34) Zhu, T.; Jiang, C.; Wang, M.; Zhu, C.; Zhao, N.; Xu, J. Skin-Inspired Double-Hydrophobic-

Coating Encapsulated Hydrogels with Enhanced Water Retention Capacity. *Adv. Funct. Mater.* **2021**, *31*, 2102433.

(35) Kee, S.; Haque, M. A.; Corzo, D.; Alshareef, H. N.; Baran, D. Self-Healing and Stretchable 3D-Printed Organic Thermoelectrics. *Adv. Funct. Mater.* **2019**, *29*, 1905426.

(36) Luo, Z.; Li, W.; Yan, J.; Sun, J. Roles of Ionic Liquids in Adjusting Nature of Ionogels: A Mini Review. *Adv. Funct. Mater.* **2022**, *32*, 2203988.

(37) Xiao, X.; Wang, M.; Chen, S.; Zhang, Y.; Gu, H.; Deng, Y.; Yang, G.; Fei, C.; Chen, B.; Lin, Y.; Dickey, M. D.; Huang, J. Lead-adsorbing ionogel-based encapsulation for impact-resistant, stable, and lead-safe perovskite modules. *Sci. Adv.* **2021**, *7*, eabi8249.

(38) Jiao, F.; Naderi, A.; Zhao, D.; Schlueter, J.; Shahi, M.; Sundström, J.; Granberg, H.; Edberg, J.; Ail, U.; Brill, J.; Lindström, T.; Berggren, M.; Crispin, X. Ionic thermoelectric paper. *J. Mater. Chem. A* **2017**, *5*, 16883-16888.

(39) Wu, B.; Guo, Y.; Hou, C.; Zhang, Q.; Li, Y.; Wang, H. From carbon nanotubes to highly adaptive and flexible high-performance thermoelectric generators. *Nano Energy* **2021**, *89*, 106487.

(40) Choi, J.; Jung, Y.; Yang, S. J.; Oh, J. Y.; Oh, J.; Jo, K.; Son, J. G.; Moon, S. E.; Park, C. R.; Kim, H. Flexible and Robust Thermoelectric Generators Based on All-Carbon Nanotube Yarn without Metal Electrodes. *ACS Nano* **2017**, *11*, 7608-7614.

(41) Wu, G.; Gao, C.; Chen, G.; Wang, X.; Wang, H. High-performance organic thermoelectric modules based on flexible films of a novel n-type single-walled carbon nanotube. *J. Mater. Chem. A* **2016**, *4*, 14187-14193.

(42) Ducros, J. B.; Buchtová, N.; Magrez, A.; Chauvet, O.; Le Bideau, J. Ionic and electronic conductivities in carbon nanotubes – ionogel solid device. *J. Mater. Chem.* **2011**, *21*, 2508-2511.

(43) Cheng, H.; Yue, S.; Le, Q.; Qian, Q.; Ouyang, J. A mixed ion-electron conducting carbon nanotube ionogel to efficiently harvest heat from both a temperature gradient and temperature fluctuation. *J. Mater. Chem. A* **2021**, *9*, 13588-13596.

(44) Wang, Y.; Kalytchuk, S.; Zhang, Y.; Shi, H.; Kershaw, S. V.; Rogach, A. L. Thickness-Dependent Full-Color Emission Tunability in a Flexible Carbon Dot Ionogel. *J. Phys. Chem. Lett.* **2014**, *5*, 1412-1420.

(45) DeSimone, J. M.; Maury, E. E.; Menceloglu, Y. Z.; McClain, J. B.; Romack, T. J.; Combes, J. R. Dispersion Polymerizations in Supercritical Carbon Dioxide. *Science* **1994**, *265*, 356-359.

(46) Johnston, K. P.; Harrison, K. L.; Clarke, M. J.; Howdle, S. M.; Heitz, M. P.; Bright, F. V.; Carlier, C.; Randolph, T. W. Water-in-Carbon Dioxide Microemulsions: An Environment for Hydrophiles Including Proteins. *Science* **1996**, *271*, 624-626.

(47) Wang, Y.; Shi, Z.; Yin, J. Facile Synthesis of Soluble Graphene *via* a Green Reduction of Graphene Oxide in Tea Solution and Its Biocomposites. *ACS Appl. Mater. Interfaces* **2011**, *3*, 1127-1133.

(48) Si, Y.; Samulski, E. T. Synthesis of Water Soluble Graphene. *Nano Lett.* **2008**, *8*, 1679-1682.

(49) Mohan, V. B.; Brown, R.; Jayaraman, K.; Bhattacharyya, D. Characterisation of reduced graphene oxide: Effects of reduction variables on electrical conductivity. *Mat. Sci. Eng. B* **2015**, *193*, 49-60.

(50) Yousefi, N.; Gudarzi, M. M.; Zheng, Q.; Aboutalebi, S. H.; Sharif, F.; Kim, J.-K. Self-alignment and high electrical conductivity of ultralarge graphene oxide–polyurethane nanocomposites. *J. Mater. Chem.* **2012**, *22*, 12709-12717.

(51) Yang, P.; Liu, K.; Chen, Q.; Mo, X.; Zhou, Y.; Li, S.; Feng, G.; Zhou, J. Wearable Thermocells Based on Gel Electrolytes for the Utilization of Body Heat. *Angew. Chem. Int. Ed.* **2016**, *55*, 12050-12053.

(52) Gao, W.; Lei, Z.; Chen, W.; Chen, Y. Hierarchically Anisotropic Networks to Decouple Mechanical and Ionic Properties for High-Performance Quasi-Solid Thermocells. *ACS Nano* **2022**, *16*, 8347-8357.

(53) Wang, H.; Zhao, D.; Khan, Z. U.; Puzinas, S.; Jonsson, M. P.; Berggren, M.; Crispin, X. Ionic Thermoelectric Figure of Merit for Charging of Supercapacitors. *Adv. Electron. Mater.* **2017**, *3*, 1700013.

(54) Duan, J.; Feng, G.; Yu, B.; Li, J.; Chen, M.; Yang, P.; Feng, J.; Liu, K.; Zhou, J. Aqueous thermogalvanic cells with a high Seebeck coefficient for low-grade heat harvest. *Nat. Commun.* **2018**, *9*, 5146.

(55) Bonetti, M.; Nakamae, S.; Roger, M.; Guenoun, P. Huge Seebeck coefficients in nonaqueous electrolytes. *J. Chem. Phys.* **2011**, *134*, 114513.

(56) Kim, S. L.; Hsu, J.-H.; Yu, C. Intercalated graphene oxide for flexible and practically large thermoelectric voltage generation and simultaneous energy storage. *Nano Energy* **2018**, *48*, 582-589.

(57) Zhao, D.; Wang, H.; Khan, Z. U.; Chen, J. C.; Gabrielsson, R.; Jonsson, M. P.; Berggren, M.; Crispin, X. Ionic thermoelectric supercapacitors. *Energy Environ. Sci.* **2016**, *9*, 1450-1457.

(58) Li, Y.; Li, Q.; Zhang, X.; Zhang, J.; Wang, S.; Lai, L.; Zhu, K.; Liu, W. Realizing record-high output power in flexible gelatin/GTA-KCl-FeCN^{4-}/$^{3-}$ ionic thermoelectric cells enabled by extending the working temperature range. *Energy Environ. Sci.* **2022**, *15*, 5379-5390.

(59) Gao, W.; Lei, Z.; Zhang, C.; Liu, X.; Chen, Y. Stretchable and Freeze-Tolerant Organohydrogel Thermocells with Enhanced Thermoelectric Performance Continually Working at Subzero Temperatures. *Adv. Funct. Mater.* **2021**, *31*, 2104071.

(60) Wu, G.; Xue, Y.; Wang, L.; Wang, X.; Chen, G. Flexible gel-state thermoelectrochemical materials

with excellent mechanical and thermoelectric performances based on incorporating Sn^{2+}/Sn^{4+} electrolyte into polymer/carbon nanotube composites. *J. Mater. Chem. A* **2018**, *6*, 3376-3380.

(61) Xu, Z.; Bando, Y.; Liu, L.; Wang, W.; Bai, X.; Golberg, D. Electrical Conductivity, Chemistry, and Bonding Alternations under Graphene Oxide to Graphene Transition As Revealed by *In Situ* TEM. *ACS Nano* **2011**, *5*, 4401-4406.

(62) Sohn, A.; Yu, C. Ionic transport properties and their empirical correlations for thermal-to-electrical energy conversion. *Mater. Today Phys.* **2021**, *19*, 100433.

(63) Jeong, M.; Noh, J.; Islam, M. Z.; Kim, K.; Sohn, A.; Kim, W.; Yu, C. Embedding Aligned Graphene Oxides in Polyelectrolytes to Facilitate Thermo-Diffusion of Protons for High Ionic Thermoelectric Figure-of-Merit. *Adv. Funct. Mater.* **2021**, *31*, 2011016.

(64) Liu, Y.; Wang, H.; Sherrell, P. C.; Liu, L.; Wang, Y.; Chen, J. Potentially Wearable Thermo-Electrochemical Cells for Body Heat Harvesting: From Mechanism, Materials, Strategies to Applications. *Adv. Sci.* **2021**, *8*, 2100669.

(65) Sayed, D. M.; Allam, N. K. All-solid-state, self-powered supercapacitors: State-of-the-art and future perspectives. *J. Energy Storage* **2022**, *56*, 105882.

(66) Lu, X.; Mi, Y. Characterization of the Interfacial Interaction between Polyacrylamide and Silicon Substrate by Fourier Transform Infrared Spectroscopy. *Macromolecules.* **2005**, *38*, 839-843.

(67) Zhang, X.; Zhang, G.; Huang, X.; He, J.; Bai, Y.; Zhang, L. Antifreezing and Nondrying Sensors of Ionic Hydrogels with a Double-Layer Structure for Highly Sensitive Motion Monitoring. *ACS Appl. Mater. Interfaces* **2022**, *14*, 30256-30267.

(68) He, S.; Wang, G.; Zhao, Z. Facile implantation of imidazole-ring into graphitic carbon nitride for efficient photocatalytic hydrogen production. *Catalysis Science & Technology* **2023**, *13*, 3489-3494.

(69) Lee, H.; Chae, S.; Jo, H.; Kim, S.; Kim, M.; Lee, J.; Lee, S.; Park, C. S.; Yoon, H. Graphene Functionalized with Imidazole Derivatives as Nanotransducers for Electrochemically Detecting Isothiazolinone Biocides. *ACS Appl. Nano Mater.* **2022**, *5*, 15962-15971.

(70) Krishnamoorthy, K.; Veerapandian, M.; Yun, K.; Kim, S. J. The chemical and structural analysis of graphene oxide with different degrees of oxidation. *Carbon* **2013**, *53*, 38-49.

(71) Zhao, Z.; Pu, R.; Wang, Z.; Jiang, J.; Liu, W. Identification of Ultraviolet Photoinduced Presolvated Electrons in Water as the Reducing Agent in the Photoreduction of Graphene Oxide. *J. Phys. Chem. C* **2023**, *127*, 3516-3522.

(72) Chang, D. W.; Lee, E. K.; Park, E. Y.; Yu, H.; Choi, H.-J.; Jeon, I.-Y.; Sohn, G.-J.; Shin, D.; Park, N.; Oh, J. H.; Dai, L.; Baek, J.-B. Nitrogen-Doped Graphene Nanoplatelets from Simple Solution Edge-Functionalization for n-Type Field-Effect Transistors. *J. Am. Chem. Soc.* **2013**, *135*, 8981-8988.

(73) Al-Gaashani, R.; Najjar, A.; Zakaria, Y.; Mansour, S.; Atieh, M. A. XPS and structural studies of high quality graphene oxide and reduced graphene oxide prepared by different chemical oxidation methods. *Ceram. Int.* **2019**, *45*, 14439-14448.

(74) Stobinski, L.; Lesiak, B.; Malolepszy, A.; Mazurkiewicz, M.; Mierzwa, B.; Zemek, J.; Jiricek, P.; Bieloshapka, I. Graphene oxide and reduced graphene oxide studied by the XRD, TEM and electron spectroscopy methods. *J. Electron Spectrosc* **2014**, *195*, 145-154.

(75) Zhang, Y.; He, J.; Wang, P.-N.; Chen, J.-Y.; Lu, Z.-J.; Lu, D.-R.; Guo, J.; Wang, C.-C.; Yang, W.-L. Time-Dependent Photoluminescence Blue Shift of the Quantum Dots in Living Cells: Effect of Oxidation by Singlet Oxygen. *J. Am. Chem. Soc.* **2006**, *128*, 13396-13401.

(76) Rodrigues, M. C. M.; Militzer, M. Application of the rolling ball algorithm to measure phase volume fraction from backscattered electron images. *Mater. Charact.* **2020**, *163*, 110273.

(77) Payton, E. J.; Phillips, P. J.; Mills, M. J. Semi-automated characterization of the γ′ phase in Ni-based superalloys *via* high-resolution backscatter imaging. *Mat. Sci. Eng. A* **2010**, *527*, 2684-2692.

(78) Yang, S.; Qiu, P.; Chen, L.; Shi, X. Recent Developments in Flexible Thermoelectric Devices. *Small Science* **2021**, *1*, 2100005.

6.3. Links and implications

This study has been prepared and is currently under submission. By results of superior S values and advanced stabilities of the as-prepared i-TE materials, we noticed that the solvent component can be removed from ionogels without flexibility and TE performance damages. This will be a progressive achievement to provide more i-TE designation strategies. However, the σ value of this as-fabricated film is still inferior. Carbon materials are abundant and well-studied in literatures. Despite the in-situ reduction of the GO component is highly difficult, it still ranks a promising inspiration for the further study.

CHAPTER 7: DISCUSSION AND CONCLUSION

7.1. Conclusion

In this project, we developed three FTE materials and installed TEGs correspondingly. In brief, the as-prepared materials are (i) p-type industrial feasible carbon-based films, (ii) n-type ionic liquid modified industrial feasible carbon-based films, and (iii) carbon modified ionogel films. Specifically, the detailed achievements are:

i. For the optimal blended specimen, namely EG_3-$GIC2_7$ (p-type), high σ of 1089 S cm^{-1}, S of 28.2 µV K^{-1}, and PF of 87 µW m^{-1} K^{-2} are obtained at room temperature. Subsequently, temperature-dependent thermoelectric performance shows a maximum PF of 94 µW m^{-1} K^{-2} at 423 K. The entire procedure of preparation needs only 10 minutes and ten pieces of batch outputs produced by industrial equipment are presented as a model. Record high cost-effectiveness of 7250 µW g m^{-1} K^{-2} \$$^{-1}$ (PF/Cost value) has been achieved, which is absolutely ahead of the existing FTE materials. Two types of flexible thermoelectric devices adapt to different application scenarios are installed based on such novel composite. An output open-circuit voltage of 3.70 mV (ΔT = 3.9 K) is achieved using human wrist as the heat source, and 1.33 mV (ΔT = 1.6 K) is achieved soaking in the river water as the cold source.

ii. Based on the as-prepared n-type ionic liquid/phenolic resin/carbon fiber/expanded graphite composite, we found that the expanded graphite as the major component enables high flexibility and the introduction of phenolic resin and carbon fiber enhances the shear resistance and toughness of the film, while the ion-induced carrier migration contributes to a high PF of 38.7 µW m^{-1} K^{-2} at 500 K. Moreover, the as-prepared composite films are fabricated by a facile one-step hot-pressing method within only 15 minutes, which possess outstanding ratios of $S^2\sigma$/cost and $S^2\sigma$/time, indicating significant efficient and cost-effective features. Besides, a flexible thermoelectric device, assembled by the as-designed hybrid films, shows a maximum output power density of 79.3 nW cm^{-2} at a temperature difference of 20 K. This work paves a new way to fabricate cost-effective and high-performance carbon-based thermoelectric hybrids with promising application potential.

iii. We also developed a super flexible, stable, self-healable, and high performance ionic thermoelectric film composed of carbon, ionic liquid, and crosslinked polymer. Comprehensive thermoelectric performance of S of -76.7 mV K^{-1}, $S^2\sigma$ of 85.9 µW m^{-1} K^{-2}, and ZT of 0.086 are achieved at 383 K, which is competitive among existing ionic thermoelectric materials. Besides, tensile strength of 219.7 kPa, elongation at break of 389 %, Young's module of 84.1 kPa, toughness of 0.4 MJ m^{-3}, and flexibility of 180° bending are simultaneously performed in this film. Notably, both the thermoelectric and the mechanical properties are well-maintained to the film after depositing in air for 7 days. Based on as-obtained outstanding performances, a 9-leg 25x25 mm^2 flexible device is in-situ prepared, generating a large output voltage of 205 mV under a temperature difference of 5.7 K. This work provides a promising and novel way to design long-term applicable high-performance ionic thermoelectric materials and facile integrated flexible devices.

7.2   Contributions

i. Academic contribution. Three novel FTE materials are designed and fabricated, enriching the material library. Main components of carbon material and ionic liquids are combined in different ways to achieve TE applications, which is still under early stages of development currently. This project may provide an innovative methodology for the designation of such type of materials. Moreover, strategies for optimizing their TE performances are raised, which offers highly efficient reference for further related research.

ii. Commercial benefit. Due to the complicated synthesis procedure and high cost of exist FTEs, large-scale industrial application of such materials is still lacking. High cost-effective industrialization attempt for FTE preparation has not been reported till now. We provide large-scale industrial feasible preparations for novel carbon-based TE materials, bringing inspirations to promote industry applications of low-cost FTE materials.

iii. Environment and Energy. FTE devices installed in this project exhibits simulation for subsequent usages of the as-prepared materials. The practical application of these devices is of great significance to solve the problem of energy shortage and environmental pollution.

7.3 Perspectives

Although we developed three kinds of carbon material/ionic liquid hybrid FTE materials with high industrialization prospects, there are still some research points under further discovery (**Figure 7.1**):

i. *Performance improvement*. For materials based on i-TE principles, the material thickness could impact both sample and device performance. However, relevant results in this aspect are still lacking till now. Systematic studies on how the film thickness will regulate the TE performance are promising and significant.

ii. *Performance improvement*. The S of the cost-effective carbon films are still low. Element doping may provide a promising routine to improve the S, decrease the κ, and boost the ZT value. However, the cost-effectiveness will decrease as well in this way.

iii. *Characteristic innovation*. After the doping the ionic liquids, the whole material becomes wet. As a result, the characterization of high doping level materials is difficult, such as the SEM, TEM, XPS, etc., where high vacuum environment needs to be established. The breakthroughs on characterization methods are under developments.

iv. *Synthesis optimal*. Regarding the carbon-hybrid ionogels, compatibility needs to be initially considered. In this project, we chose the water-soluble GO as the doping component. However, the σ of GO is much lower than rGO and CNTs. New methods to fabricate rGO *etc.* hybrid ionogels may bring further optimized performances.

v. *Device simulation*. Practical applications of as-prepared carbon-based TE devices are under simulation. Different operation scenarios can be discovered and designed according to the stability, heat-resistance, flexibility, *etc.* of the prepared devices. Besides, the prepared i-TE ionogels can be used as capacitors as well. Investigation and comparation between the real efficiencies can provide practical guidance and inspire further studies.
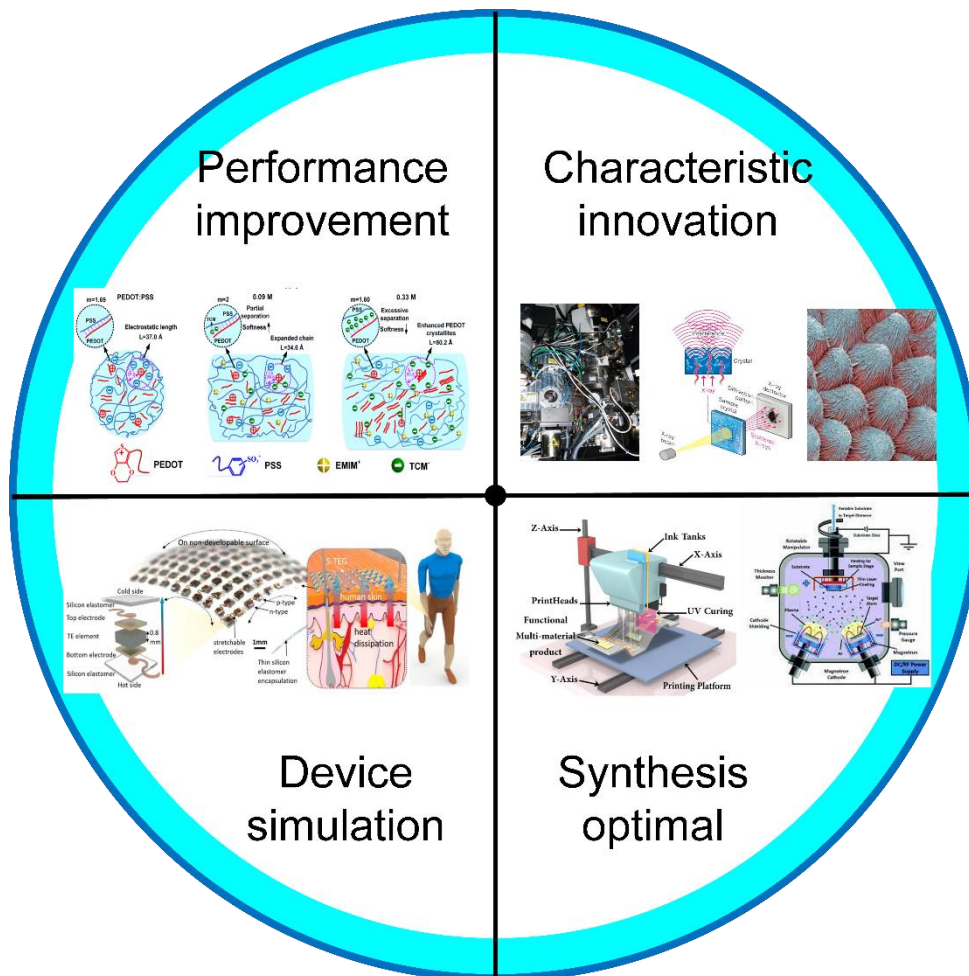
Figure 7.1. Perspectives of flexible thermoelectric materials.

REFERENCES

Aghelinejad, M., Zhang, Y., & Leung, S. N. (2019). Processing parameters to enhance the electrical conductivity and thermoelectric power factor of polypyrrole/multi-walled carbon nanotubes nanocomposites. Synthetic Metals, 247, 59-66. doi:10.1016/j.synthmet.2018.11.016

Allouhi, A. (2019). Advances on solar thermal cogeneration processes based on thermoelectric devices: A review. Solar Energy Materials and Solar Cells, 200, 109954. doi:10.1016/j.solmat.2019.109954

Bell, L. E. (2008). Cooling, Heating, Generating Power, and Recovering Waste Heat with Thermoelectric Systems. Science, 321(5895), 1457-1461. doi:10.1126/science.1158899

Blackburn, J. L., Ferguson, A. J., Cho, C., & Grunlan, J. C. (2018). Carbon-Nanotube-Based Thermoelectric Materials and Devices. Advanced Materials, 30(11), 1704386. doi:10.1002/adma.201704386

Bubnova, O., Khan, Z. U., Malti, A., Braun, S., Fahlman, M., Berggren, M., & Crispin, X. (2011). Optimization of the thermoelectric figure of merit in the conducting polymer poly(3,4-ethylenedioxythiophene). Nature Materials, 10(6), 429-433. doi:10.1038/nmat3012

Burke, J. H., & Bird, M. J. (2019). Energetics and Escape of Interchain-Delocalized Ion Pairs in Nonpolar Media. Advanced Materials, 31(12), 1806863. doi:10.1002/adma.201806863

Cao, T., Shi, X.-L., & Chen, Z.-G. (2023). Advances in the design and assembly of flexible thermoelectric device. Progress in Materials Science, 131, 101003. doi:10.1016/j.pmatsci.2022.101003

Carey, G. H., Abdelhady, A. L., Ning, Z., Thon, S. M., Bakr, O. M., & Sargent, E. H. (2015). Colloidal Quantum Dot Solar Cells. Chemical Reviews, 115(23), 12732-12763. doi:10.1021/acs.chemrev.5b00063

Checkelsky, J. G., & Ong, N. P. (2009). Thermopower and Nernst effect in graphene in a magnetic field. Physical Review B, 80(8), 081413. doi:10.1103/PhysRevB.80.081413

Chen, Y., Kou, Q., Cai, K., Yin, J., & Shen, S. (2017). The influence of hydrochloric acid doping on the microstructure and thermoelectric properties of poly(p-phenylenediamine) nanoparticles. Synthetic Metals, 227, 71-77. doi:10.1016/j.synthmet.2017.03.006

Cole, J. M. (2004). Single-crystal X-ray diffraction studies of photo-induced molecular species. Chemical Society Reviews, 33(8), 501-513. doi:10.1039/B205339J

Ding, J., Liu, Z., Zhao, W., Jin, W., Xiang, L., Wang, Z., Zeng, Y., Zou, Y., Zhang, F., Yi, Y., Diao, Y., McNeill, C. R., Di, C.-a., Zhang, D., & Zhu, D. (2019). Selenium-Substituted Diketopyrrolopyrrole Polymer for High-Performance p-Type Organic Thermoelectric Materials. Angewandte Chemie International Edition, 58(52), 18994-18999. doi:10.1002/anie.201911058

Dun, C., Hewitt, C. A., Huang, H., Montgomery, D. S., Xu, J., & Carroll, D. L. (2015). Flexible thermoelectric fabrics based on self-assembled tellurium nanorods with a large power factor. Physical Chemistry Chemical Physics, 17(14), 8591-8595. doi:10.1039/C4CP05390G

Epstein, A. J., Joo, J., Kohlman, R. S., Du, G., MacDiarmid, A. G., Oh, E. J., Min, Y., Tsukamoto, J., Kaneko, H., & Pouget, J. P. (1994). Inhomogeneous disorder and the modified Drude metallic state of conducting polymers. Synthetic Metals, 65(2), 149-157. doi:10.1016/0379-6779(94)90176-7

Fan, W., Zhang, Y., Guo, C.-Y., & Chen, G. (2019). Toward high thermoelectric performance for polypyrrole composites by dynamic 3-phase interfacial electropolymerization and chemical doping of carbon nanotubes. Composites Science and Technology, 183, 107794. doi:10.1016/j.compscitech.2019.107794

Fang, Y., Cheng, H., He, H., Wang, S., Li, J., Yue, S., Zhang, L., Du, Z., & Ouyang, J. (2020). Stretchable and Transparent Ionogels with High Thermoelectric Properties. Advanced Functional Materials, 30(51), 2004699. doi:10.1002/adfm.202004699

Gao, J., Liu, C., Miao, L., Wang, X., & Chen, Y. (2016). Free-Standing Reduced Graphene Oxide Paper with High Electrical Conductivity. Journal of Electronic Materials, 45(3), 1290-1295. doi:10.1007/s11664-015-4000-5

Gao, J., Miao, L., Liu, C., Wang, X., Peng, Y., Wei, X., Zhou, J., Chen, Y., Hashimoto, R., Asaka, T., & Koumoto, K. (2017). A novel glass-fiber-aided cold-press method for fabrication of n-type Ag_2Te nanowires thermoelectric film on flexible copy-paper substrate. Journal of Materials Chemistry A, 5(47), 24740-24748. doi:10.1039/C7TA07601K

Glaudell, A. M., Cochran, J. E., Patel, S. N., & Chabinyc, M. L. (2015). Impact of the Doping Method on Conductivity and Thermopower in Semiconducting Polythiophenes. Advanced Energy Materials, 5(4), 1401072. doi:10.1002/aenm.201401072

Goel, M., Heinrich, C. D., Krauss, G., & Thelakkat, M. (2019). Principles of Structural Design of Conjugated Polymers Showing Excellent Charge Transport toward Thermoelectrics and Bioelectronics Applications. Macromolecular Rapid Communications, 40(10), 1800915. doi:10.1002/marc.201800915

Guo, Y., Mu, J., Hou, C., Wang, H., Zhang, Q., & Li, Y. (2016). Flexible and thermostable thermoelectric devices based on large-area and porous all-graphene films. Carbon, 107, 146-153. doi:10.1016/j.carbon.2016.05.063

Gusev, V. V., Pustovalov, A. A., Rybkin, N. N., Anatychuk, L. I., Demchuk, B. N., & Ludchak, I. Y. (2011). Milliwatt-Power Radioisotope Thermoelectric Generator (RTG) Based on Plutonium-238. Journal of Electronic Materials, 40(5), 807-811. doi:10.1007/s11664-011-1579-z

Hamid Elsheikh, M., Shnawah, D. A., Sabri, M. F. M., Said, S. B. M., Haji Hassan, M., Ali Bashir, M. B., & Mohamad, M. (2014). A review on thermoelectric renewable energy: Principle parameters that affect their performance. Renewable and Sustainable Energy Reviews, 30, 337-355. doi:10.1016/j.rser.2013.10.027

Han, S., Jiao, F., Khan, Z. U., Edberg, J., Fabiano, S., & Crispin, X. (2017). Thermoelectric Polymer Aerogels for Pressure–Temperature Sensing Applications. Advanced Functional Materials, 27(44), 1703549. doi:10.1002/adfm.201703549

Hayashi, K., Shinano, T., Miyazaki, Y., & Kajitani, T. (2011). Fabrication of iodine-doped pentacene thin films for organic thermoelectric devices. Journal of Applied Physics, 109(2). doi:10.1063/1.3537831

Hicks, L. D., & Dresselhaus, M. S. (1993). Effect of quantum-well structures on the thermoelectric figure of merit. Physical Review B, 47(19), 12727-12731. doi:10.1103/PhysRevB.47.12727

Hong, M., Chen, Z.-G., Yang, L., Liao, Z.-M., Zou, Y.-C., Chen, Y.-H., Matsumura, S., & Zou, J. (2018). Achieving $zT > 2$ in p-Type AgSbTe$_{2-x}$Se$_x$ Alloys via Exploring the Extra Light Valence Band and Introducing Dense Stacking Faults. Advanced Energy Materials, 8(9), 1702333. doi:10.1002/aenm.201702333

Hsieh, Y.-Y., Zhang, Y., Zhang, L., Fang, Y., Kanakaraaj, S. N., Bahk, J.-H., & Shanov, V. (2019). High thermoelectric power-factor composites based on flexible three-dimensional graphene and polyaniline. Nanoscale, 11(14), 6552-6560. doi:10.1039/C8NR10537E

Huang, D., Wang, C., Zou, Y., Shen, X., Zang, Y., Shen, H., Gao, X., Yi, Y., Xu, W., Di, C.-a., & Zhu, D. (2016). Bismuth Interfacial Doping of Organic Small Molecules for High Performance n-type Thermoelectric Materials. Angewandte Chemie International Edition, 55(36), 10672-10675. doi:10.1002/anie.201604478

Huang, D., Yao, H., Cui, Y., Zou, Y., Zhang, F., Wang, C., Shen, H., Jin, W., Zhu, J., Diao, Y., Xu, W., Di, C.-a., & Zhu, D. (2017). Conjugated-Backbone Effect of Organic Small

Molecules for n-Type Thermoelectric Materials with ZT over 0.2. Journal of the American Chemical Society, 139(37), 13013-13023. doi:10.1021/jacs.7b05344

Huang, L., Lin, S., Xu, Z., Zhou, H., Duan, J., Hu, B., & Zhou, J. (2020). Fiber-Based Energy Conversion Devices for Human-Body Energy Harvesting. Advanced Materials, 32(5), 1902034. doi:10.1002/adma.201902034

Huewe, F., Steeger, A., Kostova, K., Burroughs, L., Bauer, I., Strohriegl, P., Dimitrov, V., Woodward, S., & Pflaum, J. (2017). Low-Cost and Sustainable Organic Thermoelectrics Based on Low-Dimensional Molecular Metals. Advanced Materials, 29(13), 1605682. doi:10.1002/adma.201605682

Inabe, T., Nakamura, S., Liang, W. B., Marks, T. J., Burton, R. L., Kannewurf, C. R., & Imaeda, K. (1985). Highly conductive metallomacrocyclic assemblies. Synthesis via electrocrystallization and single-crystal properties of a phthalocyanine molecular metal without halogen counterions. Journal of the American Chemical Society, 107(24), 7224-7226. doi:10.1021/ja00310a103

Jacobsen, C. S., Mortensen, K., Andersen, J. R., & Bechgaard, K. (1978). Transport properties of some derivatives of tetrathiafulvalene-tetracyano-p-quinodimethane (TTF-TCNQ). Physical Review B, 18(2), 905-921. doi:10.1103/PhysRevB.18.905

Jung, I. H., Hong, C. T., Lee, U.-H., Kang, Y. H., Jang, K.-S., & Cho, S. Y. (2017). High Thermoelectric Power Factor of a Diketopyrrolopyrrole-Based Low Bandgap Polymer via Finely Tuned Doping Engineering. Scientific Reports, 7(1), 44704. doi:10.1038/srep44704

Kee, S., Kim, H., Paleti, S. H. K., El Labban, A., Neophytou, M., Emwas, A.-H., Alshareef, H. N., & Baran, D. (2019). Highly Stretchable and Air-Stable PEDOT:PSS/Ionic Liquid Composites for Efficient Organic Thermoelectrics. Chemistry of Materials, 31(9), 3519-3526. doi:10.1021/acs.chemmater.9b00819

Kiefer, D., Kroon, R., Hofmann, A. I., Sun, H., Liu, X., Giovannitti, A., Stegerer, D., Cano, A., Hynynen, J., Yu, L., Zhang, Y., Nai, D., Harrelson, T. F., Sommer, M., Moulé, A. J., Kemerink, M., Marder, S. R., McCulloch, I., Fahlman, M., Fabiano, S., & Müller, C. (2019). Double doping of conjugated polymers with monomer molecular dopants. Nature Materials, 18(2), 149-155. doi:10.1038/s41563-018-0263-6

Kim, B., Shin, H., Park, T., Lim, H., & Kim, E. (2013). NIR-Sensitive Poly(3,4-ethylenedioxyselenophene) Derivatives for Transparent Photo-Thermo-Electric Converters. Advanced Materials, 25(38), 5483-5489. doi:10.1002/adma.201301834

Kim, G. H., Shao, L., Zhang, K., & Pipe, K. P. (2013). Engineered doping of organic semiconductors for enhanced thermoelectric efficiency. Nature Materials, 12(8), 719-723. doi:10.1038/nmat3635

Kwak, J. F., Beni, G., & Chaikin, P. M. (1976). Thermoelectric power in Hubbard-model systems with different densities: N-methylphenazinium-tetracyanoquinodimethane (NMP-TCNQ), and quinolinium ditetracyanoquinodimethane. Physical Review B, 13(2), 641-646. doi:10.1103/PhysRevB.13.641

Lee, B., Cho, H., Park, K. T., Kim, J.-S., Park, M., Kim, H., Hong, Y., & Chung, S. (2020). High-performance compliant thermoelectric generators with magnetically self-assembled soft heat conductors for self-powered wearable electronics. Nature Communications, 11(1), 5948. doi:10.1038/s41467-020-19756-z

Lee, J. A., Aliev, A. E., Bykova, J. S., de Andrade, M. J., Kim, D., Sim, H. J., Lepró, X., Zakhidov, A. A., Lee, J. -B., Spinks, G. M., Roth, S., Kim, S. J., & Baughman, R. H. (2016). Woven-Yarn Thermoelectric Textiles. Advanced Materials, 28(25), 5038-5044. doi:https://doi.org/10.1002/adma.201600709

Li, L., Liu, W. D., Liu, Q., & Chen, Z. G. (2022). Multifunctional Wearable Thermoelectrics for Personal Thermal Management. Advanced Functional Materials, 32(22), 2200548. doi:10.1002/adfm.202200548

Liang, D., Yang, H., Finefrock, S. W., & Wu, Y. (2012). Flexible Nanocrystal-Coated Glass Fibers for High-Performance Thermoelectric Energy Harvesting. Nano Letters, 12(4), 2140-2145. doi:10.1021/nl300524j

Liebl, J., Neugebauer, S., Eder, A., Linde, M., Mazar, B., & Stütz, W. (2009). The thermoelectric generator from BMW is making use of waste heat. MTZ worldwide, 70(4), 4-11. doi:10.1007/BF03226939

Liu, C., Xu, J., Lu, B., Yue, R., & Kong, F. (2012). Simultaneous Increases in Electrical Conductivity and Seebeck Coefficient of PEDOT:PSS Films by Adding Ionic Liquids into a Polymer Solution. Journal of Electronic Materials, 41(4), 639-645. doi:10.1007/s11664-012-1942-8

Liu, H., Hu, X. B., Wang, J. Y., & Boughton, R. I. (2002). Structure, Conductivity, and Thermopower of Crystalline Polyaniline Synthesized by the Ultrasonic Irradiation Polymerization Method. Macromolecules, 35(25), 9414-9419. doi:10.1021/ma0119326

Liu, J., Garman, M. P., Dong, J., van der Zee, B., Qiu, L., Portale, G., Hummelen, J. C., & Koster, L. J. A. (2019). Doping Engineering Enables Highly Conductive and Thermally Stable

n-Type Organic Thermoelectrics with High Power Factor. ACS Applied Energy Materials, 2(9), 6664-6671. doi:10.1021/acsaem.9b01179

Liu, J., Qiu, L., Portale, G., Torabi, S., Stuart, M. C. A., Qiu, X., Koopmans, M., Chiechi, R. C., Hummelen, J. C., & Koster, L. J. A. (2018). Side-chain effects on N-type organic thermoelectrics: A case study of fullerene derivatives. Nano Energy, 52, 183-191. doi:10.1016/j.nanoen.2018.07.056

MacLeod, B. A., Stanton, N. J., Gould, I. E., Wesenberg, D., Ihly, R., Owczarczyk, Z. R., Hurst, K. E., Fewox, C. S., Folmar, C. N., Hughes, K. H., Zink, B. L., Blackburn, J. L., & Ferguson, A. J. (2017). Large n- and p-type thermoelectric power factors from doped semiconducting single-walled carbon nanotube thin films. Energy & Environmental Science, 10(10), 2168-2179. doi:10.1039/C7EE01130J

Majumdar, A. (2009). Helping chips to keep their cool. Nature Nanotechnology, 4(4), 214-215. doi:10.1038/nnano.2009.65

Mateeva, N., Niculescu, H., Schlenoff, J., & Testardi, L. R. (1998). Correlation of Seebeck coefficient and electric conductivity in polyaniline and polypyrrole. Journal of Applied Physics, 83(6), 3111-3117. doi:10.1063/1.367119

Müller, E., Ritschel, H., & Hänsel, H. (1969). The Anisotropy of Electrical Conductivity and Thermoelectric Power in Single Crystals of the Anion Radical Salt [(C$_6$H$_5$)$_3$ AsCH$_3$]$^+$ TCNQ2$^-$. physica status solidi (b), 33(1), K55-K58. doi:10.1002/pssb.19690330168

Narayan, K., & Subramaniam, S. (2015). Focused ion beams in biology. Nature Methods, 12(11), 1021-1031. doi:10.1038/nmeth.3623

Ni, X., Liang, G., Wang, J.-S., & Li, B. (2009). Disorder enhances thermoelectric figure of merit in armchair graphane nanoribbons. Applied Physics Letters, 95(19). doi:10.1063/1.3264087

Nonoguchi, Y., Ohashi, K., Kanazawa, R., Ashiba, K., Hata, K., Nakagawa, T., Adachi, C., Tanase, T., & Kawai, T. (2013). Systematic Conversion of Single Walled Carbon Nanotubes into n-type Thermoelectric Materials by Molecular Dopants. Scientific Reports, 3(1), 3344. doi:10.1038/srep03344

Noriega, R., Rivnay, J., Vandewal, K., & Koch, F. (2013). V; Stingelin, N.; Smith, P.; Toney, MF; Salleo. A. A General Relationship between Disorder, Aggregation and Charge Transport in Conjugated Polymers. Nature Materials, 12(11), 1038-1044. doi:10.1038/nmat3722

Ogawa, M. Y., Martinsen, J., Palmer, S. M., Stanton, J. L., Tanaka, J., Greene, R. L., Hoffman, B. M., & Ibers, J. A. (1987). The (phthalocyaninato)copper iodide complex Cu(pc)I: a

molecular metal with a one-dimensional array of local moments embedded in a "Fermi sea" of charge carriers. Journal of the American Chemical Society, 109(4), 1115-1121. doi:10.1021/ja00238a021

Oh, J. Y., Lee, J. H., Han, S. W., Chae, S. S., Bae, E. J., Kang, Y. H., Choi, W. J., Cho, S. Y., Lee, J. -O., Baik, H. K., & Lee, T. I. (2016). Chemically exfoliated transition metal dichalcogenide nanosheet-based wearable thermoelectric generators. Energy & Environmental Science, 9(5), 1696-1705. doi:10.1039/C5EE03813H

Park, T., Park, C., Kim, B., Shin, H., & Kim, E. (2013). Flexible PEDOT electrodes with large thermoelectric power factors to generate electricity by the touch of fingertips. Energy & Environmental Science, 6(3), 788-792. doi:10.1039/C3EE23729J

Park, Y. W., Denenstein, A., Chiang, C. K., Heeger, A. J., & MacDiarmid, A. G. (1979). Semiconductor-metal transition in doped $(CH)_x$: Thermoelectric power. Solid State Communications, 29(11), 747-751. doi:10.1016/0038-1098(79)90153-4

Patel, S. N., Glaudell, A. M., Kiefer, D., & Chabinyc, M. L. (2016). Increasing the Thermoelectric Power Factor of a Semiconducting Polymer by Doping from the Vapor Phase. ACS Macro Letters, 5(3), 268-272. doi:10.1021/acsmacrolett.5b00887

Paul, B., Lu, J., & Eklund, P. (2017). Nanostructural Tailoring to Induce Flexibility in Thermoelectric $Ca_3Co_4O_9$ Thin Films. ACS Applied Materials & Interfaces, 9(30), 25308-25316. doi:10.1021/acsami.7b06301

Rojo, M. M., Martín, J., Grauby, S., Borca-Tasciuc, T., Dilhaire, S., & Martin-Gonzalez, M. (2014). Decrease in thermal conductivity in polymeric P3HT nanowires by size-reduction induced by crystal orientation: new approaches towards thermal transport engineering of organic materials. Nanoscale, 6(14), 7858-7865. doi:10.1039/C4NR00107A

Rowe, D. M. (2018). Thermoelectrics handbook: macro to nano: CRC press.

Russ, B., Glaudell, A., Urban, J. J., Chabinyc, M. L., & Segalman, R. A. (2016). Organic thermoelectric materials for energy harvesting and temperature control. Nature Reviews Materials, 1(10), 16050. doi:10.1038/natrevmats.2016.50

Scheunemann, D., Järsvall, E., Liu, J., Beretta, D., Fabiano, S., Caironi, M., Kemerink, M., & Müller, C. (2022). Charge transport in doped conjugated polymers for organic thermoelectrics. Chemical Physics Reviews, 3(2). doi:10.1063/5.0080820

Schlatter, S., Grasso, G., Rosset, S., & Shea, H. (2020). Inkjet Printing of Complex Soft Machines with Densely Integrated Electrostatic Actuators. Advanced Intelligent Systems, 2(11), 2000136. doi:10.1002/aisy.202000136

Seah, M. P. (1980). The quantitative analysis of surfaces by XPS: A review. Surface and Interface Analysis, 2(6), 222-239. doi:10.1002/sia.740020607

Sevilla, G. A. T., Inayat, S. B., Rojas, J. P., Hussain, A. M., & Hussain, M. M. (2013). Flexible and Semi-Transparent Thermoelectric Energy Harvesters from Low Cost Bulk Silicon (100). Small, 9(23), 3916-3921. doi:10.1002/smll.201301025

Sevinçli, H., & Cuniberti, G. (2010). Enhanced thermoelectric figure of merit in edge-disordered zigzag graphene nanoribbons. Physical Review B, 81(11), 113401. doi:10.1103/PhysRevB.81.113401

Shafiei, N., Harun, M. H., Annuar, K., Halim, M., Aras, M., & Azahar, A. (2016). Development of portable air conditioning system using peltier and seebeck effect. Journal of Telecommunication, Electronic and Computer Engineering (JTEC), 8(7), 97-100.

Shi, X., & Chen, L. (2016). Thermoelectric materials step up. Nature Materials, 15(7), 691-692. doi:10.1038/nmat4643

Shi, X., Zheng, K., Hong, M., Liu, W., Moshwan, R., Wang, Y., Qu, X., Chen, Z. -G., & Zou, J. (2018). Boosting the thermoelectric performance of p-type heavily Cu-doped polycrystalline SnSe via inducing intensive crystal imperfections and defect phonon scattering. Chemical Science, 9(37), 7376-7389. doi:10.1039/C8SC02397B

Shi, X. L., Zou, J., & Chen, Z. G. (2020). Advanced Thermoelectric Design: From Materials and Structures to Devices. Chem Rev, 120(15), 7399-7515. doi:10.1021/acs.chemrev.0c00026

Shinohara, Y., Hiraishi, K., Isoda, Y., Imai, Y., & Oikawa, H. (2008). Effect of synthetic conditions on the thermoelectric properties of polythiophene by electrolytic polymerization. AIP Conference Proceedings, 973(1), 628-633. doi:10.1063/1.2896852

Sim, D., Liu, D., Dong, X., Xiao, N., Li, S., Zhao, Y., Li, L. -J., Yan, Q., & Hng, H. H. (2011). Power Factor Enhancement for Few-Layered Graphene Films by Molecular Attachments. The Journal of Physical Chemistry C, 115(5), 1780-1785. doi:10.1021/jp1103609

Slack, G. A., & Rowe, D. (1995). CRC handbook of thermoelectrics: CRC press Boca Raton, FL.

Sun, Y., Fang, H., Pan, L., Han, M., Xu, S., Wang, X., Xu, B., & Wu, Y. (2015). Impact of Surface-Bound Small Molecules on the Thermoelectric Property of Self-Assembled Ag_2Te Nanocrystal Thin Films. Nano Letters, 15(6), 3748-3756. doi:10.1021/acs.nanolett.5b00255

Sun, Y., Sheng, P., Di, C., Jiao, F., Xu, W., Qiu, D., & Zhu, D. (2012). Organic Thermoelectric Materials and Devices Based on p- and n-Type Poly(metal 1,1,2,2-ethenetetrathiolate)s. Advanced Materials, 24(7), 932-937. doi:10.1002/adma.201104305

Tan, G., Zhao, L.-D., & Kanatzidis, M. G. (2016). Rationally Designing High-Performance Bulk Thermoelectric Materials. Chemical Reviews, 116(19), 12123-12149. doi:10.1021/acs.chemrev.6b00255

Telkes, M. (2004). The Efficiency of Thermoelectric Generators. I. Journal of Applied Physics, 18(12), 1116-1127. doi:10.1063/1.1697593

Thomson, W. (1857). 5. On a Method of Discovering Experimentally the Relation between the Mechanical Work spent and the Heat produced by the Compression of a Gaseous Fluid. Proceedings of the Royal Society of Edinburgh, 3, 69-72. doi:10.1017/S0080456800033184

Toshima, N., Oshima, K., Anno, H., Nishinaka, T., Ichikawa, S., Iwata, A., & Shiraishi, Y. (2015). Novel Hybrid Organic Thermoelectric Materials:Three-Component Hybrid Films Consisting of a Nanoparticle Polymer Complex, Carbon Nanotubes, and Vinyl Polymer. Advanced Materials, 27(13), 2246-2251. doi:10.1002/adma.201405463

Tsai, T.-C., Chang, H.-C., Chen, C.-H., Huang, Y.-C., & Whang, W.-T. (2014). A facile dedoping approach for effectively tuning thermoelectricity and acidity of PEDOT:PSS films. Organic Electronics, 15(3), 641-645. doi:10.1016/j.orgel.2013.12.023

Vavro, J., Llaguno, M. C., Fischer, J. E., Ramesh, S., Saini, R. K., Ericson, L. M., Davis, V. A., Hauge, R. H., Pasquali, M., & Smalley, R. E. (2003). Thermoelectric Power of p-Doped Single-Wall Carbon Nanotubes and the Role of Phonon Drag. Physical Review Letters, 90(6), 065503. doi:10.1103/PhysRevLett.90.065503

Vedernikov, M. V., & Iordanishvili, E. K. (1998, 28-28 May 1998). A.F. Ioffe and origin of modern semiconductor thermoelectric energy conversion. Paper presented at the Seventeenth International Conference on Thermoelectrics. Proceedings ICT98 (Cat. No.98TH8365).

Veers, P., Dykes, K., Lantz, E., Barth, S., Bottasso, C. L., Carlson, O., Clifton, A., Green, J., Green, P., Holttinen, H., Laird, D., Lehtomäki, V., Lundquist, J. K., Manwell, J., Marquis, M., Meneveau, C., Moriarty, P., Munduate, X., Muskulus, M., Naughton, J., Pao, L., Paquette, J., Peinke, J., Robertson, A., Rodrigo, J. S., Sempreviva, A. M., Smith, J. C., Tuohy, A., & Wiser, R. (2019). Grand challenges in the science of wind energy. Science, 366(6464), eaau2027. doi:doi:10.1126/science.aau2027

Venkatasubramanian, R., Siivola, E., Colpitts, T., & O'Quinn, B. (2001). Thin-film thermoelectric devices with high room-temperature figures of merit. Nature, 413(6856), 597-602. doi:10.1038/35098012

Vidinejevs, S., Chatys, R., Aniskevich, A., & Jamroziak, K. (2021). Prompt Determination of the Mechanical Properties of Industrial Polypropylene Sandwich Pipes. Materials, 14(9), 2128. doi:10.3390/ma14092128

Vining, C. B. (2009). An inconvenient truth about thermoelectrics. Nature Materials, 8(2), 83-85. doi:10.1038/nmat2361

Wan, C., Gu, X., Dang, F., Itoh, T., Wang, Y., Sasaki, H., Kondo, M., Koga, K., Yabuki, K., Snyder, G. J., Yang, R., & Koumoto, K. (2015). Flexible n-type thermoelectric materials by organic intercalation of layered transition metal dichalcogenide TiS_2. Nature Materials, 14(6), 622-627. doi:10.1038/nmat4251

Wan Mahari, W. A., Azwar, E., Foong, S. Y., Ahmed, A., Peng, W., Tabatabaei, M., Aghbashlo, M., Park, Y. K., Sonne, C., & Lam, S. S. (2021). Valorization of municipal wastes using co-pyrolysis for green energy production, energy security, and environmental sustainability: A review. Chemical Engineering Journal, 421, 129749. doi:https://doi.org/10.1016/j.cej.2021.129749

Wang, H., Wang, H., Wang, Z., Tang, L., Zeng, G., Xu, P., Chen, M., Xiong, T., Zhou, C., Li, X., Huang, D., Zhu, Y., Wang, Z., & Tang, J. (2020). Covalent organic framework photocatalysts: structures and applications. Chemical Society Reviews, 49(12), 4135-4165. doi:10.1039/D0CS00278J

Wang, Z. H., Ichimura, K., Dresselhaus, M. S., Dresselhaus, G., Lee, W. T., Wang, K. A., & Eklund, P. C. (1993). Electronic transport properties of K_xC_{70} thin films. Physical Review B, 48(14), 10657-10660. doi:10.1103/PhysRevB.48.10657

Weber, J., Potje-Kamloth, K., Haase, F., Detemple, P., Völklein, F., & Doll, T. (2006). Coin-size coiled-up polymer foil thermoelectric power generator for wearable electronics. Sensors and Actuators A: Physical, 132(1), 325-330. doi:https://doi.org/10.1016/j.sna.2006.04.054

Wood, C. (1988). Materials for thermoelectric energy conversion. Reports on Progress in Physics, 51(4), 459. doi:10.1088/0034-4885/51/4/001

Wu, D., Xie, L., Chao, X., Yang, Z., & He, J. (2019). Step-Up Thermoelectric Performance Realized in Bi_2Te_3 Alloyed GeTe via Carrier Concentration and Microstructure Modulations. ACS Applied Energy Materials, 2(3), 1616-1622. doi:10.1021/acsaem.9b00057

Xing, W., Wu, S., Liang, Y., Sun, Y., Zou, Y., Liu, L., Xu, W., & Zhu, D. (2020). Engineering the Doping Efficiency in Pentacene Thin Films for High Thermoelectric Performance. ACS Applied Materials & Interfaces, 12(26), 29540-29548. doi:10.1021/acsami.0c07822

Yang, Y., Ma, F. Y., Lei, C. H., Liu, Y. Y., & Li, J. Y. (2013). Is thermoelectric conversion efficiency of a composite bounded by its constituents? Applied Physics Letters, 102(5). doi:10.1063/1.4791684

Yao, C.-J., Zhang, H.-L., & Zhang, Q. (2019). Recent Progress in Thermoelectric Materials Based on Conjugated Polymers. Polymers, 11(1), 107. doi:10.3390/polym11010107

Yu, K., Zhou, Y., Liu, Y., Liu, F., Hu, L., Ao, W., Zhang, C., Li, Y., Li, J., & Xie, H. (2019). Near-room-temperature thermoelectric materials and their application prospects in geothermal power generation. Geomechanics and Geophysics for Geo-Energy and Geo-Resources, 6(1), 12. doi:10.1007/s40948-019-00134-z

Zhang, L., Shi, X.-L., Yang, Y.-L., & Chen, Z.-G. (2021). Flexible thermoelectric materials and devices: From materials to applications. Materials Today, 46, 62-108. doi:10.1016/j.mattod.2021.02.016

Zhang, Q. H., Huang, X. Y., Bai, S. Q., Shi, X., Uher, C., & Chen, L. D. (2016). Thermoelectric Devices for Power Generation: Recent Progress and Future Challenges Advanced Engineering Materials, 18(2), 194-213. doi:https://doi.org/10.1002/adem.201500333

Zhang, X., Tan, Q.-H., Wu, J.-B., Shi, W., & Tan, P.-H. (2016). Review on the Raman spectroscopy of different types of layered materials. Nanoscale, 8(12), 6435-6450. doi:10.1039/C5NR07205K

Zhao, W., Fan, S., Xiao, N., Liu, D., Tay, Y. Y., Yu, C., Sim, D., Hng, H. H., Zhang, Q., Boey, F., Ma, J., Zhao, X., Zhang, H., & Yan, Q. (2012). Flexible carbon nanotube papers with improved thermoelectric properties. Energy & Environmental Science, 5(1), 5364-5369. doi:10.1039/C1EE01931G

Zuzok, R., Kaiser, A. B., Pukacki, W., & Roth, S. (1991). Thermoelectric power and conductivity of iodine-doped "new" polyacetylene. The Journal of Chemical Physics, 95(2), 1270-1275. doi:10.1063/1.461107

APPENDIX A: SUPPORTING INFORMATION FOR PAPER 2

This appendix A is attached as the Supporting Information (published) for the paper 2 in chapter 4: Cheap, large-scale, and high-performance graphite-based flexible thermoelectric materials and devices with supernormal industry feasibility.

Cheap, Large-scale, and High-performance Graphite-based Flexible Thermoelectric Materials and Devices with Supernormal Industry Feasibility

Shuai Sun,[†] Xiao-Lei Shi,[†, ‡] Wei-Di Liu,[†] Ting Wu,[※] Dezhuang Wang,[※] Hao Wu,[※] Xiaoyong Zhang,[□] Yu Wang,[§] Qingfeng Liu,[※, *] and Zhi-Gang Chen[†, ‡, *]

[†] *Centre for Future Materials, University of Southern Queensland, Springfield Central, Queensland 4300, Australia.*

[‡] *School of Chemistry and Physics, Queensland University of Technology, Brisbane City QLD 4000, Australia.*

[※] *State Key Laboratory of Materials Oriented Chemistry Engineering, College of Chemistry Engineering, Nanjing Tech University, Nanjing 211800, China.*

[□] *School of Materials Science and Engineering, Anhui University of Science and Technology, Huainan 232001, China.*

[§] *Jiangxi Bluestar Xinghuo Silicone Co., Ltd., Jiujiang 330319, China.*

Correspondence should be addressed at:

*E-mail: qfliu@njtech.edu.cn and zhigang.chen@usq.edu.au
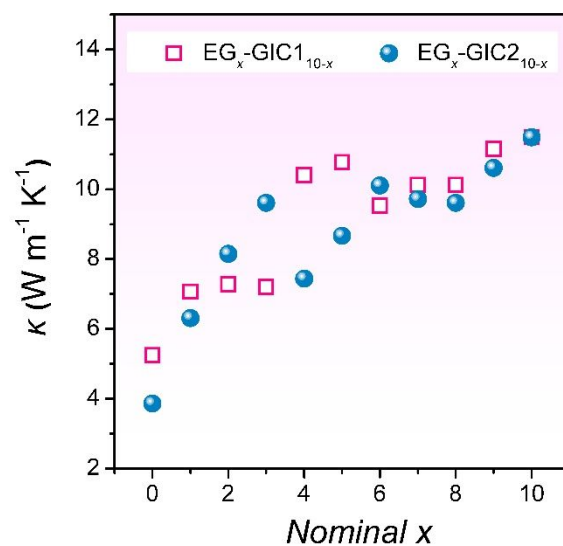
Figure S1. Vertical thermal conductivities of the as-prepared composites.
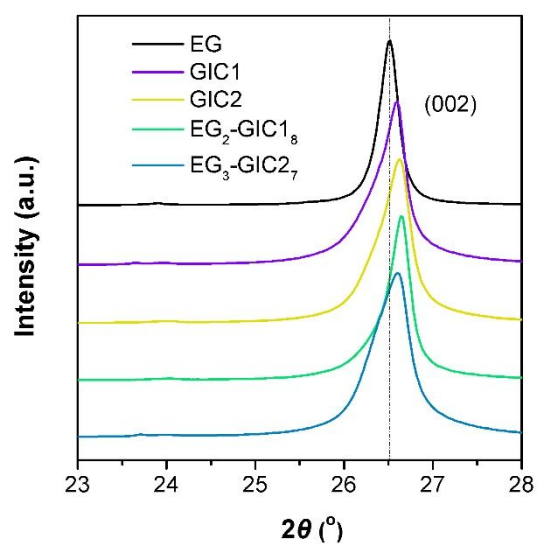
Figure S2. Enlarged XRD spetras highlighting the (002) diffraction peaks.
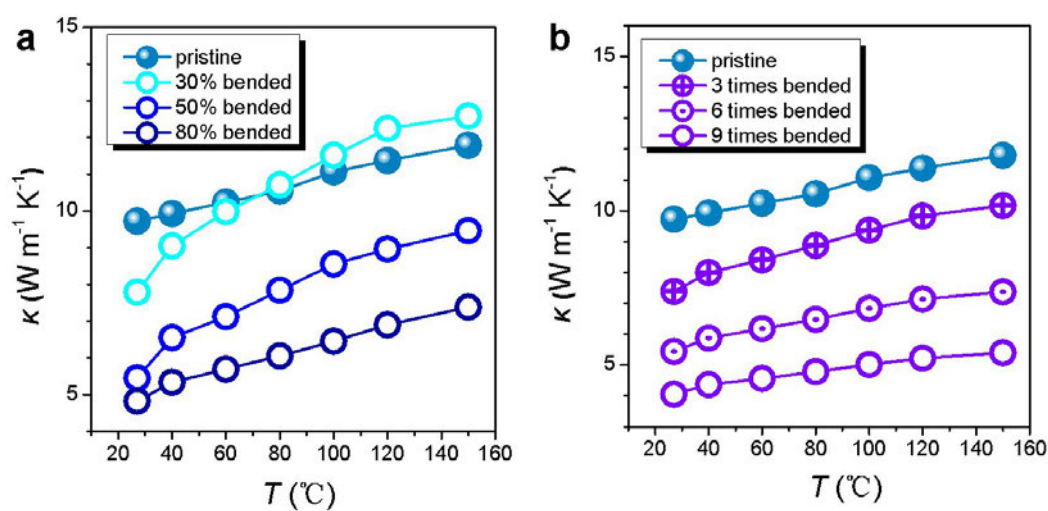
Figure S3. Thermal conductivities of EG_3-$GIC2_7$ films as a function of temperature.
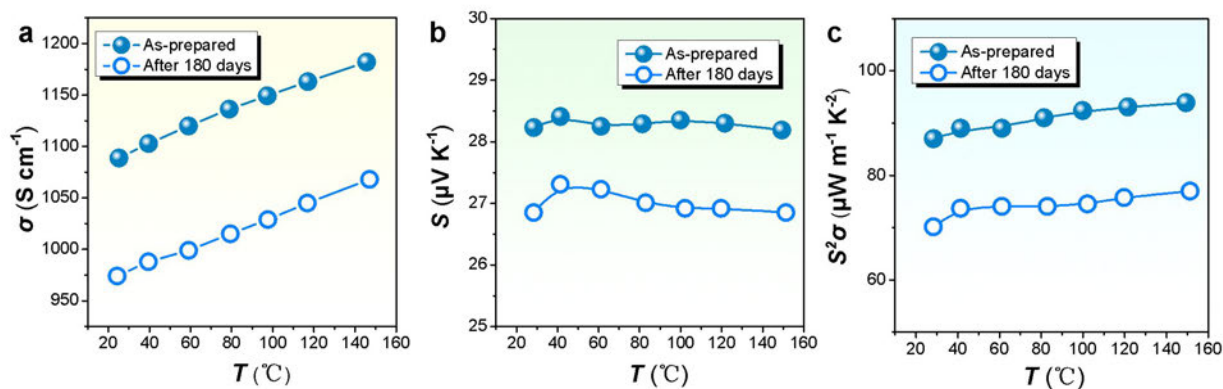
Figure S4. (a) σ, (b) S, and (c) $S^2\sigma$ of EG_3-$GIC2_7$, under as-prepared status and afer exposed in the air for 180 days.
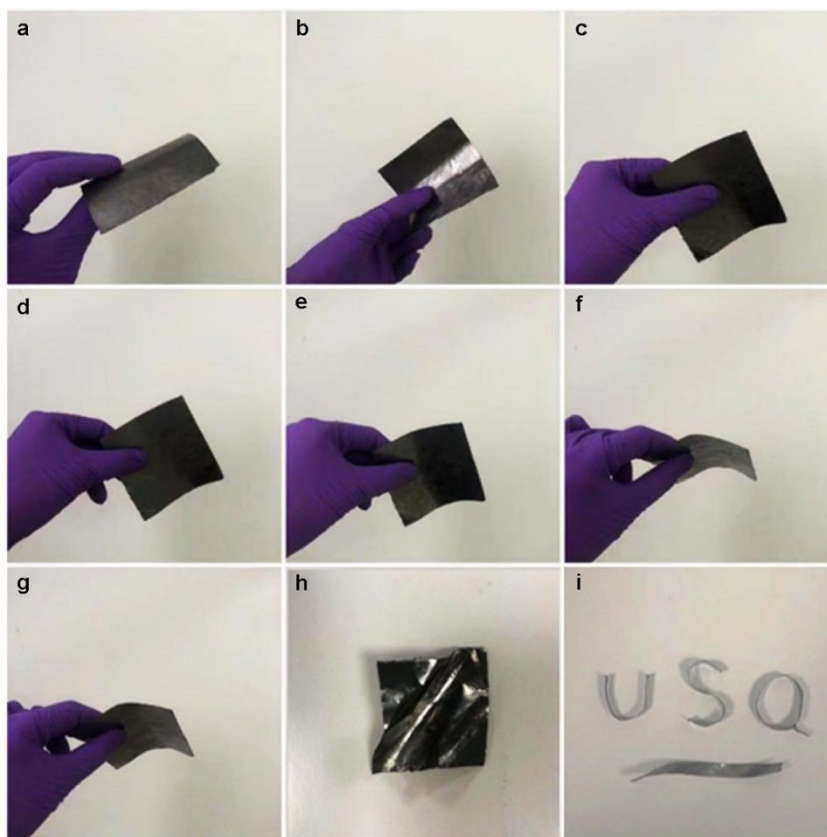
Figure S5. Arbitrary shaping images of EG$_3$-GIC2$_7$.
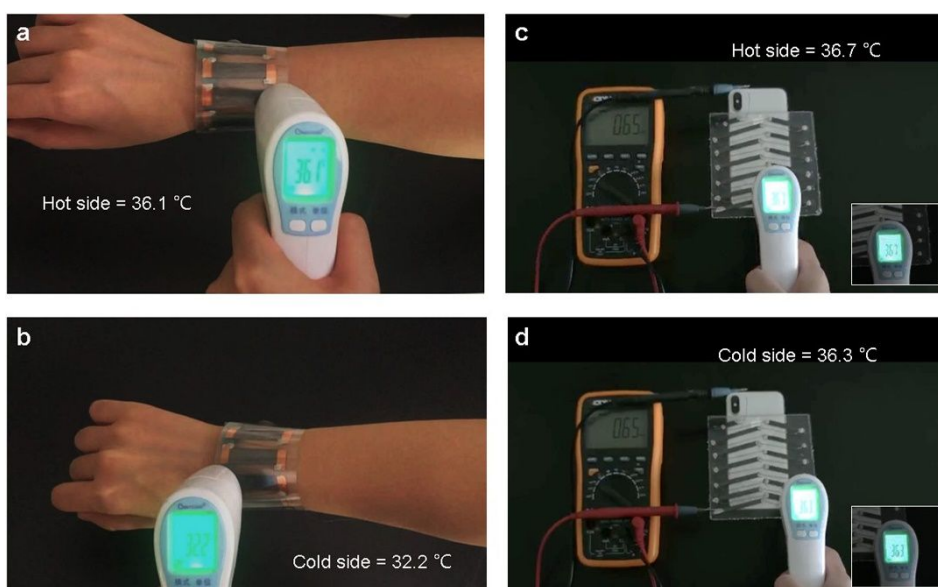
Figure S6. Temperature measurement of the hot side and cold side in conditions of (a-b) Human body as the heat source, and (c-d) Cellphone back shell as the heat source.
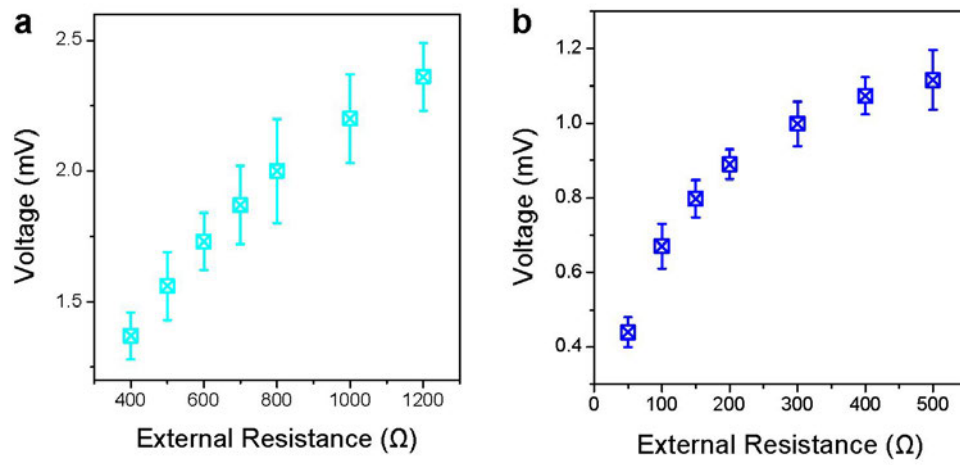
Figure S7. The voltage on the external variable resistor as a function of external resistance of (a) Device-1, and (b) Device-2.

Table S1. Comparison of thermoelectric properties and prices of the as-prepared composite EG$_3$-GIC2$_7$ and some typical flexible thermoelectric materials reported in literature.

Materials	Filler/adhesive	Loading (wt.%)	Form	Type	T (K)	σ (S cm^{-1})	S (μV K^{-1})	$S^2\sigma$ (μW m^{-1} K^{-2})	κ (W m^{-1} K^{-1})	ZT	$Price$ ($ g^{-1})	ref
This work			flexible	p	300	1089	28.2	87	-	-	0.012	
PEDOT			flexible	p	300	23	12.9	39	-	-	-	(S1)
PEDOT:PSS			flexible	p	300	453	23.1	24	-	-	117	(S2)
P3HT			flexible	p	300	250	40	38	~0.18	~0.06	188	(S3)
PANI			flexible	p	300	12.5	11	0.2	-	-	76	(S4)
Graphite			solid	p	298	1400	5	3.5	-	-	0.008	(S5)
Expanded graphite			flexible	P	300	1000	10.4	11	-	-	0.014	(S6)
Carbon fiber	Sulfate–aluminate cement	0.5	solid	p	329	-	-	2	-	0.003	0.023	(S7)
Expanded graphite	PC	50	flexible	p	300	~11.4	~26	~0.8	-	-	0.009	(S8)
Expanded graphite	PEDOT:PSS	20	flexible	p	298	213	16	5.3	-	~2.3*10^{-4}	23	(S9)
Expanded graphite	PVA/PEI	60/20	flexible	n	300	10	-25.3	0.6	~0.3	~6*10^{-4}	0.006	(S10)
Expanded graphite	ionic liquid/Sulfate–aluminate cement	3/90	solid	n	308	~0.003	~ -150	~0.67	-	-	1.25	(S11)
					345	~3	-568	94	3.296	2.06*10^{-3}		
PEDOT	rGO	17	flexible	p	300	516	16	13	-	-	-	(S12)
PEDOT:PSS	Ca$_3$Co$_4$O$_9$	10	flexible	P	300	135	18.1	4	-	-	-	(S13)
PEDOT:PSS	Sb$_2$Te$_3$	-	flexible	P	300	341	92.6	292	0.44	0.2	-	(S14)
PEDOT:PSS	SnSe	20	flexible	p	300	320	110	387	0.36	0.32	-	(S15)
PEDOT:PSS	Te NWs	7	flexible	P	300	19.3	163	51	0.22	0.1	-	(S16)
PEDOT:PSS	Te NWs	-	flexible	p	300	215	115	284	0.22	0.39	-	(S17)

S-6

PEDOT:PSS	SWCNTs	85	flexible	P	300	3300	20	132	0.45-0.69	0.03	-	(S18)
PEDOT:PSS	Bi_2Te_3	10	flexible	n	300	55	-110	67	0.558	0.04	-	(S19)
P3HT	Te NWs	25	flexible	p	300	-	285	-	-	-	-	(S20)
P3HT	Bi_2Te_3 NWs	15	flexible	P	300	11.23	110	14	0.75	-	-	(S21)
PANI	Graphene	50	flexible	p	300	123	34	14	0.46	-	-	(S22)
CNTs	PANI	15.8	flexible	p	300	61.47	28.6	5	0.50	0.003	-	(S23)
CNTs	PEDOT:PSS	65	flexible	P	300	380	27	25	0.34	0.02	-	(S24)
CNTs	PDMS	60	flexible	p	300	68	51	18	-	0.0039	-	(S25)
SWCNTs	PANI	58.6	flexible	P	300	125	40	20	1.5	0.004	-	(S26)
SWCNTs	PEDOT:PSS	50	flexible	p	300	900	30	84	-	-	-	(S27)
SWCNTs	PPy	60	flexible	P	300	400	22	20	-	-	-	(S28)
Graphene	PANI	55	flexible	p	300	856	15	19	-	-	-	(S29)
Graphene	PEDOT:PSS	97	flexible	P	300	637	26.8	45.7	-	-	-	(S2)
RGO	PEDOT:PSS	97	flexible	p	300	1160	17	32.6	-	-	-	(S30)

Table S2. Preliminary experiment results of thermoelectric properties of different as-prepared commercial-carbon based composite materials.

Samples composition [a]	σ (S cm^{-1})	S (μV K^{-1})	$S^2\sigma$ (μW m^{-1} K^{-2})
EG (12 MPa 5min) [b]	1017	13.4	18.26
EG (13.5 MPa 10min) [b]	534	12.4	8.21
Commercial Graphite Paper [c]	870	6.85	4.08
34% EG + 60% GIC1	1214	23.48	66.9
34% EG powder + 60% GIC1	985	23.51	54.44
34% EG powder + 60% GIC1 + 6% PF	419	19.1	15.29
34% NG powder + 60% GIC1 + 4% PF + 2% PVB	531	19.7	20.6
EG powder	692	13.9	13.37
34% NG powder + 60% GIC1 + 6% PPS	218	20.1	8.81
60% NG powder + 34% GIC1 + 6% PF	431	20.5	18.11
60% NG powder + 34% GIC1 + 6% PVDF	104	26.2	7.14
34% NG powder + 60% GIC1 + 6% PVDF	40	25.5	2.6
34% NG powder + 60% GIC1 + 6% PF	246.2	18.02	7.99
30% GIC1 + 15% NG powder + 49% CB + 6% PF	124	10.9	1.47
60% GIC1 + 34% NG powder + 6% PBA	166	21.4	7.6
60% GIC1 + 34% NG powder + 4% PBA + 2% PVB	316	23.1	16.86
50% EG + 42.5% CB + 6% PF	281	8.5	2.03
94% EG + 6% PF	796	11.4	10.34
60% EG + 34% GIC1 + 6% PF	830	14	16.27
60% EG + 34% NG powder + 6% PF	802	12.6	12.73
34% EG + 60% NG powder + 6% PF	600	11.7	8.21
45% GIC1 + 25% NG powder + 20% CB + 10% PF	581	15.5	13.96
60% NFG1 + 34% NG powder + 6% PF	698	9.6	6.43
60% NFG2 + 34% NG powder + 6% PF	1039	10.5	11.45
60% GIC1 + 34% NG powder + 6% PF	450	17.4	13.6
60% GIC2 + 34% NG powder + 6% PF	833	18.12	27.35
78.5% EG + 12% GIC2 + 8% CB + 1.5% PVDF	694	11	8.4
78.5% EG + 12% GIC2 + 8% CB + 1.5% PF	525	11.5	6.94
58.5% EG + 24% GIC2 + 16% NG powder + 1.5% PVDF	884	14.9	19.63
58.5% EG + 24% NG powder + 16% GIC2 + 1.5% PVDF	1019	14.3	20.84
78.5% EG + 12% GIC2 + 8% NG powder + 1.5% PVDF	1012	13.5	18.44
78.5% EG + 12% NG powder + 8% GIC2 + 1.5% PVDF	1174	13	19.84
78.5% EG + 20% GIC2 + 1.5% PVDF	935	11.6	12.58
58.5% EG + 40% GIC2 + 1.5% PVDF	695	11.4	9.03
58.5% EG + 40% GIC2 + 1.5% PF	885	12.1	12.96
58.5% EG + 24% GIC2 + 16% NG powder + 1.5% PF	820	10.2	8.53
58.5% EG + 40% GIC2 + 1.5% PVDF	900	13.8	17.14
58.5% EG + 40% GIC2 + 1.5% PF	550	11.8	7.66

[a] EG powder stands for expanded graphite powder which is 90 mesh before expending, NG powder stands for natural graphite powder, CB stands for carbon black, NFG1 stands for 170 mesh natural

flake graphite, NFG2 stands for 90 mesh natural flake graphite, PVB stands for poly(vinyl butyral), PPS stands for poly(phenylene sulfide), PBA stands for poly(butyl acrylate).

[b] According to the thermoelectric results here, all of the other samples are hot-pressed under the condition of 12 MPa, 5min.

[c] Purchased from Qingdao Dong Kai Carbon Co., Ltd. (Shandong, China) with a thickness of 0.3 μm.

Table S3. Preliminary experiment results of thermoelectric properties of the particals with different EG sizes.

Samples composition	σ (S cm^{-1})	S (μV K^{-1})	$S^2\sigma$ (μW m^{-1} K^{-2})
EG_2-GIC2$_8$ [a]	863	21.6	40.26
EG_4-GIC2$_6$	1088	25.2	69.91
EG_6-GIC2$_4$	1209	21.7	56.93
EG_8-GIC2$_2$	1020	11.2	12.79
EG'_2-GIC2$_8$ [b]	811	21.5	37.49
EG'_4-GIC2$_6$	990	24.6	59.91
EG'_6-GIC2$_4$	1021	21.5	47.20
EG'_8-GIC2$_2$	1102	13.8	20.99

[a] EG stands for expanded graphite powder which is 90 mesh before expending, GIC1 stands for 170 mesh graphite intercalation on compounds powder.

[b] EG' stands for expanded graphite powder which is 50 mesh before expending, GIC1 stands for 170 mesh graphite intercalation on compounds powder.

Table S4. Detailed XRD characteristic wavenumbers, integral areas and I_D/I_G values of EG, GIC1, GIC2, EG_2-GIC1$_8$ and EG_3-GIC2$_7$.

Samples	D band		G band		G' band		I_D/I_G
	Wavenumber (cm^{-1})	Integral area	Wavenumber (cm^{-1})	Integral area	Wavenumber (cm^{-1})	Integral area	
EG	1345	426.5	1580	9170.3	2719	9089.4	0.047
GIC1	1354	557.2	1580	8367.1	2724	7602.5	0.067
GIC2	1359	535.1	1580	8570.8	2720	8251.2	0.062
EG_2-GIC1$_8$	1352	987.6	1580	10420.4	2720	9987.7	0.095
EG_3-GIC2$_7$	1354	786.8	1580	8340.3	2721	8113.6	0.094

Table S5. Detailed element content ratios of EG, GIC1, GIC2, EG_2-$GIC1_8$, and EG_3-$GIC2_7$ provided by XPS measurements.

Samples	C1s content (%)	N1s content (%)	O1s content (%)	S2p content (%)
EG	96.57	0.56	2.68	0.19
GIC1	71.62	4.42	19.41	4.55
GIC2	75.55	3.94	16.83	3.68
EG_2-$GIC1_8$	94.54	1.02	3.93	0.50
EG_3-$GIC2_7$	96.68	0.67	2.42	0.23

Table S6. Thermoelectric properties of EG_3-$GIC2_7$ films after different bending cycles.

EG_3-$GIC2_7$ bending cycles	σ (S cm^{-1})	S (μV K^{-1})	$S^2\sigma$ (μW m^{-1} K^{-2})
pristine	1089	28.2	86.60
1	1238	25.6	81.13
2	1058	26.2	72.63
3	995	27.1	73.07
4	989	27.6	75.34
5	1107	25.6	72.55
6	996	26.3	68.89
7	989	27.2	73.17
8	998	26.4	69.56
9	986	26.9	71.35
10	967	27.4	72.60

Table S7. Thermal conductivities of EG_3-$GIC2_7$ films after different bending ratios and bending cycles.

Bending ratios (%)	κ [a] (W m^{-1} K^{-1})	Bending cycles [b]	κ (W m^{-1} K^{-1})
0	9.72	0	9.72
10	8.40	1	7.79
20	7.57	2	7.23
30	7.79	3	7.38
40	6.10	4	6.51
50	5.45	5	5.97
60	5.33	6	5.44
70	5.36	7	6.12
80	4.82	8	4.78
-	-	9	4.05
-	-	10	3.65

Table S8. Hall coefficients and carrier concentrations n of EG_3-$GIC2_7$ films after different bending cycles.

Bending cycles ᵃ	Hall coefficient ᵇ (m^3 C^{-1})	n ᶜ ($\times 10^{20}$ m^{-3})
0	0.04128	1.5141
1	0.04096	1.5257
2	0.04198	1.4889
3	0.04168	1.4995
4	0.04138	1.5103
5	0.04087	1.5293
6	0.04210	1.4845
7	0.04163	1.5012
8	0.04108	1.5216
9	0.04066	1.5373
10	0.04123	1.5159

Table S9. The open-circuit voltage of Device-1 after different bending ratios and bending cycles.

Bending ratios (%)	Average open-circuit voltage (mV)	20 times fluctuation range [a] (mV)	Bending cycles [b]	Open-circuit voltage (mV)	20 times fluctuation range (mV)
0	3.72	3.32~4.08	0	3.72	3.22~4.18
10	3.56	3.28~3.97	1	3.71	3.24~4.00
20	3.63	3.25~4.02	2	3.74	3.12~4.19
30	3.67	3.22~4.12	3	3.65	3.05~4.13
40	3.62	3.17~4.17	4	3.67	3.13~4.21
50	3.58	2.95~4.08	5	3.70	3.01~4.27
60	3.65	2.81~4.37	6	3.62	2.88~4.29
70	3.52	2.70~4.35	7	3.57	2.83~4.16
80	3.47	2.68~4.46	8	3.64	2.96~4.22
-	-	-	9	3.61	2.85~4.38
-	-	-	10	3.56	2.76~4.01

[a] Open-circuit voltage fluctuation range among 20 times' measurements.

[b] Bending ratios of all cycles were kept at 30 %.

Table S10. The open-circuit voltage of Device-2 after different bending ratios and bending cycles.[a]

Bending ratios (%)	Average open-circuit voltage (mV)	20 times fluctuation range [b] (mV)	Bending cycles [c]	Average open-circuit voltage (mV)	20 times fluctuation range (mV)
0	1.31	0.94~1.67	0	1.31	0.94~1.67
10	1.33	1.02~1.65	1	1.30	0.91~1.63
20	1.29	1.02~1.72	2	1.33	0.88~1.56
30	1.30	0.96~1.63	3	1.27	0.90~1.66
40	1.28	0.91~1.60	4	1.29	0.93~1.69
50	1.29	0.96~1.65	5	1.30	0.99~1.71
60	1.26	0.89~1.63	6	1.27	0.85~1.60

70	1.29	0.95~1.59	7	1.31	1.04~1.70
80	1.27	0.87~1.61	8	1.28	0.88~1.59
-	-	-	9	1.26	0.91~1.67
-	-	-	10	1.29	0.86~1.64

[a] Tests were conducted in the scene of submerging in the river water as cold side ($\Delta T = 1.6$ °C).

[b] Open-circuit voltage fluctuation range among 20 times' measurements.

[c] Bending ratios of all cycles were kept at 30 %.

Table S11. Thermoelectric properties and thicknesses of EG_3-$GIC2_7$ films with different pressing pressures and pressing times.

EG_3-$GIC2_7$ pressing method	σ (S cm^{-1})	S (μV K^{-1})	$S^2\sigma$ (μW m^{-1} K^{-2})	Thickness (mm)
8 MPa	709	23.9	40.50	0.34
10 MPa	940	24.5	56.40	0.31
12 MPa	1089	28.2	86.60	0.32
15 MPa	982	25.8	65.37	0.30
15 MPa, 1 time [a]	1089	28.2	86.60	0.32
15 MPa, 3 time	1230	24.9	76.26	0.30
15 MPa, 5 time	1138	24.5	68.31	0.25
15 MPa, 7 time	1091	21.2	49.03	0.23

[a] 5 min for each time.

Table S12. Sizes of the samples corresponding to the measurement of the thermoelectric performances.[a]

Samples	Length (mm)	Width (mm)	Thickness (mm)
EG	22.13	7.91	0.31
GIC1	21.02	7.37	0.30
GIC2	22.89	7.58	0.30
EG_1-$GIC1_9$	21.68	7.97	0.28
EG_2-$GIC1_8$	22.10	7.62	0.30
EG_3-$GIC1_7$	21.53	7.32	0.27

EG$_4$-GIC1$_6$	21.95	7.59	0.28
EG$_5$-GIC1$_5$	22.64	7.44	0.31
EG$_6$-GIC1$_4$	21.72	7.48	0.30
EG$_7$-GIC1$_3$	22.55	7.27	0.31
EG$_8$-GIC1$_2$	21.96	7.73	0.32
EG$_9$-GIC1$_1$	22.12	7.30	0.31
EG$_1$-GIC2$_9$	22.02	7.85	0.31
EG$_2$-GIC2$_8$	21.87	7.46	0.28
EG$_3$-GIC2$_7$	22.77	7.25	0.32
EG$_4$-GIC2$_6$	22.60	7.32	0.30
EG$_5$-GIC2$_5$	21.82	7.61	0.29
EG$_6$-GIC2$_4$	22.35	7.55	0.30
EG$_7$-GIC2$_3$	22.33	7.59	0.32
EG$_8$-GIC2$_2$	21.92	7.81	0.31
EG$_9$-GIC2$_1$	21.75	7.32	0.31

[a] Samples were used for the measurement of the thermoelectric properties shown in **Figures 2a-c**.

REFERENCES

(S1) Xu, K.; Chen, G.; Qiu, D. Convenient construction of poly(3,4-ethylenedioxythiophene)–graphene pie-like structure with enhanced thermoelectric performance. *J. Mater. Chem. A* **2013**, *1*, 12395.

(S2) Yoo, D.; Kim, J.; Kim, J. H. Direct synthesis of highly conductive poly(3,4-ethylenedioxythiophene):poly(4-styrenesulfonate) (PEDOT:PSS)/graphene composites and their applications in energy harvesting systems. *Nano Res.* **2014**, *7*, 717-730.

(S3) Qu, S.; Yao, Q.; Wang, L.; Chen, Z.; Xu, K.; Zeng, H.; Shi, W.; Zhang, T.; Uher, C.; Chen, L. Highly anisotropic P3HT films with enhanced thermoelectric performance via organic small molecule epitaxy. *NPG Asia Mater.* **2016**, *8*, e292-e292.

(S4) Reddy, B. N.; Deepa, M.; Joshi, A. G.; Srivastava, A. K. Poly(3,4-Ethylenedioxypyrrole) Enwrapped by Reduced Graphene Oxide: How Conduction Behavior at Nanolevel Leads to Increased Electrochemical Activity. *J. Phys. Chem. C* **2011**, *115*, 18354-18365.

(S5) Andrei, V.; Bethke, K.; Rademann, K. Adjusting the thermoelectric properties of copper(I) oxide-graphite-polymer pastes and the applications of such flexible composites. *Phys. Chem. Chem. Phys.* **2016**, *18*, 10700-10707.

(S6) Wei, J.; Zhao, L.; Zhang, Q.; Nie, Z.; Hao, L. Enhanced thermoelectric properties of cement-based composites with expanded graphite for climate adaptation and large-scale energy harvesting. *Energ. Buildings* **2018**, *159*, 66-74.

(S7) Wei, J.; Zhang, Q.; Zhao, L.; Hao, L.; Yang, C. Enhanced thermoelectric properties of carbon fiber reinforced cement composites. *Ceram. Int.* **2016**, *42*, 11568-11573.

(S8) Javadi, R.; Choi, P. H.; Park, H. S.; Choi, B. D. Preparation and Characterization of P-Type and N-Type Doped Expanded Graphite Polymer Composites for Thermoelectric Applications. *J. Nanosci. Nanotechnol.* **2015**, *15*, 9116-9119.

(S9) Culebras, M.; Gómez, C. M.; Cantarero, A. Thermoelectric measurements of PEDOT:PSS/expanded graphite composites. *J. Mater. Sci.* **2012**, *48*, 2855-2860.

(S10) Piao, M.; Kim, G.; Kennedy, G. P.; Roth, S.; Dettlaff-Weglikowska, U. Preparation and characterization of expanded graphite polymer composite films for thermoelectric applications. *Phys. Status Solidi B* **2013**, *250*, 2529-2534.

(S11) Wei, J.; Li, X.; Wang, Y.; Chen, B.; Qiao, S.; Zhang, Q.; Xue, F. Record high thermoelectric performance of expanded graphite/carbon fiber cement composites enhanced by ionic liquid 1-butyl-3-methylimidazolium bromide for building energy harvesting. *J. Mater. Chem. C* **2021**, *9*, 3682-3691.

(S12) Xu, K.; Chen, G.; Qiu, D. In situ chemical oxidative polymerization preparation of poly(3,4-ethylenedioxythiophene)/graphene nanocomposites with enhanced thermoelectric performance. *Chem. Asian J.* **2015**, *10*, 1225-1231.

(S13) Liu, C.; Jiang, F.; Huang, M.; Lu, B.; Yue, R.; Xu, J. Free-Standing PEDOT-PSS/Ca3Co4O9 Composite Films as Novel Thermoelectric Materials. *J. Electron. Mater.* **2010**, *40*, 948-952.

(S14) We, J. H.; Kim, S. J.; Cho, B. J. Hybrid composite of screen-printed inorganic thermoelectric film and organic conducting polymer for flexible thermoelectric power generator. *Energy* **2014**, *73*, 506-512.

(S15) Ju, H.; Kim, J. Chemically Exfoliated SnSe Nanosheets and Their SnSe/Poly(3,4-ethylenedioxythiophene):Poly(styrenesulfonate) Composite Films for Polymer Based Thermoelectric Applications. *ACS Nano* **2016**, *10*, 5730-5739.

(S16) See, K. C.; Feser, J. P.; Chen, C. E.; Majumdar, A.; Urban, J. J.; Segalman, R. A. Water-processable polymer-nanocrystal hybrids for thermoelectrics. *Nano Lett.* **2010**, *10*, 4664-4667.

(S17) Bae, E. J.; Kang, Y. H.; Jang, K. S.; Cho, S. Y. Enhancement of Thermoelectric Properties of PEDOT:PSS and Tellurium-PEDOT:PSS Hybrid Composites by Simple Chemical Treatment. *Sci. Rep.* **2016**, *6*, 18805.

(S18) Moriarty, G. P.; De, S.; King, P. J.; Khan, U.; Via, M.; King, J. A.; Coleman, J. N.; Grunlan, J. C. Thermoelectric behavior of organic thin film nanocomposites. *J. Polym. Sci. Part B: Polym. Phys.* **2013**, *51*, 119-123.

(S19) Zhang, B.; Sun, J.; Katz, H. E.; Fang, F.; Opila, R. L. Promising thermoelectric properties of commercial PEDOT:PSS materials and their bi2Te3 powder composites. *ACS Appl. Mater. Inter.* **2010**, *2*, 3170-3178.

(S20) Yang, Y.; Lin, Z.-H.; Hou, T.; Zhang, F.; Wang, Z. L. Nanowire-composite based flexible thermoelectric nanogenerators and self-powered temperature sensors. *Nano Res.* **2012**, *5*, 888-895.

(S21) He, M.; Ge, J.; Lin, Z.; Feng, X.; Wang, X.; Lu, H.; Yang, Y.; Qiu, F. Thermopower enhancement in conducting polymer nanocomposites via carrier energy scattering at the organic–inorganic semiconductor interface. *Energ. Environ. Sci.* **2012**, *5*, 8351.

(S22) Abad, B.; Alda, I.; Díaz-Chao, P.; Kawakami, H.; Almarza, A.; Amantia, D.; Gutierrez, D.; Aubouy, L.; Martín-González, M. Improved power factor of polyaniline nanocomposites with exfoliated graphene nanoplatelets (GNPs). *J. Mater. Chem. A* **2013**, *1*, 10450.

(S23) Meng, C.; Liu, C.; Fan, S. A promising approach to enhanced thermoelectric properties using carbon nanotube networks. *Adv. Mater.* **2010**, *22*, 535-539.

(S24) Kim, D.; Kim, Y.; Choi, K.; Grunlan, J. C.; Yu, C. Improved thermoelectric behavior of nanotube-filled polymer composites with poly(3,4-ethylenedioxythiophene) poly(styrenesulfonate). *ACS Nano* **2010**, *4*, 513-523.

(S25) Prabhakar, R.; Hossain, M. S.; Zheng, W.; Athikam, P. K.; Zhang, Y.; Hsieh, Y.-Y.; Skafidas, E.; Wu, Y.; Shanov, V.; Bahk, J.-H. Tunneling-Limited Thermoelectric Transport in Carbon Nanotube Networks Embedded in Poly(dimethylsiloxane) Elastomer. *ACS Appl. Energ. Mater.* **2019**, *2*, 2419-2426.

(S26) Yao, Q.; Chen, L.; Zhang, W.; Liufu, S.; Chen, X. Enhanced thermoelectric performance of single-walled carbon nanotubes/polyaniline hybrid nanocomposites. *ACS Nano* **2010**, *4*, 2445-2451.

(S27) Song, H.; Qiu, Y.; Wang, Y.; Cai, K.; Li, D.; Deng, Y.; He, J. Polymer/carbon nanotube composite materials for flexible thermoelectric power generator. *Compos. Sci. Technol.* **2017**, *153*, 71-83.

(S28) Liang, L.; Gao, C.; Chen, G.; Guo, C.-Y. Large-area, stretchable, super flexible and mechanically stable thermoelectric films of polymer/carbon nanotube composites. *J. Mater. Chem. C* **2016**, *4*, 526-532.

(S29) Wang, L.; Yao, Q.; Bi, H.; Huang, F.; Wang, Q.; Chen, L. Large thermoelectric power factor in polyaniline/graphene nanocomposite films prepared by solution-assistant dispersing method. *J. Mater. Chem. A* **2014**, *2*, 11107.

(S30) Li, F.; Cai, K.; Shen, S.; Chen, S. Preparation and thermoelectric properties of reduced graphene oxide/PEDOT:PSS composite films. *Synthetic Met.* **2014**, *197*, 58-61.

APPENDIX B: SUPPORTING INFORMATION FOR PAPER 3

This appendix B is attached as the Supporting Information (published) for the paper 3 in chapter 5: Ultrafast and cost-effective fabrication of high-performance carbon-based flexible thermoelectric hybrid films and their devices.

Ultrafast and cost-effective fabrication of high-performance carbon-based flexible thermoelectric hybrid films and their devices

Shuai Sun[a,b], Xiao-Lei Shi[b*], Meng Li[b], Ting Wu[c], Liangcao Yin[c], Dezhuang Wang[c], Qingfeng Liu[c], and Zhi-Gang Chen[b*]

[a] *Centre for Future Materials, University of Southern Queensland, Springfield Central, Queensland 4300, Australia.*

[b] *School of Chemistry and Physics and Center for Materials Science, Queensland University of Technology, Brisbane City QLD 4000, Australia.*

[c] *State Key Laboratory of Materials Oriented Chemistry Engineering, College of Chemistry Engineering, Nanjing Tech University, Nanjing 211800, China.*

*E-mail: xiaolei.shi@qut.edu.au (XLS); zhigang.chen@qut.edu.au (ZGC)
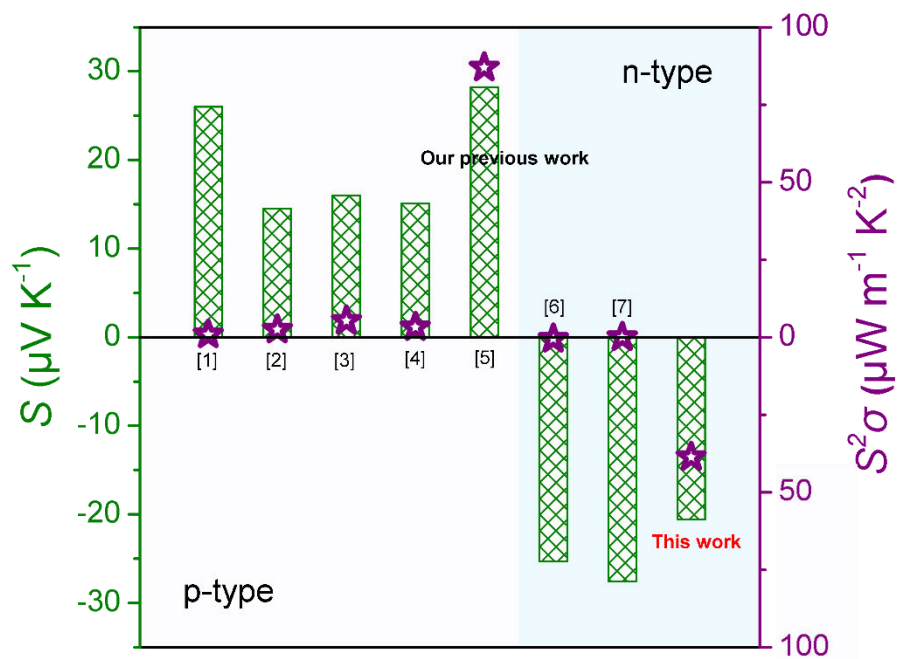
Figure S1. Comparison of the Seebeck coefficients S and power factors $S^2\sigma$ of $EG_{70}CF_{27}PF_3IL_6$ (this work) with other traditional carbon-based materials [1-7].

Figure S2. Scanning electron microscopy (SEM) images of $EG_{70}CF_{27}PF_3IL_6$ corresponding to the energy dispersive spectrometer (EDS) mapping results.
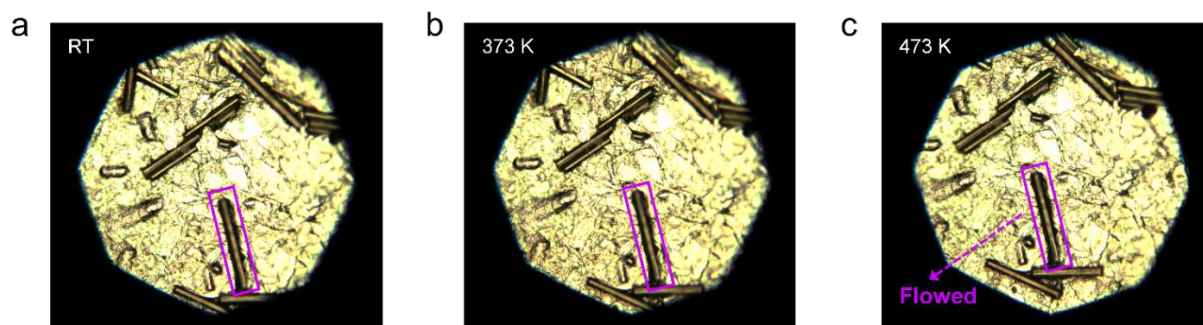
Figure S3. Polarizing optical microscope (POM) imagines of $EG_{70}CF_{27}PF_3IL_6$ at (**a**) 273 K, (**b**) 373 K, and (**c**) 473 K.

a

b

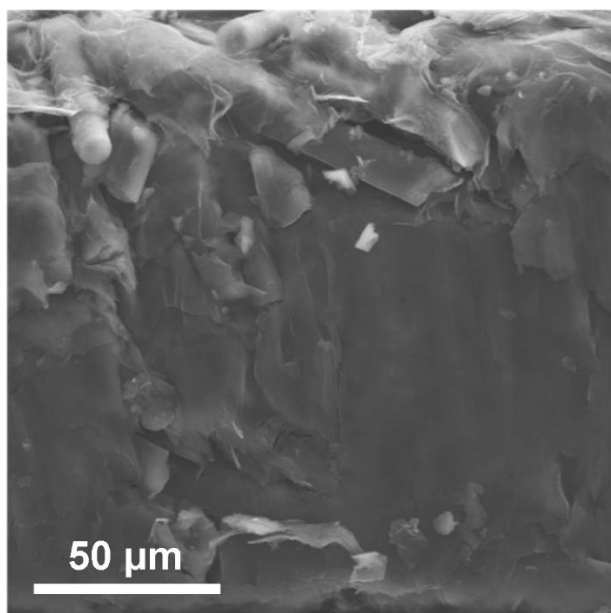Vertical view   Heat stage   Temperature meter

Universal meter   Universal meter   Circuit   Variable
(current mode)   (voltage mode)   connection   resistor
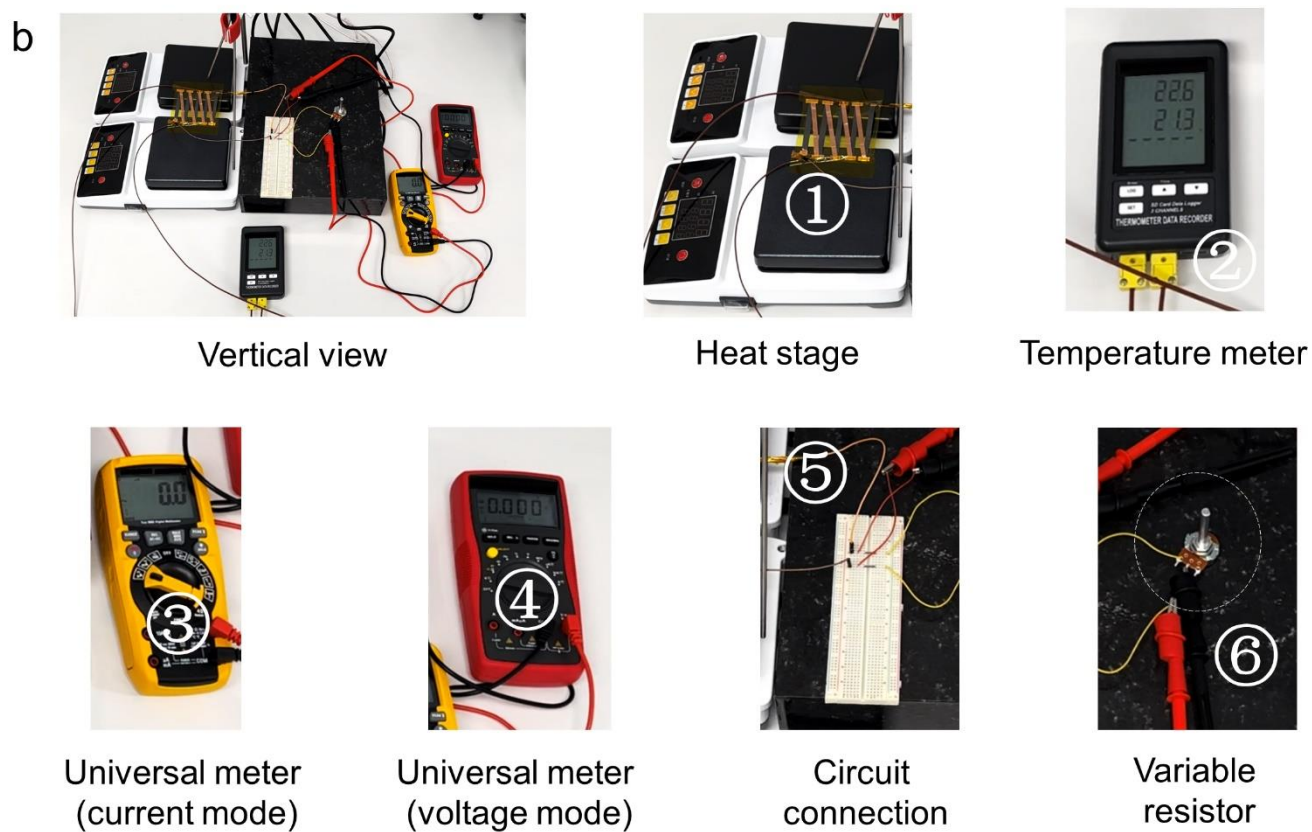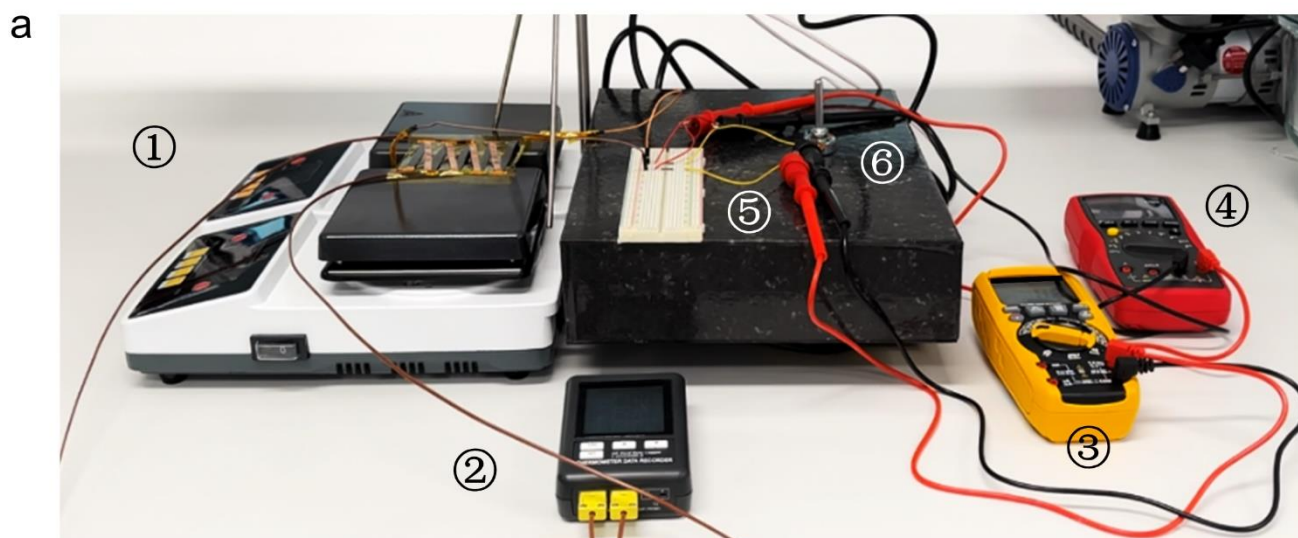
Figure S4. (a) Structure and (b) elements of the equipment connection to evaluate the as-fabricated device (based on $EG_{70}CF_{27}PF_3IL_6$) properties.

166
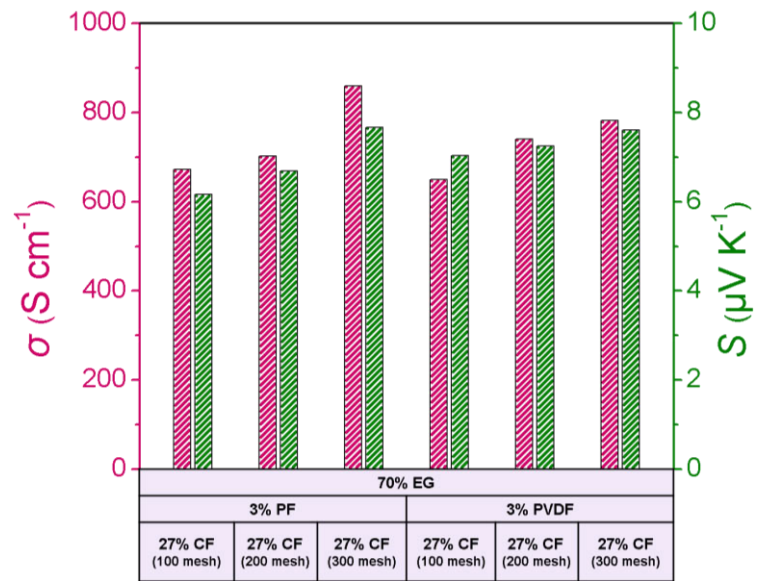
Figure S5. Electrical conductivitiy σ and S of $EG_{70}CF_{27}PF_3$ and $EG_{70}CF_{27}PVDF_3$ with different particle sizes.

Figure S6. Thermoelectric properties comparation including (**a**) σ, S and (**b**) $S^2\sigma$ of EG$_{70}$CF$_{27}$PF$_3$IL$_x$ introducing ionic liquids by the method of soak and spray respectively.

Table S1. Detailed element content ratios of EG$_{70}$CF$_{27}$PF$_3$, EG$_{70}$CF$_{27}$PF$_3$IL$_2$, EG$_{70}$CF$_{27}$PF$_3$IL$_6$, and EG$_{70}$CF$_{27}$PF$_3$IL$_{10}$ provided by X-ray photoelectron spectroscopy (XPS) measurements.

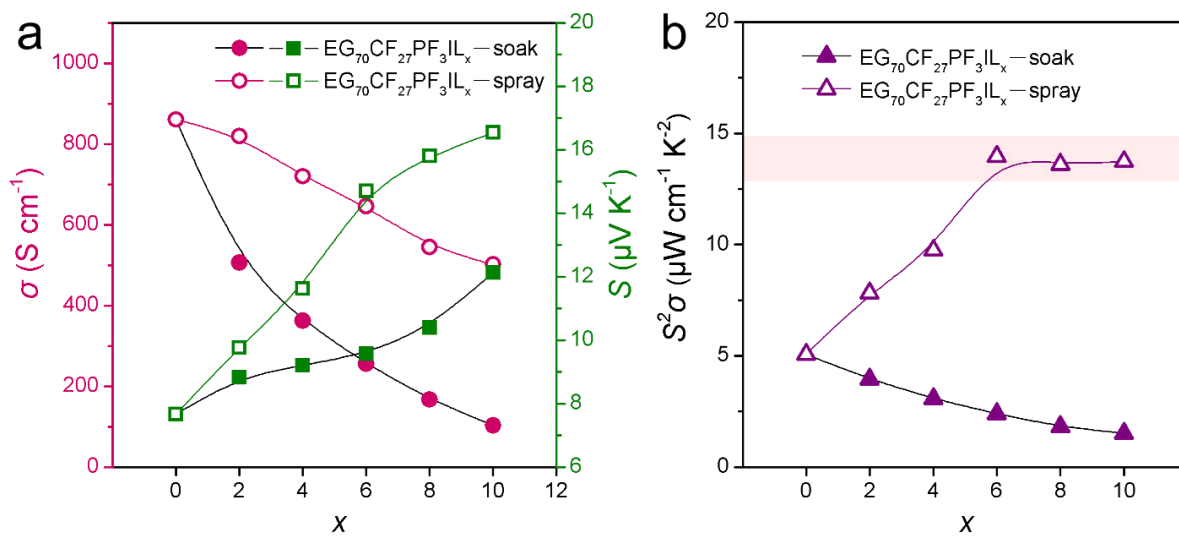| Samples	C1s content (%)[a]	N1s content (%)[a]	O1s content (%)[a]	Calculated compounds[b]
EG$_{70}$CF$_{27}$PF$_3$	89.57	–	10.43	
EG$_{70}$CF$_{27}$PF$_3$IL$_2$	88.96	0.80	10.24	EG$_{70}$CF$_{27}$PF$_3$IL$_{2.33}$
EG$_{70}$CF$_{27}$PF$_3$IL$_6$	88.79	2.15	9.05	EG$_{70}$CF$_{27}$PF$_3$IL$_{6.54}$
EG$_{70}$CF$_{27}$PF$_3$IL$_{10}$	87.89	3.30	8.81	EG$_{70}$CF$_{27}$PF$_3$IL$_{10.38}$

[a] All of the element contents displayed are counted by atom%.

[b] The theoritical compounds of EG$_{70}$CF$_{27}$PF$_3$IL$_x$ are estimatedly calculated by the fomular of $x = \dfrac{c_N \times \frac{M_{[EMIM:DCA]}}{n_N}}{(c_C \times 12 + c_N \times 14 + c_O \times 16) - c_N \times \frac{M_{[EMIM:DCA]}}{n_N}}$, where n_N .is the number of nitrogen atoms in [EMIM:DCA] molecule (namely 5), $M_{[EMIM:DCA]}$ is the relative molecular mass of [EMIM:DCA] molecule (namely 177), and c_N, c_C, c_N, c_O are contents of the corresponding element shown in **Table S1**. Herein, the EG$_{70}$CF$_{27}$PF$_3$ contents are treated as an integration and hydrogen contents in EG$_{70}$CF$_{27}$PF$_3$ are neglected.

Table S2. Detailed X-ray diffraction (XRD) normalized peak area and I_{002}/I_{004} of $EG_{70}CF_{27}PF_3$, $EG_{70}CF_{27}PF_3IL_2$, $EG_{70}CF_{27}PF_3IL_6$, and $EG_{70}CF_{27}PF_3IL_{10}$.

Samples	Normalized peak area		A_{002}/A_{004}
	(002)	(004)	
$EG_{70}CF_{27}PF_3$	0.3207	0.0113	28.38
$EG_{70}CF_{27}PF_3IL_2$	0.3290	0.0182	18.08
$EG_{70}CF_{27}PF_3IL_6$	0.3266	0.0209	15.63
$EG_{70}CF_{27}PF_3IL_{10}$	0.3220	0.0204	15.78

Table S3. Comparison of the σ, S, $S^2\sigma$, ZT, tensile strength, and elongation at break of as-prepared $EG_{70}CF_{27}PF_3IL_6$, and some carbon-based thermoelectric materials reported in literature. Here PC is the abbreviation for polycarbonate, PANI is the abbreviation for polyaniline, PEDOT:PSS is the abbreviation for poly(3,4-ethylenedioxythiophene):poly(styrene sulfonate), GIC is the abbreviation for graphite intercalation on compounds, PVA is the abbreviation for polyvinyl alcohol, PEI is the abbreviation for polyethyleneimine, SWCNT is the abbreviation for single-walled carbon nanotube, PP is the abbreviation for polypropylene, PPy is the abbreviation for polypyrrole, CFF is the abbreviation for carbon fiber fabric, and GO is the abbreviation for graphene oxide.

Samples	σ (S cm^{-1})	S (μV K^{-1})	$S^2\sigma$ (μW m^{-1} K^{-2})	ZT	Tensile strength (MPa)	Elongation (%)	Ref.
$EG_{70}CF_{27}PF_3IL_6$	911.7	−20.6	38.7	1.7×10^{-3}	1.52	4.27	this work
EG-PC	11.4	~26.0	~0.8	–	–	–	[1]
EG-PANI	116.0	14.5	2.4	–	–	–	[2]
EG-PEDOT:PSS	213.0	16.0	5.3	–	–	–	[3]
Graphite-PEDOT	80.1	15.1	3.2	–	–	–	[4]
EG_3GIC_7	1089.0	28.2	87.0	0.026	0.68	0.84	[5]
EG-PVA-PEI	~10	−25.3	0.6	–	–	–	[6]
SWCNT-PP-IL	0.8	−27.6	0.057	8.5×10^{-5}	–	–	[7]
SWCNT-PEDOT:PSS-IL	1602.6	33.4	182.7	–	6.8	7.1	[8]
SWCNT-PPy	399.0	22.2	19.7	–	14.2	3.2	[9]
Bi_2Te_3-CFF	~280	−33.6	33.4	–	5.3	10.0	[10]
Treated GO fiber	~23.0	~19.3	~1.0	–	99.5	0.96	[11]
SWCNT-PC	~55.0	~34.0	6.2	–	54	~1.5	[12]

Table S4. Tensile strength, elongation at break, and thickness of $EG_{70}CF_{27}PF_3$, $EG_{70}CF_{27}PF_3IL_2$, $EG_{70}CF_{27}PF_3IL_6$, and $EG_{70}CF_{27}PF_3IL_{10}$.

Samples	Tensile strength (MPa)	Elongation (%)	Thickness (mm)
$EG_{70}CF_{27}PF_3$	1.55	6.4	0.10
$EG_{70}CF_{27}PF_3IL_2$	1.65	6.4	0.09
$EG_{70}CF_{27}PF_3IL_6$	1.52	4.27	0.11
$EG_{70}CF_{27}PF_3IL_{10}$	1.28	2.64	0.09

REFERENCES

(1) Javadi, R.; Choi, P. H.; Park, H. S.; Choi, B. D. Preparation and Characterization of P-Type and N-Type Doped Expanded Graphite Polymer Composites for Thermoelectric Applications. *J. Nanosci. Nanotechno.* **2015**, *15*, 9116-9119.

(2) Pan, C.; Zhang, L.; Pan, Z.; Chen, M.; Liu, Y.; Huang, G.; Na, H.; Wang, W.; Qiu, H.; Gao, J. A Simple Strategy to Fabricate Polyaniline/Expanded Graphite Composites with Improved Power Factor. *Mater. Chem. Phys.* **2015**, *167*, 315-319.

(3) Culebras, M.; Gómez, C. M.; Cantarero, A. Thermoelectric Measurements of PEDOT:PSS/Expanded Graphite Composites. *J. Mater. Sci.* **2013**, *48*, 2855-2860.

(4) Du, Y.; Li, H.; Jia, X.; Dou, Y.; Xu, J.; Eklund, P. Preparation and Thermoelectric Properties of Graphite/Poly(3,4-Ethyenedioxythiophene) Nanocomposites. *Energies* **2018**, *11*, 2849.

(5) Sun, S.; Shi, X.-L.; Liu, W.-D.; Wu, T.; Wang, D.; Wu, H.; Zhang, X.; Wang, Y.; Liu, Q.; Chen, Z.-G. Cheap, Large-Scale, and High-Performance Graphite-Based Flexible Thermoelectric Materials and Devices with Supernormal Industry Feasibility. *ACS Appl. Mater. Interfaces* **2022**, *14*, 8066-8075.

(6) Piao, M.; Kim, G.; Kennedy, G. P.; Roth, S.; Dettlaff-Weglikowska, U. Preparation and Characterization of Expanded Graphite Polymer Composite Films for Thermoelectric Applications. *physica status solidi (b)* **2013**, *250*, 2529-2534.

(7) Voigt, O.; Krause, B.; Pötschke, P.; Müller, M. T.; Wießner, S. Thermoelectric Performance of Polypropylene/Carbon Nanotube/Ionic Liquid Composites and Its Dependence on Electron Beam Irradiation. *J. Compos. Sci.* **2022**, *6*, 25.

(8) Deng, W.; Deng, L.; Hu, Y.; Zhang, Y.; Chen, G. Thermoelectric and Mechanical Performances of Ionic Liquid-Modulated PEDOT:PSS/SWCNT Composites at High Temperatures. *Soft Sci.* **2021**, *1*, 14.

(9) Liang, L.; Gao, C.; Chen, G.; Guo, C.-Y. Large-Area, Stretchable, Super Flexible and Mechanically Stable Thermoelectric Films of Polymer/Carbon Nanotube Composites. *J. Mater. Chem. C* **2016**, *4*,

526-532.

(10) Shi, T.; Chen, M.; Zhang, C.; Mao, Z.; Liang, J.; Liu, Z.; Zhang, J.; Zhang, Q.; Pan, L.; Wang, Y.; Wan, C.; Zong, P.-a. Modifying Carbon Fiber Fabric for Flexible Thermoelectric Energy Conversion. *Appl. Surf. Sci.* **2023**, *610*, 155479.

(11) Lin, Y.; Liu, J.; Wang, X.; Xu, J.; Liu, P.; Nie, G.; Liu, C.; Jiang, F. An Integral *p-n* Connected All-Graphene Fiber Boosting Wearable Thermoelectric Energy Harvesting. *Compos. Commun.* **2019**, *16*, 79-83.

(12) Zhang, Y.; Hu, Y.; Li, Z.; Deng, L.; Chen, G. Decoupling the Trade-Off between Thermoelectric and Mechanical Performances for Polymer Composites *via* Interfacial Regulation. *Compos. Sci. Technol.* **2022**, *222*, 109373.

APPENDIX C: SUPPORTING INFORMATION FOR PAPER 4

This appendix C is attached as the Supporting Information (under submission) for the paper 4 in chapter 6: Stable, self-healable and high-performance graphene-oxide-modified flexible ionogel thermoelectric films and their devices.

Supporting Information

Stable, Self-Healable, and High-Performance Graphene-Oxide-Modified Flexible Ionogel Thermoelectric Films and Their Devices

Shuai Sun,[1,2] Xiao-Lei Shi,[2]* Wanyu Lyu,[2] Min Hong,[1] Wenyi Chen,[2,3] Meng Li,[2] Tianyi Cao,[2] Boxuan Hu,[2] Qingfeng Liu,[4] and Zhi-Gang Chen[1,2]*

[1]Centre for Future Materials, University of Southern Queensland, Springfield Central, Queensland 4300, Australia;

[2]School of Chemistry and Physics and Center for Materials Science, Queensland University of Technology, Brisbane City QLD 4000, Australia;

[3]School of Mechanical and Mining Engineering, The University of Queensland, Brisbane, Queensland 4072, Australia;

[4]State Key Laboratory of Materials Oriented Chemistry Engineering, College of Chemistry Engineering, Nanjing Tech University, Nanjing 211800, China;

* E-mail address: xiaolei.shi@qut.edu.au (XLS); zhigang.chen@qut.edu.au (ZGC)

Experimental details

Materials: Acrylamide (AM, ≥99.0 %), 1-butyl-3-methylimidazolium chloride (BMIM:Cl, ≥99.0 %), ammonium persulfate (APS, ≥98.0 %), N,N′-methylenebis acrylamide (MBA, ≥99.5 %), graphene oxide (GO, 2 mg mL^{-1}, dispersion in H$_2$O), and deionized water were purchased from Sigma-Aldrich (Brisbane, Australia) and used as received.

Fabrication of the PAM$_{0.3}$-BMIM:Cl$_{0.6}$-GO$_x$ films: Typically, metered BMIM:Cl, 1.5 g AM, 0.005 g APS (as the initiator), 0.0075 g MBA (as the crosslinking agent) and 4.0 g deionized water (as the solvent) were mixed homogeneously in a sample bottle. Afterwards, the solution was transferred into an ice bath, where metered GO solution was dropped to the solution. After feeding all these raw materials, the obtained solution was ultrasonically dispersed for 2 h with constant ice bath. Subsequently, the PAM$_{0.3}$-BMIM:Cl$_{0.6}$-GO$_x$ ionogels were synthesized *via* the free radical polymerization. Specifically, the prepared solution was poured into a designed glass module (with cover) and nitrogen purged to remove air. Afterwards, the above film-like molded solution was cured in a 333 K bake oven for 100 min. At last, the bare ionogel film was annealed at 383 K under air environment for 5 h, obtaining the as-prepared ionic thermoelectric film. The fabricated samples were denoted as PAM$_{0.3}$-BMIM:Cl$_{0.6}$-GO$_x$, where 0.3, 0.6, and x are the mass content of PAM, BMIM:Cl, and GO solution respectively. For instance, PAM$_{0.3}$-BMIM:Cl$_{0.6}$-GO$_1$ were pre-prepared by the solution of 1.5 g AM, 3.0 g BMIM:Cl, 5.0 g GO solution, 0.005 g VA-044, 0.0075 g MBA and 4.0 g deionized water before curing.

Self-healing process of the as-prepared PAM$_{0.3}$-BMIM:Cl$_{0.6}$-GO$_1$: In this work, the σ and S of the self-healed PAM$_{0.3}$-BMIM:Cl$_{0.6}$-GO$_1$ film are tested for the comparation of stability. The self-healing ability is endowed by the hydrogen bonds between PAM amino-groups and BMIM:Cl and the self-healing process is conducted as follows: tailored PAM$_{0.3}$-BMIM:Cl$_{0.6}$-GO$_1$ film is cut into two pieces and separated from each other, then they were reattached again and close contacted ensured by the self-adhesivity at room temperature. After healing for 10 h, the recovered film was applied for further

characterizations.

Fabrication of thermoelectric device: Based on $PAM_{0.3}$-$BMIM:Cl_{0.6}$-GO_1, the thermoelectric device was integrated. A 1 mm thick silicone plate was cut into 25×25 mm^2 size and the internal patterns were also designed and cut. Specifically, 9 pieces of 5×5 mm^2 holes are designed for thermoelectric legs and slits between them are designed for the penetration of copper foils. Subsequently, above-mentioned prepared mixture solutions were dropped into the holes in the silicone plate and cured, annealed using the introduced fabrication method. After finishing the integration process, copper foiled were pasted onto the thermoelectric legs in an end-to-end manner. No glues were added here because of the $PAM_{0.3}$-$BMIM:Cl_{0.6}$-GO_1 is self-adhesive. By pasting two layers of polyimide tapes at the top and bottom surfaces for isolation, the as-prepared thermoelectric device was obtained.

Characterizations: Chemical structures of as-prepared inongels are determined by attenuated total reflectance Fourier transform infrared reflection (Nicolet iS50 FT-IR, USA) spectra with a wavenumber of 500−4000 cm^{-1}. The resolution was set as 4 cm^{-1}. Crystal structures were investigated by X-ray diffraction (Rigaku SmartLab XRD, Japan) using a 9 kW Cu rotating anode source. The operating scan rate is 0.02° s^{-1}. Characteristics of the GO component was analyzed from the Raman spectra (Witec Confocal Raman microscope, Germany) within the range of 100−3000 cm^{-1}. The selected laser wavelength was 532 nm. X-ray Photoemission Spectroscopy (Kratos Axis Supra XPS, Japan) was employed to determine the element content and binding information. Scanning electron microscopy equipped with energy-dispersive X-ray spectroscopy (JEOL 7001F SEM, Japan) was used for detecting the surface morphologies and element distributions. The samples were platinum sprayed before testing. Microforce testing system (Tytron 250 MTS, USA) was employed for the tensile properties determination. The tensile speed is 1 mm min^{-1} and each data was defined by an average of at least five measurements. Toughness data was obtained by calculating the area within the corresponding stress-strain curve. For thermoelectric properties, the S and σ values were measured using a four-probe method (ZEM-3, NETZSCH, Germany) in high-vacuum atmosphere. The κ values

were calculated from $\kappa = D \times C_p \times \rho$, in which C_p is the specific heat capacity measured by DSC (NETZSCH, Germany) *via* the sapphire method, D is the thermal diffusivity coefficient measured by laser-flash diffusivity method (LFA467, NETZSCH, Germany), and ρ is measured by a gas pycnometer method (Ultrapyc 5000, Austria).
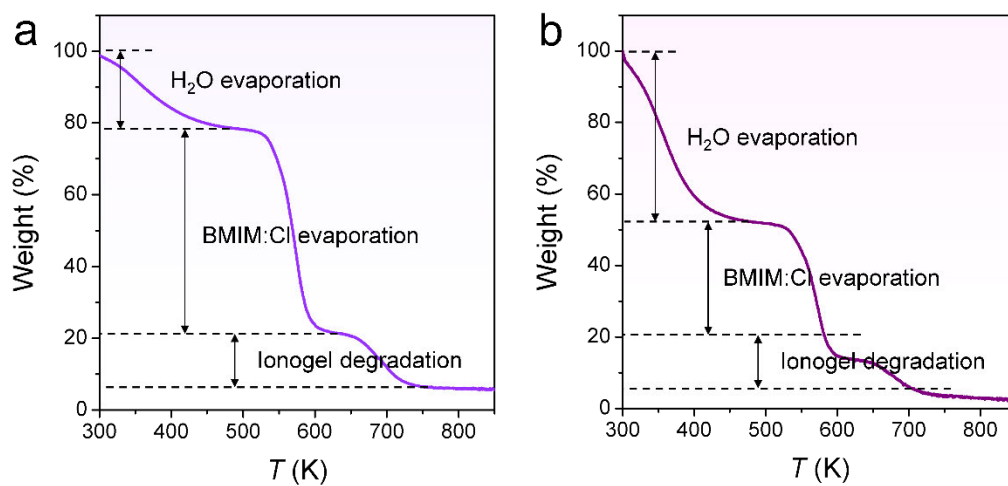
Figure S1. Comparison of the Thermogravimetric analysis (TGA) curves of (**a**) unannealed $PAM_{0.3}$-$BMIM:Cl_{0.6}$-GO_1 as final product in this work and (**b**) unannealed $PAM_{0.3}$-$BMIM:Cl_{0.6}$-GO_1 under the air environment.
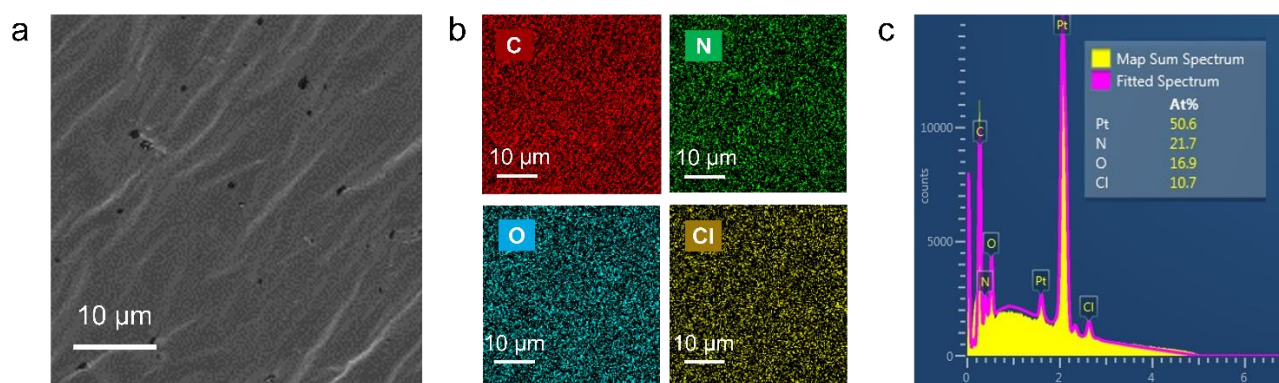
Figure S2. (**a**) Scanning electron microscopy (SEM) image, (**b**) corresponding X-ray spectroscopy (EDS) mapping for C, N, O, and Cl elements, and (**c**) corresponding EDS spectra of a random area of $PAM_{0.3}$-$BMIM:Cl_{0.6}$-GO_1 after placing in the air for 7 days.

Table S1. Detailed element content ratios of pristine GO, $PAM_{0.3}$-$BMIM{:}Cl_{0.6}$, $PAM_{0.3}$-$BMIM{:}Cl_{0.6}$-$GO_{0.4}$, annealed $PAM_{0.3}$-$BMIM{:}Cl_{0.6}$-GO_1 as final product in this work, and unannealed $PAM_{0.3}$-$BMIM{:}Cl_{0.6}$-GO_1 provided by X-ray photoelectron spectroscopy (XPS) measurements.

Samples	C1s content (%)[a]	N1s content (%)[a]	O1s content (%)[a]	Cl2p content (%)[a]
pristine GO	75.36	1.05	23.59	−
$PAM_{0.3}$-$BMIM{:}Cl_{0.6}$	73.21	13.09	9.30	4.40
$PAM_{0.3}$-$BMIM{:}Cl_{0.6}$-$GO_{0.4}$	75.91	10.17	10.27	3.65
As-prepared $PAM_{0.3}$-$BMIM{:}Cl_{0.6}$-GO_1	75.19	11.53	9.67	3.60
Unannealed $PAM_{0.3}$-$BMIM{:}Cl_{0.6}$-GO_1	72.29	12.97	10.96	3.78

[a] All of the element contents displayed are counted by atom%.

Table S2. Comparison of the tensile strength, elongation at break, Young's module, toughness, and 180° bending angle between $PAM_{0.3}$-$BMIM$:$Cl_{0.6}$-GO_1 film developed in this work and reported typical ionic thermoelectric films.[1-3] Here PVA is the abbreviation for poly(vinyl alcohol), PMMA is the abbreviation for polymethylmethacrylate, SWCNT is the abbreviation for single-wall carbon nanotube.

Samples	Tensile strength (kPa)	Elongation (%)	Young's module (kPa)	Toughness (MJ m^{-3})	180° bending ability	Ref.
$PAM_{0.3}$-$BMIM$:$Cl_{0.6}$-GO_1	219.7	389	84.1	0.4	Yes	This work
PAM-Fe^{2+}/Fe^{3+}	50	250	~30	~0.08	Yes	[1]
PVA-Fe^{2+}/Fe^{3+}	120	220	~25	~0.26	N.A.	[2]
PMMA-SWCNT-Sn^{2+}/Sn^{4+}	32	260	~16	~0.05	Yes	[3]

References

(1) Yang, P.; Liu, K.; Chen, Q.; Mo, X.; Zhou, Y.; Li, S.; Feng, G.; Zhou, J. Wearable Thermocells Based on Gel Electrolytes for the Utilization of Body Heat. *Angew. Chem. Int. Ed.* **2016**, *55*, 12050-12053.

(2) Gao, W.; Lei, Z.; Zhang, C.; Liu, X.; Chen, Y. Stretchable and Freeze-Tolerant Organohydrogel Thermocells with Enhanced Thermoelectric Performance Continually Working at Subzero Temperatures. *Adv. Funct. Mater.* **2021**, *31*, 2104071.

(3) Wu, G.; Xue, Y.; Wang, L.; Wang, X.; Chen, G. Flexible gel-state thermoelectrochemical materials with excellent mechanical and thermoelectric performances based on incorporating Sn^{2+}/Sn^{4+} electrolyte into polymer/carbon nanotube composites. *J. Mater. Chem. A* **2018**, *6*, 3376-3380.